Author:
Yang, Chaolong

Title:
Electrochemical study of bismuth chalcogenides

Electrochemical Study of Bismuth Chalcogenides

By

Chaolong Yang

H. H. Wills Physics laboratory
UNIVERSITY OF BRISTOL

A dissertation submitted to the University of Bristol in accordance with the requirements of the degree of DOCTOR OF PHILOSOPHY in the Faculty of Science.

May 2021

Word count:

ABSTRACT

Bismuth chalcogenides have been studied as thermoelectric materials, layered materials and topological insulators. They have shown considerable promise in many areas, including but not limited to energy conversion, surface catalysis and quantum computing. However, there is still a long way to go before some of the most exciting applications become practical. One important constraint is their stability in air or solution. Although the studies of bismuth chalcogenides after exposure to air or water have led to different conclusions, the majority of work shows that air or water can modify their surface chemistry and electronic properties.

Here, X-ray photoelectron spectroscopy was used to measure in-situ cleaved, air exposed, electrochemically modified and thiol functionalized single-crystal $Bi_2Te_{0.9}Se_{2.1}$ samples. The results not only demonstrated the ability to control their surface chemistry in an electrochemical environment but also confirmed the feasibility of thiol functionalization. Pourbaix diagrams were used to identify probable products for electrochemical oxidation and reduction. For thiol functionalization, the difference between 1,5′-pentanedithiol and 1-pentanethiol was also discussed.

Next, electrochemical scanning tunnelling microscopy experiments were carried out for different bismuth chalcogenides in pH 3 electrolyte. The images for freshly cleaved samples showed atomically smooth terraces and steps with height equal to the expected quintuple layer thickness (1 nm). After electrochemical oxidation, clear surface dissolution accompanied by pit formation was observed. With increasing oxidation time, these pits only expanded in the lateral direction, keeping a pit depth of about 1 nm. Three probable dissolution modes were discussed to explain the positive correlation between the pit coverage and the oxidation time.

Electrochemical impedance measurements were carried out for freshly cleaved, pre-oxidized and subsequently reduced single-crystal Bi_2Se_3 samples in pH 7 electrolyte. Electrochemical oxidation significantly increased the Bi_2Se_3 charge transfer resistance whereas electrochemical reduction had the ability to lower the transfer resistance to its original value. Electrochemical scanning tunnelling microscopy experiments were also carried out in pH 7 electrolyte to link surface morphology with impedance data. The images and Pourbaix diagrams suggested that the increase of charge transfer resistance may be attributed to bismuth oxides.

Metal electrodeposition on bismuth chalcogenides was also studied with the same set-up. A preliminary study of Ag deposition was recorded. Reversible epitaxial growth of bismuth films on single-crystal Bi_2Se_3 surface was observed.

ACKNOWLEDGEMENTS

Firstly, I would like to thank my supervisor Walther Schwarzacher for his support throughout my doctoral studies. He has helped me so much in the last three years, not only with my research project but also with my daily life. His enthusiasm and devotion to this work have inspired me to overcome a series of difficulties to become a capable researcher. His unremitting efforts to improve my experimental skills as well as my spelling and grammar have helped me to finish my studies and the thesis. There is no doubt that the knowledge and experiences which I got from him would benefit my future life. I would like to thank Richard Brooke for his time spent mentoring me at the start of my studies and for all the work developing the experimental set-up. He also helped me to learn about British culture and become a member of the research community. Our hard works in the labs and those pleasant conversations in pubs are memorable. I would like to thank Yingkai Huang and Mark Golden at the University of Amsterdam and Fengqi Song at Nanjing University for providing high-quality samples. I would like to thank Rashida Parveen for her great help on electrochemical works and for all the delicious food she prepared for group dinner. Many thanks to Mattia Cattelan for his guidance on X-ray photoelectron spectroscopy. Many thanks to Neil Fox for all the gold evaporation and for being the interviewer of my annual progress monitoring. Many thanks to Natasa Vasiljevic for her helps on my study, especially for those helpful discussions on electrochemistry. Many thanks also to Magnus Loutit at the physics electronics workshop for the repair of the experimental equipment.

I am extremely appreciative of the great amount of help I have received from our group members Gary Sitbon, Keisha Michael, Nathan Missault, Frederick Cook, Sarah Alsalhi and Aswathi Koorikkat. It is amazing to work with you guys! Thanks for sharing ideas, experimental equipment and emotions.

I would like to thank the China Scholarship Council (CSC) for its financial support.

Finally, I would like to thank my friends and family, especially my parents and my girlfriend Yefeng Lin for their emotional support throughout my PhD studies. Thanks for their understanding and waiting.

AUTHOR'S DECLARATION

I declare that the work in this dissertation was carried out in accordance with the requirements of the University's Regulations and Code of Practice for Research Degree Programmes and that it has not been submitted for any other academic award. Except where indicated by specific reference in the text, the work is the candidate's own work. Work done in collaboration with, or with the assistance of, others, is indicated as such. Any views expressed in the dissertation are those of the author.

SIGNED: ..... DATE: .....

TABLE OF CONTENTS

LIST OF FIGURES

Figure **Page**

CHAPTER 1

INTRODUCTION

The main goal of the work described here is to study the surface chemistry of the single-crystal bismuth chalcogenides in an electrochemical environment, and in particular, to investigate the effects of electrochemical oxidation, electrochemical reduction and electrochemical redeposition. A series of experiments were carried out to characterize the sample surfaces then evaluate the effects of the electrochemical treatments. Chemical treatments are also investigated for comparison. Furthermore, electrodeposition of metal materials on bismuth chalcogenides expands the research scopes. Since the methods and strategies used to study bismuth chalcogenides under electrochemical control are also suitable for other chalcogenides or layered materials, this thesis could provide a reference for electrochemical study of similar systems.

This chapter will introduce the research object of the thesis and the basic concepts of the research tools.

1.1 Bismuth chalcogenides

Bismuth chalcogenides have attracted the attention of multidisciplinary researchers because they can play a variety of roles in different research areas.

One of the important research areas is thermoelectricity. The thermoelectric figure of merit (ZT) is a well-established metric to evaluate thermoelectric materials. It is calculated from the Seebeck coefficient (S), electrical resistivity (ρ) and thermal conductivity (K), see equation 1.1. Bismuth chalcogenides possess narrow band gaps, giving them both a high Seebeck coefficient and a low electrical resistivity, therefore a high ZT . Bi_2Te_3 was reported to be one of the best performing currently available n-type thermoelectric materials [3-5]. Furthermore, complex bismuth chalcogenides were studied and suggested to have lower lattice thermal conductivity, therefore higher ZT [6]. A peak ZT of 1.4 (increased about 40%) at 100°C was achieved by a p-type nanocrystalline BiSbTe bulk alloy [7].

(1.1) $$ZT(T) = (S^2/\rho K)T$$

Bismuth chalcogenides consist of strongly bonded quintuple layers (QLs) with the layer structure chalcogenide - Bi - chalcogenide - Bi - chalcogenide. The QLs are weakly bonded to each other via van der Waals interactions. As layered materials, intercalated ions or atoms can be used to modify their electronic structure and optical/magnetic properties [8, 9]. Chemical intercalation of zero-valent metals into 2D Layered Bi_2Se_3 nanoribbons was reported [10]. This method allowed intercalation of metal atoms such as Ag, Au, Co, Cu, In, Ni and Sn.

Furthermore, bismuth chalcogenides Bi_2Te_3 and Bi_2Se_3 are model topological insulators (TIs). They behave as insulators in bulk but possess topologically protected metallic surface states (topological surface states - TSS) [11-16]. These surface states are topologically protected due to a non-trivial topological index of the material and cannot be removed without magnetic impurities (robustness of TSS). Spin and momentum locking in these topological states lead to new ways of generating a spin-polarized current, paving the way for novel types of spintronic devices [17-21]. In addition, dissipation-less spin currents can be generated in TSSs because backscattering is forbidden [22-24]. These would lower energy consumption and related heat effects for information transmission.

Figure 1.1 shows the band structure of topological insulator. The two branches of the topological surface states are spin-polarized. This coupling is knowns as spin-momentum locking. The linear energy-momentum relation of these surface states leads to “Dirac cone” structures in three-dimensional

momentum space. The vertexes of the "Dirac cone" structures are the "Dirac points" (Figure 1.1 only shows the cross-section of one "Dirac cone"). The position of the "Dirac points" varied from the composition of the materials. Angle-resolved photoemission spectroscopy (ARPES) is a powerful method to reveal the band structure of topological insulator, see Figure 1.2. The surface states and the Dirac point of Bi_2Se_3 are clear. Furthermore, Ref.[11] and [25] indicate that doping of topological insulator is an efficiency way to tune the relative position of "Dirac points" to the Fermi level (Figures 1.2 and 1.3). Therefore, Fermi level of the $Sn_{0.01}Bi_{1.99}Te_2Se$ samples used in the experiments should be shifted, although measuring the band structure is beyond the scope of the thesis.

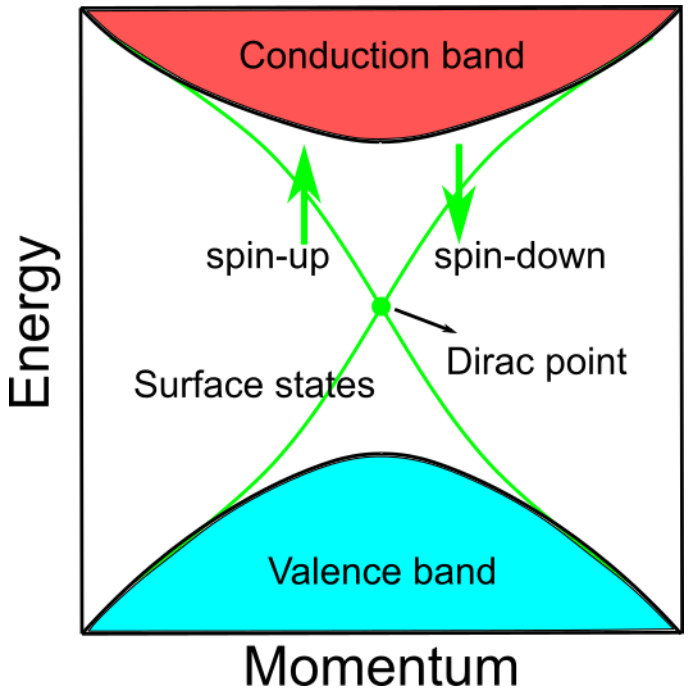

Figure 1.1. Band structure of topological insulators.

The topological surface states also make bismuth chalcogenides interesting candidates for catalysis. These states provide fast and dissipation-less electron transport channels for electrochemical reactions. Due to their robustness, topological surface states may also serve as a robust electron bath for the charge transfer during chemical reactions [26]. Both positive and negative effects on the hydrogen evolution reaction for different metal clusters supported on Bi_2Se_3 were reported [26, 27]. Significant photochemical and electrochemical hydrogen evolution with Bi_2Te_3 and Bi_2Se_3 as catalysts were also observed [28, 29]. Furthermore, the combination of transition metal dichalcogenides and bismuth

chalcogenides may improve catalytic efficiency. Heterostructured MoS_2/Bi_2Se_3 nanoflowers with higher hydrogen evolution reaction activity than pristine MoS_2 and Bi_2Se_3 was reported [30].

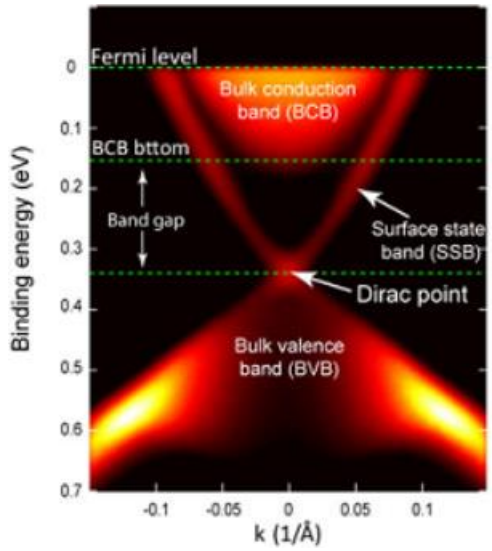

Figure 1.2. ARPES of the topological insulator Bi_2Se_3. Adapted from Ref.[11]

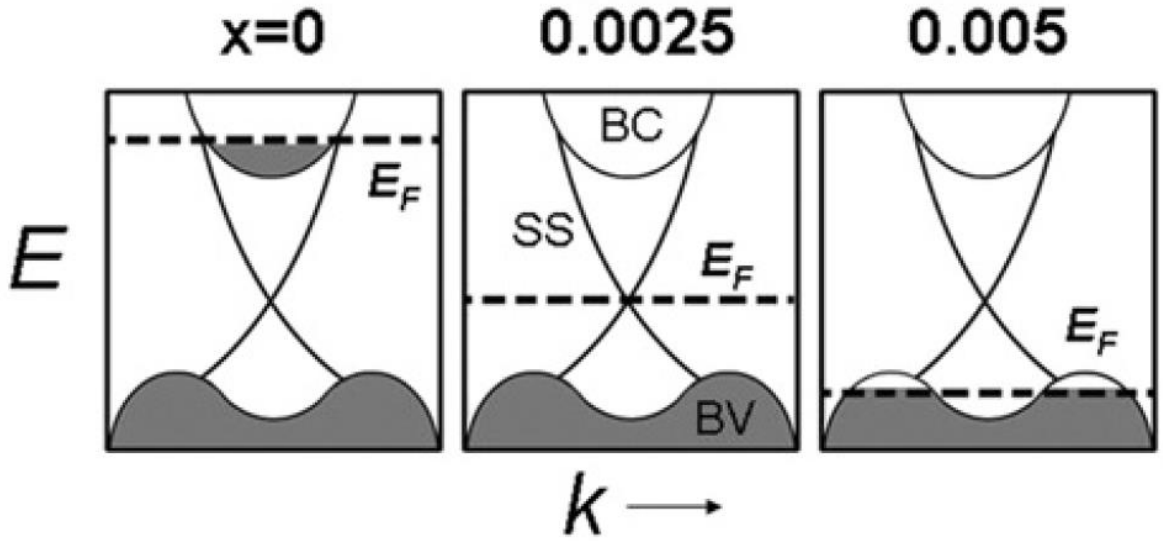

Figure 1.3. Diagrams showing the change of the bulk Fermi level of Ca-doped $Bi_{2-x}Ca_xSe_3$. Adapted from Ref.[25].

1.2 Electrochemistry

A reduction-oxidation (redox) reaction is a type of chemical reaction that involves a transfer of electrons between two species. The loss of electrons is called oxidation, while the gain of electrons is called reduction. Consequently, atoms or molecules which lose electrons are the oxidation products, while

atoms or molecules which gain electrons are the reduction products. The reaction follows the charge conservation principle. Therefore oxidation products and reduction products coexist to keep the net amount of charge unchanged.

A redox reaction that is caused by an external voltage or accompanied by an electric current is called an electrochemical reaction. Electrochemistry is the branch of physical chemistry that studies electrochemical reactions and related phenomena. The application of a predetermined potential or current to an object is called electrochemical control. It is an inexpensive method to protect the surface from oxidation and a powerful tool to modify surface chemistry. Since bismuth chalcogenides are easily affected by surface oxidation and their exotic properties strongly depend on their surface chemistry, the study of bismuth chalcogenides under electrochemical control is of great importance.

Various electrochemical techniques such as cyclic voltammetry (CV), electrochemical impedance spectroscopy (EIS) and electrochemical scanning tunnelling microscopy (EC-STM) will be discussed. These techniques were carried out using a three-electrode arrangement or a four-electrode arrangement based on the former. For the three-electrode arrangement, the working electrode, the counter electrode and the reference electrode play different roles. The voltage is applied between the working electrode and the electrolyte by a potentiostat. Therefore the reaction of interest is expected to occur on the working electrode. The counter electrode drives a current through the cell to balance the charge added or removed by the working electrode. The reference electrode provides a stable and well-defined reference potential to measure and control the potential of the working electrode. Since the reference electrode acts as a reference during electrochemical experiments, no current is passed through this electrode.

Before discussing the electrochemical experiments of bismuth chalcogenides, several basic but very important concepts are introduced (based on Ref.[31]).

1.2.1 Electrical double layer

The electrode-solution interface behaves like a capacitor. At a given potential, there will exist an excess or deficiency of electrons (q^M) in a very thin layer (<0.1 Å) on the electrode surface, and an excess of either cations or anions (q^S) in solution in the vicinity of the electrode surface. At all times, q^M and q^S have the same absolute value, but different signs. Therefore, the interface could be characterized by

a double-layer capacitance, C_d . However, C_d is often a function of potential, which is different with the voltage-independent real capacitors.

In constructing models for interfacial structure, the solution side of the double layer is thought to be made up of several "layers". The closest region to the electrode contains absorbed solvent molecules and specifically adsorbed species. Since the dipole moments of the solvent molecules induce a strong interaction with ions which is known as solvation, the ions in the solution are covered by solvation shells. For specifically adsorbed species, parts of the solvation shells break, hence the species can be tightly bound to the electrode surface. The reactions between the electrode and these species strongly depend on their chemical properties, therefore the term "specifically" uses. The locus of the electrical centres of the specifically adsorbed species is called the inner Helmholtz plane (IHP), which is at a distance x_1 . Solvated ions can only approach the electrode to a distance x_2 . The reactions between the electrode and these ions are independent of their chemical properties because only long-term electrostatic forces are involved. Therefore, these ions are said to be nonspecifically adsorbed. The locus of centres of the nearest solvated ions is called the outer Helmholtz plane (OHP). The three-dimensional region for nonspecifically adsorbed ions to distribute is called the diffuse layer. It extends from the OHP into the bulk solution. The thickness of the diffuse layer depends on the reaction time and the diffusion coefficients of involved species.

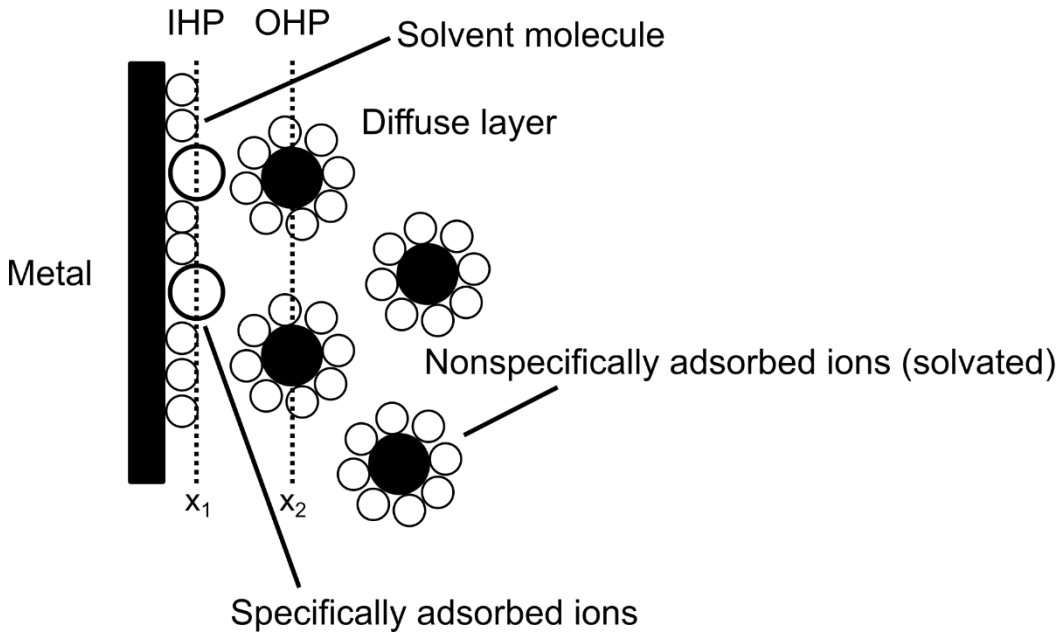

Figure 1.4. Diagram of the electrical double layer model.

1.2.2 Butler-Volmer equation and exchange current

If the electron transfer process is sluggish compared to mass transfer, the reaction is determined by electrode kinetics. Consider two substances A and B that are linked by simple reactions:

(1.2) $$A \underset{k_b}{\overset{k_f}{\rightleftharpoons}} B$$

The rates of the forward and reverse reactions are proportional to the concentrations of A and B:

(1.3) $$\begin{aligned} v_f &= k_f C_A \\ v_b &= k_b C_B \end{aligned}$$

Therefore, the net conversion rate of A to B is given by:

(1.4) $$v_{net} = k_f C_A - k_b C_B$$

From experimental facts, the rate constants k has the form:

(1.5) $$k = Ae^{-E_A/RT}$$

Where E_A is the activation energy and can be understood as the change in standard internal energy in going from one of the minima to the maximum in the reaction picture. Therefore, the rate constants could be written as:

(1.6) $$k = Ae^{-T\Delta S/RT} e^{-(\Delta H - T\Delta S)/RT} = A' e^{-\Delta G/RT}$$

Considering the changes of $\Delta G_f'$ and $\Delta G_b'$ caused by the change of electrode potential $\Delta E = E - E^{0'}$ for a one-electron process, their relationships are: $|\Delta G_f'| + |\Delta G_b'| = F(E - E^{0'})$ (see Figure 1.5), where F is the Faraday constant.

Therefore, ΔG_f and ΔG_b could be written as:

(1.7) $$\begin{aligned} \Delta G_f' &= \alpha F \Delta E \\ \Delta G_b' &= -(1-\alpha) F \Delta E \end{aligned}$$

Where $0 < \alpha < 1$ is the transfer coefficient.

The rate constants are:

$$
\begin{aligned}
k_f &= A_f \exp(-\Delta G_{0f} / RT)\exp(-\alpha f(E-E^{0'})) = k_{f0}\exp(-\alpha f(E-E^{0'}) \\
k_b &= A_b \exp(-\Delta G_{0b} / RT)\exp((1-\alpha) f(E-E^{0'})) = k_{b0}\exp((1-\alpha) f(E-E^{0'}))
\end{aligned}
\tag{1.8}
$$

Where $f = F / RT$.

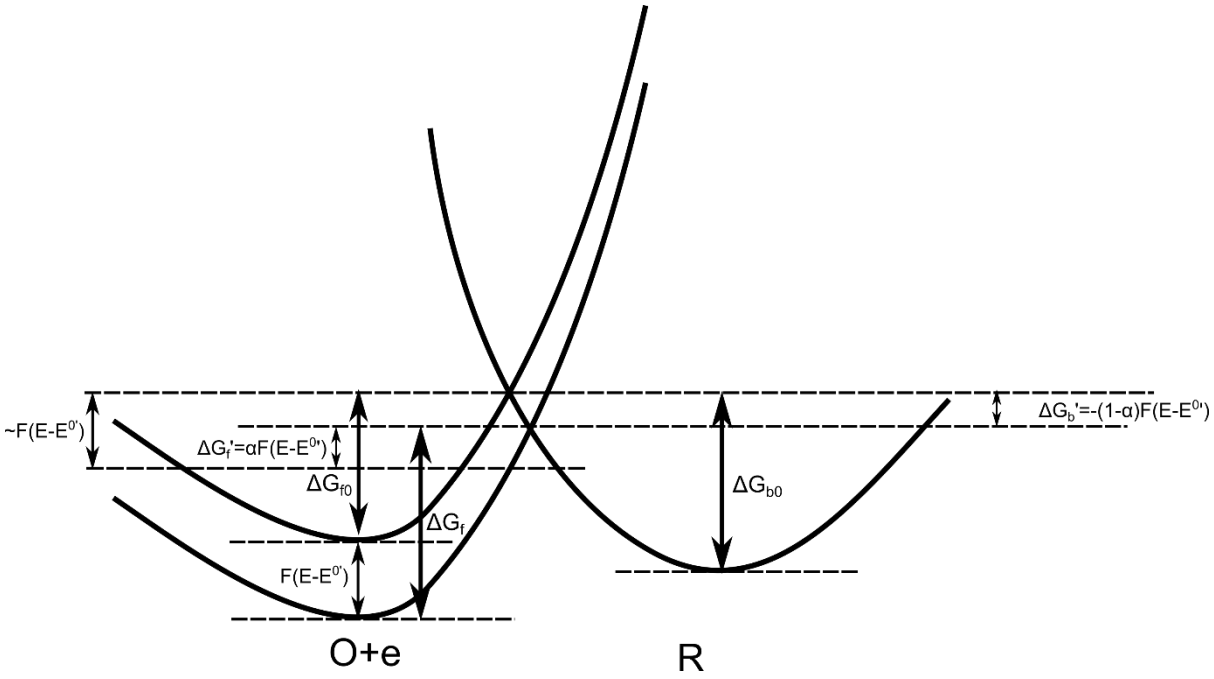

Figure 1.5. Diagram for derivation of equation 1.7.

If the potential $E^{0'}$ is chosen to let $k_{f0} = k_{b0} = k_0$ (k_0 is known as the standard rate constant), the net current is (combination of equation 1.4 and equation 1.8):

$$
i = FAv_{net} = FAk_0[C_O(0,t)e^{-\alpha f(E-E^{0'})} - C_R(0,t)e^{(1-\alpha) f(E-E^{0'})}] \tag{1.9}
$$

Equation 1.9 is known as the Butler-Volmer formulation of electrode kinetics. At equilibrium, the net current is zero. The surface concentrations are equal to bulk concentrations. Magnitude of the balanced forward and backward currents is the exchange current i_0 :

$$
i_0 = FAk_0 C_{Obulk} e^{-\alpha f(E_{eq}-E^{0'})} = FAk_0 C_{Rbulk} e^{(1-\alpha) f(E_{eq}-E^{0'})} \tag{1.10}
$$

Nernst relation (for one-electron process) can be derived from equation 1.10:

$$
C_{Obulk} e^{-\alpha f(E_{eq}-E^{0'})} = C_{Rbulk} e^{(1-\alpha) f(E_{eq}-E^{0'})} \tag{1.11}
$$

$$\frac{C_{Obulk}}{C_{Rbulk}} = e^{f(E_{eq}-E^{0'})}$$

$$E_{eq} = E^{0'} + \frac{1}{f}\ln(\frac{C_{Obulk}}{C_{Rbulk}}) = E^{0'} + \frac{RT}{F}\ln(\frac{C_{Obulk}}{C_{Rbulk}})$$

To work with i_0, equation 1.9 can also be expressed as the current-overpotential equation:

(1.12) $$i = i_0[\frac{C_O(0,t)}{C_{Obulk}}e^{-\alpha f\eta} - \frac{C_R(0,t)}{C_{Rbulk}}e^{(1-\alpha)f\eta}]$$

where $\eta = E - E_{eq}$ is the overpotential.

1.2.3 Diffusion limitation

Consider an electrochemical reaction, when a stable current is obtained, the rates of all reaction steps in a series are the same. The facile steps cannot reach their maximum rates because they have to wait the most sluggish step to dispose their products or creates their reactants. Therefore, the rate of the overall reaction is controlled by the most sluggish step called the rate-determining step (RDS). This rate-determining step could be mass transfer, electron transfer at the electrode surface, chemical reactions preceding or following the electron transfer or other surface reactions. If mass transfer is the rate-determining step, which means that the rates of other steps are very rapid compared to the mass-transfer process, the rate of the electrode reaction is governed by the rate at which the electroactive species is brought to the surface by mass transfer. The reaction is said to be diffusion limited.

For one-dimensional diffusion, Fick's first law states that the flux $J(x,t)$ is proportional to the concentration gradient $\frac{\partial C}{\partial x}$:

(1.13) $$J(x,t) = -D\frac{\partial C(x,t)}{\partial x}$$

To derive this equation, assume $N(x)$ and $N(x+\Delta x)$ molecules are immediately to left and right of location x with an area A, where Δx is the step size (Figure 1a). During the time increment Δt, half of them move Δx in either direction by the random walk process. Therefore, the net flux $J(x,t)$ through x is given by:

(1.14) $$J(x,t) = \frac{1}{A}\frac{\frac{N(x)}{2} - \frac{N(x+\Delta x)}{2}}{\Delta t} = \frac{\Delta x^2}{2\Delta t}\frac{C(x) - C(x+\Delta x)}{\Delta x}$$

where $D = \frac{\Delta x^2}{2\Delta t}$ is the diffusion coefficient.

The species into and out of a space between location x and $x + \Delta x$ with an area A (Figure 1b) is given :

$$\Delta N = (J(x) - J(x + \Delta x))A\Delta t \tag{1.15}$$

Therefore the change in concentration at x is:

$$\frac{\partial C(x,t)}{\partial t} = \frac{\Delta N}{A\Delta x \Delta t} = \frac{J(x,t) - J(x+\Delta x,t)}{\Delta x} = -\frac{\partial J(x,t)}{\partial x} \tag{1.16}$$

Combination of equation 1.13 and equation 1.16 yields:

$$\frac{\partial C(x,t)}{\partial t} = D\frac{\partial^2 C(x,t)}{\partial x^2} \tag{1.17}$$

which describes the change in concentration C with time (Fick's second law).

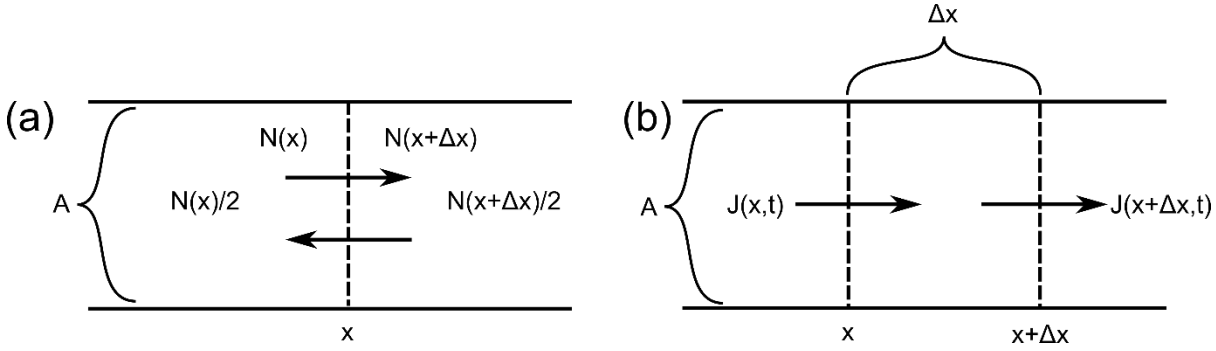

Figure 1.6. Diagrams for derivation of equation 1.13 and equation 1.17.

Under the boundary conditions:

$$\begin{aligned} &C(x,0) = C_{bulk} \\ &\lim_{x\to\infty} C(x,t) = C_{bulk} \\ &C(0,t) = 0 \text{ (for } t > 0) \end{aligned} \tag{1.18}$$

solution of the diffusion equations is the Cottrell equation:

$$i(t) = \frac{nFAD^{1/2}C_{bulk}}{\pi^{1/2}t^{1/2}} \tag{1.19}$$

It gives the current-time response for a mass transfer controlled reaction. The current is inversely proportional to the square root of time. Once the reaction begins, the concentration of the reactant at the electrode surface becomes smaller than its concentration in bulk solution and the thickness of the diffusion layer increases with time. If the reactant is being disposed as fast as it can be brought to the

electrode surface, the reaction reaches the maximum rate and the concentration of the reactant at the electrode surface is zero. In this case, the concentration gradient could be simply evaluated as the division of the bulk concentration and the thickness of the diffusion layer. Therefore, the concentration gradient decreases with time. According to Fick's first law, one could expect that the reaction rate also decreases with time.

1.2.4 Other related concepts

Open circuit potential, passivation, faradaic current and electrochemical potential are introduced below, because they are concepts related to the subsequent electrochemical experiments.

The open-circuit potential is also called the zero-current potential or the rest potential. It is the potential measured when a high impedance voltmeter is placed across the electrochemical cell.

Passivation refers to a material becoming less affected or corroded by the environment. The process involves creation of a shielding layer (usually an oxide layer) via chemical reaction with other reactants or spontaneous oxidation in the air. In the thesis, passivation refers to the increasing of the resistance to electrochemical oxidative dissolution. It may be attributed to the residual or redeposited oxides, but it could also be caused by the decreasing of the dangling bonds on the surface.

The faradaic current is the current generated by the reduction or oxidation of some chemical substance at an electrode. If there are several redox reactions occurring simultaneously, the net faradaic current is the algebraic sum of all the faradaic currents flowing through an indicator electrode. For an electrochemical reaction, the mass of reactants consumed or products created at the electrode is directly proportional to the faradaic current I and the reaction time t.

(1.20) $$m = KIt$$

Where K is the electrochemical equivalent, which represents the mass transported by 1 coulomb of electric charge.

For an inert metal electrode contact with a solution, the equilibrium condition is that the Fermi levels of the two phases be equal, this process is the alignment of the Fermi levels. In an electrochemical system, the Fermi level of the species is the electrochemical potential μ_e. It is related to the chemical potential μ and the electrical energy $zF\Phi$.

(1.21) $$\mu_e = \mu + zF\Phi = \mu^0 + RT\ln a + zF\Phi$$

Where μ^0 is the standard chemical potential, a is the activity of the species, z is the charge of the species, F is the Faraday constant, Φ is the potential.

Therefore, the equilibrium condition could be described as the electrochemical potentials of electrons are the same in both phases.

1.3 Scanning tunnelling microscope

The Scanning tunnelling microscope (STM) is an instrument for collecting information about a surface and manipulating its structure at the atomic level based on the concept of quantum tunnelling. In 1981, Gerd Binning and Heinrich Rohrer invented this instrument at the IBM Zurich Research Laboratory. Since the superior spatial resolution of STM and its ability to manipulate an individual atom significantly promoted the development of nanoscience, the invention won them the Nobel Prize in Physics in 1986. Subsequently, many variants were developed for studies in solution, at high pressure or at high temperature in addition to air and ultrahigh vacuum.

Quantum tunnelling describes the phenomenon whereby a particle has the possibility to disappear from one side of a potential barrier and appear on the other side even though the particle does not have enough energy to cross over the top of the barrier.

Considering a one-dimensional rectangular potential barrier, the time-independent Schrödinger equation for the wave function ψ(x) is:

(1.22) $$H\varphi(x) = \left[-\frac{\hbar^2}{2m}\frac{d^2}{dx^2} + V(x) \right] \varphi(x) = E\varphi(x)$$

where H is the Hamiltonian, $\hbar$ is the reduced Planck constant, m is the mass, E is the energy of the particle and $V(x)$ is the potential barrier with height $V_0 > 0$ and width a (the barrier is positioned between $x = 0$ and $x = a$ and can be shifted to any x position without changing the final results).

(1.23) $$V(x) = \begin{cases} 0 & if\ x < 0 \\ V_0 & if\ 0 < x < a \\ 0 & if\ x > a \end{cases}$$

Since the barrier divides the space into three parts, the wavefunction can be written as:

(1.24) $$\varphi_1(x) = e^{ik_1 x} + re^{-ik_1 x} \qquad x < 0$$

$$\varphi_2(x) = Ae^{ik_2x} + Be^{-ik_2x} \quad 0 < x < a$$

$$\varphi_3(x) = te^{ik_1x} \qquad\qquad x > a$$

Where r is the reflection amplitude and t is the transmission amplitude.

(1.25) $$k_1 = \sqrt{\frac{2mE}{\hbar}}$$

Considering the boundary conditions and the continuity conditions, t can be solved as:

(1.26) $$t = 2k_1k_2e^{-ik_1a} / \left[2k_1k_2\cos(k_2a) - i(k_1^2 + k_2^2)\sin(k_2a) \right]$$

If the energy of the particle is larger than the height of the potential barrier ($E > V_0$):

k_2 and the transmission probability T are:

(1.27) $$k_2 = \frac{\sqrt{2m(E - V_0)}}{\hbar}$$

(1.28) $$T = |t|^2 = 1 / \left[1 + \frac{V_0^2 \sin^2(k_2a)}{4E(E - V_0)} \right]$$

Since T is restricted to the interval from 0 to 1, the reflection probability $R = 1 - T$ is larger than zero, which means the particle may be reflected from the barrier with a non-zero probability.

If the energy of the particle is smaller than the height of the potential barrier ($E < V_0$), the situation is different because k_2 is a pure imaginary:

(1.29) $$k_2 = i\sqrt{\frac{2m(V_0 - E)}{\hbar}} = ik$$

(1.30) $$T = |t|^2 = 1 / \left[1 + \frac{V_0^2 \sinh^2(ka)}{4E(V_0 - E)} \right]$$

Equation 1.30 demonstrates that there is a non-zero probability for the particle to be transmitted through the barrier. For $ka \gg 1$ (the weak tunnelling limit), the transmission probability can be simplified:

(1.31) $$T \approx \frac{16k_1^2k^2}{(k_1^2+k^2)^2}e^{-2ka} = Ae^{-2ka}$$

Equation 1.31 means that the transmission is exponentially suppressed with the barrier width.

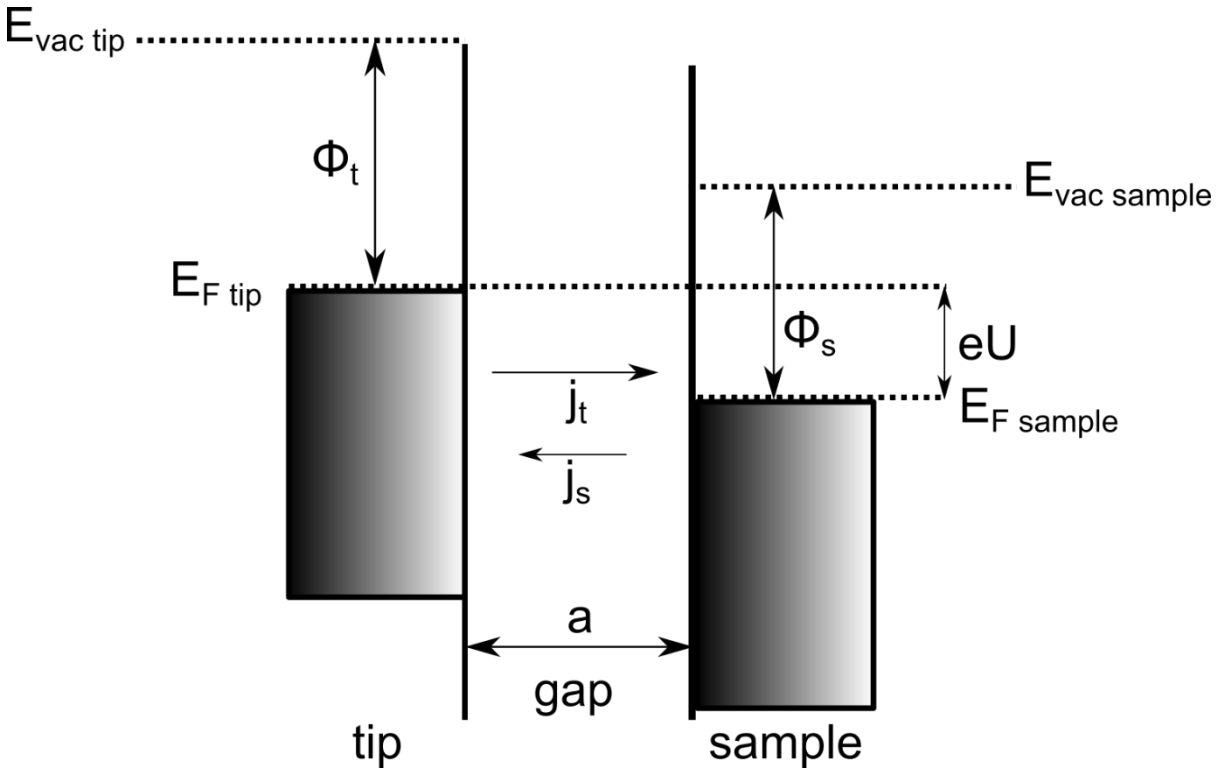

Figure 1.7. Diagram of the STM tunnelling junction.

For STM, consider a tip-vacuum-sample tunnelling junction shown in Figure 1.7. The work function of tip and sample are Φ_t and Φ_s. Without a voltage bias, the probability for the electrons to be transmitted from tip to sample is equal to the probability for the electrons to be transmitted from sample to tip, therefore the net tunnelling current is zero ($j_t = j_s$). If a negative voltage bias U is applied to the tip, Fermi level of the tip shifts eU. If the vacuum level of the tip is set to zero, an electron at the Fermi level has the energy $-\Phi_t$. Electrons that have the energy between $-\Phi_t$ and $-\Phi_t - eU$ could generate a net tunnelling current ($j_{net} = j_t - j_s$). Since eU is very small, the energy of the tunnelling electron is close to $-\Phi_t$, therefore the transmission probability:

(1.12) $$T \propto e^{-2ka}$$

$$k = \frac{\sqrt{2m\Phi_t}}{\hbar} \approx 0.51\sqrt{\Phi_t}\text{Å}^{-1}$$

The local density of states (LDOS) is defined as a sum over n:

(1.13) $$\rho_s(x,E) \equiv \frac{1}{\varepsilon}\sum_{E-\varepsilon}^{E}\left|\varphi_n(x)\right|^2$$

If the ε is small enough, the LDOS represents the number of states per unit sample volume at a certain place and an energy E. If the voltage bias is small enough, the tunnelling current can be written as:

(1.14) $$I \approx \rho_s(0,E_F)e^{-2ka} \approx \rho_s(0,-\Phi_t)e^{-1.02\sqrt{\Phi_t}a}$$

the barrier width a is the distance between the sample and the tip. In normal case, the typical value of Φ is about 4eV, which means that the current would decrease to $1/e^2$ of the original value if the distance increase 1 Å.

If the tip-sample bias is constant and changes in the LDOS are ignored, the tunnelling current reflects the tip-sample distance due to its superior sensitivity to the distance. A fixed tunnelling current results in a fixed tip-sample distance. In this case, the tip's scanning trace is an equidistant line along the sample surface and reflects the surface morphology (constant current mode). If the tip-sample bias is constant and the morphology variations are ignored, the scanning trace reflects the LDOS instead of the morphology. For real measurements, neither LDOS nor morphology fluctuations can be ignored. Therefore, the scanning trace contains information on both the morphology and LDOS.

In practical applications, lateral and vertical manipulation of the tip is achieved by a piezo tube. The tip is attached to a piezo tube consisting of three mutually perpendicular piezoelectric transducers to control the tip position in x,y and z-direction, respectively. These transducers are based on the converse piezoelectric effect, which is the deformation of certain solid materials when an electrical field is applied. This effect is capable of manipulating the tip position due to its reversibility and the linear relationship between the applied electrical field and the deformation.

There are three basic modes for STM measurement: constant current mode; constant height mode and scanning tunnelling microscope (STS) mode. Constant current mode is the most frequently used mode of obtaining STM images. In this mode, an electronic feedback loop is used to adjust the tip/sample distance. The tunnelling current is amplified and compared to a set value. The difference is then

amplified to provide negative feedback to drive the piezoelectric transducers in the z-direction. For example, if the tunnelling current is smaller than the set value, the amplified current would deform the piezo to decrease the tip/sample distance, leading to a larger tunnelling current and vice versa. In the ideal case, constant current means a constant gap between the tip and the surface, therefore the collected data directly related to the surface morphology of the sample.

In constant height mode, the feedback is turned off after approaching the tip to the desired position, then the surface is scanned with the tip at a constant height while measuring the tunnelling current *I* as a function of the tip position. In this case, the surface morphology will be reflected in the fluctuation of the tunnelling current. Since the scanning speed of the constant current mode is restricted by the frequency of the feedback, constant height mode usually provides higher scanning speed than constant current mode. However, if the sample surface is rough in microscale, constant height mode may lead to tip crash.

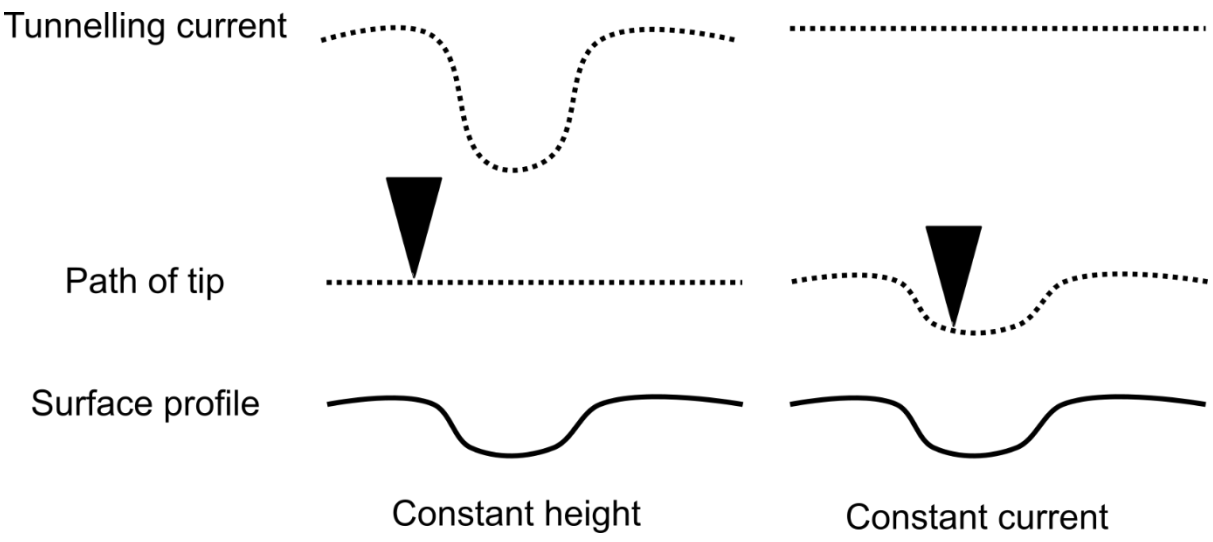

Figure 1.8. Constant height and constant current modes.

Scanning tunnelling spectroscopy (STS) is a mode of scanning tunnelling microscopy in which the voltage between the tip and the sample is varied to obtain the information on the local electronic structure of the surface. The initial stage of the STS measurement is similar to constant height mode. The tip is placed above the sample with a fixed height by turning off the feedback. Next, the electron tunnelling current is measured as a function of electron energy by varying the voltage between the tip

and the sample. The spectra are usually obtained by plotting the sample bias on the X-axis and plotting the change of the current with the bias (dI/dV) on the Y-axis. Besides, the second derivative (d^2I/dV^2) characteristic can be used to study the phonon assisted processes. STS is a powerful tool to investigate the local density of electronic states of the sample surface. However, measuring STS at room temperature is limited by thermal noise. In this thesis, all the STM images are collected in constant current mode.

Conventional STM experiments are carried out in ambient conditions or under vacuum. In principle, samples for STM measurements have to fulfil two conditions: they must be flat and conductive. In practice, samples including metals, doped semiconductors, specific organic molecules and even biological materials can be characterized by STM. Its exceptional imaging resolution is of great help to study atomic-scale structures. Many exotic nanostructures and atomic-scale phenomena were revealed by STM imaging [32-37]. Further information is available from scanning tunnelling spectroscopy (STS), a current-voltage spectroscopic mode of STM to measure the local density of states [38, 39]. It was used to probe surface electronic structure such as surface states, energy gaps, pseudogaps and charge density waves [40-45]. In addition, molecular manipulation using STM can be considered a basic tool of nanoscience [46, 47]. Different manipulation modes, including pushing, pulling and sliding were utilized to move (laterally), rotate or switch the phase of target molecules [48-51].

Since the overall aim of this thesis is to study surface chemistry and characterize the surface morphology of bismuth chalcogenides, an electrochemical scanning tunnelling microscope (EC-STM), which combines a normal STM with electrochemical control, is a particularly powerful tool. The EC-STM measures surface morphology and local electronic properties in an electrochemical environment. It can be used to study physical and chemical processes, including electrochemical redox reactions, electrodeposition, electrocatalysis, adsorption and desorption [52-57]. In particular, the EC-STM is capable of investigating the oxidation and corrosion of an atomically flat surface. For example, the oxidation of 1018 carbon steel in borate medium was characterized by EC-STM [58]. Microstructures consisting of Fe-α or a mixture of Fe-α and Fe_3C as well as the corresponding corrosion mechanisms were identified. Oxidative corrosion of the surface of highly oriented pyrolytic graphite (HOPG) was also studied by EC-STM [53]. The EC-STM images demonstrate that the corrosion occurred first at step edges and then progressed toward terraces. These images also reveal that platinum and oxygen could enhance oxidative corrosion. In other work, the initial stages of the electrochemical oxidation of Au(110) in 0.1M H_2SO_4 was imaged by EC-STM [59]. This process starts with the formation of gold oxide atomic

rows. Conversely, EC-STM can also be used to study the cathodic regeneration of a clean surface from a pre-oxidized surface [60]. Well-ordered oxide-free Cu(100) was generated from an air-oxidized and disordered electrode. In this thesis, EC-STM was also used to study the electrochemical oxidation and reduction of surfaces, but for bismuth chalcogenides.

1.4 Proposed experiments

The proposed experiments and the structure of this thesis are described below. First, in Chapter 2 the technical details of the EC-STM are described. These include the preparation of the samples and the STM tips and the polypyrrole coated quasi-electrodes, as well as the parameters of the EC-STM system and the procedure of a standard EC-STM experiment. In addition, the mechanisms of electrochemical impedance spectroscopy and X-ray photoelectron spectroscopy are also discussed. Electrochemical and X-ray photoelectron spectroscopy measurements for electrochemically modified and thiol functionalised single-crystal $Bi_2Te_{0.9}Se_{2.1}$ are described in Chapter 3. X-ray photoelectron spectroscopy data for air exposed samples are presented as control. The results demonstrate the ability to control and characterize the surface oxidation of single-crystal $Bi_2Te_{0.9}Se_{2.1}$ in an electrochemical environment and confirm the feasibility of further EC-STM experiments. Chapter 4 focusses on EC-STM study of several kinds of bismuth chalcogenides in pH 3.0 0.05M Na_2SO_4 solution. EC-STM images are used to analyse the process of oxidative dissolution. Furthermore, the tip effects are observed and discussed. EC-STM and electrochemical impedance spectroscopy measurements for single-crystal Bi_2Se_3 in 0.1M $NaClO_4$ and 3mM $K_3[Fe(CN)_6]$, 0.1M $NaClO_4$ are described in Chapter 5. The surface morphologies are linked to the electrochemical impedance spectra. These results are discussed in relation to those obtained in Chapter 4. As an extension of the study in Chapter 5, metal electrodeposition on single-crystal Bi_2Se_3 is discussed in Chapter 6. Finally, the conclusion and future plan are discussed in Chapter 7.

CHAPTER 2

MEASUREMENT TECHNIQUES

2.1 Preparation of single-crystal samples

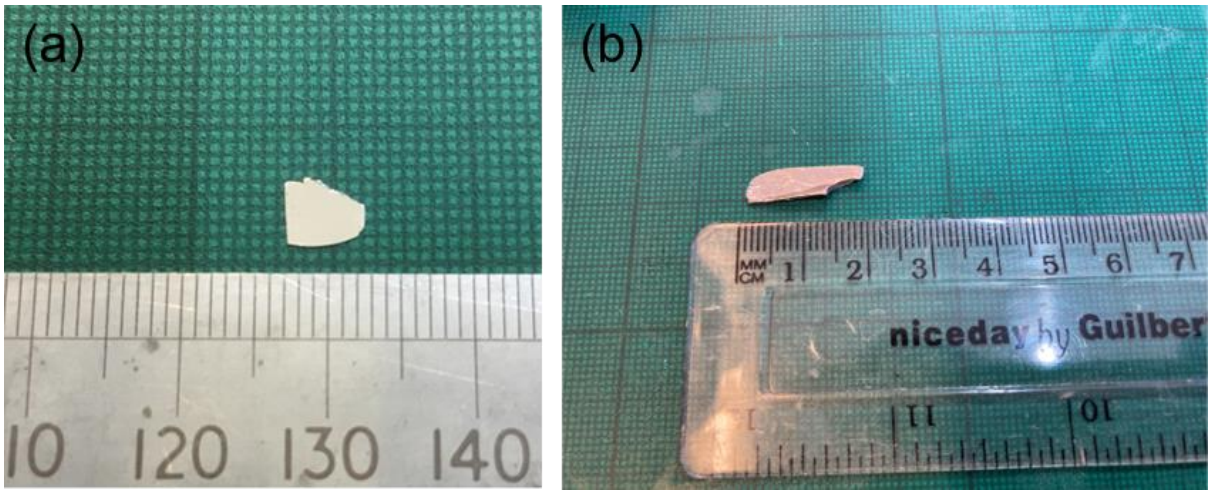

Figure 2.1. Photo of TI crystals. (a) A typical crystal from Amsterdam. (b) A typical crystal from Nanjing.

2.1.1 Fixing the sample and isolating the sample edges

Single crystals of bismuth chalcogenides were grown by a modified Bridgman method. The starting materials were high-purity (99.9999%) elemental Sn, Bi, Se, and Te purchased from Alfa Aesar. Two groups of crystals were prepared by different collaborators, as shown in Figure 2.1. Crystals from the University of Amsterdam were flakes with suitable size for EC-STM measurements, while crystals from Nanjing University had a relatively large size and needed further cutting.

A razor blade was used to cut the crystal. Although the crystal is not dangerous in its bulk state, dust generated during cutting is harmful. Therefore appropriate personal protective equipment (PPE), including respirator, safety goggles and nitrile gloves, is necessary.

The preparation procedure of bismuth chalcogenides samples is introduced. First, the two parts of the silver epoxy (EPO-TEK) were mixed with the required ratio (10:1) by two wooden rods. Next, the mixed epoxy was transferred to the substrate to attach the crystal flake. The substrate was heated to 100°C for 1 hour to cure the epoxy. Finally, No.7 brand transparent nail polish was used to insulate the edge and surrounding area of the flake because it is non-conducting and waterproof. The substrate was heated to 50°C to cure the nail polish

2.1.2 Sample cleaving

A well-prepared sample can be used for several experiments by repetitively cleave the crystal to obtain an oxide-free surface. Cleaving was carried out by sticking carbon tape to the flake and then pulling the tape away in air to leave a freshly cleaved surface.

Cleaving bismuth chalcogenides in air has been reported to coexist with different terminations [61, 62]. For example, cleaving Bi_2Se_3 under conditions where intercalation of ambient gases can occur increased the possibility of getting a Bi-terminated surface, whereas cleaving Bi_2Se_3 in a high vacuum led to a Se-terminated surface. For most of the experiments described in this thesis, samples were stored and cleaved in air because they would be measured in an ambient environment. Although there was a possibility of getting a Bi-terminated surface after cleaving, no terrace with a height of 0.4nm was observed during measurements (0.4nm is the thickness of the expected Bi-terminated structure).

2.2 Cyclic Voltammetry

Cyclic voltammetry is a potential sweep method. During measurement, information of the reaction can be gained by sweeping the potential with time linearly (Equation 2.1) and recording the $i-E$ curve directly. Since the scan rate is a constant, recording current versus potential is equivalent to recording current versus time, but the former is the customary form of representing the data.

For a reversible system, the rate of electron transfer is rapid at the electrode surface, so the ratio of the oxidized species and the reduced species is dictated by the Nernst equation (Equation 2.2) which relates the potential of an electrochemical reaction (E) to the standard electrode potential (E^0), temperature (T) and activities of the oxidized (Ox) and reduced (Red) analyte in the system at equilibrium.

(2.1) $$E(t) = E_i - vt$$

(2.2) $$E = E^0 + \frac{RT}{nF}\ln\frac{(Ox)}{(Red)}$$

In principle, combined equation 2.1 and 2.2 with the boundary conditions (equation 1.18), one could get the mathematical solution of cyclic voltammetry for reversible system. However, the process requires mathematical knowledge such as Laplace transformation and convolution theorem. Therefore, only some useful conclusions are listed [31].

The peak current is:

(2.3) $$i_p \propto n^{3/2} A D^{1/2} C v^{1/2}$$

Where n is the charge of the species, A is the area of the sample, D is the diffusion coefficient, C is the concentration of the species, v is the scan rate.

The potential difference between peak and half-peak is:

(2.4) $$\left|E_p - E_{p/2}\right| = 2.20\frac{RT}{nF} = 56.5/n \text{ (mV)}$$

The potential difference between anodic and cathodic peaks is:

(2.5) $$\Delta E_p = E_{pa} - E_{pc} \approx 2.3\frac{RT}{nF} = 59/n \text{ (mV)}$$

Therefore, the peak current of the reversible reaction is proportional to $v^{1/2}$. Equation 2.4 and 2.5 are useful diagnostics of a reversible reaction.

The cyclic voltammogram can be explained qualitatively. If the electrode potential E is scanned, the concentrations of the species will change continuously. The transition between oxidized and reduced species at the electrode surface leads to a faradaic current, which is observed in the cyclic voltammetry curve (Figure 2.2). The current increases rapidly as more of the reduced species is oxidized at the electrode surface. As the potential is scanned more positive, the concentration of the reduced species is steadily depleted near the electrode as they are converted to oxidized species, and the Faradaic current starts to depend on the delivery of additional reduced species from the bulk solution. In the meantime, the diffusion layer which contains the oxidized species at the surface of the electrode grows, leading to a slow down of mass transport of the reduced species. Thus, the current decreases as the scan continues, which results in the observed oxidation current peak (Figure 2.2). The subsequent electrochemical reduction can be explained the same way. The oxidized species present at the electrode surface are converted to reduced species as the applied potential becomes negative enough. The reduction current is also restricted by the diffusion process, leading to the reduction current peak.

Electrochemical reversibility describes the rate of electron transfer. If the barrier to transfer electrons is low enough, the equilibrium is easy to establish when the applied potential changes, which means that the system remains in equilibrium throughout the potential scan. It also means that the Nernst equation works throughout the potential scan. In this case, the peak current ratio i_{pa}/i_{pc} is 1 and the standard electrode potential E^0 is given by the mean of the peak potentials.

If the barrier is high, the electron transfer rate is slow. The "delay" of electron transfer results in the "delay" of oxidation or reduction reactions, therefore increasing the peak potential separation. In this case, one would expect that the peak potential separation increases with the increase in the scan rate (if the reactions are chemically reversible).

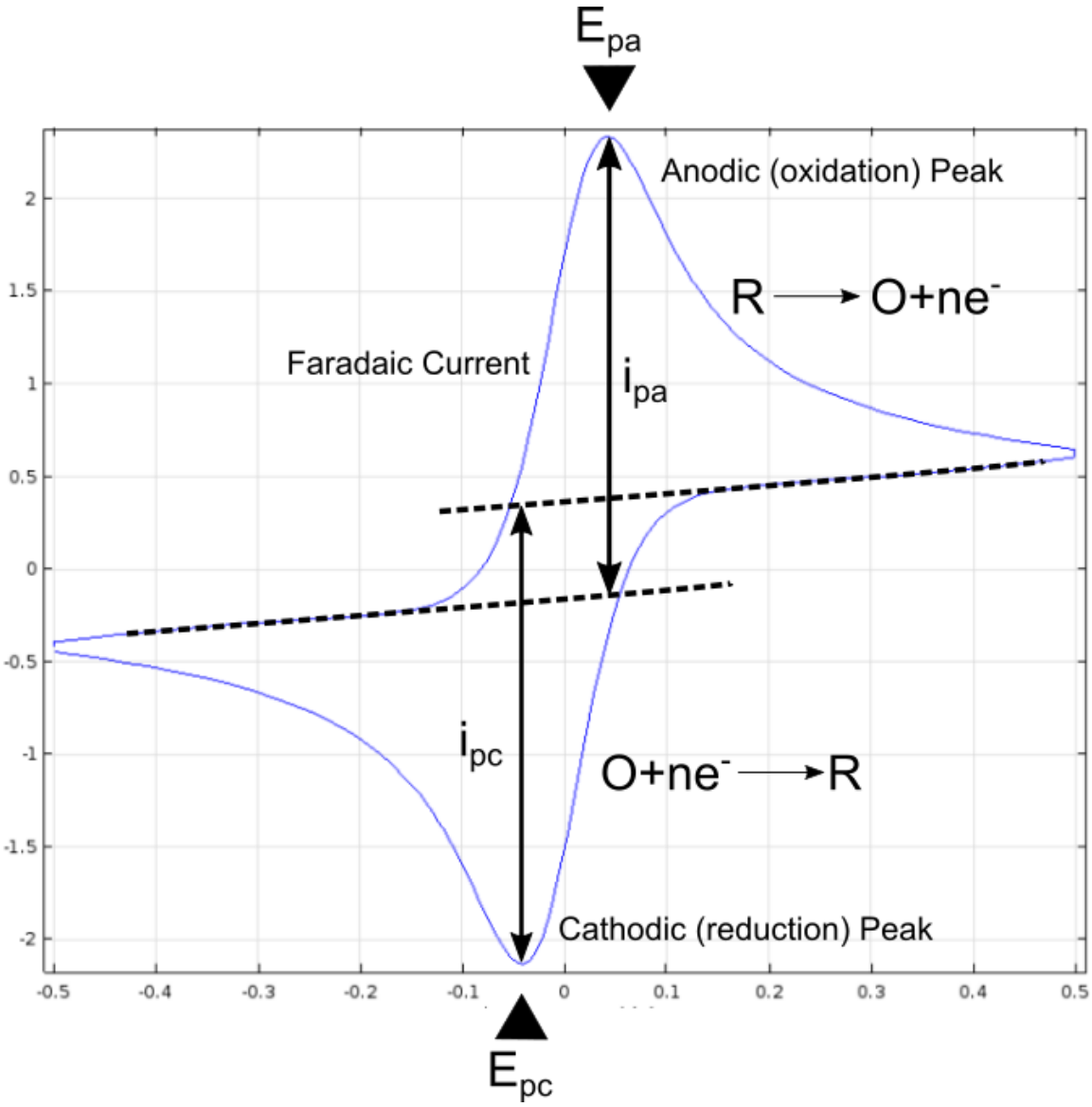

Figure 2.2. A typical cyclic voltammetry curve for an electrochemically reversible process.

2.3 Electrodes, electrochemical cell and STM tips

2.3.1 Selection of electrodes

The selection of the reference electrode depends on several factors. The counter electrode should avoid polarisation, dissolution and passivation during the experiments. Otherwise, it may influence the actual behaviour of the working electrode. It is expected to have no oxidation or reduction peaks in supporting electrolytes within the working window. Therefore, a platinum wire or foil was used as a counter electrode because it is stable within the working window and it does not electrochemically polarise. The selection of the reference electrode is more complicated. Different conventional reference electrodes have different applications. The Silver/Silver Chloride (Ag/AgCl) electrode is the most popular type of laboratory reference electrode due to its simplicity and lack of toxicity. However, if the electrode is used in a high pH solution for a long period of time, hydroxide ions can contaminate the electrode by forming AgOH. In addition, the Ag/AgCl electrode is not suitable for electrolytes that contain halides because its standard electrode potential is very sensitive to traces of bromide ions. The saturated calomel (Hg/Hg_2Cl_2) electrode (SCE) has a reputation of being more robust, but many works reported that the chloride concentration in solution heavily influenced the behaviour of the electrochemical system [63-67]. The Mercury/Mercurous Sulfate (Hg/Hg_2SO_4) electrode (MSE) was used in the experiments that will be discussed in this thesis to avoid chloride ions. A MSE consists of a platinum wire, a mixture of Hg_2SO_4 and liquid mercury, a saturated electrolyte solution of K_2SO_4 and a glass tube with a porous ceramic electrode liquid junction. The relevant half cell equation is shown in equation 2.6.

(2.6) $$H_2SO_{4(s)} + 2e^- \rightarrow 2Hg_{(liq)} + SO_4^{2-}$$

The MSE electrode in saturated K_2SO_4 has an open circuit potential of +0.65V with respect to a normal hydrogen electrode (NHE). It can work well in acidic or neutral pH electrolytes, which meets the demand of the proposed experiments.

2.3.2 Preparation of polypyrrole quasi-electrode

For EC-STM experiments, because the space of the cell is quite limited, conventional reference electrodes cannot be used without the specially designed adaptor. An alternative was a polypyrrole (ppy) quasi-electrode fabricated by coating a platinum wire with polypyrrole [68]. Compared to other simple alternatives such as Pt wire, it performed quite well.

The polypyrrole quasi-electrode was prepared by electropolymerisation of pyrrole. The composition of the electropolymerisation solution was 0.01M pyrrole and 0.1M tetrabutylammonium hexaflurophosphate in acetonitrile. A 0.25mm Pt wire was annealed with a blow torch to get rid of any oxide or polypyrrole residue. The electropolymerisation was carried out by a conventional potentiostat using a standard cyclic voltammetry procedure. The potential of the Pt wire was swept from -1.0V to 0.7V vs MSE 50 times. The potential was held at 0.4V for 10 seconds after the 50 cycles to partially oxidise the ppy film. The quasi-electrode was found to have open circuit potentials of +0.31V vs SCE and -0.11V vs MSE, which is consistent with the expected potential difference between SCE and MSE of -0.4V.

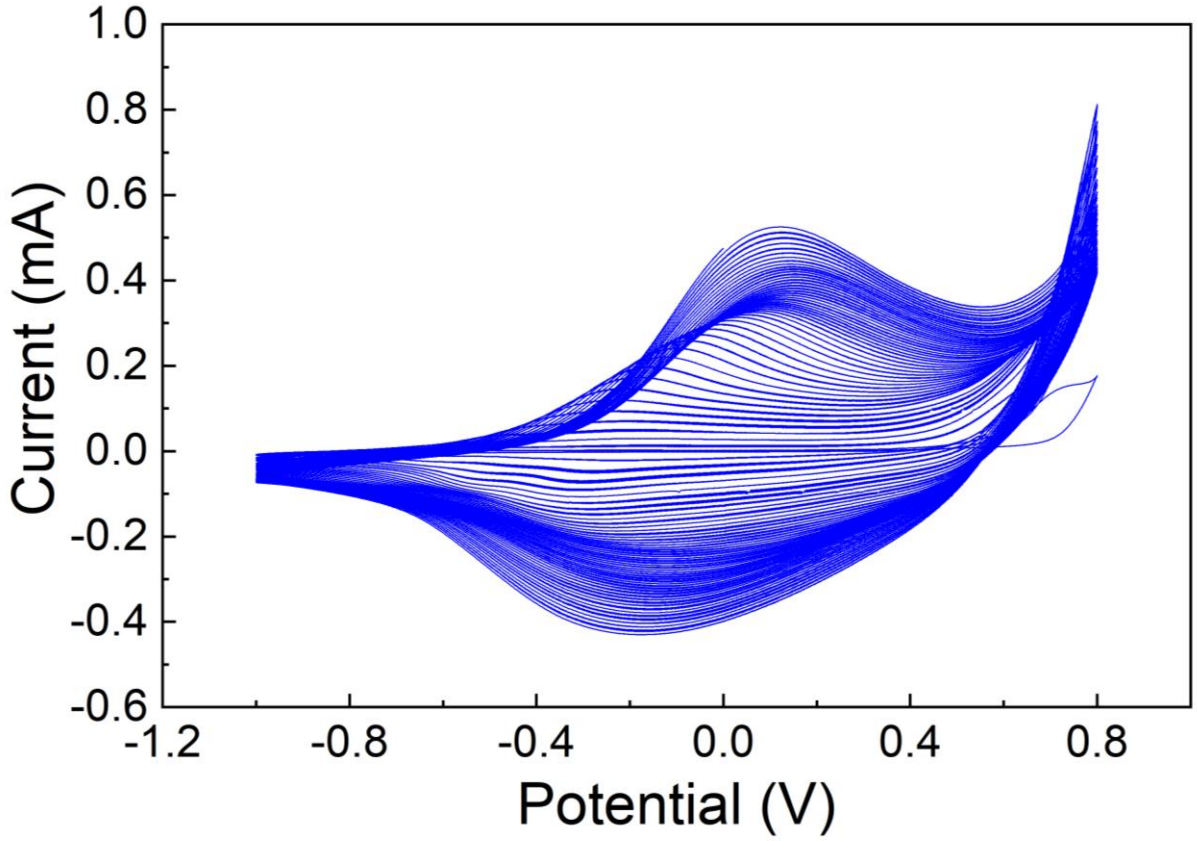

Figure 2.3. An example of the current vs potential curves (50 cycles) during the electropolymerisation of pyrrole. The scan rate was 0.1V/s.

2.3.3 Electrochemical cell

In this section, electrochemical cells for different techniques are introduced. For normal cyclic voltammetry and electrochemical impedance spectroscopy, a conventional three-electrode cell was used. A sample isolated with Kapton tape (See Figure 2.4) was used as a working electrode. A Pt wire

or a Pt foil was used as a counter electrode, while a mercury-mercurous sulfate electrode was used as a reference electrode.

For EC-STM experiments, a home-made Teflon cell with a Pt ring counter electrode was used. Figure 2.5 shows the cell and a polypyrrole coated Pt wire quasi-reference electrode. This quasi-reference electrode was easy to operate and normally fairly stable. However, the ppy-coated layers exfoliated progressively with increasing working time and it behaved unstably if the pH of the electrolyte changed. An adaptor was designed by Dr. Richard Brooke (see Figure 2.6) to use a conventional reference electrode. The adaptor provided enough space to hold the glass vessel of conventional reference electrodes. A 10mL syringe was used to store the electrolyte. The whole adaptor was connected to the electrochemical cell via an electrolyte filled PTFE tube (acting as a Luggin capillary).

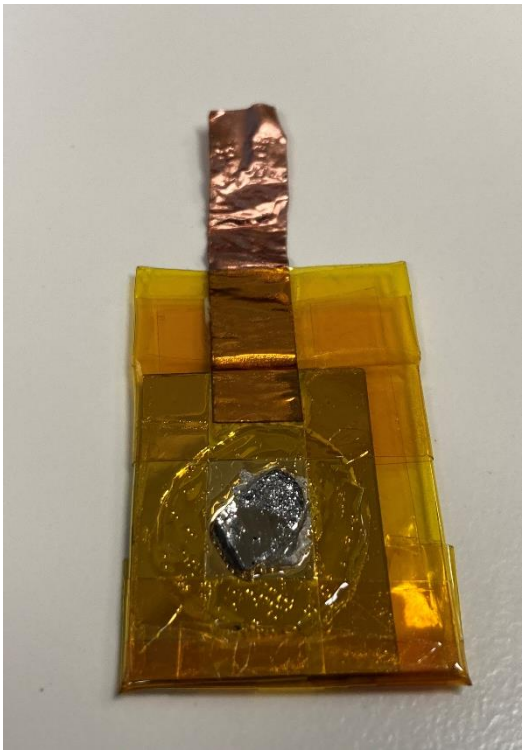

Figure 2.4. The photo of a sample for conventional electrochemical experiments.

This set-up is more reliable than the former, but there is a risk of leaving some bubbles in the tube or inside the adaptor, which may lead to loss of electrochemical control. Therefore, the open circuit potential (OCP) was checked once the cell was filled. If the OCP had an unexpected value, it usually meant that the link between the reference electrode and the electrochemical cell had problems. These

could usually be solved by disconnecting the adaptor and refilling it. The EC-STM cell was emptied by glass pipette before the operations mentioned above.

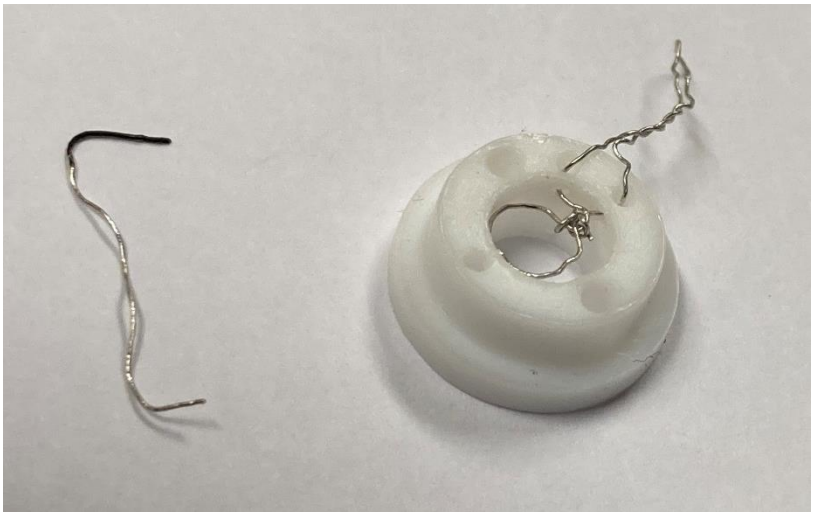

Figure 2.5. The photo of a STM cell and a polypyrrole coated Pt wire quasi-reference electrode.

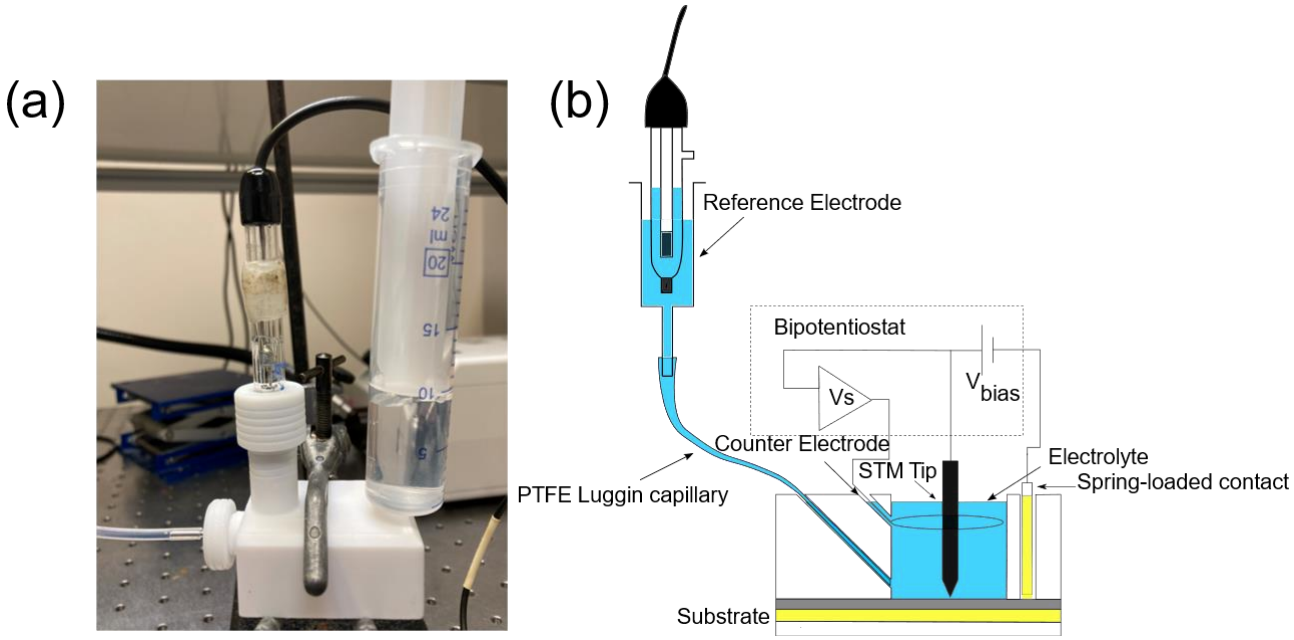

Figure 2.6. (a) A photo of the adaptor set-up. (b) Diagram of the four-electrode set-up.

The four-electrode set-up is based on operational amplifiers. Figure 2.7 is the circuit diagram of operational amplifier. The two input terminals are called the inverting input (top) and the noninverting input (bottom). The fundamental property of the amplifier is that the output e_0 is the inverted, amplified voltage of the input e_s.

(2.7) $$e_0 = -Ae_s$$

Where e_s is the voltage difference between the inverting input and the noninverting input, A is the open-loop gain. Two connection lines that provide power to the operational amplifier are omitted in the diagram.

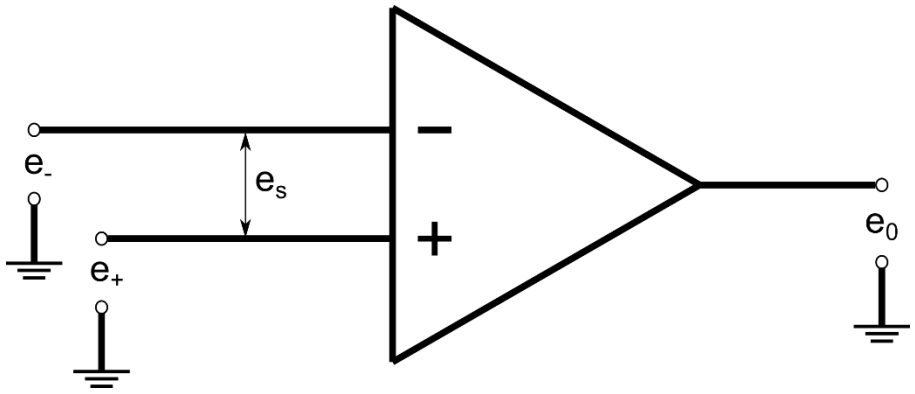

Figure 2.7. Diagram of an operational amplifier.

Potentiostat is based on the current adders circuit of operational amplifier, see Figure 2.8.

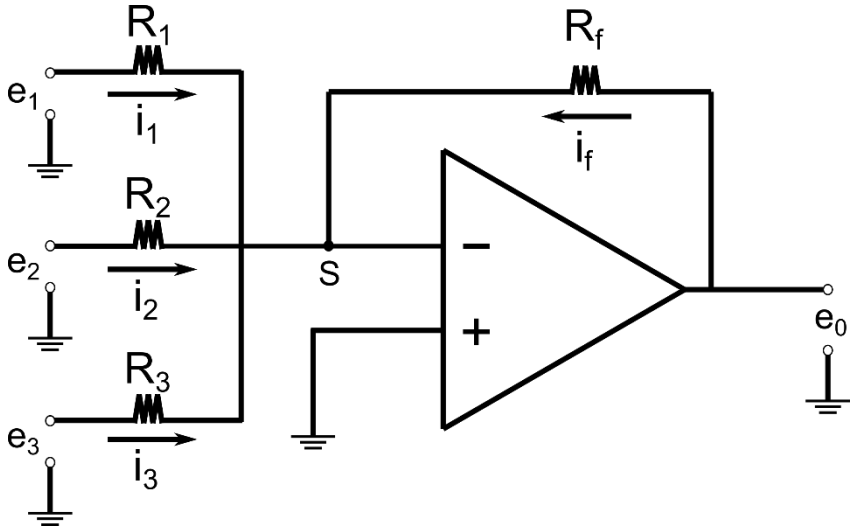

Figure 2.8. The current adders circuit.

According to Kirchhoff's law, the sum of all the currents into the summing point S must be zero.

(2.8) $$i_f = -(i_1 + i_2 + i_3)$$

(2.9) $$\frac{e_0}{R_f} = -(\frac{e_1}{R_1} + \frac{e_2}{R_2} + \frac{e_3}{R_3})$$

Therefore, the output is the sum of independently scaled input voltages.

Bipotentiostat based on the adder concept are shown in Figure 2.9 (Ref. [31]). Electrode 1 is controlled as the working electrode in a simple potentiostat (the left part of Figure 2.9) whereas electrode 2 uses electrode 1 as a reference point (the right part of Figure 2.9). If the potential of electrode 1 is set to be e_1, electrode 2 is offset with respect to electrode 1 by $\Delta e = e_2 - e_1$, where e_2 is the potential of electrode 2 with respect to the reference.

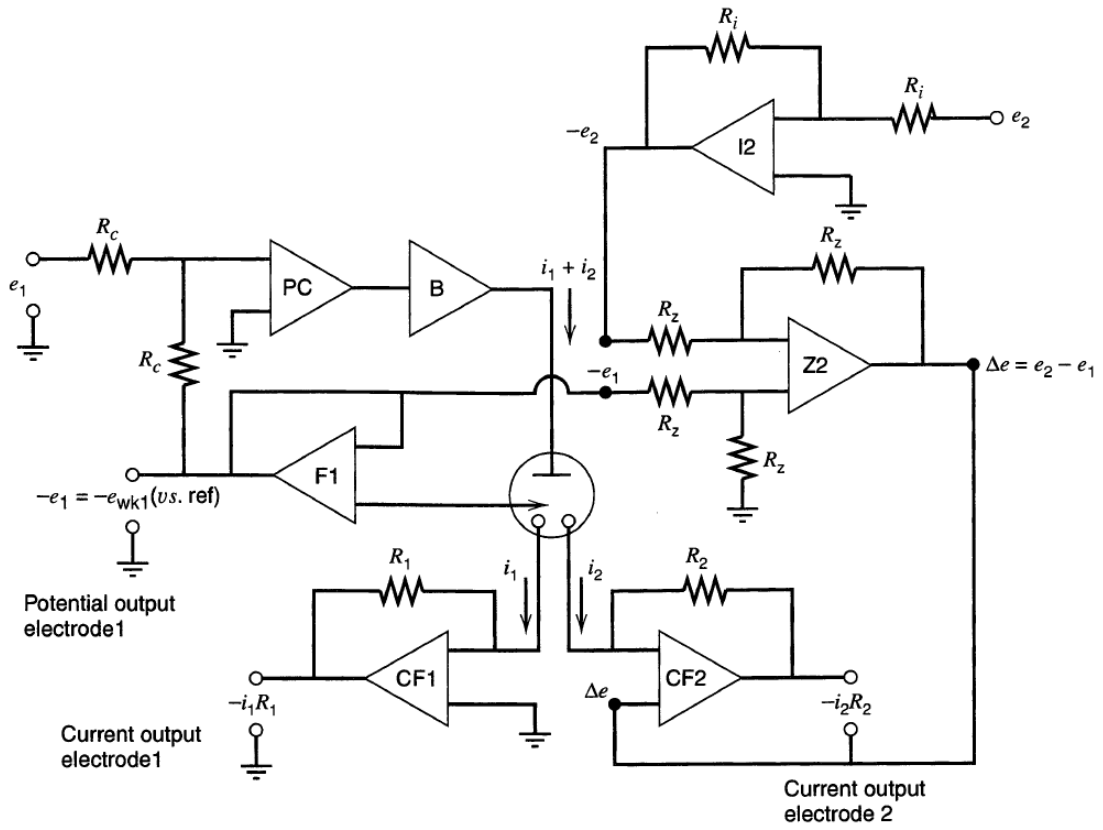

Figure 2.9. Circuit of the bipotentiostat. Ref.[31]

2.3.4 Preparation of STM tips

Au STM tips were prepared by electrochemical etching as described in Ref.[69]. The composition of the etching solution was 50% ethanol with 50% HCl. A Pt ring with a diameter of around 10mm was used as a cathode. The Au wire was fixed by a crocodile clip and then positioned through the centre of the ring. The heights of the ring and the wire were adjusted to submerge them in the solution by approximately 5mm, see Figure 2.10. A Keithley 2400 source meter was used to apply 2.4 V DC voltage

to the Au wire. During the etching process, Au experienced oxidative dissolution at the anode while hydrogen evolution happened at the cathode and released considerable amounts of bubbles. With increasing etching time, the radius of the Au wire at the air-solution interface decreased and the wire tapered towards a point close to the interface. Finally, the bottom part of the wire detached when the constriction could no longer support its weight, whereas the top part of the wire was rinsed with copious ethanol and Milli-Q water (resistivity 18.2MΩ.cm at 25°C) then collected as a STM tip.

A typical current vs time curve is shown in Figure 2.11. The progressively decreased current was accompanied by frequent spikes. Once the current fell below the threshold value 0.001A, the DC voltage was automatically switched off via software written in LabView by Dr.Stuart Box. The whole process took 10 min to 15 min. In an electrochemical environment, the typical faradaic current for uncoated tips is much larger than the tunnelling current. If the total current is dominated by the faradaic current, EC-STM measurements are unrealizable. Therefore, the tip was insulated with Apiezon wax to minimize the electrochemical current. A soldering iron with a split tip was held in a clamp stand and heated to the desired temperature (usually 230°C to 245°C, depending on the wax). Molten wax was coated on the split tip to fill the slit. The STM tip was driven by an adjustable holder to pass through the slit. During this process, the STM tip was coated with wax. The coating process was sometimes repeated 2 or 3 times to ensure that the whole tip was covered by wax, but too many repetitions may damage the apex of the tip. Because of surface tension, the very end of the tip remained exposed when the wax cured, which made the tip still suitable for detecting tunnelling current.

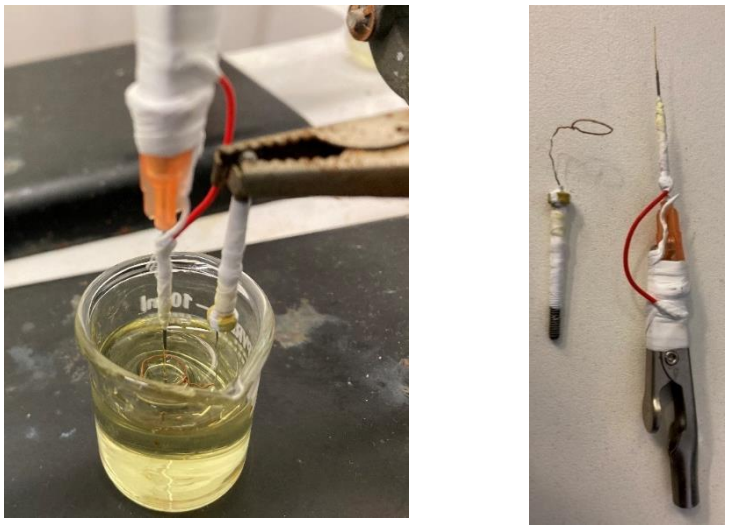

Figure 2.10. Photos of the tip etching set-up.

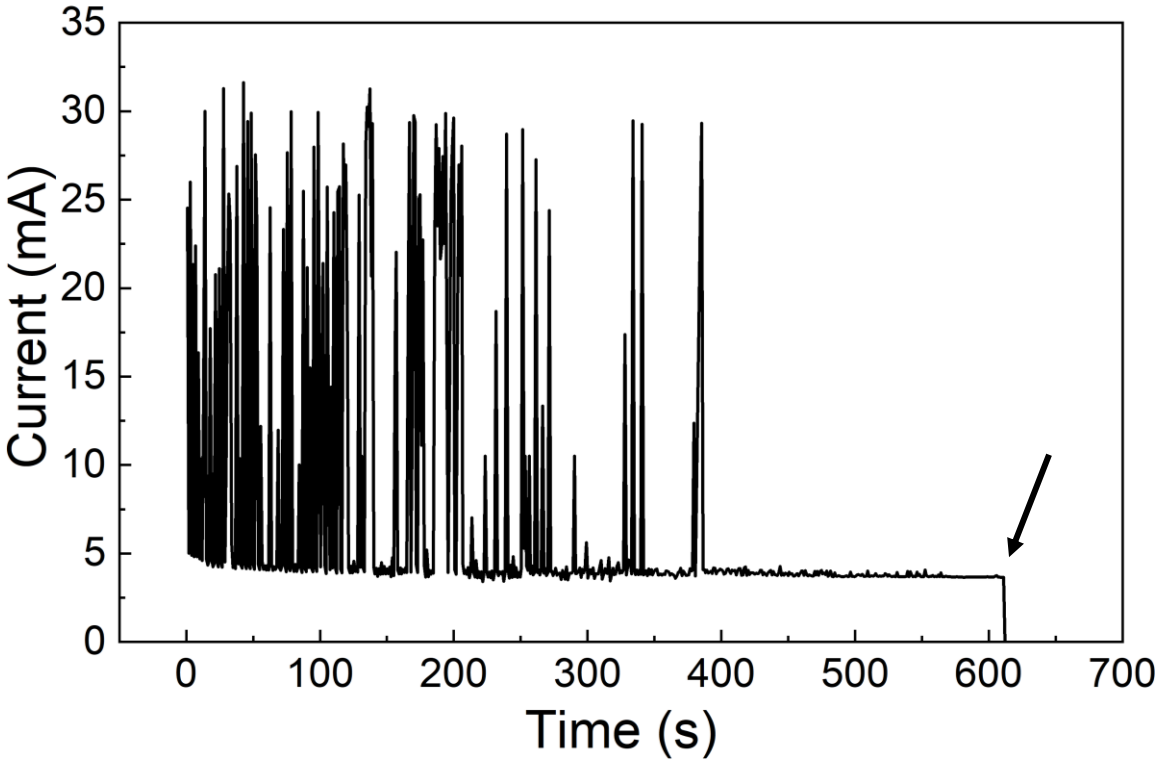

Figure 2.11. An example of the current vs time curve during the etching of an Au STM tip. The arrow indicates the time at which the etching is completed.

2.4 Setting EC-STM experiments

2.4.1 STM Parameters

An Agilent 5100 STM was used for EC-STM study that will be discussed in this thesis. Picoview 1.20 imaging and analysis software package from Keysight Technologies was used for data collection.

There are various parameters to manipulate the STM system (the main window of Picoview is shown in Figure 2.12). Among these parameters, the bias and the setpoint current are used to determine the Z position of the tip due to the negative exponential relationship between the tunnelling current and the tip-sample distance. In general, increasing the setpoint current without changing the bias or decreasing the bias without changing the set point current could bring the tip close to the surface and vice versa. Since the STM tip is grounded, the bias is applied to the sample.

The feedback system tries to minimize the difference between the tunnelling current and the setpoint current after approaching the tip. The strength of the feedback can be adjusted by two parameters: the integral gain and the proportional gain. If the feedback is too low, the response from the controlling

electronics will be slow, which results in artefacts such as apparent "tails" behind protrusions. These appear on the side of a feature that is scanned last. If the feedback is too high, it will introduce high-frequency excitations, which results in noticeable spikes on the topography image and profile lines. For Agilent 5100 STM, these parameters have a default value of 1% and need adjusting during measurements.

Applying a pulse is widely used to adjust the tip condition because it can change the shape of the tip and remove unwanted particles picked up by the tip during the scanning [70, 71]. The applied voltage during the pulse, the pulse duration, and the distance to move the tip during the pulse are adjustable.

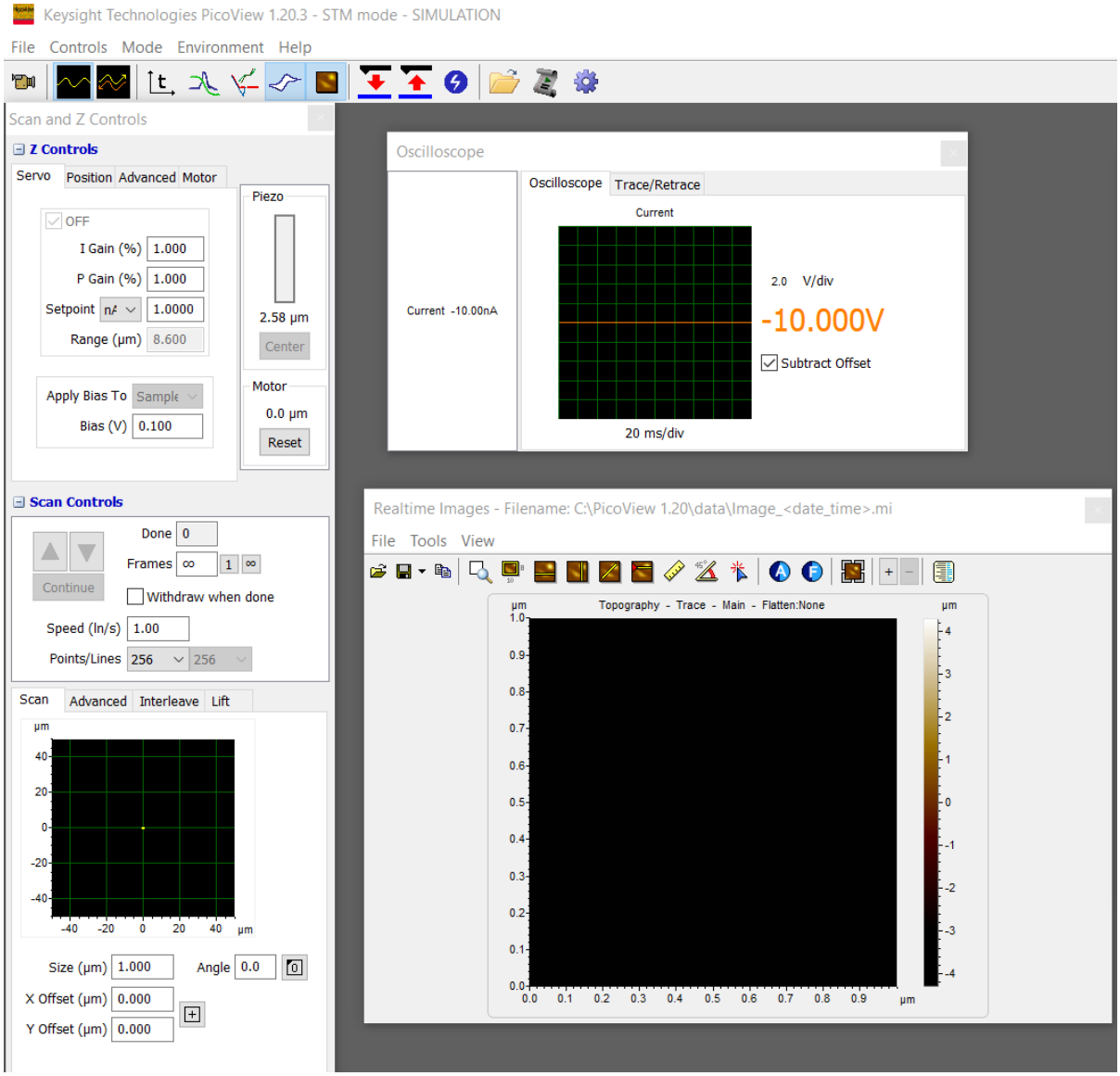

Figure 2.12. The main window of Picoview software.

Since applying pulses may change the local surface morphology, the tip is moved away from the imaging area in advance.

Parameters including the speed of the motor, the interval of withdrawing the tip, and the stop current are used to control Z-direction movement of the tip. Parameters including the scan speed, the size of the scan area, the rotation angle of the scan area, and the position of the scan area are used to control the imaging process. The scan speed is the number of profile lines collected in one second. The speed of the tip can be calculated from the scan speed and the size of the scan area. In general, a higher tip speed can reduce the influence of drift, but it also affects the stability of the tip and the resolution. A lower tip speed is good for collecting high-resolution images, but it requires a small drift rate. The angle of the scan area can be adjusted to check whether a feature in the image is an artefact because the real feature changes with the scanning angle, whereas one that originates from electrical noise remains the same. Switching the scan direction also helps artefacts detection, as scan up and scan down generate different images if there is a constant drift, see Figure 2.13. Furthermore, the overscan function is used to optimize the images. By setting the percentage of extra scan beyond the defined scan area, the beginning (relatively unstable) part of each profile line was not used to construct the images.

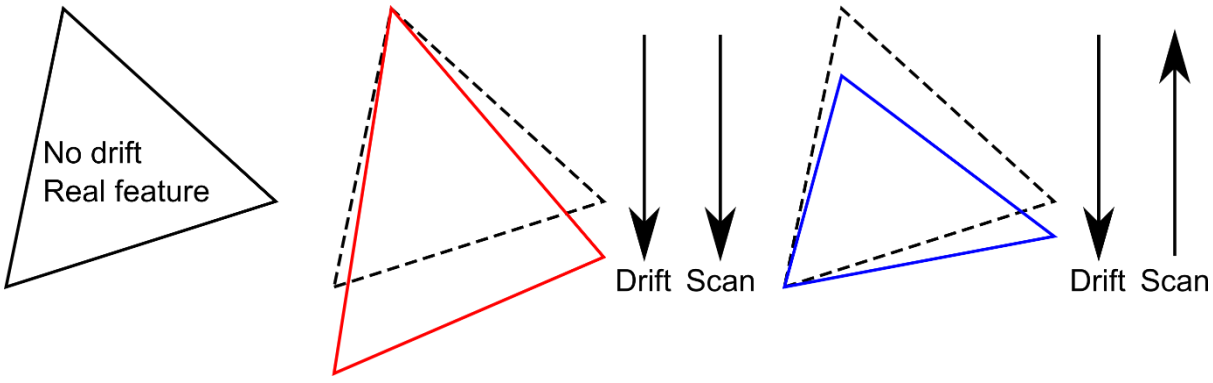

Figure 2.13. Diagrams to show the influences of vertical drift.

Parameters for the electrochemistry part are used to set up electrochemical control. The sample potential is the most basic parameter to determine the potential of the sample versus the reference electrode. The potential of the tip versus the reference electrode can be determined by one of the two dependent parameters: the tip potential or the bias between the sample and the tip. For cyclic

voltammetry technique, the initial potential of the sweep, the lower/upper limit of the sweep, the final potential of the sweep, the sampling interval and the rate of sweep are set before measuring. For pulse voltammetry technique, the initial potential of the sweep, the potential and the duration of each potential step, the final potential of the sweep and the sampling interval are determined before applying pulse steps.

2.4.2 The procedure of an EC-STM experiment

A standard EC-STM experiment consists of four steps: assembling the EC-STM cell; approaching and adjusting the tip; modifying the sample surface; characterizing the sample surface.

A sample prepared as described was fixed on the sample holder by two copper sheets and springs, see Figure 2.14. A spring electrode was used to connect the sample and the sample holder. The connection was checked by a multimeter before approaching the tip. A Pt wire counter electrode was fixed in the EC-STM cell and electrically connected to the sample holder.

If a MSE was used as a reference electrode, it was fixed in an electrolyte-filled adaptor. The adaptor was connected to the Teflon cell via a Luggin capillary while the MSE was electrically connected to the sample holder. If a ppy-coated Pt wire was used as a quasi-reference electrode, it was fixed and connected in a similar way as the counter electrode.

A wax-insulated tip prepared as described was fixed in the tip tube of the scanner, see Figure 2.15. The opposite end of the tip was twisted a little bit to avoid detachment.

The tip-sample distance was invisible because the sample was covered by the Teflon cell. Therefore the rough approach was carried out manually with a bare holder and a bare gold substrate. By rotating the knob of the step motor, a reasonable gap between the tip and the bare substrate was left. The subsequent precise approach was carried out by the STM system. The step motor kept approaching the tip while the tunnelling current was detected. Once the tunnelling current reached the set value, the approach finished.

The tip condition can be estimated from profile lines or images collected during measurements. The strength of the feedback can be evaluated by checking whether there are “tails” behind the measured protrusion or whether there are spikes in the image. If the tip has adsorbed low conductivity contaminants, profile lines show fewer features than usual. Enhanced feedback achieved by increasing the integral/proportional gain can be used to “shake” the tip and get rid of these clusters. Multiple tips

give rise to the artefact of repeated features. Increasing the gain, changing the bias or the tip potential may eliminate these mini tips.

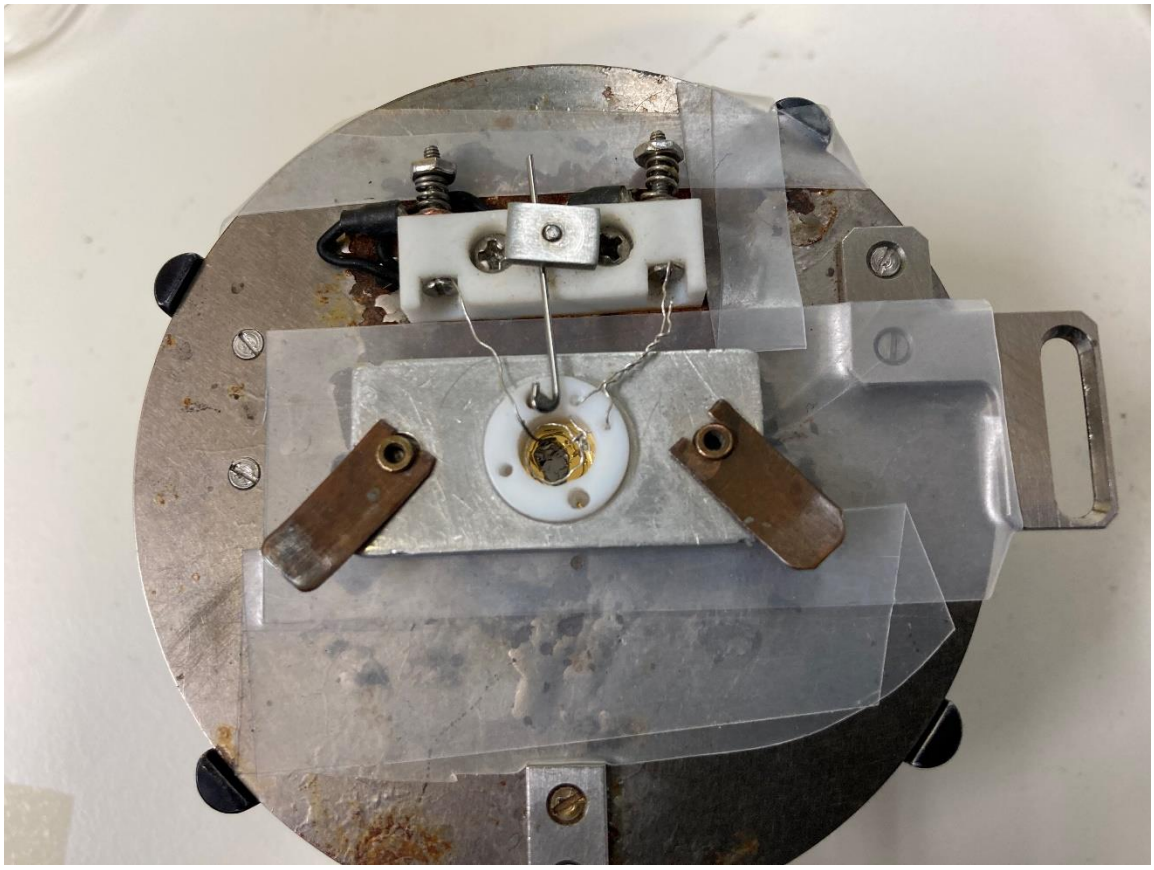

Figure 2.14. Photo of the assembled sample holder.

EC-STM is capable of modifying the sample surface because it supports two techniques: cyclic voltammetry and pulse voltammetry. Cyclic voltammetry technique is performed by repetitively sweeping the potential of the working electrode in a predetermined range and measuring the current at the working electrode simultaneously. Current versus the applied potential traces are plotted. This technique is widely used to study the electrochemical properties of a system, including the electrochemical stability window, the redox potentials, the electrochemical reversibility, and the electron transfer kinetics of the working electrode or the electrolyte [72-76]. Pulse voltammetry technique is based on stepwise changes in the potential of an electrode. Using this technique, electrochemical processes are studied by applying a serial of potential steps and recording the response

currents simultaneously [77-79]. During the modification process, the relative parameters which were introduced in the last section are frequently adjusted. Finally, the sample was imaged by EC-STM with suitable parameters.

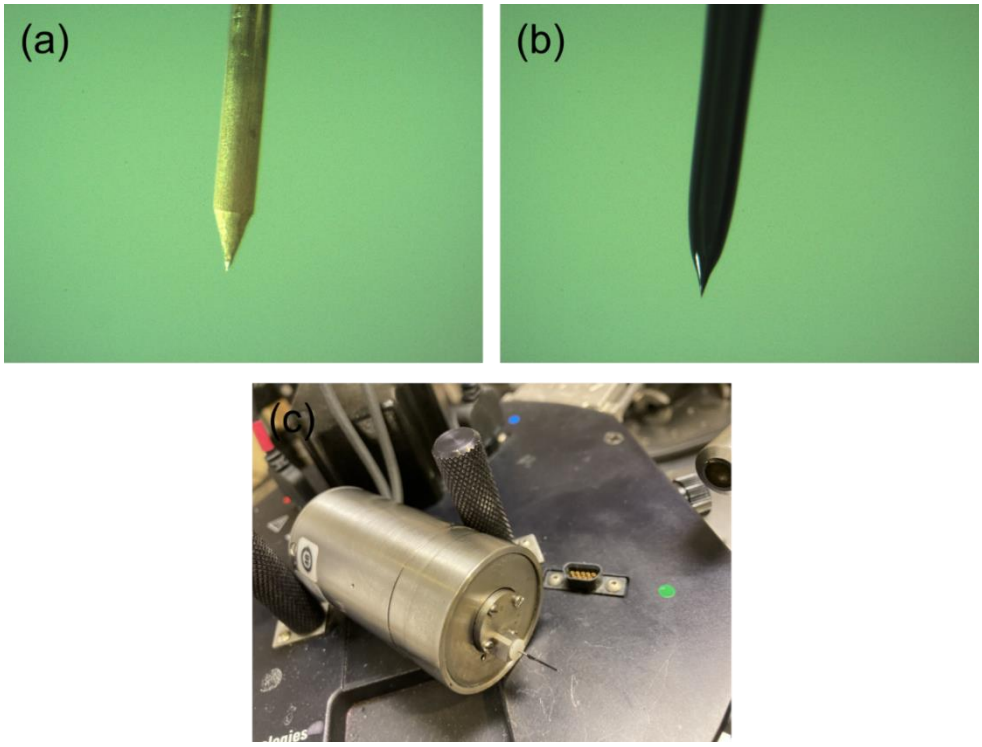

Figure 2.15. Optical microscope images of (a) an electrochemically etched Au STM tip and (b) an Apiezon wax coated Au STM tip. (c) A photo of the STM scanner with a coated Au STM tip.

2.5 Electrochemical impedance spectroscopy (EIS)

2.5.1 electrochemical impedance plots

Electrochemical impedance spectroscopy (EIS) is a perturbative technique for studying the dynamics of an electrochemical process based on its response to an applied potential. During the measurement, a small amplitude AC excitation signal is added to the applied DC polarisation potential. The response current is recorded and analysed to extract resistive and capacitive properties of the electrochemical process.

The impedance spectrum is obtained by varying the frequency of the AC excitation signal, typically from several tens of kHz to 0.1Hz. As the ratio of potential and current for an AC system, the impedance is a complex number that can be presented in two ways. The first is via the real part Z' and imaginary

part Z'' as a function of frequency, while the second is as a vector in the complex plan. The two most popular plots for impedance spectra, the Nyquist plot and the Bode plot, originate from these.

The Nyquist plot is obtained by plotting the real part of the impedance Z' on the X-axis and plotting the negative imaginary impedance $-Z''$ on the Y-axis. It is widely used in electrochemistry because parameters such as the solution resistance and the transfer resistance are easy to read from the plot (if the equivalent circuit is simple enough). However, the Nyquist plot is difficult to understand if the equivalent circuit is complicated.

The Bode plot is a logarithmic plot of the frequency on the X-axis and the impedance and the phase shift on double Y axes. Each component is easy to determine from the Bode plot. The number of time constants corresponds to the number of peaks. In addition, the frequency information which is not visible in the Nyquist plot is well shown in the Bode plot.

Consider the current-overpotential equation (equation 1.12), if the solution is well stirred, the surface concentration is close to the bulk concentration. Therefore, it is simplified to the butler-Volmer equation:

(2.10) $$i = i_0[e^{-\alpha f \eta} - e^{(1-\alpha) f \eta}]$$

If the overpotential η is very small. Considering the approximation $e^x \approx 1 + x$, equation 2.10 can be expressed as:

(2.11) $$i = -i_0 f \eta$$

The ratio $-\eta / i$ is the charge transfer resistance R_{ct}:

(2.12) $$-\frac{\eta}{i} = \frac{1}{i_0 f} = \frac{RT}{i_0 F}$$

Charge transfer resistance is the resistance to the process of electron transfer from one phase to another and can be measured by impedance spectroscopy.

2.5.2 Simple components and equivalent circuits

Three basic components and a typical equivalent circuit will introduce in this section (Ref.[31]).

The resistor follows Ohm's law for both DC and AC currents. The impedance of a resistor only has a real part equal to the resistance R. In the Nyquist plot, the resistor is a single point ($Z' = R, -Z'' = 0$). In the Bode plot, the resistor is two horizontal lines, showing constant impedance ($Z = R$) without phase shift ($\varphi = 0^\circ$).

A capacitor stores electrical energy as an electric field. Its ability to store charge is defined as the capacitance C, the charge that can be stored per unit applied potential. In AC circuits, the impedance of a capacitor can be expressed by equation 2.13, where f is the frequency of the sinusoidal signal. Z' and Z'' for a capacitor (equation 2.14) are obtained by comparing equation 2.13 with the standard form of Z ($Z = Z' + iZ''$). Therefore, a capacitor is a straight line along the Y-axis in the Nyquist plot. The relationship between $\log|Z|$ and $\log f$ is equation 2.15. The phase angle φ is determined by equation 2.16. Hence, a horizontal line ($\varphi = 90^\circ$) and a linear curve with negative slope ($-1/2\pi C$) are plotted in the Bode plot.

(2.13) $$Z_c = -i\frac{1}{2\pi fC}$$

(2.14) $$Z' = 0,\ Z'' = -\frac{1}{2\pi fC}$$

(2.15) $$\log|Z| = -\frac{1}{2\pi C}\log f$$

(2.16) $$\tan\varphi = -\frac{Z''}{Z'}$$
$$\varphi = 90^\circ$$

An inductor is a component that stores energy in a magnetic field when an electric current flows through it. The property of storing energy is defined as the inductance *L*, the ratio of the magnetic flux and the current generating the magnetic flux. The impedance of an inductor can be expressed as equation 2.17. Z' and Z'' (equation 2.18) are extracted from equation 2.17. An inductor is also a straight line along the Y-axis in the Nyquist plot due to the lack of a real part. The impedance-frequency relationship and the phase shift are deduced via the same method as for capacitor (equations 2.19 and 2.20). The Bode plot shows a horizontal line ($\varphi = -90^\circ$) and a straight line with a positive slope ($2\pi L$).

(2.17) $$Z_L = 2\pi ifL$$

(2.18) $$Z' = 0,\ Z'' = 2\pi fL$$

(2.19) $$\log|Z| = 2\pi L\log f$$

(2.20)
$$\tan\varphi = -\frac{Z''}{Z'}$$
$$\varphi = -90^{\circ}$$

An equivalent circuit consists of a series of components and each component represents a part of the electrochemical process. Therefore, the equivalent circuit should create the same impedance spectrum as the real electrochemical process. Randles circuit (Figure 2.16) is the most commonly used equivalent circuit for interpreting impedance spectra. It consists of a resistor R_s, representing the uncompensated solution resistance, in series with a parallel circuit having a capacitor Cdl representing the double layer in one branch and a resistor R_{ct}, representing the charge transfer resistance, in series with a Warburg impedance Z_W representing semi-infinite diffusion, in the other.

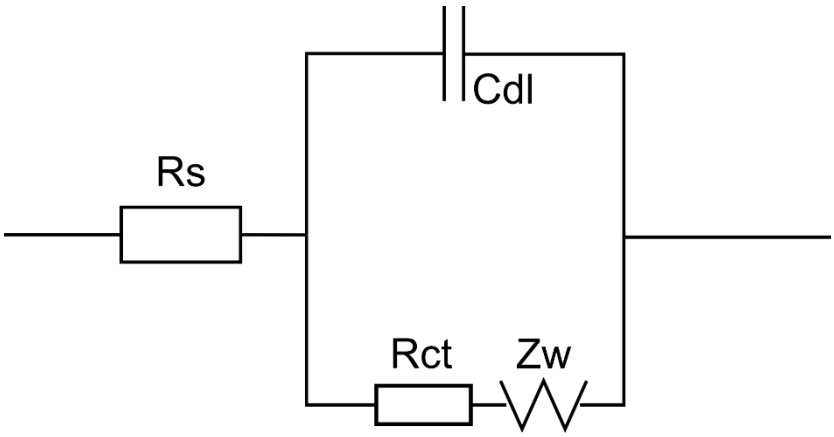

Figure 2.16. Randles circuit. Rs, Cdl, Rct and Zw are represent the uncompensated solution resistance, the double layer capacitor, the charge transfer resistance and the Warburg impedance, respectively.

The Warburg impedance is a virtual electrical component only used to describe the diffusion effect. During an electrochemical process, species close to the electrode interface are consumed. For high AC frequencies, the depletion is not detected. However, at low AC frequencies, there is enough time to deplete active species. Therefore, the EC current decreases due to the lack of species, whereas the applied DC potential remained the same, which increases the impedance. The Warburg impedance Z_W is introduced (equation 2.21) to simulate the increasing impedance, where A_w is the Warburg coefficient.

(2.21) $$Z_w = \frac{A_w}{\sqrt{2\pi f}} + \frac{A_w}{i\sqrt{2\pi f}}$$

The Randles circuit describes a faradaic reaction controlled by semi-infinite diffusion. The current goes through the solution, so there is a serial solution resistance R_s. The faradaic reaction described by the charge transfer resistance occurs in parallel with the charging of the double layer described by the double layer capacitor C_{dl}. The Warburg impedance Z_W is in the same branch as the transfer resistance because the semi-infinite diffusion is associated with the faradaic reaction. At high AC frequencies, the depletion of reactants is not detected. Therefore, the Randles circuit is simplified as R_s in series with a parallel circuit having C_{dl} in one branch and R_{ct} in the other (Figure 2.17a). Consider the $R_{ct}C_{dl}$ parallel circuit:

(2.22) $$Z = \frac{Z_1 Z_2}{Z_1 + Z_2} = \frac{R_{ct}}{iwC_{dl}R_{ct} + 1} = \frac{R_{ct}}{1 + (wR_{ct}C_{dl})^2} - i\frac{wR_{ct}^2 C_{dl}}{1 + (wR_{ct}C_{dl})^2}$$

$$Z' = \frac{R_{ct}}{1 + (wR_{ct}C_{dl})^2}$$

$$Z'' = -\frac{wR_{ct}^2 C_{dl}}{1 + (wR_{ct}C_{dl})^2}$$

$$-\frac{Z''}{Z'} = wR_{ct}C_{dl}$$

$$Z' = \frac{R_{ct}}{1 + (-\frac{Z''}{Z'})^2}$$

$$(Z' - \frac{R_{ct}}{2})^2 + (Z'')^2 = (\frac{R_{ct}}{2})^2$$

The derivation above indicates that the Nyquist plot of the $R_{ct}C_{dl}$ parallel circuit is a semicircle, where $(\frac{R_{ct}}{2}, 0)$ is the centre and $\frac{R_{ct}}{2}$ is the radius. Therefore, the Nyquist plot of the Randles circuit at high AC frequencies is a semicircle, where $(R_s + \frac{R_{ct}}{2}, 0)$ is the centre and $\frac{R_{ct}}{2}$ is the radius.

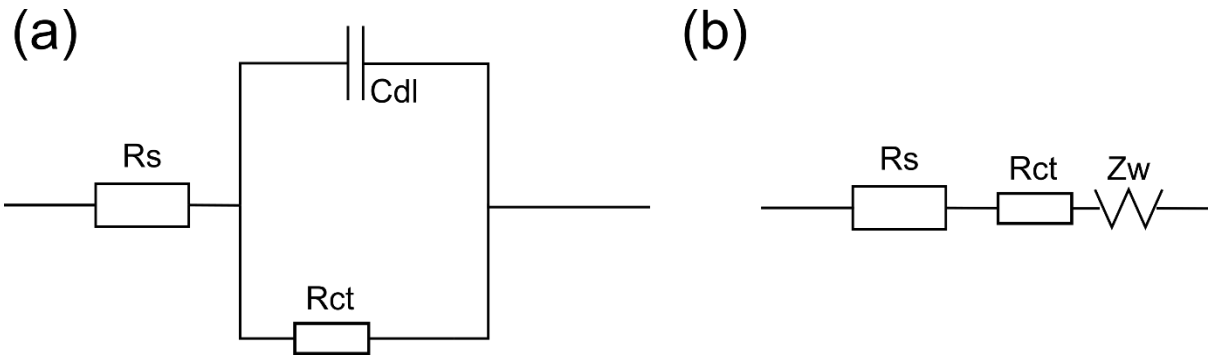

Figure 2.17. Two simplified circuits at (a) high AC frequencies and (b) low AC frequencies, respectively.

At low AC frequencies, the capacitor C_{dl} could be seem as open circuit, hence the Randles circuit is simplified as $(R_s + R_{ct})$ in series with the Warburg impedance (Figure 2.17b).

(2.23)
$$\tan\varphi = -\frac{Z''}{Z'} = -\left(\frac{-A_w/\sqrt{2\pi f}}{A_w/\sqrt{2\pi f}}\right) = 1$$
$$\varphi = 45°$$

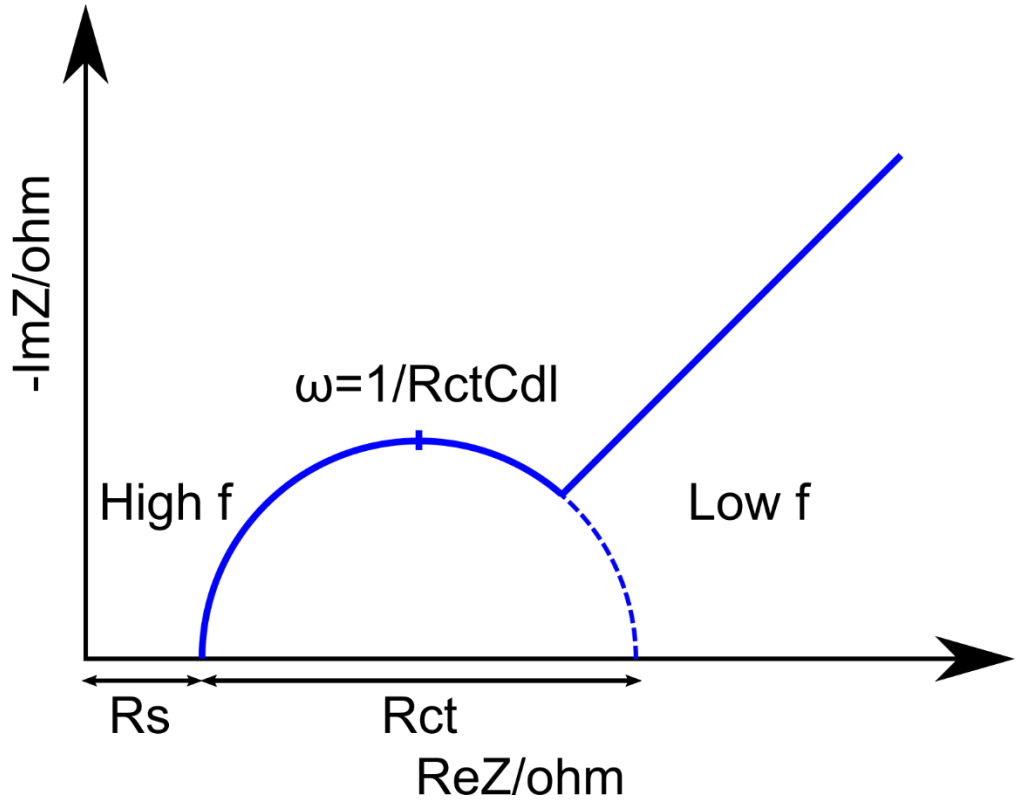

Figure 2.18. A typical Nyquist plot of the Randles circuit.

Therefore, the Nyquist plot of the Randles circuit at low AC frequencies is a 45° straight line.

Combine high frequency and low frequency, the Nyquist plot of the Randles circuit contains a semicircle and an extended 45° arm (Figure 2.18). Values of the solution resistance R_s and the total resistance ($R_s + R_{ct}$) are obtained from the intercepts of the semicircle with the X-axis. In terms of more complicated electrochemical processes, impedance responses can contain multiple semicircles or other features.

2.6 X-ray photoelectron spectroscopy (XPS)

2.6.1 Mechanism of XPS

X-ray photoelectron spectroscopy (XPS) is an advanced surface-sensitive technique for analysing the surface chemistry of a material. Information including the elemental composition, the chemical state of the elements within a material can be extracted from X-ray photoelectron spectra.

The basic physics of XPS is energy conservation. The kinetic energy and number of electrons that escape from the surface of the material are measured while the material is irradiated by a beam of X-rays. The binding energy E_b of an emitted electron can be determined by equation 2.24, where E_{photon} is the energy of the X-ray photons, $E_{kinetic}$ is the kinetic energy of the emitted electron and Φ is the work function.

(2.24) $$E_b = E_{photon} - (E_{kinetic} + \Phi)$$

E_{photon} is given by hv, where h is the Planck constant and v is the frequency of the photon.

Figure 2.19 is the energy level diagram of the sample and the spectrometer. Fermi levels of the sample and the spectrometer are aligned. Binding energy E_b, work functions of the sample Φ_1 and the spectrometer Φ_2, the kinetic energy of a free photoelectron above the sample E_{k1} and the kinetic energy of the photoelectron measured by the spectrometer E_{k2} are shown.

Therefore, the binding energy E_b is:

$$E_b = E_{photon} - (E_{k1} + \Phi_1) = E_{photon} - (E_{k2} + \Phi_2)$$

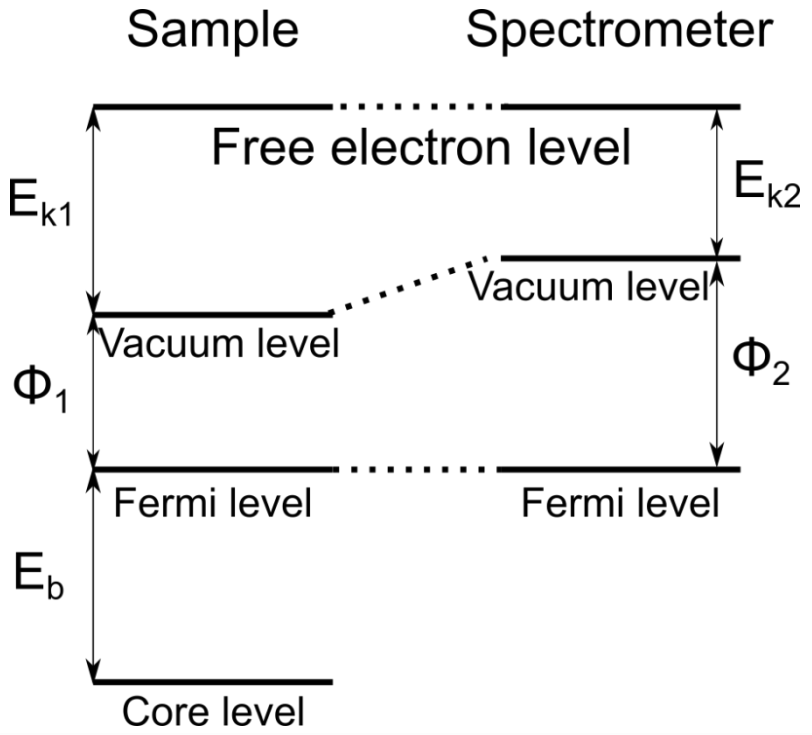

Figure 2.19. Energy level diagram of XPS.

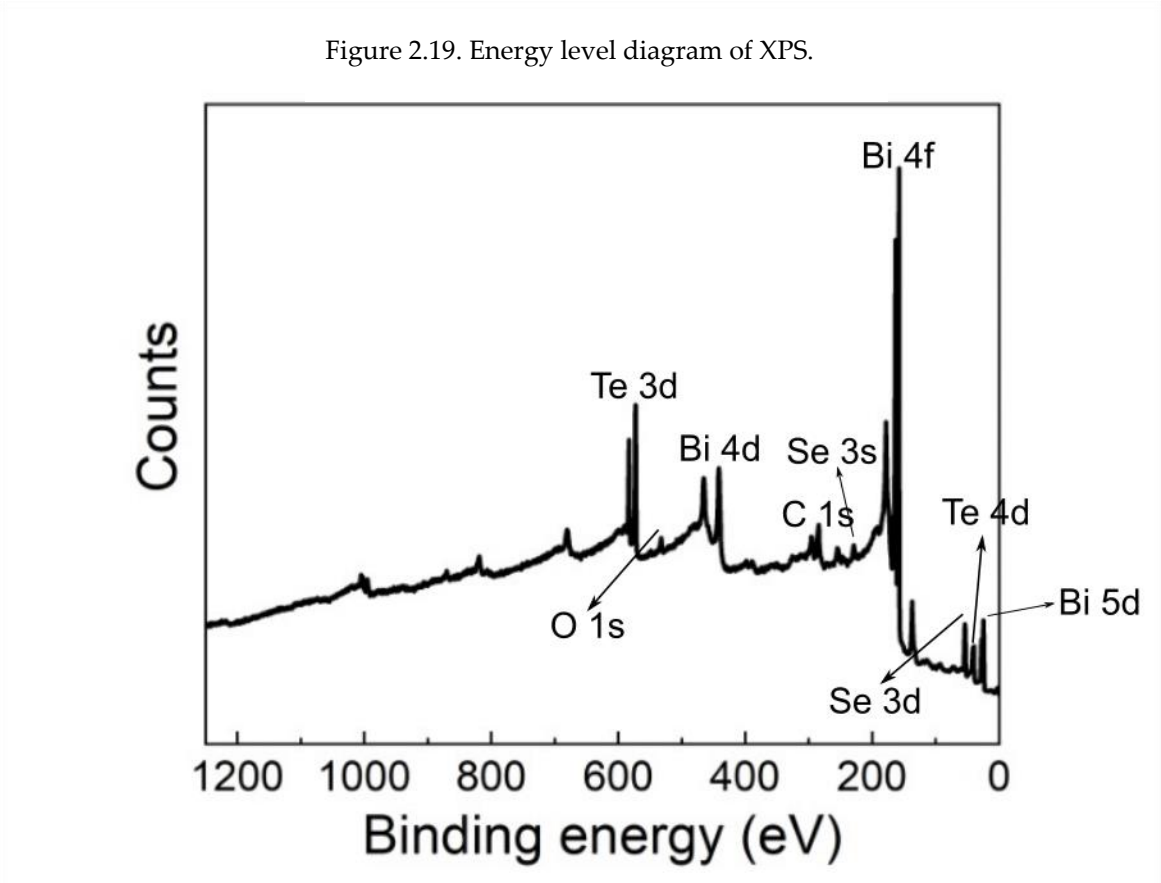

Figure 2.20. A typical X-ray photoelectron spectrum (survey spectrum for in-situ cleaved $Bi_2Te_{0.9}Se_{2.1}$.

The binding energy of the electron is the energy required to free the electron from its atomic orbital. It originates from the electromagnetic interaction between the electron and the nucleus as well as other

electrons of the atom. Considering that every element has its own electronic structure, the measured binding energy can be used to determine the elemental composition of the sample. In addition, the binding energy is affected by the local bonding environment of the element, therefore the measured data provides the chemical state information of the element. A typical X-ray photoelectron spectrum of in-situ cleaved $Bi_2Te_{0.9}Se_{2.1}$ is shown in Figure 2.20. The X-axis represents the binding energy (usually starting from the high binding energy side), while the Y-axis records the signal intensity (the total number of photoelectron counts per second). The position of a peak on the X-axis usually indicates the binding energy of an electron in a certain atomic orbit of a certain element. Since Bi 4f, Te 3d and Se 3d peaks are the most clear peaks for Bi, Te and Se respectively, they were selected for XPS measurements which will be discussed in chapter 3.

In some cases, software is used to separate elemental information from interfering peaks. Once positions of peaks are obtained, they are compared with the XPS database to determine the elemental composition and the chemical state.

2.6.2 Setting XPS measurements

XPS measurements were carried out at the Bristol NanoESCA Facility (Figure 2.21). The sample was mounted on a copper foil using conductive silver epoxy and then cleaved in air or under high vacuum in the XPS load-lock chamber, depending on which experiment was carried out. The sample was fixed

Figure 2.21. A photo of the Bristol NanoESCA Facility.

on the transfer rod in the load-lock chamber. The load-lock chamber was pumped and the pressure was monitored. Once the pressure reached an ideal level, the valve between the load-lock chamber and the preparation chamber was opened. The sample was transferred to the position for XPS measurements. Before measurements, the signal intensity was checked. The position of the sample was adjusted to maximise the signal intensity.

The start energy, the end energy, the energy step, the number of sweeps and the dwell time were set before measuring. The start energy and the end energy determine the range of each sweep, while the energy step, the number of sweeps and the dwell time affect the quality of the spectrum. In general, the smaller the energy step is, the higher the resolution is. Increasing the number of sweeps can increase the signal to noise ratio. The dwell time is the duration of each measuring step. The higher the dwell time, the higher the number of detected electrons. Collected counts were normalised by dividing the dwell time and the number of sweeps to get photoelectrons counts per second per sweep to plot XP spectra. These spectra can be further analysed using fitting software such as XPS Peak.

CHAPTER 3

ELECTROCHEMICAL/CHEMICAL MODIFICATION AND X-RAY PHOTOELECTRON SPECTROSCOPY OF BISMUTH CHALCOGENIDES

This chapter focuses on electrochemical oxidation, electrochemical reduction and thiol functionalization of bismuth chalcogenide $Bi_2Te_{0.9}Se_{2.1}$ single crystals. XPS measurements for these samples are compared with in-situ cleaved and air exposed samples. The first goal is to see whether it is possible to modify the surface chemistry by electrochemical oxidation and reduction in a way that can be detected by XPS. The second goal is to form thiol SAMs on the surface and to see whether the thiol functionalization can protect the surface from oxidation.

The ability to work in air or solution is a precondition for most practical applications of bismuth chalcogenides, but attempts to study the properties of Bi_2Se_3 and Be_2Te_3 following exposure to air or water have shown conflicting results. The majority of work indicates that exposure to air or water can modify topological insulators surface chemistry, but the inertness of Bi_2Se_3 and Bi_2Te_3 also has been reported. For example, XPS was used to reveal the rapid formation of native oxide on Bi_2Se_3 nanoribbons under ambient conditions [80] and study the stability of vacuum-cleaved Bi_2Se_3 surfaces [81]. For Bi_2Se_3 nanoribbons, the BiOx peak intensity increased with increasing air exposure time while the SeOx peak was negligible for samples with a relatively short time exposure. The different

sensitivities of the two elements toward oxidation were attributed to the particular tendency of O_2 to react with Bi or the higher vapour pressure of Se. For vacuum-cleaved Bi_2Se_3, a Bi_2 layer accompanied by a depletion of selenium in the near-surface region was formed after short exposure to the atmosphere. Next, two different reconstructed surfaces were observed after long-term exposure. In the first the Bi_2 layer oxidised completely, while in the second the surface returned to a state which was similar to the initial state. Furthermore, strong modification of the topological surface states for Bi_2Te_3 after air exposure was reported [82]. Quantum well states near the exposed surface may complicate the transport properties of these states. However, the stability of Bi_2Se_3 and Bi_2Te_3 in the ambient environment and the inertness of low-defect Bi_2Se_3 towards O_2 and NO_2 were also reported [83-85]. No bismuth and selenium oxides were detected during XPS measurements, although DFT methods predicted that bismuth-oxygen bonds could form where there are Se vacancies.

Since this conflict may in turn influence bismuth chalcogenides applications, it is important to further study how exposure to air or water can modify their surface chemistry.

The work discussed in this chapter has been published (Langmuir 2019,35,8,2983-2988) [86] and some text has been taken from this paper, which was written by the author of this thesis with only limited input from his co-authors.

3.1 Electrochemical modification of $Bi_2Te_{0.9}Se_{2.1}$ single crystals

3.1.1 Crystal structure of bismuth chalcogenides

The structure of bismuth chalcogenides is introduced in this section. Since the surface chemistry of bismuth chalcogenides is strongly related to their structure, knowing this is of great help for understanding the results of the further experiments. As described in Chapter 1, the basic structural unit of bismuth chalcogenides is the quintuple layer (QL) with the layer structure chalcogenide - Bi - chalcogenide - Bi - chalcogenide. The QLs are weakly bonded to each other via van der Waals interactions. $Sn_{0.01}Bi_{1.99}Te_2Se$, Bi_2Se_3 and $Bi_2Te_{0.9}Se_{2.1}$ were the crystals available for the experiments discussed in this thesis. Since the different crystals have different outermost layers, these crystals provide an excellent opportunity to study different surface chemistries. Calculations suggest that Te prefers to replace Se from the outermost layers of each quintuplet [87]. Therefore, the outermost layers of $Sn_{0.01}Bi_{1.99}Te_2Se$, Bi_2Se_3 and $Bi_2Te_{0.9}Se_{2.1}$ QLs are Te, Se and their mixture (0.45Te/0.55Se), respectively.

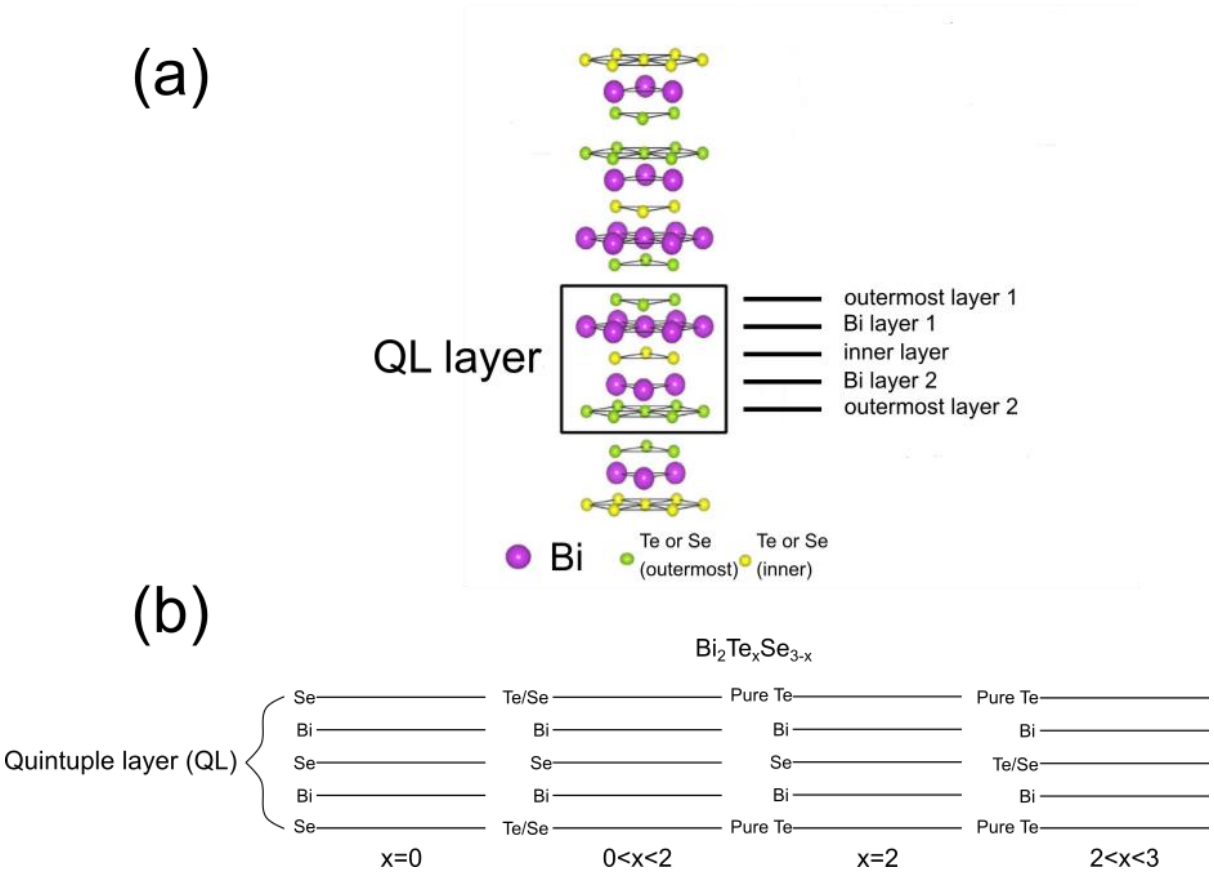

Figure 3.1 (a) Crystal structure of bismuth chalcogenides. Adapted from Ref.[1]. (b) Diagrams of bismuth chalcogenides with different compositions, showing Te replacement.

The crystal structure of bismuth chalcogenides is shown in Figure 3.1a. A basic structural unit, the quintuple layer (QL layer), is indicated. This chalcogenides-Bi-chalcogenides-Bi-chalcogenides structure has a thickness of about 1.0nm. Figure 3.1b shows the evolution of bismuth chalcogenides with the change of stoichiometry.

3.1.2 Cyclic voltammograms of a freshly cleaved $Bi_2Te_{0.9}Se_{2.1}$ sample

Since the aim was to study the effects of electrochemical oxidation and reduction, the potentials at which oxidation or reduction took place slowly and controllably were chosen following cyclic

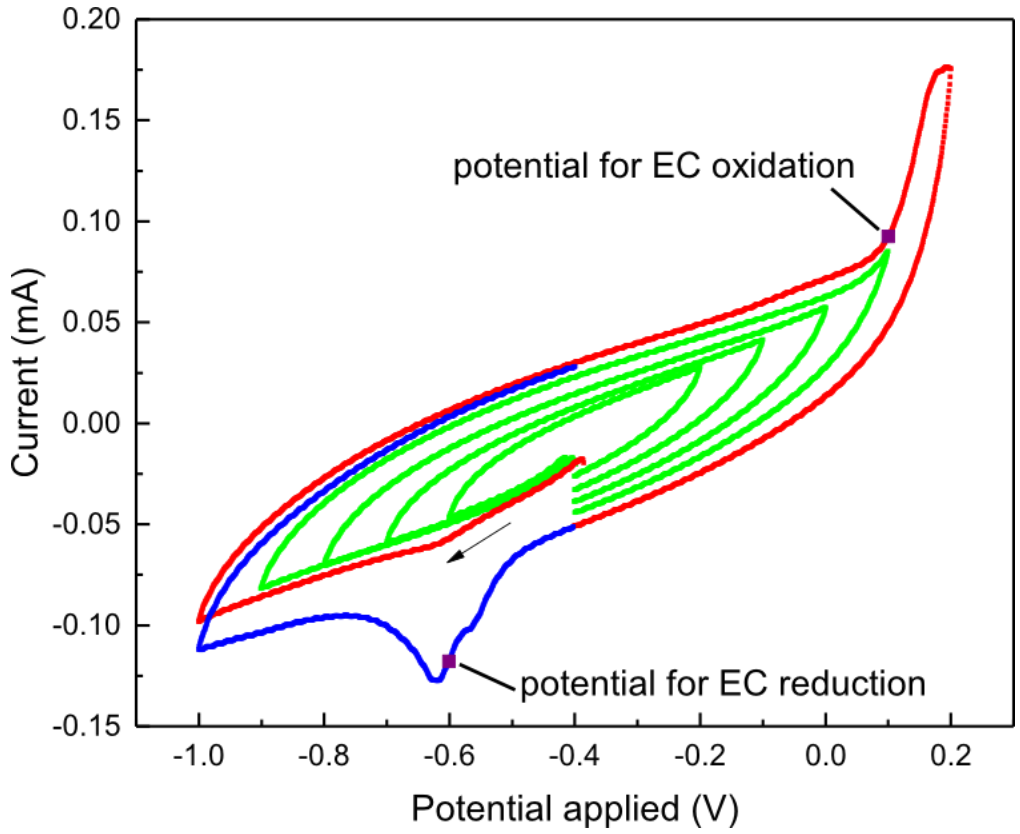

Figure 3.2. Cyclic voltammograms for a freshly cleaved $Bi_2Te_{0.9}Se_{2.1}$ single crystal as the scan range is extended. The green traces are for the ranges (-0.6V,-0.2V), (-0.7V,-0.1V), (-0.8V,0.0V), and (-0.9V,0.1V) successively. The scan rate was 50mV/s. The red trace is the first cycle for the range (-1.0V, 0.2V), while the blue one is part of the second cycle for the same range. The black arrow shows the scan sense, while the purple squares mark the potentials at which the electrochemical oxidation and reduction experiments described later were performed.

voltammetry (CV) measurements. These measurements were carried out for a freshly cleaved $Bi_2Te_{0.9}Se_{2.1}$ sample which was prepared by the method described in Chapter 2. For all the electrochemical experiments discussed in this chapter, the electrolyte was 0.05M Na_2SO_4 aqueous

solution at pH 3.0 (adjusted by H_2SO_4 addition); A Mercury/Mercurous Sulfate electrode and a Pt foil were used as a reference electrode and a counter electrode, respectively. Cyclic voltammograms (CVs) were performed using an Autolab PGSTAT302 potentiostat.

The turning points of the CVs were extended successively to determine the potential at which significant oxidation commences, see Figure 3.2. The CV for which the positive turning point is 0.1V and the negative turning point is -0.9V starts to show evidence of a redox reaction. The small reduction peak (marked) at around -0.6V in the CV that covers the range between 0.2 and -1.0V corresponds to the oxidation peak (marked) starting at around 0.1V in the previous cycle. Furthermore, the oxidation current above 0.1V in this cycle is much more obvious, leading to a pronounced reduction peak at -0.6V in the next cycle. There is a potential range around (-0.4, -0.2V) that can protect the surface from both oxidation and reduction because no oxidation or reduction currents are observed in this region. The stability of a surface maintained in this potential region was confirmed by XPS measurements (see later). Therefore, EC-STM study in this potential region should be feasible.

3.1.3 Electrochemical oxidation and reduction of $Bi_2Te_{0.9}Se_{2.1}$

Potentials derived from the CVs were used for subsequent electrochemical oxidation and reduction experiments. To enable XPS measurements, which will be discussed later, the sample to be modified was mounted on a copper foil using conductive silver epoxy. Kapton tape and insulating epoxy were used to insulate the exposed copper surface to avoid current leakages. The electrolyte and electrodes used in these experiments were the same as those used in the cyclic voltammetry measurements. The electrolyte was degassed before and during the experiments by replacing dissolved air with nitrogen gas through a glass pipette connecting to a compressed nitrogen cylinder to eliminate the influence of oxygen (Figure 3.3). Electrochemical redox experiments were performed using a Biologic SP-150 potentiostat.

The oxidation potential (0.1V), the reduction potential (-0.6V) and the rest potential which protects the surface from both oxidation and reduction (-0.3V) were used in the electrochemical oxidation, reduction and protection experiments, respectively. During the experiments, the currents of the redox reactions were recorded and integrated to get the total charges, see Figure 3.4.

From the figure, the oxidation current was stable at around 0.05mA for a period of 50 seconds approximately, followed by a rapid decrease with increasing time. The total charge passed was about 3mC. Since each Se or Te atom loses six electrons during the oxidation process (from -2 to +4), the

amount of dissolved $Bi_2Te_{0.9}Se_{2.1}$ was calculated to be about 1.7E-9 mol. Furthermore, the weight of dissolved $Bi_2Te_{0.9}Se_{2.1}$ was determined from its molar mass to be about 1.19E-6 g. Assuming the density of $Bi_2Te_{0.9}Se_{2.1}$ is 7.1g per cm^3 (the weighted average of the densities of Bi_2Te_3 and Bi_2Se_3), the volume was calculated to be 1.6E-7 cm^3 and the thickness was calculated to be about 16nm as the sample surface area of dissolved $Bi_2Te_{0.9}Se_{2.1}$ was estimated to be 0.1cm^2. The rapid current decrease suggests surface passivation, which could occur for the following reasons. Firstly, part of the oxidation products that absorb on the surface may block further oxidative dissolution. Secondly, the outer QLs may be more easily dissolved due to defects that originate from cleaving or air exposure. Therefore, once these "active" QLs are depleted, the inner QLs are exposed and cannot be dissolved at the set potential.

The second explanation is supported by Politano et al.[88]. They investigated the chemical reactivity of Bi_2Se_3 single crystals toward oxygen and water by synchrotron radiation XPS and reported that their samples were inert toward oxygen in the temperature range 300-550K but reactive toward water at room temperature. They noted that the robustness toward surface oxidation conflicted with Ref.[80] and attributed this discrepancy to the difference in crystalline quality of the investigated samples. Since

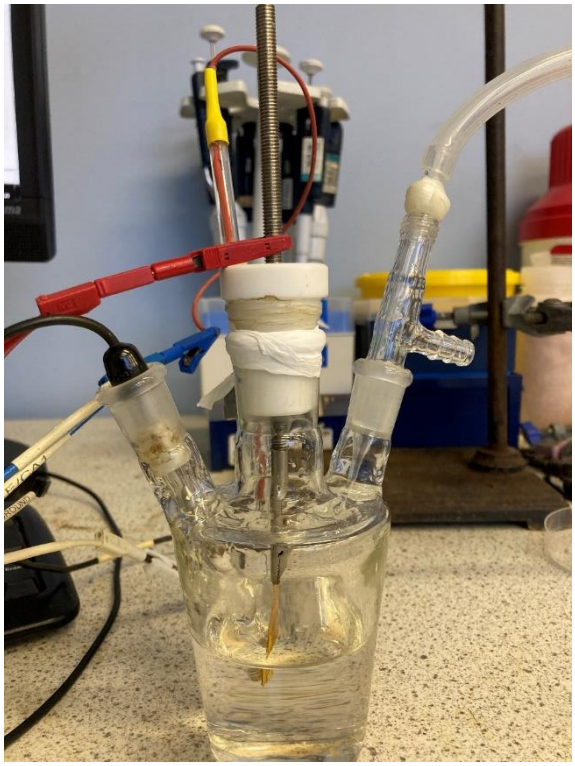

Figure 3.3. The four-neck electrochemical cell including the working electrode (sample), the reference electrode (a MSE electrode in the photo), the counter electrode (a Pt wire electrode in the photo) and a glass pipette that is connected to a nitrogen gas cylinder for degassing.

surface oxidation is strongly related to surface defeats, a surface with the absence of defects is expected to be inert toward oxygen.

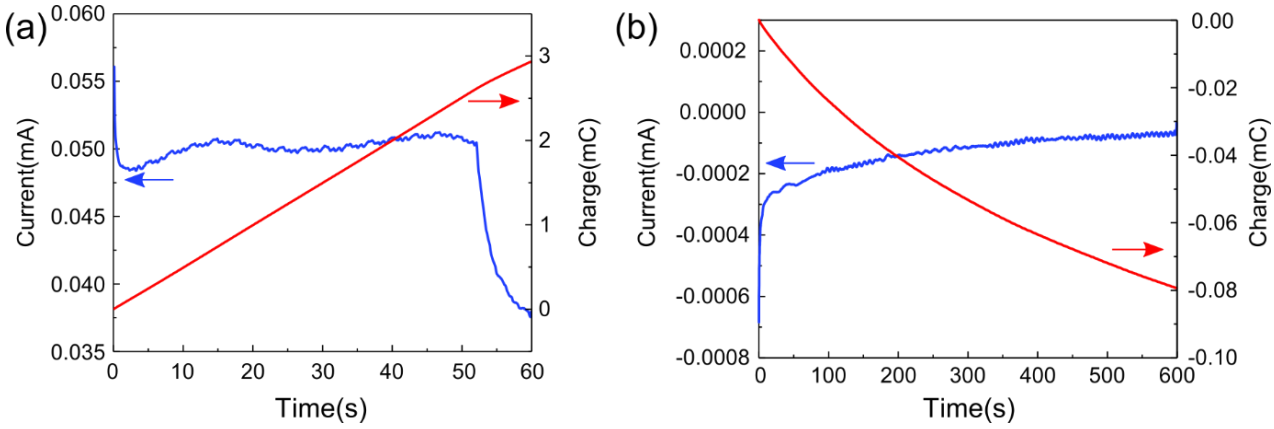

Figure 3.4. Current (blue lines) and charge (red lines) versus time for the electrochemical oxidation (a) and reduction processes (b).

There are two intermediate steps to make the oxidized sample suitable for XPS measurements. First, the oxidized sample was rinsed with copious Milli-Q water to remove the residual electrolyte. Second, the copper tape used to connect the sample and the crocodile clip was removed because its adhesive may release gas and affect the pressure of the chamber.

The oxidized sample was treated as described and measured by XPS. After XPS measurements, the sample was used for an electrochemical reduction experiment without further cleaving. With the exception of the applied potential, all the conditions for electrochemical reduction were the same as those for electrochemical oxidation. Compared to the electrochemical oxidation, the current and the total charge passed were significantly smaller, which indicates that only a small part of oxidation products remained on the sample surface (Figure 3.4). Three probable situations are considered. (1) Most of the oxidation products were dissolved, but a small part of the products remained on the sample surface. Since the surface lost a large part of the oxidation products, there was a mismatch of oxidation and reduction current/charge. (2) The oxidation products dissolved completely, but residue of the electrolytes on the sample surface reacted with air or sample to generate oxides when the sample was taken out from the electrochemical cell. Since residue of the electrolytes contained soluble oxidation products such as Bi^{3+} and the concentration of these species increased due to evaporation of the electrolytes, oxides may be formed by chemical reactions. (3) The oxidation products dissolved

completely, but the newly exposed surface oxidised in air after the sample was taken out. The electrochemical oxidation may activate the sample surface by creating dangling bonds. Consider that the passivation may be attributed to accumulation of the oxidation products, therefore, it is more possible that the assumption (1) describes the actual situation. Finally, the reduced sample was also used to get XPS data.

3.2 Thiol functionalisation of $Bi_2Te_{0.9}Se_{2.1}$

Self-assembled monolayers (SAMs) of organic molecules are molecular monolayers formed spontaneously on substrates by adsorption of organic molecules from vapour or solution. SAMs are divided into two groups. In the first case, no head group that has a strong affinity to the substrate and anchors the molecule to it, so the monolayer does not interact strongly with the substrate. In the second case, the monolayer is created in two steps. Firstly, the head groups chemically adsorb onto a substrate from either vapour or solution. Secondly, the tail groups slowly organise their direction to assemble. This process continues until the whole surface is covered by a single monolayer. Compared to physically absorbed Langmuir-Blodgett (LB) films, SAMs are relatively stable because they lower the surface free energy of the substrate.

Thiol-metal bonds have an energy of about 100kJ/mol, therefore the bonds are relatively stable in a variety of temperatures, solvents and electrochemical environments. For example, the thiolate-gold bond is semi-covalent and has a strength close to that of the gold-gold bond. Since the alkanethiol SAMs are stable and tightly packed on metals, they have been used to protect reactive metal surfaces, e.g. Ni or Co from oxidation [89-91].

However, no work has previously studied whether thiols can bond to a bismuth chalcogenide surface. If thiols can bond to this surface, one would expect that the corresponding SAMs could protect the surface from oxidation and maintain the TSSs (if it has TSSs). Therefore, SAMs on bismuth chalcogenides could be useful for any molecular spintronic devices that exploit the TSSs.

3.2.1 Thiol functionalisation using 1,5′-pentanedithiol and 1-pentanethiol

1,5′-pentanedithiol and 1-pentanethiol were used for thiol functionalisation. The structures of these molecules are shown in Figure 3.5. There were several reasons for choosing these molecules. Firstly, short chain alkanethiols have relatively lower toxicity and higher volatility, which makes them suitable for preparing SAMs from their vapour. Secondly, the length of the carbon chain also influences the

conductance of the molecule. Since short chain alkanedithiols have relatively higher conductance, their conductance in molecular electronic devices would be higher. In addition, the bonding mode of 1-pentanethiol is relatively simple, therefore comparing it with 1,5′-pentanedithiol is helpful for determining the bonding mode of the latter.

Vapour phase surface functionalisation has been widely used to obtain amine and thiol SAMs [92-94]. This simple and straightforward method provides some benefits over solution methods. Following this idea, thiol functionalisation was achieved by placing a freshly cleaved sample in a small beaker and then putting the small beaker in a large beaker that contains 1,5′-pentanedithiol or 1-pentanethiol - see figure 3.5. The large beaker was sealed with parafilm and left in a fume cupboard for 48 hours before the sample was removed. The thiols were expected to vaporise, then adsorb on the $Bi_2Te_{0.9}Se_{2.1}$ surface and form a compact layer to protect the surface from oxidation. Before measurements, the sample was rinsed in copious amounts of ethanol to remove extra thiols.

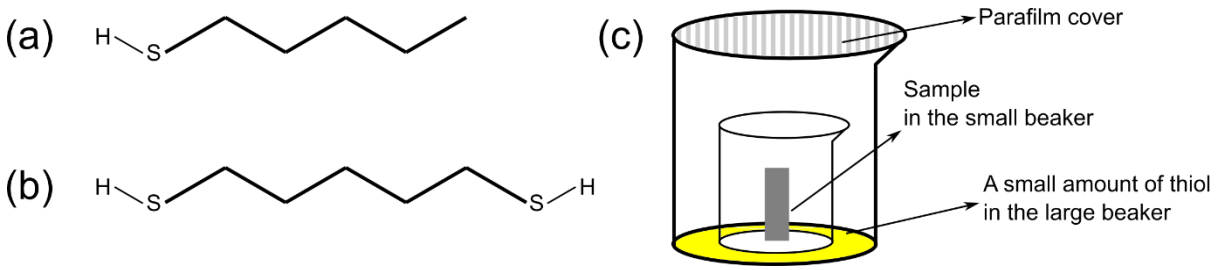

Figure 3.5. Structures of (a) 1-Pentanethiol (PT) and (b) 1,5-Pentanedithiol (PDT). (c) Diagram of the two-beaker setup.

3.2.2 CVs and EIS before and after thiol functionalisation

To check whether the thiol functionalisation affects the electrochemical response of the surface, figure 3.6 compares CVs for a freshly cleaved surface and one on which 1,5′-pentanedithiol was adsorbed. The clean surface is much more electrochemically active than the functionalised surface. There are clear oxidation and reduction peaks. Compared to the CVs in Ref.[95], these peaks are linked to corresponding electrochemical processes. The mains peaks at ~0.1V (peak A) and ~-0.6V (peak B) in the first cycle represent bismuth chalcogenides oxidation and reduction, respectively. Consider the existence of elemental Bi, Te, Se due to the growth process, another clear anodic peak (peak C) in the first cycle corresponds to the oxidation of elemental Se and Te to species in oxidation state +4. The small cathodic peak at ~-1.1V (peak D) result from cathodic stripping of bismuth chalcogenides (reduction of

Bi^{3+} in the compound to Bi^0 and reduction of "bound" Se, Te in the compound to soluble Se, Te species). Besides, the small anodic peak at ~-0.4V (peak E) can be assigned to the oxidation of elemental Bi to Bi^{3+}. The anodic peak at ~0.0V (peak F) in the second cycle is different from peak A and C because products of the first cycle are involved in the oxidation reactions of the second cycle.

Separation of the main peaks is larger than the value calculated by equation 2.5, which suggests that the reaction is not reversible. The relatively large separation could be explained by the following reasons. Firstly, the electrode kinetics of the reaction are sluggish, therefore the reaction does not occur at values one would predict from thermodynamics. An additional potential (overpotential) beyond the thermodynamic requirement is needed to activate the reaction to a detectable rate, hence the separation of the main peaks increases. Secondly, the reaction is not chemically reversible, which means that reversing the faradaic current cannot reverse the chemical reaction. The reduction products of the oxidized species may be different from the initial species because the stoichiometry of the reduction products is not necessarily be identical to the starting material. The irreversibility is also indicated by the difference of peak currents ($i_{pa} / i_{pc} \neq 1$). Peaks A, B, C and F disappear after thiol functionalisation, indicating that the surface has been passivated by adsorbed 1,5'-pentanedithiol. Electrochemical impedance measurements were carried out for $Bi_2Te_{0.9}Se_{2.1}$ before and after thiol functionalisation to check whether the treatment could influence the transport of electrons through the interface.

The measurements were performed using an Autolab PGSTAT302 potentiostat with FRA2 electrochemical impedance spectroscopy module. The frequency range for the AC signal was 100000 to 0.1 Hz, and its RMS amplitude 10 mV. A simple Randles circuit described in Chapter 2 was used to analyse the results, according to which the diameter of the semi-circular feature in the impedance spectrum is equal to the charge transfer resistance R_{ct}. Since the passivation suppressed the redox currents, the charge transfer resistance increased significantly. The corresponding electrochemical impedance spectra are shown in Figure 3.7 (Nyquist plot). From the Nyquist plot, the charge transfer resistance increases from about 400 Ω to 22000 Ω after thiol functionalisation. However, the origin of the second semicircle shown in the insert is still not clear.

In contrast, EIS for the 1-pentanethiol functionalised sample are similar to the corresponding data for the freshly cleaved sample, see Figure 3.8. In principle, one would expect SAMs of 1-pentanethiol to be better ordered than SAMs of 1,5'-pentanedithiol. 1-pentanethiol molecules tend to vertically bond to the sample surface in parallel with each other because a 1-pentanethiol molecule only has one thiol

group to bond to the sample surface, whereas a 1,5′-pentanedithiol molecule has two thiol groups at each end of the carbon chain, which allows 1,5′-pentanedithiol to "lie down" on the surface.

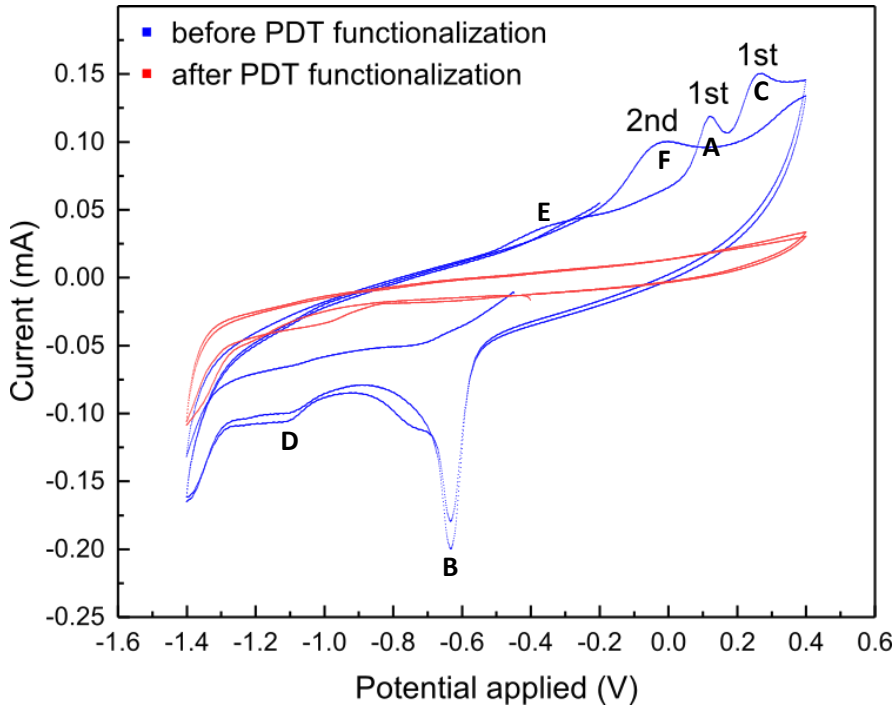

Figure 3.6. Cyclic voltammograms for a $Bi_2Te_{0.9}Se_{2.1}$ sample before (blue) and after pentanedithiol (PDT) adsorption (red). The scan rate was 50mV/s.

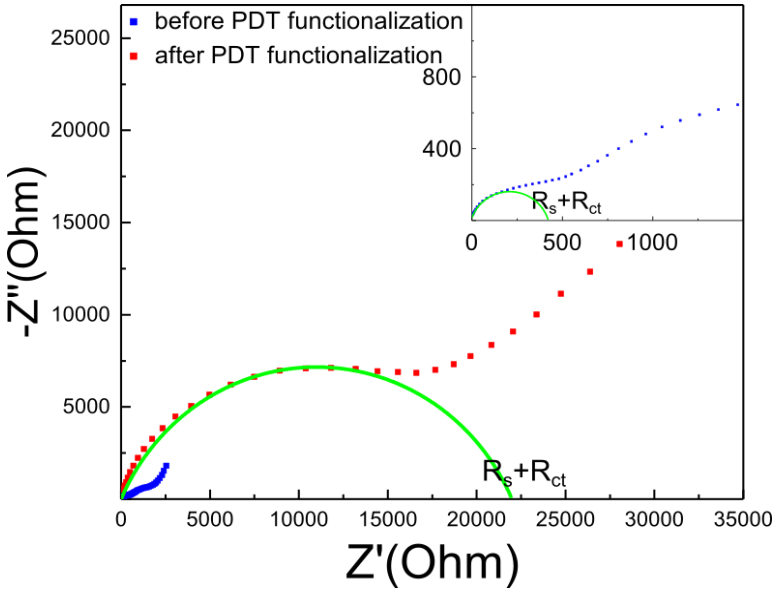

Figure 3.7. Electrochemical impedance data for a $Bi_2Te_{0.9}Se_{2.1}$ sample before (blue) and after 1,5′-pentanedithiol adsorption (red). Z' and Z'' are respectively the real and imaginary parts of the electrochemical impedance. The green semicircles are fits to the data and the insert is a magnification of the EIS before 1,5′-pentanedithiol functionalisation.

Spontaneously polymerisation of 1,4′-benzenedithiol provides a new idea to explain the thiol functionalisation process. 1,4′-benzenedithiol has two conductance values in vapour (the lower one was two orders of magnitude lower than the higher one). According to the literature, the lower value was attributed to the dimeric 1,4′-benzenedithiol junction, while the higher value was attributed to the monomer 1,4′-benzenedithiol junction [96]. Specifically, S-S bond was detected by in-situ surface enhanced Raman spectroscopy [97], which indicates that disulfide-mediated dimerisation of 1,4′-benzenedithiol contributed to the low conductance feature.

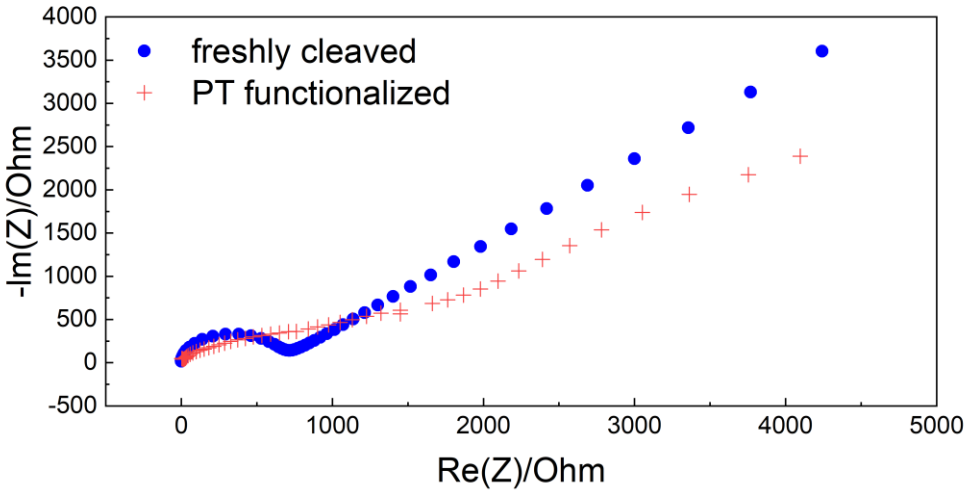

Figure 3.8. Electrochemical impedance data for a $Bi_2Te_{0.9}Se_{2.1}$ sample before and after 1-pentanethiol adsorption.

Since the disulfide bond is a weak covalent bond [98, 99], the 1,5′-pentanedithiol molecules may be polymerised into a thick layer, whereas the 1-pentanethiol molecules cannot (Figure 3.9). Even if neither 1,5′-pentanedithiol nor 1-pentanethiol bond to the chalcogenide surface, a layer of polymerised 1,5′-pentanedithiol could adsorb physically to the surface. In either case, the different electrochemical responses after 1,5′-pentanedithiol and 1-pentanethiol treatments are reasonable. The attempt to functionalise dichalcogenide MoS_2 showed that MoS_2 could not be easily functionalised in the absence

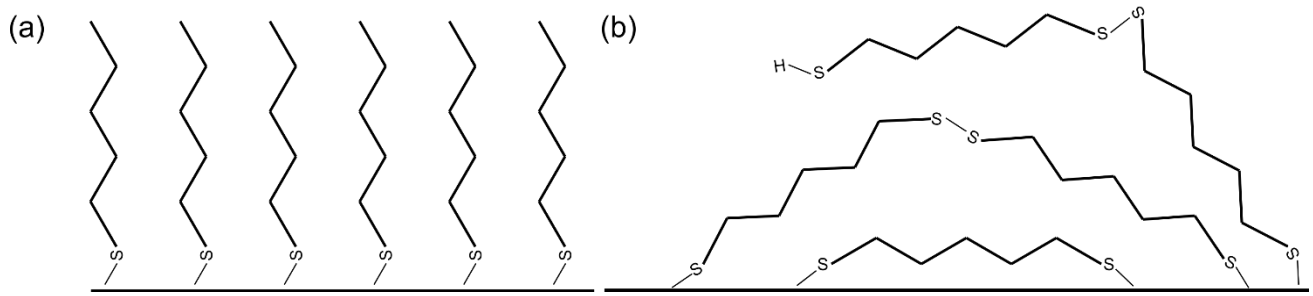

Figure 3.9. Diagrams showing the suggested functionalisation of (a) 1-pentanethiol (b) 1,5′-pentanedithiol.

of defects [100]. This mechanism may also be applied to $Bi_2Te_{0.9}Se_{2.1}$, hence the thiol related bonds may only form where there are Se or Te vacancies.

3.3 X-ray photoelectron spectroscopy characterisation

X-ray photoelectron spectroscopy is a powerful technique to determine elemental composition and the corresponding chemical state, as described in Chapter 2. Here, the XPS technique was used to characterize freshly cleaved, air exposed, electrochemically modified and thiol functionalised $Bi_2Te_{0.9}Se_{2.1}$ samples. The changes in surface chemistry after different treatments could be detected. For example, surface oxidation was evident in the spectra as extra peaks that relate to oxide species. The results for air exposure samples are supported by works which reported that exposure to air could modify bismuth chalcogenide surface chemistry [80, 81]. The results for electrochemically oxidised and reduced samples are original in that they demonstrate the ability to control and characterize the surface oxidation of bismuth chalcogenides in an electrochemical environment for the first time. In addition, the results for thiol functionalised samples are consistent with their CVs, showing the difference between alkanethiol and alkanedithiol.

3.3.1 XPS for freshly cleaved samples and air exposed samples

Four samples were prepared and studied by XPS to determine the effect of air exposure. The first sample was cleaved with carbon tape under high vacuum in the XPS load-lock chamber. The other three samples were cleaved in air then exposed 20 min, 2 hours and 2 days, respectively, before transferring into the high vacuum system. Bi 4f, Te 3d and Se 3d XPS of these four samples are plotted (Figure 3.10) because they were the clearest peaks for the corresponding elements on the survey spectrum.

The effect of air exposure is noticeable. No obvious signs of oxidation are shown in the spectra for the first and the second samples, whereas clear peaks corresponding to oxide species are shown in the spectra for the third and the fourth samples. Furthermore, different elements show different sensitivities to air exposure. For the 2 hours air exposed sample, satellite peaks at 576.1 and 586.5eV are observed in addition to the main peaks at 572.4 and 582.8eV. These satellite peaks are consistent with previous measurements on TeO_2 [101]. However, Bi 4f and Se 3d XPS for this sample are quite similar to those XPS for the in-situ cleaved sample, which indicates Bi and Se were little affected by exposure

to air for 2 hours. For the 2 days air exposed sample, all three elements were oxidised to different extents. Te 3d and Bi 4f show clear signs of oxidation, while Se 3d shows limited signs of oxidation.

The different sensitivities toward air exposure may be explained by the composition of the outermost layers and the differences in electronegativity. The electronegativities of Bi and Te are similar (2.02 and 2.1, respectively), while the electronegativity of Se is higher (2.55), which indicates that Se is more difficult to oxidise than Bi and Te. Furthermore, the outermost layers of each QL are expected to be Te/Se mixtures rather than Bi, which may explain why Te oxidises more than Bi.

Figure 3.10 also shows that the surface oxidised on the timescale of the experiment. This oxidation timescale is smaller than the timescale shown in Ref.[80] because Bi 4f XPS for the 2 days air exposed sample in this experiment shows clear oxide peaks whereas Bi 4f XPS for the 2 days air exposed nanoribbons in Ref.[80] did not show signs of oxidation. Since the samples used in this experiment were cleaved in air, the defect density should be higher than the corresponding parameter for the Bi_2Se_3 nanoribbons in Ref.[80]. The higher defect density results in faster surface oxidation, which is consistent with the suggestion of Ref.[83].

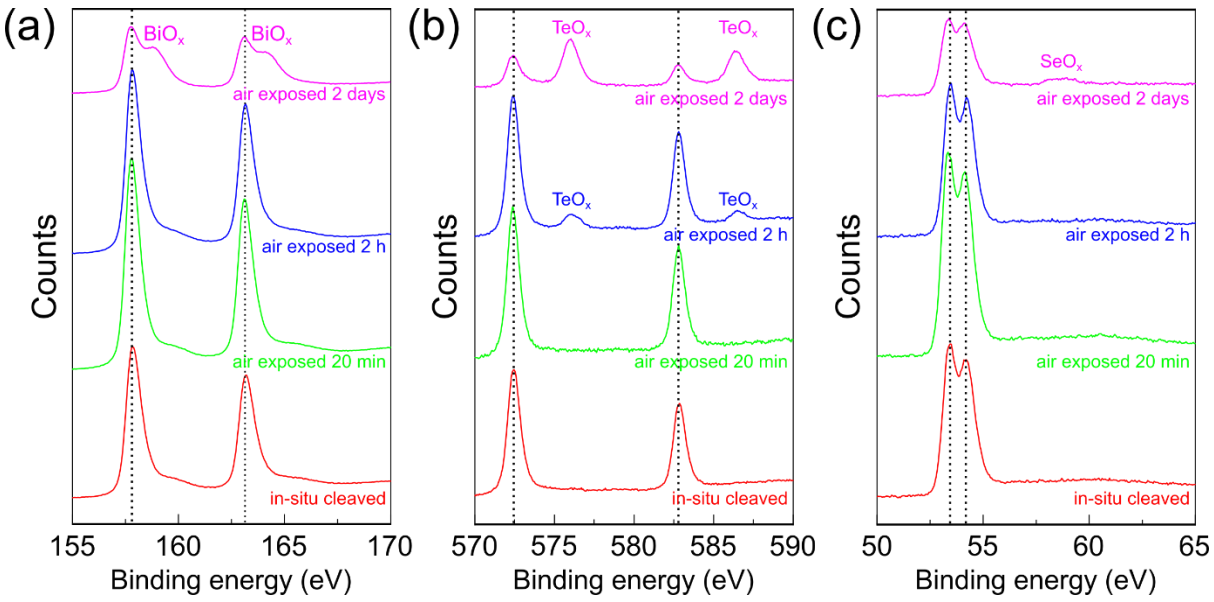

Figure 3.10. Bi 4f (a), Te 3d (b) and Se 3d (c) XPS for in-situ cleaved, 20 min air exposed, 2h air exposed and 2-day air exposed samples.

There are several possible oxidation paths. For the reaction only involving $Bi_2Te_{0.9}Se_{2.1}$ and oxygen, the oxides BiO_x, TeO_x and SeO_x are expected [80]. For the reaction only involving water, Zhang et al.[102] suggested that the reaction products for Bi_2Te_3 and water are H_2Te and hydrated Bi compounds. Since the samples used in the experiments were $Bi_2Te_{0.9}Se_{2.1}$, the products would be H_2Te, H_2Se and Bi

compounds. For oxidation in an ambient environment, the scenario is more complicated because either oxygen or water may be involved [103, 104]. With the exception of oxides and hydrides, Ref.[81] observed neutral Se on long-term air exposed Bi_2Se_3. Therefore, neutral elements are also considered as possible products.

3.3.2 XPS for electrochemically oxidised and reduced samples

Figure 3.11 compares a sample maintained in the aqueous 0.05M Na_2SO_4 electrolyte for 2h at the rest potential -0.3V with an in-situ cleaved sample, and one that was exposed to air for 2h (the same sample as Figure 3.10). The electrochemically protected sample was similar to the in-situ cleaved sample, whereas the sample which was exposed to air for the same time started to show evidence of surface oxidation.

The similarity of the two samples indicates that the $Bi_2Te_{0.9}Se_{2.1}$ surface is oxide-free at the rest potential. Therefore, electrochemical control could be an inexpensive alternative to ultra-high vacuum as a means to maintain a bismuth chalcogenide surface free of oxide. This observation also suggests that bismuth chalcogenides would be a feasible platform for EC-STM study. For the electrochemical redox

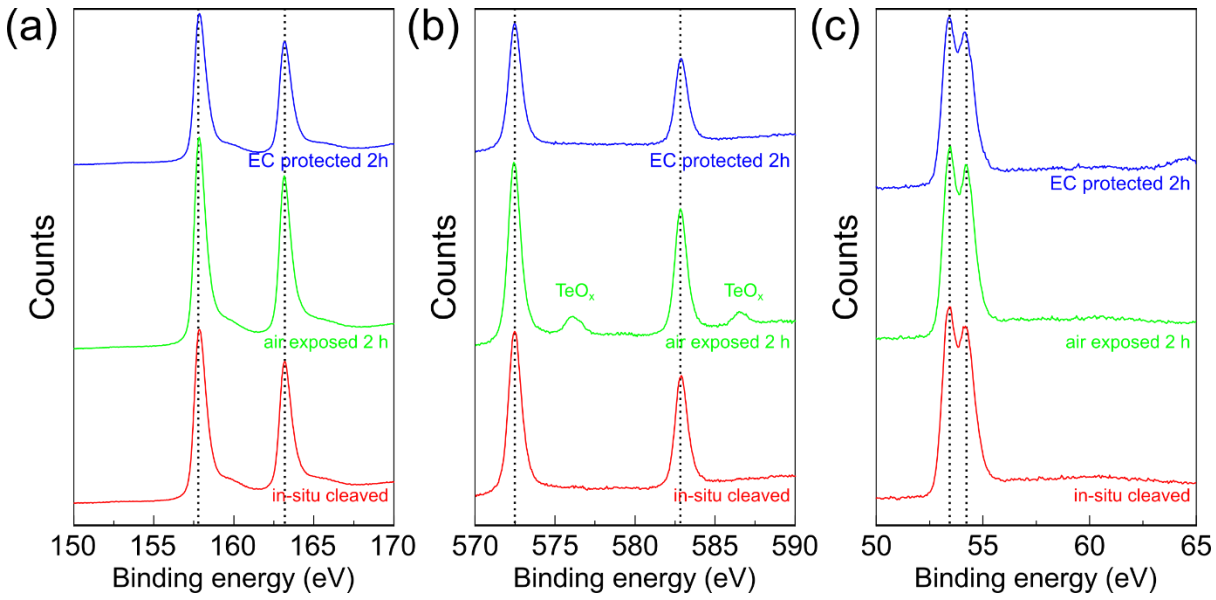

Figure 3.11. Bi 4f (a), Te 3d (b) and Se 3d (c) XPS for in-situ cleaved, 2h air exposed and 2h electrochemically protected samples. The Te 3d XPS of the 2h air exposed sample shows oxidation peaks (middle curve in (b)), whereas the in-situ cleaved sample and the electrochemically protected sample show no evidence of oxidation. The small peak in the top curve of Figure 3.11c is because of Na 2s rather than oxidized Se and may be attributed to the residual electrolyte (Na_2SO_4).

experiments, there are several questions. Firstly, whether the surface chemistry of $Bi_2Te_{0.9}Se_{2.1}$ can be modified by electrochemical oxidation in a way that is clearly observable by XPS. Secondly, if so, how the effects of electrochemical oxidation and air exposure compare. Thirdly, to what extent the effects of electrochemical oxidation can be reversed electrochemically.

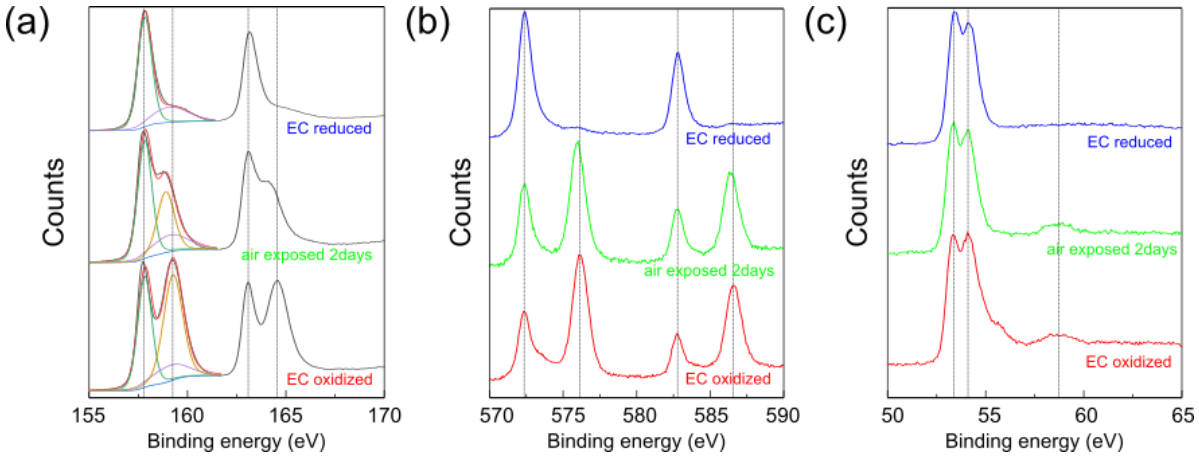

Figure 3.12. Bi 4f (a), Te 3d (b) and Se 3d (c) XPS for electrochemically (EC) oxidised (bottom), 2 days air exposed (middle) and EC reduced (top) samples.

To answer these questions, Figure 3.12 compares the XPS for a sample that experienced electrochemical oxidation, the same sample after subsequent electrochemical reduction and a sample that experienced 2 days air exposure (the same sample as Figure 3.10). The Bi, Te and Se oxide peaks for the electrochemically oxidised sample are even more prominent than the corresponding peaks for the 2-days air exposed sample, which indicates that the electrochemical oxidation has a significant effect. The centre of the Bi 4f7/2 oxide peak is at 159.2 eV for the electrochemically oxidized sample, while it is at 158.8eV for the 2 days air exposed sample. Since the systematic error of the XPS instrument is much less than 0.4eV, this shift may be due to different oxide species forming during electrochemical oxidation and air exposure. Any shifts in the other peaks are negligible. The electrochemically reduced sample is quite similar to the in-situ cleaved sample, despite minimal oxidation of the former [105]. This small difference may originate from incomplete reduction or the rinsing and transferring steps after electrochemical reduction. The small shoulder on the Bi 4f7/2 peak that is shown in the top curve in Figure 3.12a is not associated with oxide. It was observed in XPS of single-crystalline Bi_2Se_3 prepared by Zhang et al.[106], although they did not explain the origin either. Nevertheless, the data shows that the change in the surface chemistry produced by electrochemical oxidation can also be reversed by electrochemical methods.

For surface oxidation in an electrochemical environment, one probable reaction path (equation 3.1) is similar to the reactions for Bi_2Se_3 and Bi_2Te_3 electrodeposition but in reverse [107-109]. Oxidation products are expected to be solvated Bi^{3+} ions and soluble $HTeO_2^+$ and $HSeO_2^+$ species in oxidation state +4, whereas reduction at the cathode is expected to be hydrogen evolution (equation 3.2). If this is true, one would expect the majority of oxidation products to enter solution. In this case, one could expect a mismatch between the oxidation and reduction currents because only a small part of oxidation products are reduced on the sample surface. In fact, this mismatch is observed in Figure 3.4.

(3.1) $$Bi_2Te_{0.9}Se_{2.1} + 6H_2O \leftrightarrow 2Bi^{3+} + 0.9HTeO_2^+ + 2.1HSeO_2^+ + 18e^- + 9H^+$$

(3.2) $$18e^- + 18H^+ \leftrightarrow 9H_2$$

However, the XPS data for the electrochemically oxidised sample indicate that there are oxides on the surface. According to the Pourbaix diagram of Bi (Figure 3.13), Bi^{3+} could convert to $Bi(OH)^{2+}$, BiO^+ and Bi_2O_3 in pH3 solution at 0.1V with respect to MSE, see equations 3.3-3.6.

(3.3) $$Bi^{3+} + H_2O \leftrightarrow Bi(OH)^{2+} + H^+$$

(3.4) $$Bi^{3+} + H_2O \leftrightarrow BiO^+ + 2H^+$$

(3.5) $$2Bi(OH)^{2+} + H_2O \leftrightarrow Bi_2O_3 + 4H^+$$

(3.6) $$2BiO^+ + H_2O \leftrightarrow Bi_2O_3 + 2H^+$$

Therefore, in-situ precipitation of Bi_2O_3 during electrochemical oxidation may explain the Bi oxides peaks in XPS. However, the precipitation of oxide is extremely sensitive to Bi^{3+} concentration. In the case of this experiment, the concentration of Bi^{3+} is very low, hence the Bi oxide is more likely to form on removing the sample from the electrolyte. When the sample is taken out, the residual electrolyte evaporates and the concentration of Bi^{3+} increases, leading to Bi_2O_3 precipitation.

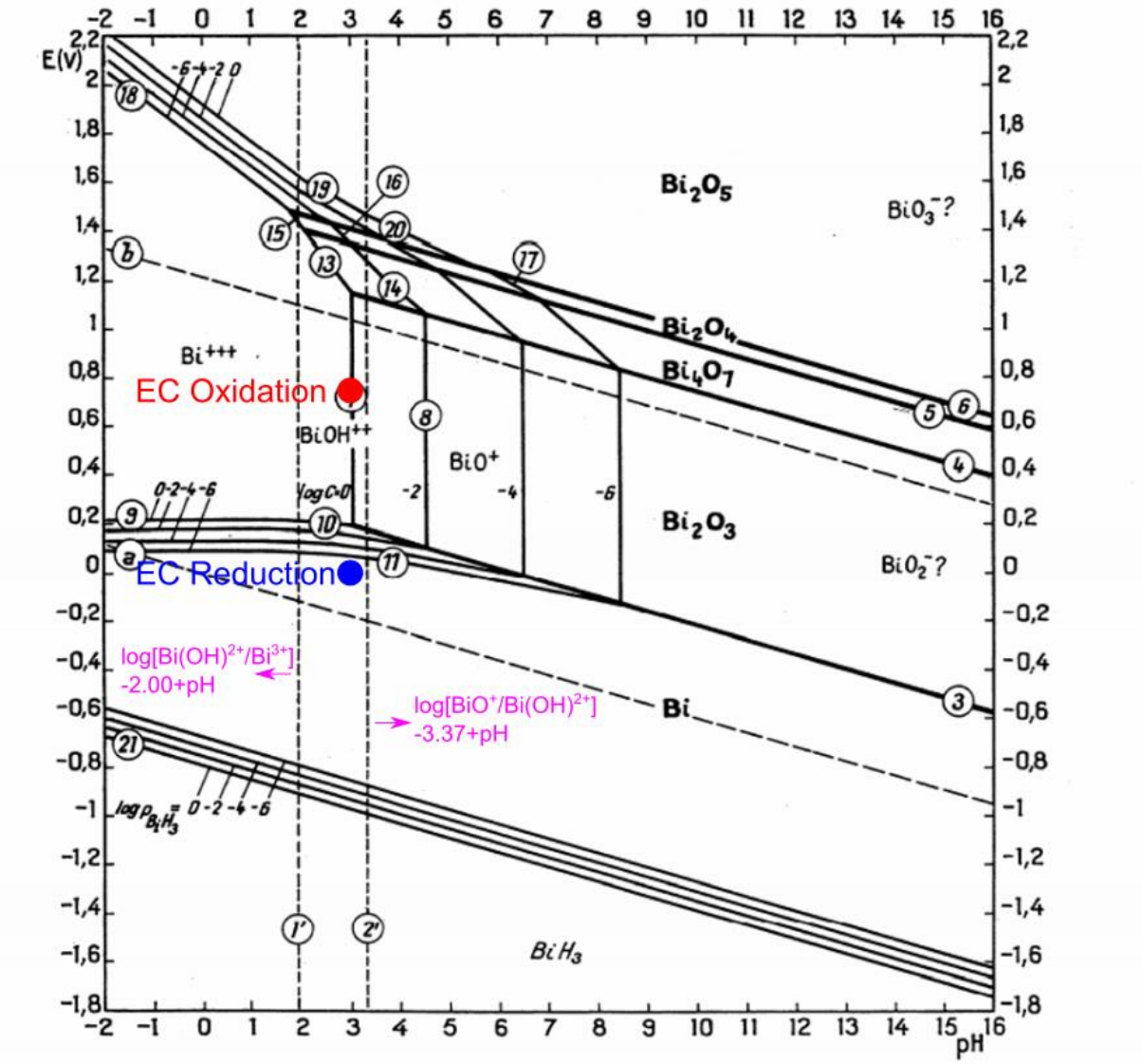

Figure 3.13. Pourbaix diagram of Bi. The electrochemical oxidation conditions are represented by the red dot (pH3, 0.1V vs MSE, which is about 0.75V vs SHE). The electrochemical reduction conditions are represented by the blue dot (pH3, -0.6V vs MSE, which is about 0.05V vs SHE). Adapted from Ref.[110].

The Pourbaix diagram of Te is shown in Figure 3.14. Small amounts of $HTeO_2^+$ may convert to H_2TeO_4, TeO_2 and TeO_3, see equations 3.7-3.9.

(3.7) $$HTeO_2^+ \leftrightarrow TeO_2 + H^+$$

(3.8) $$HTeO_2^+ + 2H_2O \leftrightarrow H_2TeO_4 + 3H^+ + 2e^-$$

(3.9) $$H_2TeO_4 \leftrightarrow TeO_3 + H_2O$$

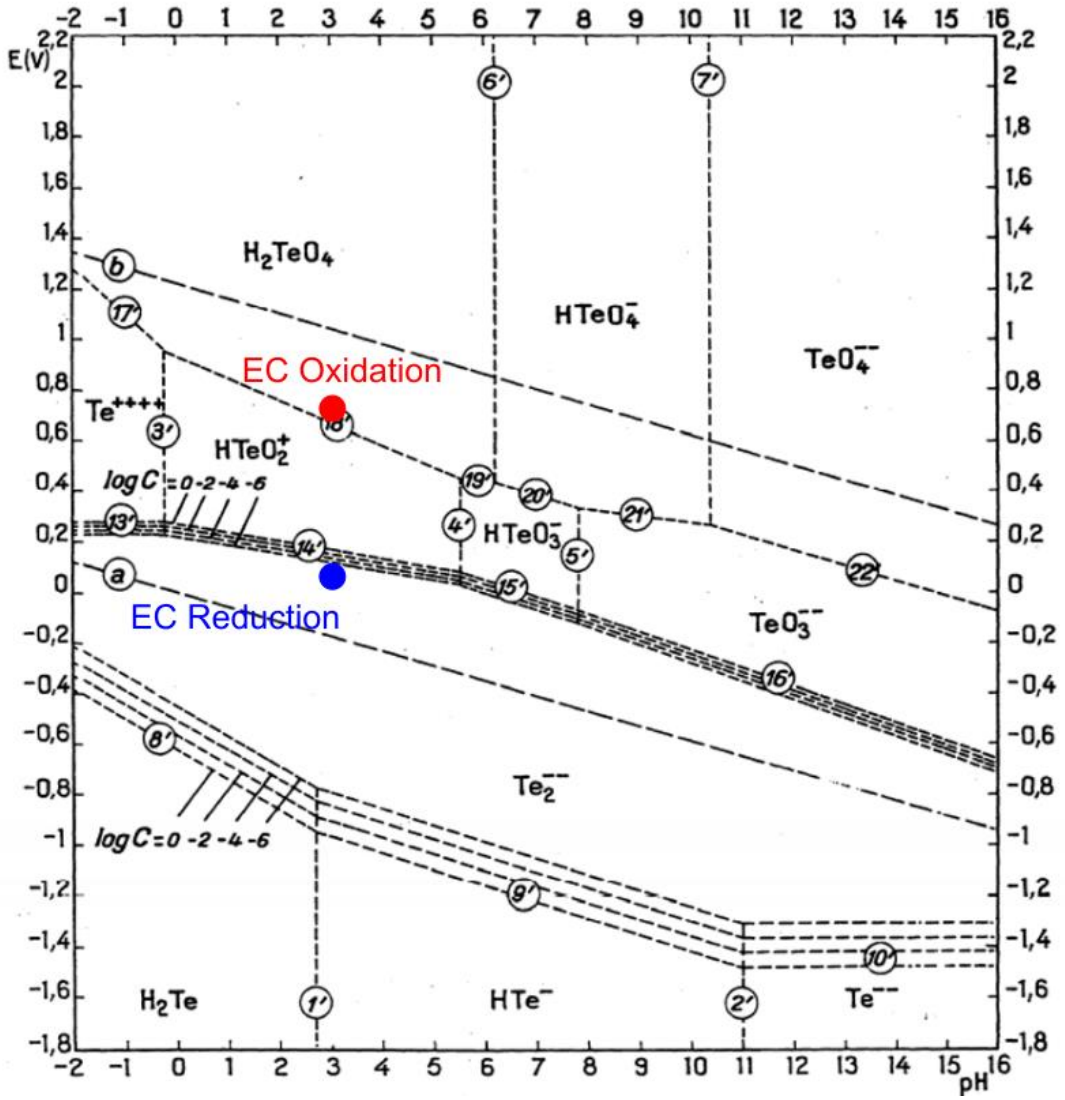

Figure 3.14. Pourbaix diagram of Te. The electrochemical oxidation conditions are represented by the red dot (pH3, 0.1V vs MSE, which is about 0.75V vs SHE). The electrochemical reduction conditions are represented by the blue dot (pH3, -0.6V vs MSE, which is about 0.05V vs SHE). Adapted from Ref.[110].

Similar to Bi XPS, Te oxides peaks may be attributed to small amounts of TeO_2 and TeO_3 adsorb on the surface. Precipitation of Te oxides may happen during the process of electrochemical oxidation (in-situ) or after the sample is taken out (ex-situ).

Figure 3.15 shows the Pourbaix diagram of Se. Equation 3.10-3.12 are probable reactions in pH3 solution at 0.1V with respect to MSE.

(3.10) $$HSeO_2^+ + H_2O \leftrightarrow HSeO_3^- + 2H^+$$

(3.11) $$HSeO_3^- + H_2O \leftrightarrow SeO_4^{2-} + 3H^+ + 2e^-$$

(3.12) $$HSeO_3^- + H^+ \leftrightarrow H_2SeO_3$$

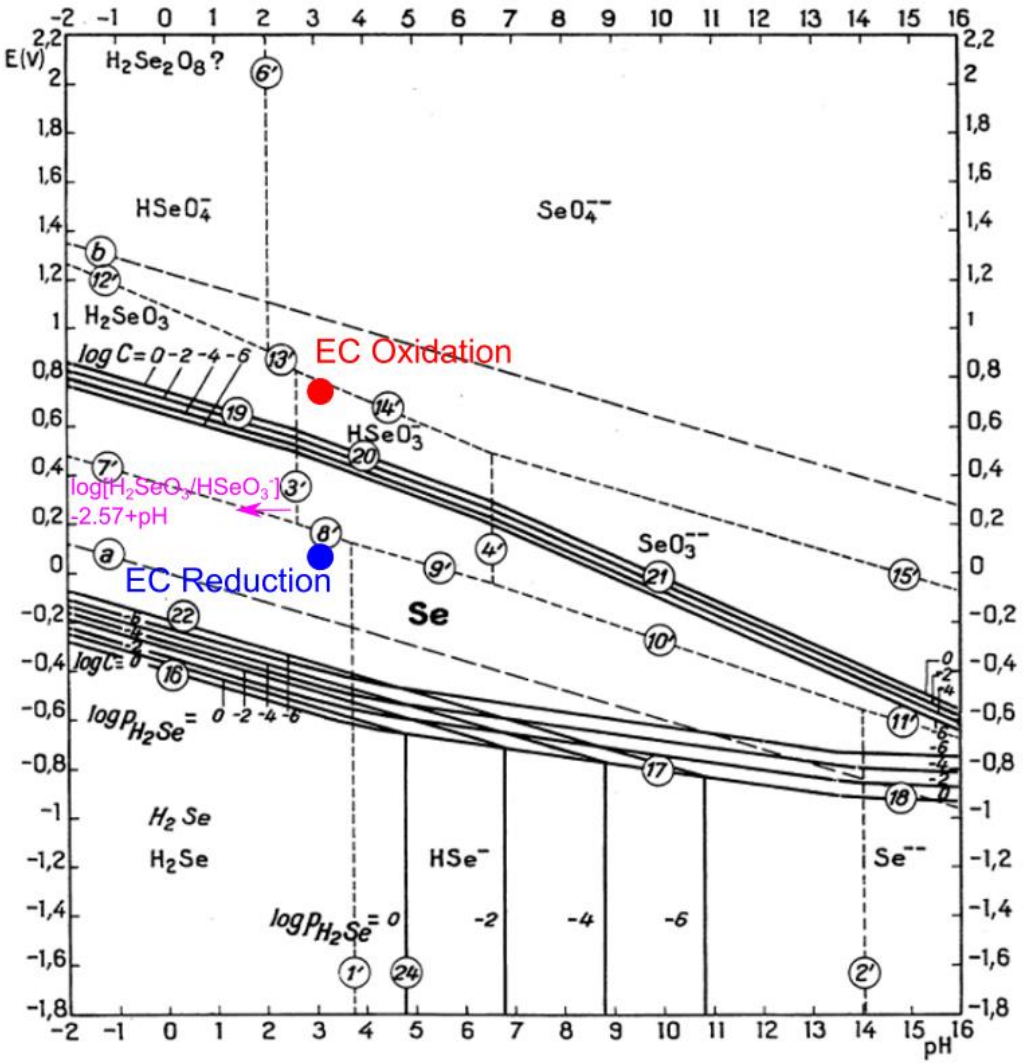

Figure 3.15. Pourbaix diagram of Se. The electrochemical oxidation conditions are represented by the red dot (pH3, 0.1V vs MSE, which is about 0.75V vs SHE). The electrochemical reduction conditions are represented by the blue dot (pH3, -0.6V vs MSE, which is about 0.05V vs SHE). Adapted from Ref.[110]According to the diagram, most of Se oxidation products exist in the form of $HSeO_3^-$, but small amounts of $HSeO_3^-$ could convert to SeO_4^{2-} or H_2SeO_3 as equation 3.11 and 3.12 describe. Similarly, SeO_2 and SeO_3 could be formed in-situ (although the Pourbaix diagram does not discuss these two oxides) or ex-situ.

Notably, the Se oxides peak for the electrochemically oxidized sample in Figure 3.12c is not as clear as Bi and Te oxides peaks for the same sample in Figure 3.12a-b. This difference may be attributed to the different sensitivities of Bi, Te and Se toward oxidation which have been discussed, but the solubility of the oxidation products can also influence the intensities of oxides peaks. If the solubility of Se oxidation products is higher than the solubility of Bi and Te oxidation products, one would expect that the adsorbed Se oxides are less than the adsorbed Bi and Te oxides, therefore the intensity of the Se oxides peak could lower than the intensities of the other two.

For electrochemical reduction, the Pourbaix diagrams of three individual elements indicate that Bi, Te, Se are stable in the forms of Bi^0, Te^{2-} and Se^0 in pH3 electrolyte at -0.6V with respect to MSE. However, the deposition potential of a binary compound from two cations with similar Nernst potentials may be more positive than the potential where either cation reduces individually. This process is known as mutually induced codeposition and is applied to Bi_2Se_3 electrodeposition [95]. The potential at which Bi_2Se_3 is deposited when both Bi^{3+} and $HSeO^{2+}$ are present in the solution is more positive than the reduction potentials of Bi^{3+} and $HSeO^{2+}$. Therefore, one would expect that the reduction product of this experiment is $Bi_2Te_xSe_{3-x}$ rather than elemental Bi, Te or Se. The stoichiometry of the redeposited clusters will not necessarily be identical to that of the starting material. It may depend on how much oxides were remained on the surface after electrochemical oxidation.

Since the Pourbaix diagram is calculated from the Nernst equation, it is a plot of possible thermodynamically stable phases (for aqueous electrochemical systems) and it applies to the system at equilibrium or with a very large exchange current. The latter would mean that the electrode kinetics are very facile. In this case, a tiny overpotential could draw the required net current because the net current is only a small fraction of the exchange current. The overpotential could be regarded as an infinitesimal driving force, hence the system is always kept in equilibrium. For electrochemical

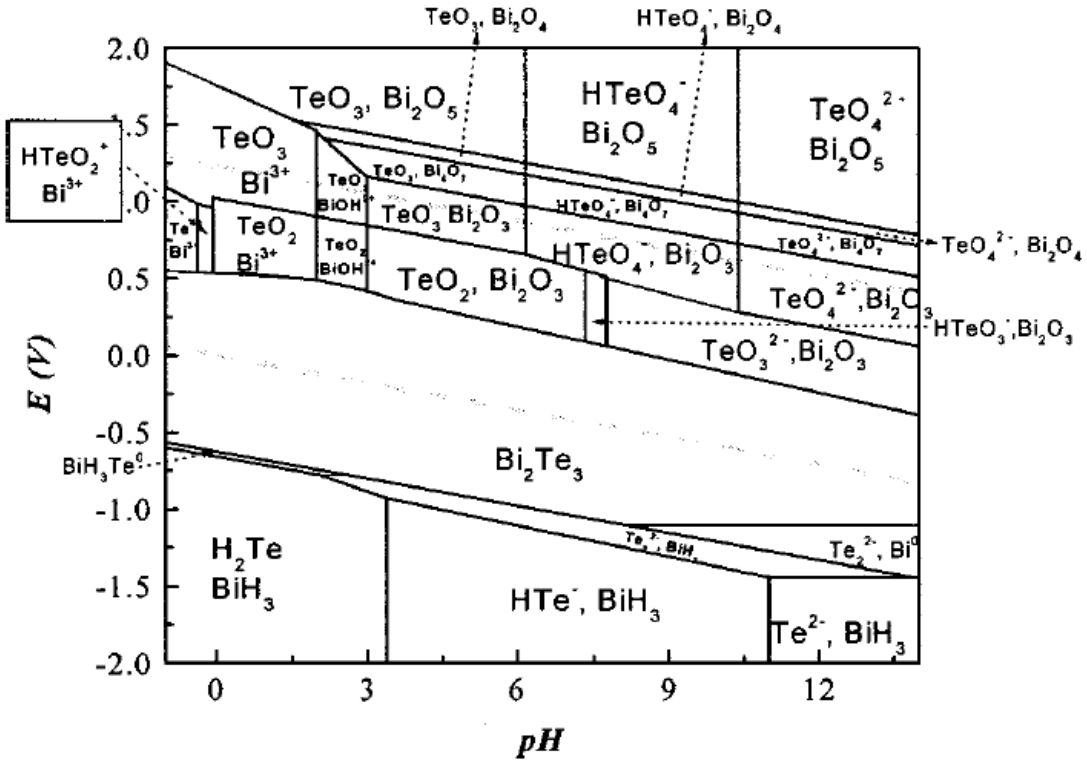

Figure 3.16. Pourbaix diagram of Bi_2Te_3. Ref.[108].

oxidation and reduction of bismuth chalcogenides, the reactions appear to be electron transfer controlled (which will be discussed latter). Therefore, Pourbaix diagram may not apply to the system until it achieves equilibrium.

Furthermore, there are limitations of the 'single compound' Pourbaix diagrams because they only reflect the evolution of the individual elements without the influence of other elements. To study the binary or ternary bismuth chalcogenides, one should consider the interactions of involved elements. For example, mutually induced codeposition facilitate the deposition of bismuth chalcogenides, therefore the actual deposition potential for bismuth chalcogenides is more positive than the potentials shown in 'single compound' Pourbaix diagrams for reducing the individual elements (compared Figures 3.13 and 3.14 to Figure 3.16). Besides, for ternary bismuth chalcogenides, deposition is more easily to happen when precise stoichiometry is not achieved, which makes the situation more complicated. However, 'single compound' Pourbaix diagrams still provides a method to qualitatively estimate the reaction products.

3.3.3 XPS for thiol functionalised samples

The samples prepared as described in Section 3.2.1 were characterized by XPS to check whether the thiol functionalisation protects the surface from oxidation. Figure 3.17 compares the XPS for a 1,5'-pentanedithiol functionalised sample, a 1-pentanethiol functionalised sample and an unprotected

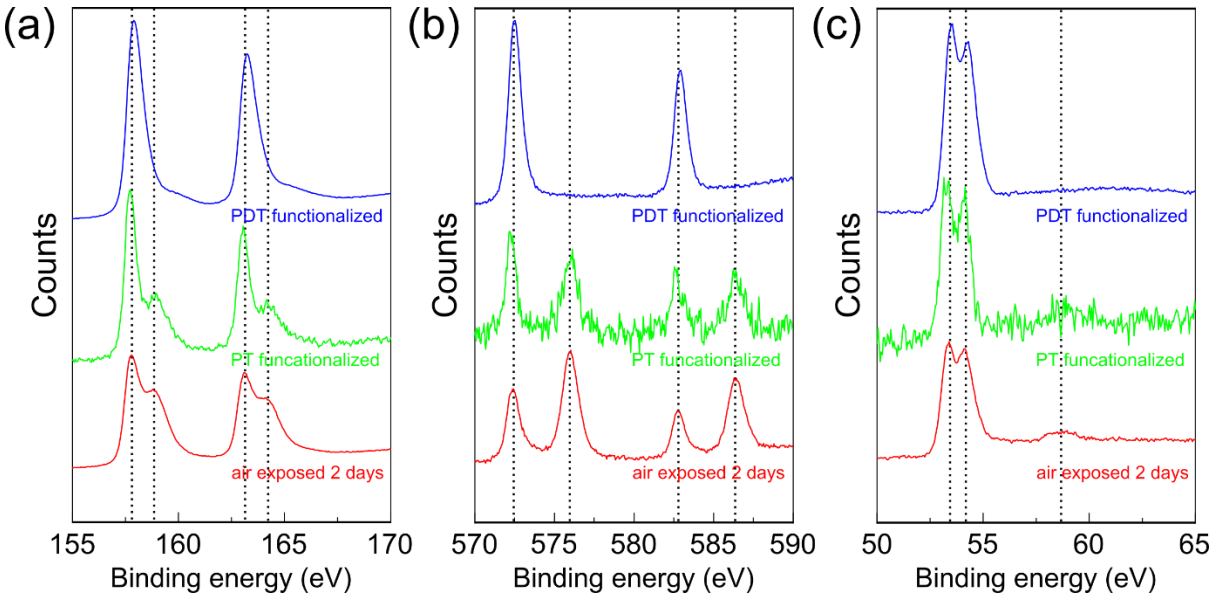

Figure 3.17. Bi 4f (a), Te 3d(b) and Se 3d (c) XPS for an unprotected sample (bottom - the same data as the middle curves of Figure 3.11), a PT functionalise sample (middle) and a PDT functionalised sample (top) after each was exposed to air for 2 days. The lower signal to noise ratio of the middle curves is due to the smaller detecting area.

sample (each sample was exposed to air for 2 days). Compared to previous results, 1,5′-pentanedithiol functionalised sample is similar to the in-situ cleaved sample. No clear evidence of oxidation can be detected, which indicates that 1,5′-pentanedithiol can protect the surface from oxidation. However, the 1-pentanethiol functionalised sample is different. Clear oxidation peaks are observed, although these peaks have lower intensities than the corresponding peaks for the unprotected sample. The results indicate that 1-pentanethiol also reduced oxidation to some extent. As discussed before, 1-pentanethiol may form a well-ordered but thin layer, whereas 1,5′-pentanedithiol may form a disordered but thicker layer due to polymerisation. The thicker layer blocks surface charge transfer, and therefore affects the electrochemical response of the sample, as shown in Section 3.2.2. On the other hand, it also provides better protection against surface oxidation, see Figure 3.17.

3.4 Chapter Discussion

Electrochemical modification and thiol functionalization of $Bi_2Te_{0.9}Se_{2.1}$ were carried out. XPS measurements for these samples are compared with in-situ cleaved and air exposed samples.

Parts of the results are consistent with the expectations. (1) XPS for the in-situ cleaved sample do not show obvious signs of surface oxidation. (2) XPS for the long-term air-exposed samples have prominent oxidation peaks, showing the effects of surface oxidation in air. (3) XPS for the electrochemically protected sample show no evidence of surface oxidation, which demonstrates the feasibility of electrochemical protection. (4) XPS for the electrochemically oxidised sample provide more clues of surface oxidation than XPS for the air-exposed samples, which suggests that electrochemical oxidation is more effective than air exposure. (5) XPS for the electrochemically reduced sample are similar to XPS for the in-situ cleaved sample, showing the reversibility of electrochemical modification. (6) XPS for the 1,5′-pentanedithiol functionalised sample show no evidence of surface oxidation, which suggests that thiol functionalisation could protect bismuth chalcogenides from air oxidation.

However, some phenomena are unexpected. (1) The timescale of air oxidation is slightly different from the data given by the literature. This discrepancy may be attributed to the difference of sample quality or the randomness of sample cleaving. (2) Compared to 1,5′-pentanedithiol, functionalisation of 1-pentanethiol has less effects on surface protection. Spontaneously polymerisation of 1,5′-pentanedithiol may explain its better efficiency of surface passivation. (3) During the electrochemical oxidation experiment, a rapid decrease of the oxidation current was observed due to possible surface passivation.

3.5 Chapter Summary

This chapter demonstrates the ability to control and characterize the surface oxidation of single-crystal $Bi_2Te_{0.9}Se_{2.1}$ in an electrochemical environment and compares the results to atmospheric oxidation and surface functionalisation by thiols. XPS and electrochemical techniques were used to study the electrochemical modification and thiol functionalisation of single-crystal $Bi_2Te_{0.9}Se_{2.1}$. Results for in-situ cleaved, air exposed, electrochemically modified, and thiol functionalised samples showed (i) the timescale of surface oxidation in an ambient environment; (ii) the feasibility of maintaining an oxide-free surface under electrochemical control for EC-STM study; (iii) different sensitivities of Bi, Te and Se toward air oxidation; (iv) the transition between dissolution and passivation during electrochemical oxidation; (v) the partial reversibility of electrochemical oxidation and (vi) the feasibility of thiol functionalisation. Electrochemical oxidation of different bismuth chalcogenides studied by EC-STM will be discussed in Chapter 4.

CHAPTER 4

ELECTROCHEMICAL SCANNING TUNNELLING MICROSCOPY STUDY OF BISMUTH CHALCOGENIDE SINGLE CRYSTALS

In Chapter 3, the surface chemistry of bismuth chalcogenide $Bi_2Te_{0.9}Se_{2.1}$ single crystals was modified by electrochemical methods and detected by XPS technique. The results suggested that bismuth chalcogenides would be a feasible platform for EC-STM study. Therefore, attempts to characterize the morphology of bismuth chalcogenides in an electrochemical environment by EC-STM were made. The first goal was to see whether it is possible to image bismuth chalcogenide surfaces in an electrochemical environment by EC-STM. The second goal was to study the evolution of the surfaces during electrochemical oxidation. The third goal was to compare different bismuth chalcogenides to understand differences in these materials and the origin of surface oxidation. This chapter will introduce the procedures of the EC-STM experiments and present the EC-STM images of freshly cleaved and electrochemically oxidized bismuth chalcogenides. The images of the fixed areas show the

surface evolution with increasing oxidation time, while the images of the randomly selected areas were used to study the relationship between surface morphology and oxidation time.

Attempts to date to study the properties of bismuth chalcogenides following exposure to air or water have led to conflicting conclusions as described in Chapter 3. Specifically, the degradation of bismuth chalcogenides in different environments has been studied by (non-electrochemical) STM because its outstanding spatial resolution enables morphology characterization on the nanoscale. In contrast to techniques such as X-ray photoelectron spectroscopy and electrochemical impedance spectroscopy that deliver integrated data from the whole sample, STM can provide real-space information. Of particular relevance to the present work, ultrahigh vacuum STM showed that dosing Bi_2Te_3 with water led to the formation of pits in the top QL [102]. In this study, only the top QL reacted with water, which indicates that the newly exposed QL was passivated. Furthermore, Bi_2Te_3 was imaged in UHV, nitrogen, ambient and organic solvent environments by STM [111]. The surface stability was much less in the latter two, with clear evidence of surface modification during STM scans. However, no EC-STM study has been reported. Since surface chemistry is strongly dependent on surface morphology, any features shown in STM images may influence the surface chemistry of surrounding areas. Further, considering that electrochemical control could modify the surface chemistry, EC-STM that combines a normal STM with electrochemical control may be a powerful tool to study both surface morphology and chemistry of bismuth chalcogenides. Here, EC-STM experiments were carried out to expand the research field of bismuth chalcogenides. Surface morphology and chemistry were linked with controllable parameters such as oxidation potential and oxidation time.

The work discussed in this chapter has been published (Langmuir 2019,35,47,15100-15105) [112] and some text has been taken from this paper, which was written by the author of this thesis with only limited input from his co-authors.

4.1 CVs for bismuth chalcogenides

For all the electrochemical experiments discussed in this chapter, the electrolyte was 0.05M Na_2SO_4 aqueous solution at pH 3.0 (adjusted by H_2SO_4 addition); A polypyrrole coated quasi-electrode (ppy) and a Pt ring were used as a reference electrode and a counter electrode, respectively.

In preparation for the STM measurements, CVs were carried out in the STM cell (which should have been described in Chapter 2). Figure 4.1 shows CVs measured for freshly cleaved $Sn_{0.01}Bi_{1.99}Te_2Se$ (a), Bi_2Se_3 (b) and $Bi_2Te_{0.9}Se_{2.1}$ (c) samples (these samples were imaged by EC-STM later). The scan rate was 50mV/s while the open circuit potential was about -0.1V. All CVs show clear anodic peaks and corresponding cathodic peaks. Taking the CVs for $Sn_{0.01}Bi_{1.99}Te_2Se$ as an example, in the first scan, there is a clear anodic peak between 0.1 and 0.2 V, while further anodic peaks are seen at more positive potentials. On the second and subsequent scans, a large cathodic peak corresponding to the reduction of the products of the previous scan is observed around -0.6 V. Two initial anodic peaks are replaced by a broad anodic peak starting around 0.0V. Subsequent cycles differ from the first due to the oxidation and reduction of electrochemical reaction products.

In most cases, the sample potential should protect the surface from both oxidation and reduction during imaging. Since the faradaic current between -0.3 V and -0.1 V is minimal, this potential region is suitable for $Sn_{0.01}Bi_{1.99}Te_2Se$ imaging. From the corresponding CVs, the potential regions for the other two samples are similar.

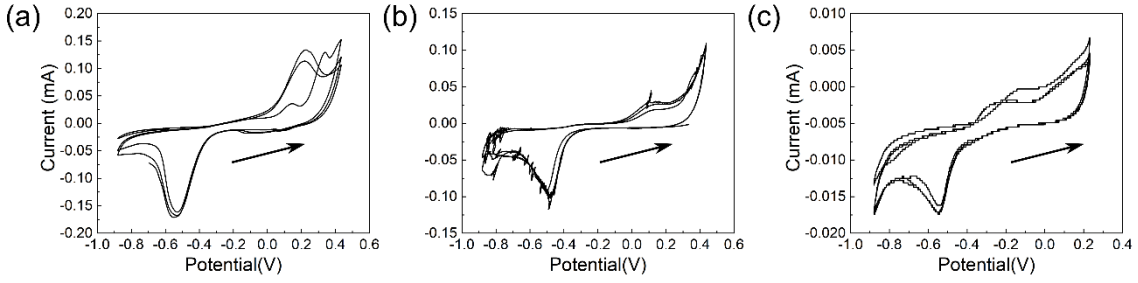

Figure 4.1. Cyclic voltammetry of a freshly cleaved (a) $Sn_{0.01}Bi_{1.99}Te_2Se$, (b) Bi_2Se_3 (c) and $Bi_2Te_{0.9}Se_{2.1}$. The scan rate was 50mV/s.

Similar features are observed in CVs for Bi_2Se_3, despite several spikes observed close to the cathodic limit of the second scan. Compared to CVs measured in normal three-electrode cells, CVs measured in the EC-STM cell are more sensitive to disturbances because the volume of the EC-STM cell is very limited. The anodic limit of CVs for $Bi_2Te_{0.9}Se_{2.1}$ is more negative than the corresponding values for the

other two, but the oxidation tendency is still clear. Since the outermost layers of $Sn_{0.01}Bi_{1.99}Te_2Se$, Bi_2Se_3, $Bi_2Te_{0.9}Se_{2.1}$ and the oxidation products from these layers are different [87], the position of the large cathodic peak shifts by about 0.1V.

4.2 EC-STM images for bismuth chalcogenides

EC-STM images obtained during or after electrochemical oxidation were compared with images for freshly cleaved samples to study the changes in surface morphology. The experiments were carried out using the procedure described in Chapter 2 at room temperature. The bias between the sample and the tip was fixed at -0.1V while the potential between the sample and the reference electrode was adjusted. It was important to avoid too large a bias as well as the accompanying large faradaic current to ensure the wax coating on the tip was stable on the timescale of the experiments.

4.2.1 EC-STM images for freshly cleaved bismuth chalcogenides

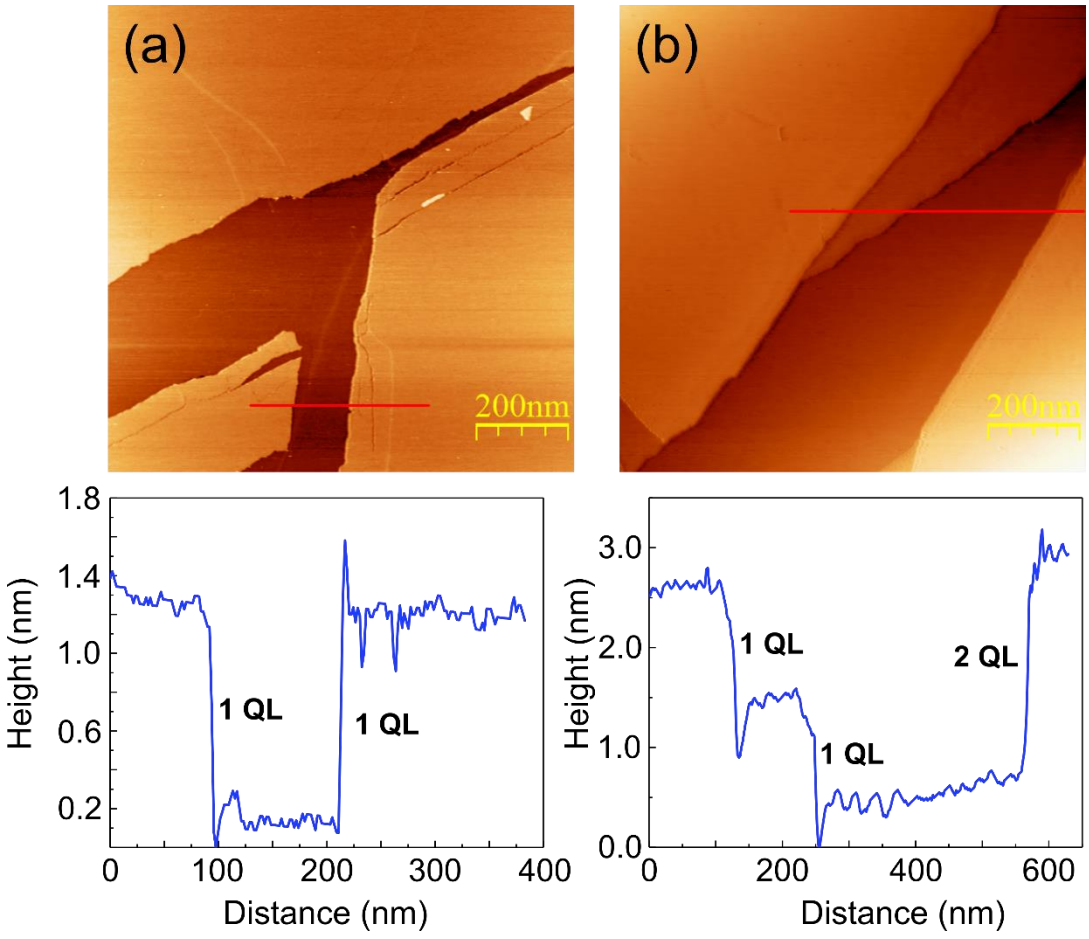

Figure 4.2. Images and surface profiles along the red lines of freshly cleaved (a) $Sn_{0.01}Bi_{1.99}Te_2Se$ (b) Bi_2Se_3.

The natural way to evaluate the effects of electrochemical oxidation is to compare the surface morphologies of bismuth chalcogenides before and after electrochemical oxidation. Hence typical EC-STM images of freshly cleaved bismuth chalcogenides at the rest potential are shown in Figure 4.2. The surfaces are smooth over hundreds of nm. Steps with the height equal to the expected QL thickness (1nm) or an integral multiple of the QL thickness are observed, which indicates the coexistence of monolayer steps and multilayer steps. Importantly, the surfaces can remain stable for several hours at the rest potential, whether or not they are simultaneously scanned. The stability of the bismuth chalcogenides at the rest potential was indicated by CVs and XPS in Chapter 3. Here, it is confirmed by in situ imaging directly.

4.2.2 EC-STM images obtained during oxidation

Several experiments were then carried out to study samples during oxidation. Figure 4.3 shows a series of images showing a fixed area of a $Bi_2Te_{0.9}Se_{2.1}$ sample that was experiencing mild electrochemical oxidation.

The surface underwent slow oxidation at a potential that was close to the starting point of the oxidation peak in Figure 4.1. Clear surface dissolution accompanied by pit formation was observed. These pits expanded in the lateral direction with increasing oxidation time until the whole quintuple layer dissolved. The surface height histograms show the evolution of the surface and indicate an average pit depth of about 1nm. The newly exposed surface exhibits significantly higher stability than the original surface, suggesting a sort of passivation. This phenomenon is consistent with the passivation of Bi_2Te_3 surface towards water described in Ref.[102]. The relation between surface oxidation and surface defects was discussed in Chapter 3 and could explain this passivation.

The STM images in the literature for a Bi_2Te_3 surface which was continuously scanned in ambient conditions showed similar surface morphology to Figure 4.3 [111]. The first scan showed a flat surface with pits one QL deep, and during the subsequent scans the pits expanded until the top QL had been removed. The reduced surface stability in an ambient environment was attributed to the adsorption of molecular species. Since the dissolution of the first QL can be achieved in air without electrochemical control, the dissolution observed in Figure 4.3 could be partly due to non-electrochemical factors such as tip effects. However, the electrochemical oxidation must play a role because the surface being scanned at the rest potential can remain stable for several hours. One possibility is either air exposure

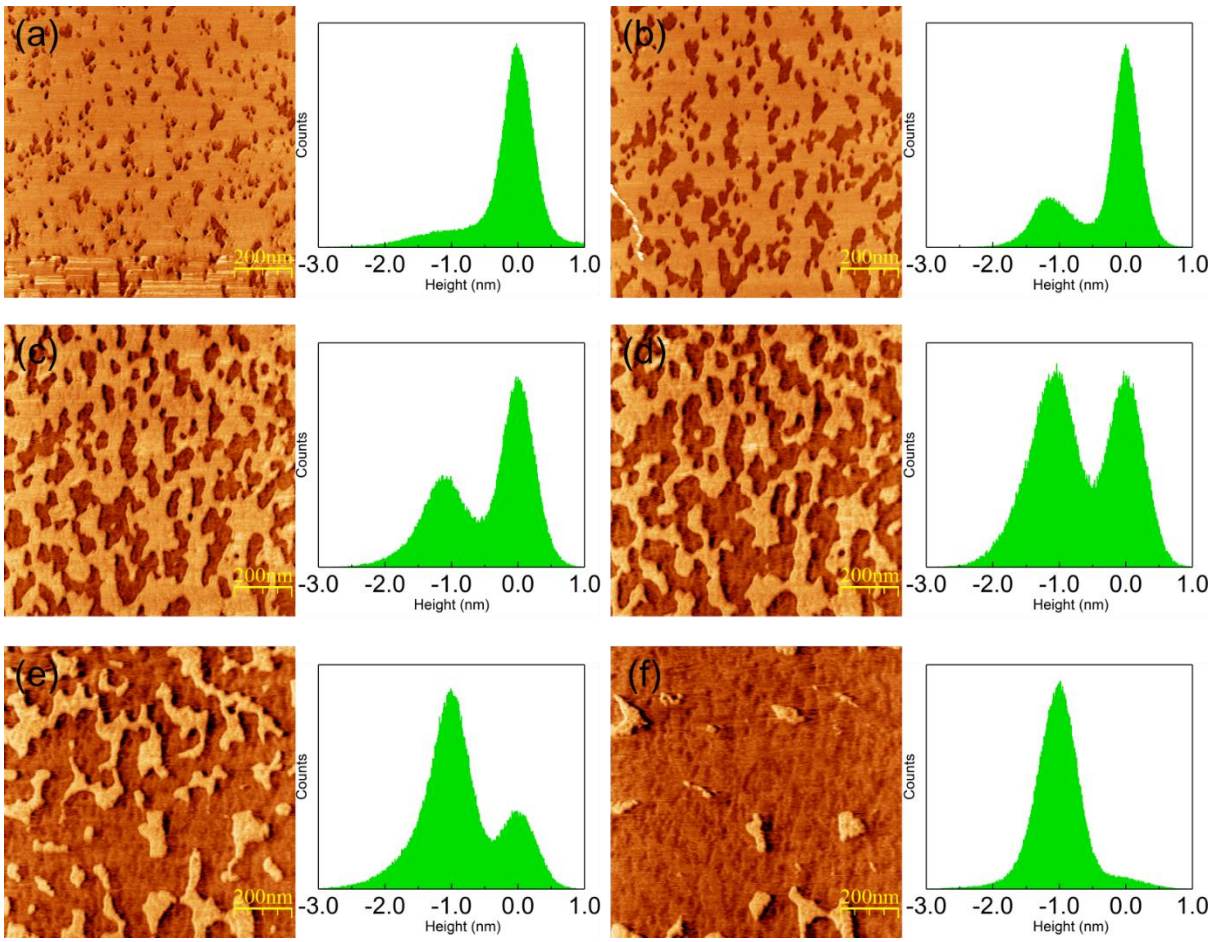

Figure 4.3. (a)-(f) $Bi_2Te_{0.9}Se_{2.1}$, continuously imaged at the oxidation potential E=0.1V vs ppy, shown at t=0 min, 10 min, 20 min, 30 min, 40 min, 50 min, respectively. Inserts are surface height histograms.

or electrochemical oxidation can make the outermost QL more easily removed by the STM tip. The effects of the STM tip will be discussed in the next section. Furthermore, the removal timescale for Bi_2Te_3 in an ambient environment in Ref.[111] is faster than the oxidative dissolution timescale for $Bi_2Te_{0.9}Se_{2.1}$ in this experiment. In principle, electrochemical oxidation should be more effective than air oxidation, but the opposite could occur for the following reasons. Firstly, the Te outermost layers of Bi_2Te_3 are more sensitive to oxidation than the mixed Te/Se outermost layers of $Bi_2Te_{0.9}Se_{2.1}$. Secondly, the Bi_2Te_3 used in Ref.[111] may have a higher density of defects, hence the removal rate was also higher than the $Bi_2Te_{0.9}Se_{2.1}$ used in this experiment. Thirdly, the tip effects in air may be stronger than the tip effects in solution, therefore the surface which was scanned in air may be affected by a larger interaction and thus removed faster.

4.2.3 Tip effects

The similarity of the $Bi_2Te_{0.9}Se_{2.1}$ and Bi_2Te_3 surfaces following scanning in different conditions may be due to tip effects that have long been noted and studied theoretically or experimentally. For example,

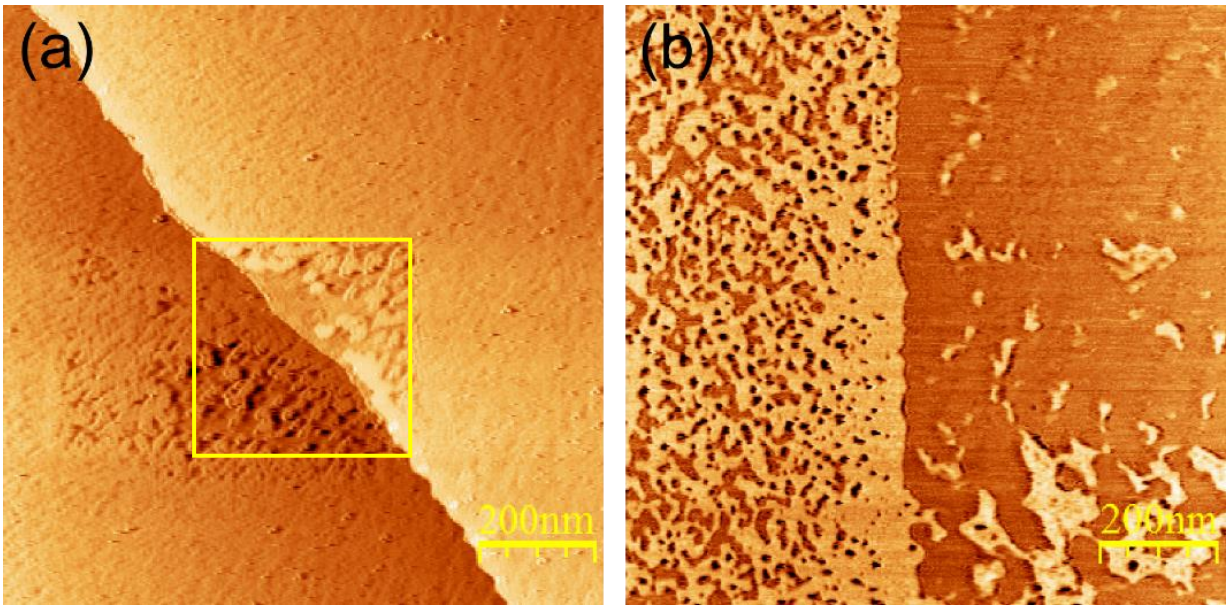

Figure 4.4. The evidence of tip effects. (a) E=0.0V, after scanning the central area for 30 mins. (b) E=0.1V, after scanning the right side 16 times for about 80 min, the scanning area was changed to include the left side and this image was taken.

the disappearance of adsorbed CO molecules during STM measurements was attributed to tip effects [113, 114]. Calculations suggested reorientation of adsorbed molecules and significant changes in the obtained images. Furthermore, current injection from the STM tip could move the adsorbed molecules laterally [115-117]. This effect depends on various factors, including the band structure of the acceptor. More importantly, the electric field around the STM tip may localize the excitations induced by inelastic electron tunnelling [118] and weaken or strengthen chemical bonds, giving STM the potential to influence local chemistry. Significant tip effects were observed during these measurements. Dissolution appeared to be more rapid where scanning took place than elsewhere, see Figure 4.4. The central area in Figure 4.4(a) was continuously scanned for 30 min before the scan area was enlarged. The marked rectangle area shows clear oxidative dissolution, whereas other areas do not. Figure 4.4 (b) was obtained by moving the scan area 500nm left after the previous area was scanned 16 times over about 80 min. Again, the area which experienced multiple scans dissolved faster than the area scanned for the first time, which provides evidence for tip effects. Since the bias between sample and tip was fixed at -0.1V, the tip might be expected to impede oxidative dissolution because the sample potential is more

negative than the tip potential. However, tip effects caused oxidative dissolution in Figure 4.4a and enhanced dissolution in Figure 4.4b, so the potential difference between sample and tip is unlikely to be responsible. The shielding effect of STM tip was observed during Cu deposition. A very large shielding of the diffusive flux of Cu^{2+} ions to the areas under the STM tip reduced the deposition rate of Cu [119, 120]. However, shielding a certain kind of ions is also unlikely to enhance oxidative dissolution. If the tip effects are not electrical effects or shielding effect, one would expect that the tip-sample interaction influences the surface dissolution mechanically. AFM tip-enhanced Cu deposition and dissolution were reported and attributed to tip-sample force [121]. This force could remove or disrupt the naturally occurring oxygen adlayers, hence create active sites for Cu deposition and dissolution.

One possible explanation is that the tip effects observed in these experiments are attributed to tip-sample force, but the oxidation potential is a precondition for dissolution. Unlike the normal electrochemical oxidative dissolution, tip-enhanced dissolution is a combined effect of tip-sample force and the applied potential. It may be divided into three steps. First, the oxidation potential activates the whole surface, but dissolution is impeded by "barriers". Since dissolution may start from surface defects such as Se/Te vacancies, the "barriers" may influence these vacancies, therefore obstruct the dissolution. Considering that the chemical composition of the as-grown crystals may deviate from the ideal stoichiometry to some extent, the "barriers" that block these defects could be intrinsic elemental Bi that originates from the crystal growth process. The "barriers" could also be oxygen adlayers discussed in Ref.[121] for AFM, although the tip-sample interaction for STM is a different nature. Next, the "barriers" in the scanned area are removed by mechanical influence. As a consequence, the scanned area dissolves at a higher rate than areas without scanning. In addition, the affected range of the tip influence is apparent from Figure 4.4. The tip effects appear to be highly localized because the continuously scanned area and the affected area match well.

For further study, more experiments are needed to evaluate the contribution of pure electrical effects. For tip effects dominated by an isotropic electric field, circular dissolution of the area beneath the tip would be expected. In addition, changing the bias between the sample and the tip may affect the influence of the tip. Experiments that study the relationship between the bias and the tip effects may lead to quantitative results.

4.2.4 EC-STM images for electrochemically oxidized samples obtained at the rest potential

The sample was oxidized for successive intervals at a predetermined potential to minimize tip effects. After each oxidation stage, the sample was imaged at the rest potential. Particularly, the tip was withdrawn before each oxidation stage and re-approached afterwards to reduce its influence on the oxidation process and keep the tip condition stable. The withdrawal distance was limited to about several μm to avoid drift.

The $Sn_{0.01}Bi_{1.99}Te_2Se$ sample was oxidized for successive intervals of 2 minutes at an applied potential of +0.05V with respect to the polypyrrole quasi-reference. After each oxidation stage, the sample was returned to the rest potential (-0.3V vs ppy) then imaged. A selection of results is presented in Figure 4.5.

Again, the pit density and coverage increased progressively with increasing oxidation time. The depth of the pits was generally equal to the thickness of a complete chalcogenide QL (1 nm) and did not change with oxidation time, showing a layer-by-layer dissolution mode. Moreover, oxidative dissolution took place on smooth terraces, in contrast to the redeposition that was concentrated on the step edges.

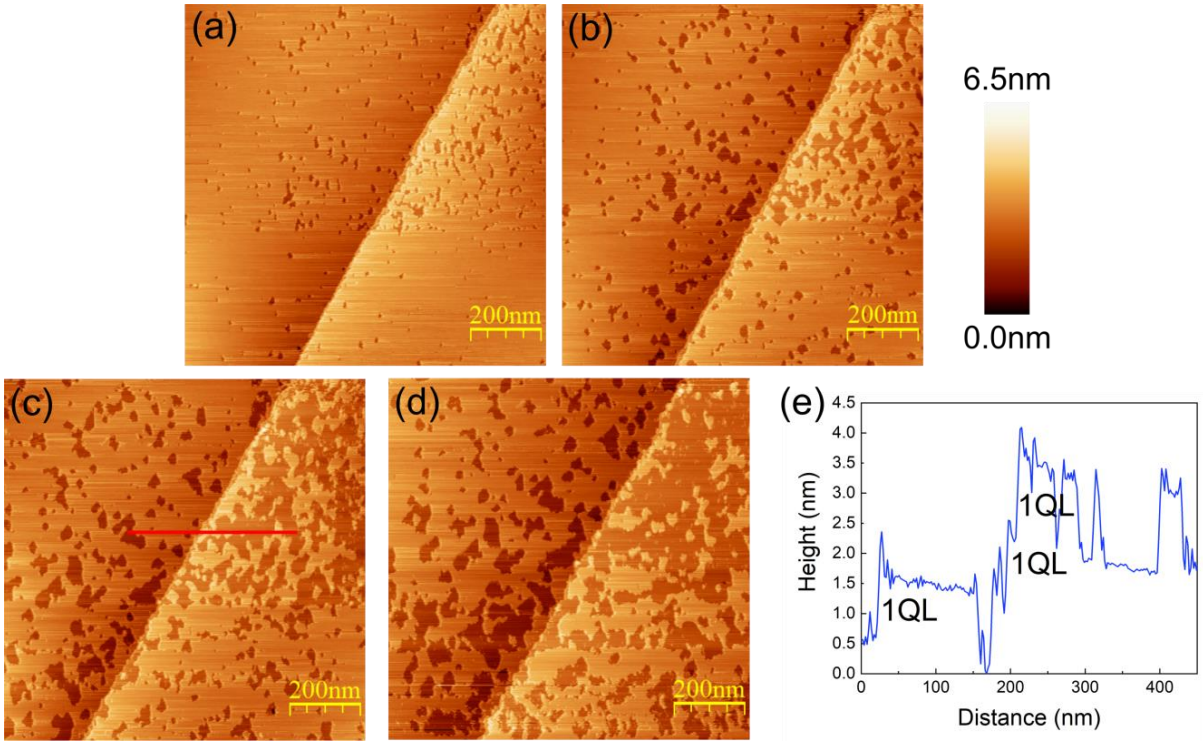

Figure 4.5. $Sn_{0.01}Bi_{1.99}Te_2Se$ surface imaged at E=-0.3V vs ppy, after oxidative dissolution at E=0.05V for (a) 4 min, (b) 12 min, (c) 18 min and (d) 24 min. (e) shows the surface profile along the red line in (c). Colour height scale is 6.5nm.

Figure 4.6 is a higher magnification image of part of the $Sn_{0.01}Bi_{1.99}Te_2Se$ surface shown in Figure 4.5. Although the newly revealed surface was passivated to some extent, a few pits were observed to form in the second QL. The apparent greater stability of the inner QL under electrochemical oxidation conditions could also be due to a lack of defects. In principle, perfect bismuth chalcogenides are relatively inert because there are no dangling bonds on the surface. Mild oxidation is expected to start from surface defects such as Se/Te vacancies [83, 88]. Since the outermost QL has a higher density of defects than the inner QLs due to cleaving or the short air exposure, it is reasonable that the reaction rate reduces after dissolving the outermost QL. The passivation is also consistent with the previously discussed literature [102]. In addition to pit formation, irregular clusters appeared where the dissolution took place.

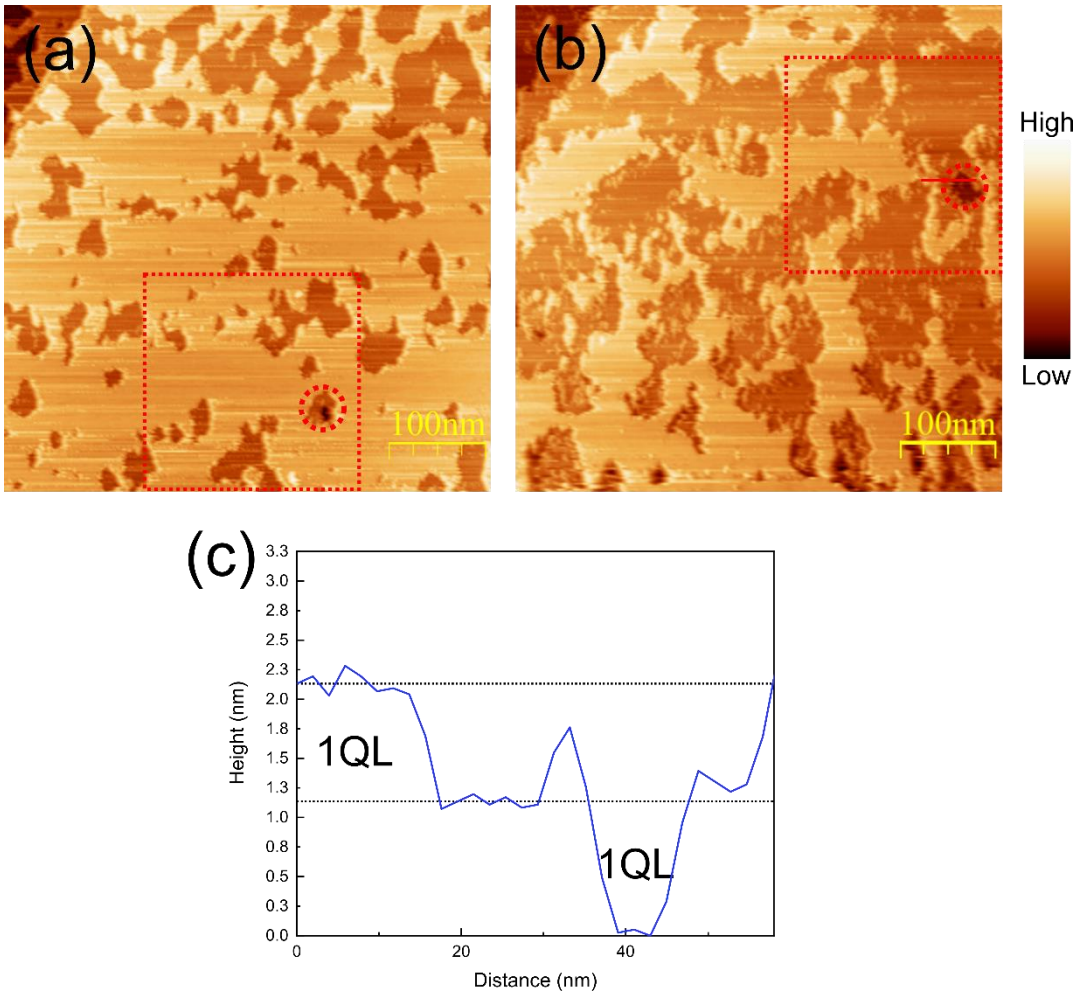

Figure 4.6. Higher magnification images showing parts of the $Sn_{0.01}Bi_{1.99}Te_2Se$ surface shown in Figure 4.6 after oxidative dissolution at E=0.05 V for (a) 18 min and (b) 36 min. The squares indicated by red dotted lines indicate the same area in each figure. All images were acquired at rest potential (E=-0.3V vs ppy). (c) shows the surface profile along the red line in (b). Colour height scale is 5nm.

Similar to $Bi_2Te_{0.9}Se_{2.1}$ which has been discussed in Chapter 3, the oxidation products are expected to be solvated Bi^{3+}ions, soluble $HTeO_2^+$ and $HSeO_2^+$ species in oxidation state +4 (since the amount of Sn is very limited, Sn related reactions are ignored). According to the Pourbaix diagrams and the discussion in Chapter 3, the clusters could be the corresponding oxides (mainly Bi_2O_3), but the existence of an intermediate structure due to incomplete oxidation could not be ruled out because their height is the same or less than that of a complete QL. Furthermore, the oxidation potential of this experiment (+0.05V

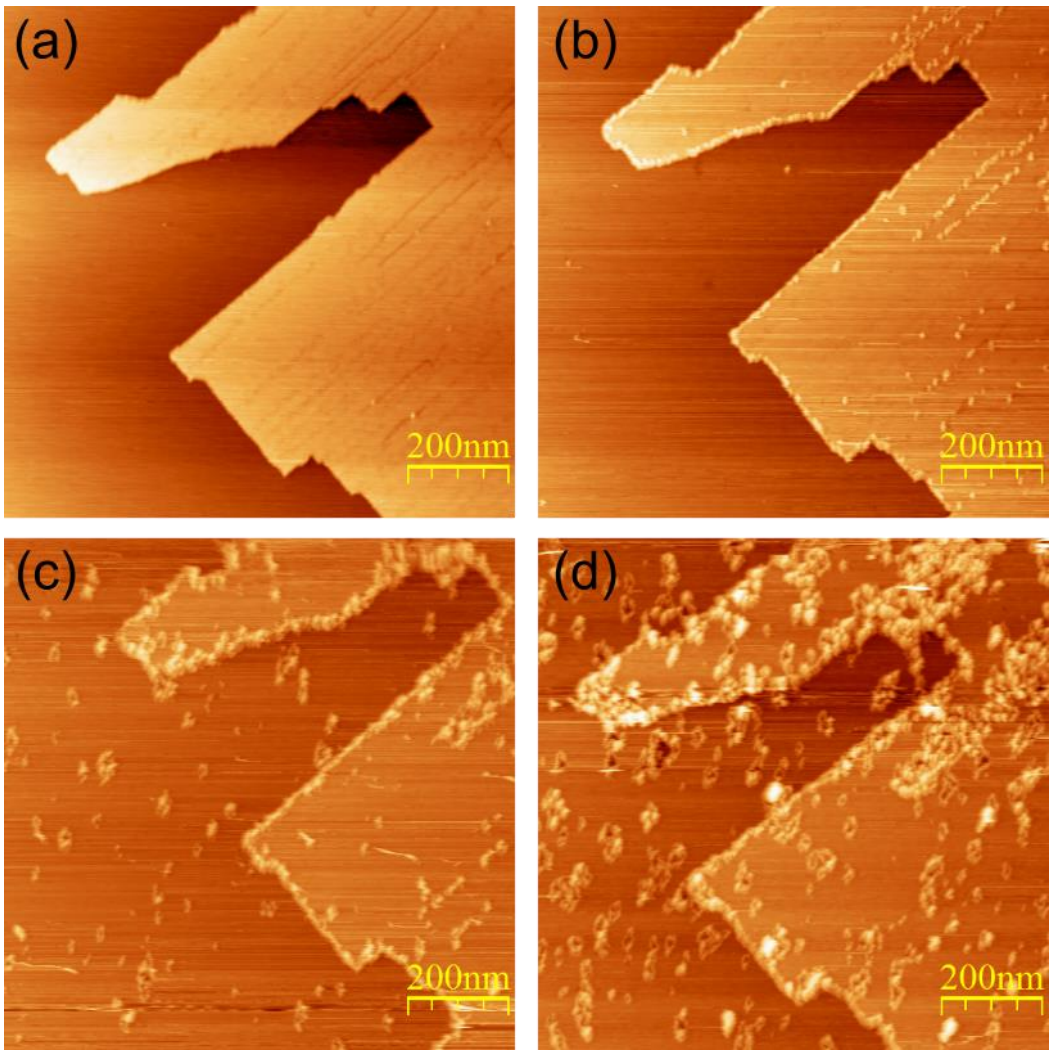

Figure 4.7. Bi_2Se_3, imaged at E=-0.4V vs ppy. (a) Freshly cleaved surface. (b)-(d) after oxidative dissolution at E=0.13V for 20s, 120s, 180s.

vs ppy) is more negative than the oxidation potential used in Chapter 3 (+0.1V vs MSE, which is about +0.2V vs ppy), therefore one would expect that the yield of oxides also decreases. Redeposition of dissolved components was observed when a more negative potential was applied after oxidative dissolution, see Figure 4.7 and Figure 4.8. Figure 4.7 shows a series of images of Bi_2Se_3 at -0.4V with respect to the polypyrrole quasi-reference, following electrochemical oxidation at an applied potential

of +0.13V for 20, 120 and 180 seconds. -0.4V was chosen as the imaging potential because clusters start to appeal at this potential. Considering the mutually induced codeposition and the Ref.[95] discussed in Chapter 3, these clusters should be redeposited Bi_2Se_3. Noticeably, the literature also used a similar potential to deposit Bi_2Se_3 from the solution containing Bi^{3+} and $HSeO^{2+}$, although the pH of their solution is lower (0.2-0.4).

Figure 4.8 was acquired at -0.6V with respect to the polypyrrole quasi-reference, following electrochemical oxidation at an applied potential of +0.15V for 20 seconds. Bright clusters with a wide distribution of heights (up to 2.5nm) decorated the edges of the step and pits. These clusters appear to be the products of reductive deposition rather than residue because most of the clusters are higher than 1QL. Similar to what was observed in Figure 4.7, the redeposition occurred primarily at step edges. The conditions for redeposition are appropriate electrochemical oxidation and a relatively negative imaging potential. Since the redox potentials for this experiment are similar to the parameters used in Chapter3, the redeposition products could be $Bi_2Te_xSe_{3-x}$, according to the discussion in Chapter 3. Again, the stoichiometry of the redeposited clusters will not necessarily be identical to that of the starting material.

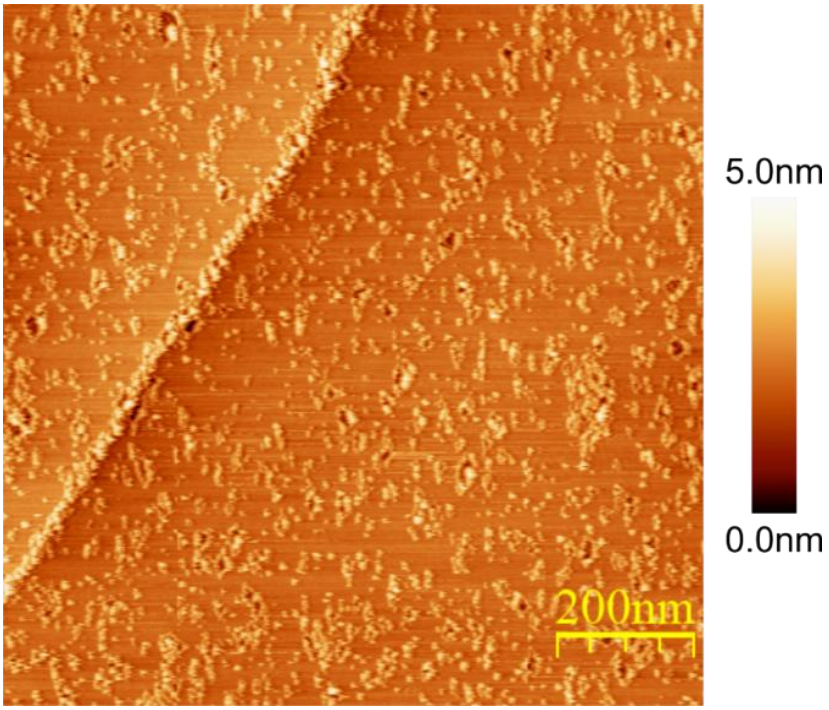

Figure 4.8. Image showing redeposition of dissolved components. E=-0.6V vs ppy, after oxidative dissolution at 0.15V for 20s. Colour height scale is 5nm.

4.2.5 Statistical study of the electrochemical oxidation process

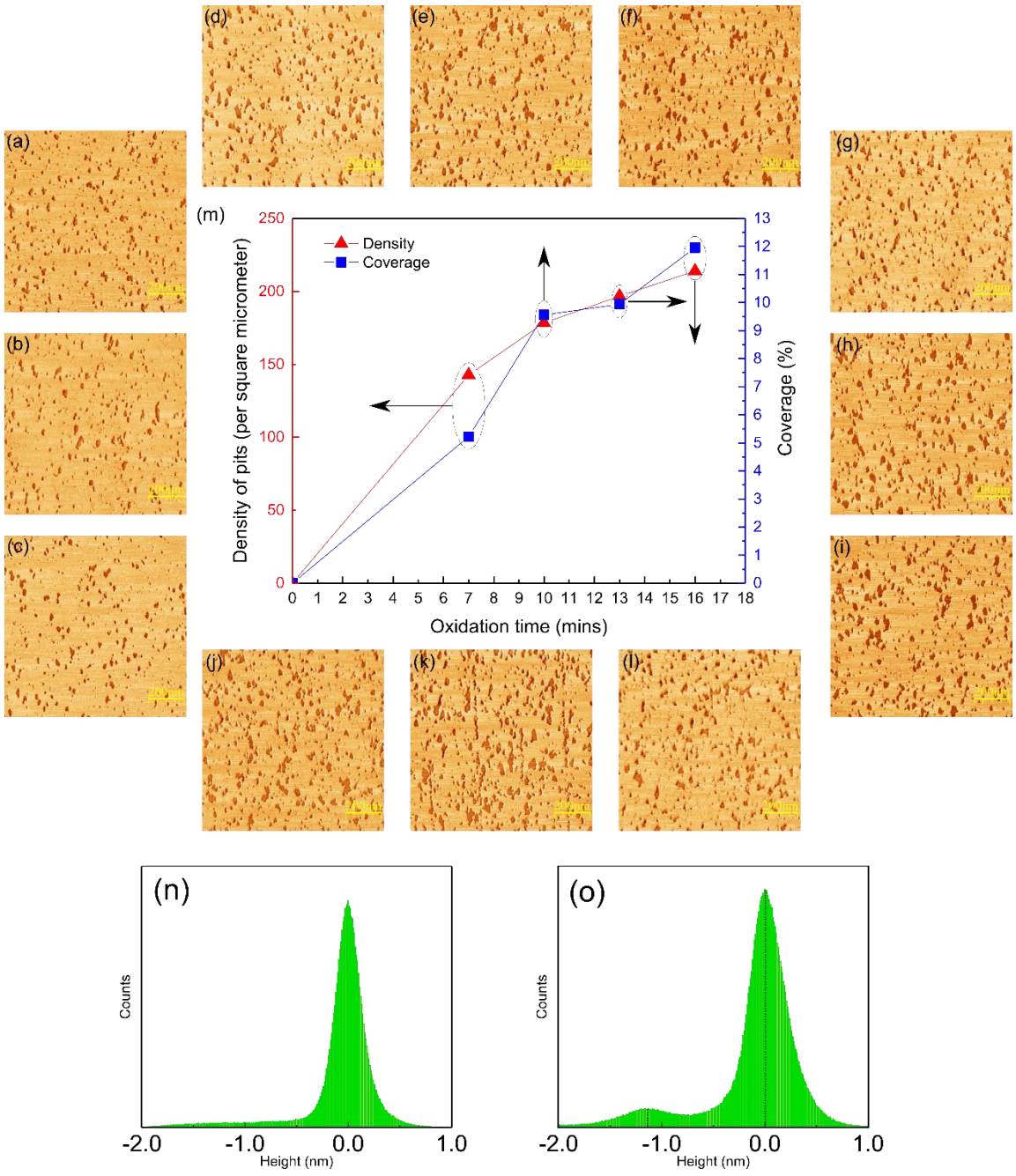

Figure 4.9. Randomly selected $Sn_{0.01}Bi_{1.99}Te_2Se$ areas imaged at E=-0.3V. (a)-(c) Areas 1-3, after oxidative dissolution at E=0.05V for 7 min. (d)-(f) Areas 4-6, after oxidative dissolution at E=0.05V for 10 min. (g)-(i) Areas 7-9, after oxidative dissolution at E=0.05V for 13 min. (j)-(l), Areas 10-12, after oxidative dissolution at E=0.05V for 16 min (m) Pit density and coverage as a function of oxidation time. (n) Surface height analysis of (a)-(c). (o) Surface height analysis of (g)-(i).

The freshly cleaved surface is assumed to be spatially uniform. However, the upper area imaged in Figure 4.6 appeared to dissolve faster than the lower area, which indicates that the sample surface may be spatially non-uniform. In addition, since the tip was immersed in the electrolyte during the

electrochemical oxidation process, it may still affect the dissolution to some extent. Therefore, to avoid any potential tip effects and to minimize the influence of spatial difference, the extent of dissolution as a function of oxidation time for randomly selected areas was studied. The oxidation potential was +0.05V with respect to the polypyrrole quasi-reference. Before each oxidation stage, the STM tip was removed from the electrolyte to avoid any tip influence. After each oxidation stage, several different areas were randomly selected then imaged. The resulting data and the images used to calculate them are shown in Figure 4.9. In this experiment, there was no evidence of some parts of the sample dissolving faster than others. The pit density and coverage calculated from the collected images using ImageJ both increased with increasing oxidation time, see Figure 4.9 (m).

Figure 4.10 shows the results for a similar experiment with a more positive oxidation potential (+0.1V with respect to the polypyrrole quasi-reference). The pit coverage also increased with increasing oxidation time, while the pit density was not calculated because pits overlapped at high coverage. Since the applied potential was more positive, the dissolution rate significantly increased.

A similar experiment was carried out for $Bi_2Te_{0.9}Se_{2.1}$ to compare different bismuth chalcogenides. Notably, oxidized $Bi_2Te_{0.9}Se_{2.1}$ shows different surface morphology, see Figure 4.11. The pits on $Sn_{0.01}Bi_{1.99}Te_2Se$ have a similar size and are distributed homogeneously, whereas the pits on $Bi_2Te_{0.9}Se_{2.1}$ have a range of sizes and are distributed unevenly. Calculations suggest that the structures of $Sn_{0.01}Bi_{1.99}Te_2Se$ and $Bi_2Te_{0.9}Se_{2.1}$ QLs are Te-Bi/Sn-Se-Bi/Sn-Te and Te/Se-Bi-Se-Bi-Te/Se, respectively [87]. Hence, the heterogeneous morphology of $Bi_2Te_{0.9}Se_{2.1}$ may be attributed to different dissolution rates of Te and Se in the outermost layers. Since the outermost layers of $Sn_{0.01}Bi_{1.99}Te_2Se$ are pure Te, the oxidative dissolution would be expected to occur on the whole surface at the same rate. Since each part of the surface has the same composition, every pit edge would be expected to expand at the same rate, leading to a relatively uniform pit size. The situation is different for $Bi_2Te_{0.9}Se_{2.1}$. Its outermost layers consist of Te and Se. The distribution of Te and Se may be heterogeneous on the nanoscale, therefore Te- and Se-rich areas are expected to exist. The Te-rich areas may be more easily dissolved than the Se-rich areas because Te is more sensitive to oxidation, leading to a non-uniform pit distribution.

A positive correlation between the pit coverage and the oxidation time is shown in Figure 4.9-Figure 4.11, but the exact relationship between these two parameters is still not clear. The coverage versus time curve is determined by the mode of dissolution. Three probable modes lead to different curve shapes. (a) If the whole surface dissolves at a constant rate, the second derivative of the curve is zero. Therefore, a linear coverage versus time curve is expected. (b) Suppose each undissolved part of the first quintuple

layer has the same possibility to be dissolved at any time. In that case, the second derivative of the curve will be negative because the ratio of the undissolved area to the dissolved area will decrease with increasing oxidation time. Therefore, the coverage versus time curve has a positive but decreasing slope. The slope will approach zero if the newly revealed quintuple layer is passivated. (c) If each point at a pit edge has the same possibility to be dissolved at any time, the second derivative of the curve is expected to increase initially, then decrease because the total length of pit edges increases initially due to the formation of new pits and the extension of existing pits, then decreases due to the overlap of pits.

Mode (a) and (b) are excluded by the curves shown in Figure 4.10 and Figure 4.11, because the dissolution ates are very low in the initial stages. Therefore, mode (c) is the most probable dissolution mode.

For mode (c), based on the progressive nucleation discussed in Ref.[122], consider a simplified model in which all pits that do not touch another pit are circular. In analogy with the growth of two-dimensional layers, one can derive a relationship between the dissolution rate R and the oxidation time t.

For a single pit with radius $r(t)$, the number $N(t)$ of molecules dissolving into the solution obeys the equation:

$$\frac{dN(t)}{dt} = 2\pi k r(t) \tag{4.1}$$

where k is the rate constant for oxidative dissolution at the pit edge. Defining the area covered by the pit as $S(t)$ and the number of bismuth chalcogenide molecules per unit area as ρ we obtain:

$$\frac{dS(t)}{dt} = \frac{k}{\rho} 2\pi r(t) \tag{4.2}$$

For a circular pit, one can calculate $r(t)$:

$$r(t) = \frac{k}{\rho} t \tag{4.3}$$

Equations 4.1-4.3 hold as long as the pit does not touch other pits and the sample boundary.

In a real situation, there will be many pits dissolving simultaneously. The Avrami equation relates the area S that is actually covered by pits to the extended area S_{ex} that would be covered by pits if they did not overlap.

(4.4) $$S = 1 - \exp(-S_{ex})$$

For progressive pit nucleation, assume that new pits are form at a constant rate K. The extended area for a pit formed at a time t' is:

(4.5) $$S_{ex0} = \pi \frac{k^2}{\rho^2}(t - t')^2$$

Integrating over t' and multiplying by K, the total extended area S_{ex} is given by:

(4.6) $$S_{ex} = K\pi \frac{k^2 t^3}{3\rho^2}$$

Therefore, the actual area covered by pits is:

(4.7) $$S = 1 - \exp(-K\pi \frac{k^2 t^3}{3\rho^2})$$

The dissolution rate is given by:

(4.8) $$R(t) = \frac{dN(t)}{dt} = \rho \frac{dS(t)}{dt} = K\pi \frac{k^2 t^2}{\rho} \exp(-K\pi \frac{k^2 t^3}{3\rho^2})$$

Equation 4.8 predicts a dissolution rate that first rises then rapidly decreases. If the constant $K\pi \frac{k^2}{\rho}$ is set as 1, ρ is set as 100000, equation 4.8 can be written as:

(4.9) $$R(t) = K\pi \frac{k^2 t^2}{\rho} \exp(-K\pi \frac{k^2 t^3}{3\rho^2}) = t^2 \exp(-\frac{t^3}{3\rho}) = t^2 \exp(-\frac{t^3}{300000})$$

The plot of equation 4.9 shows the expected tendency, see Figure 4.12. Although the pits observed in the experiments have irregular shape, the overall tendency should be similar to the above discussion.

However, this mode has not been completely confirmed because the oxidation time of the experiments does not cover the dissolution of the whole quintuple layer and the time intervals between

measurements are too large. For the experiment shown in Figure 4.9, the first image was collected after electrochemical oxidation for 7 min, hence the data for the initial dissolution is missing. In this situation, if the first quintuple layer needs "activation" before dissolving, that could also explain the shapes of the curves in Figure 4.10 and Figure 4.11. Therefore, further experiments should pay more attention to the initial and the final dissolution stages of the first quintuple layer.

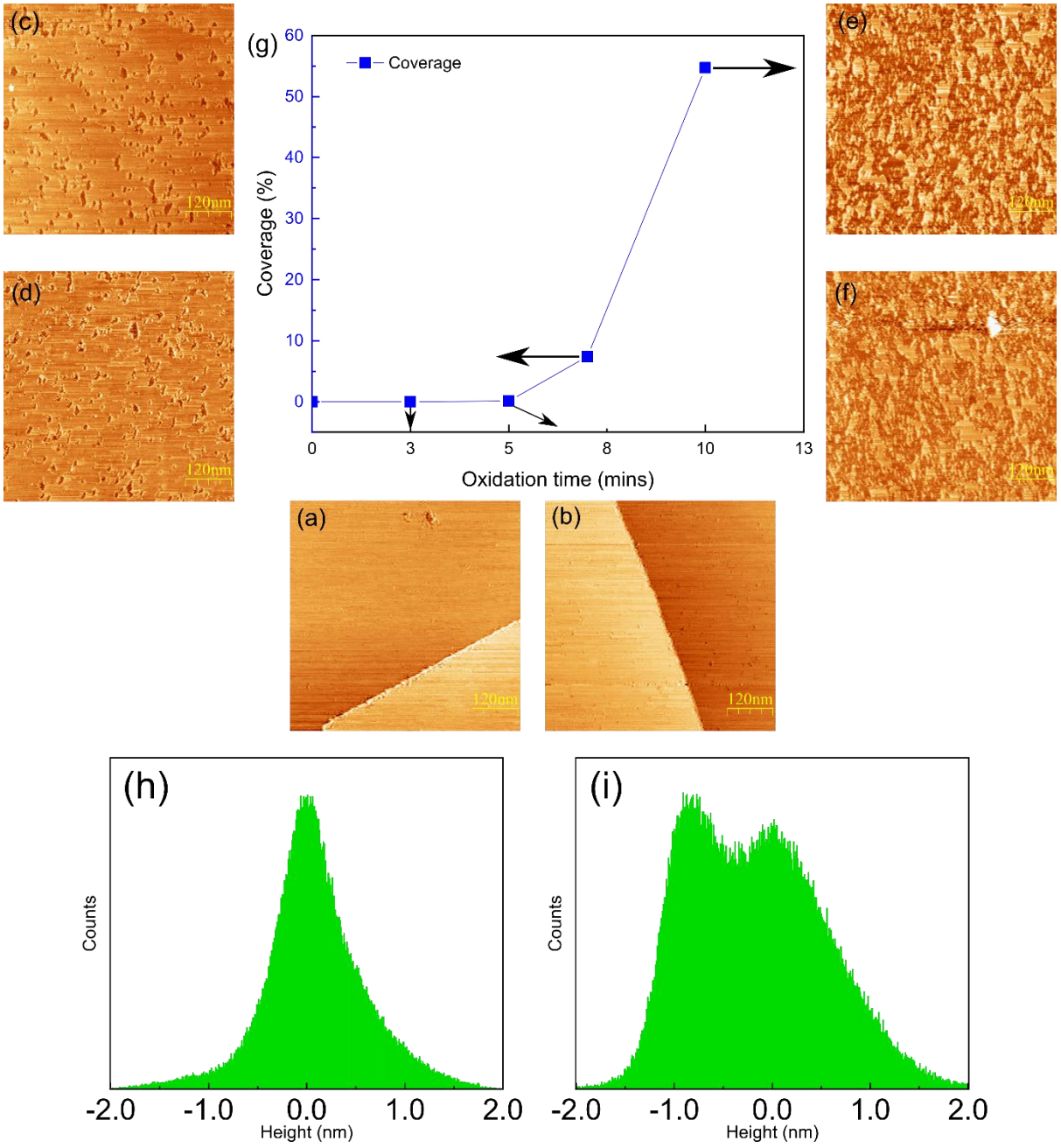

Figure 4.10. Randomly selected $Sn_{0.01}Bi_{1.99}Te_2Se$ areas imaged at E=-0.3V. (a) Area 1, after oxidative dissolution at 0.1V for 3 min. (b) Area 2, after oxidative dissolution at 0.1V for 5 min. (c)-(d) Areas 3-4, after oxidative dissolution at 0.1V for 7 min. (e)-(f) Areas 5-6, after oxidative dissolution at 0.1V for 10 min. (g) Pit coverage as a function of oxidation time.(h) Surface height analysis of (c)-(d). (i) Surface height analysis of (e)-(f).

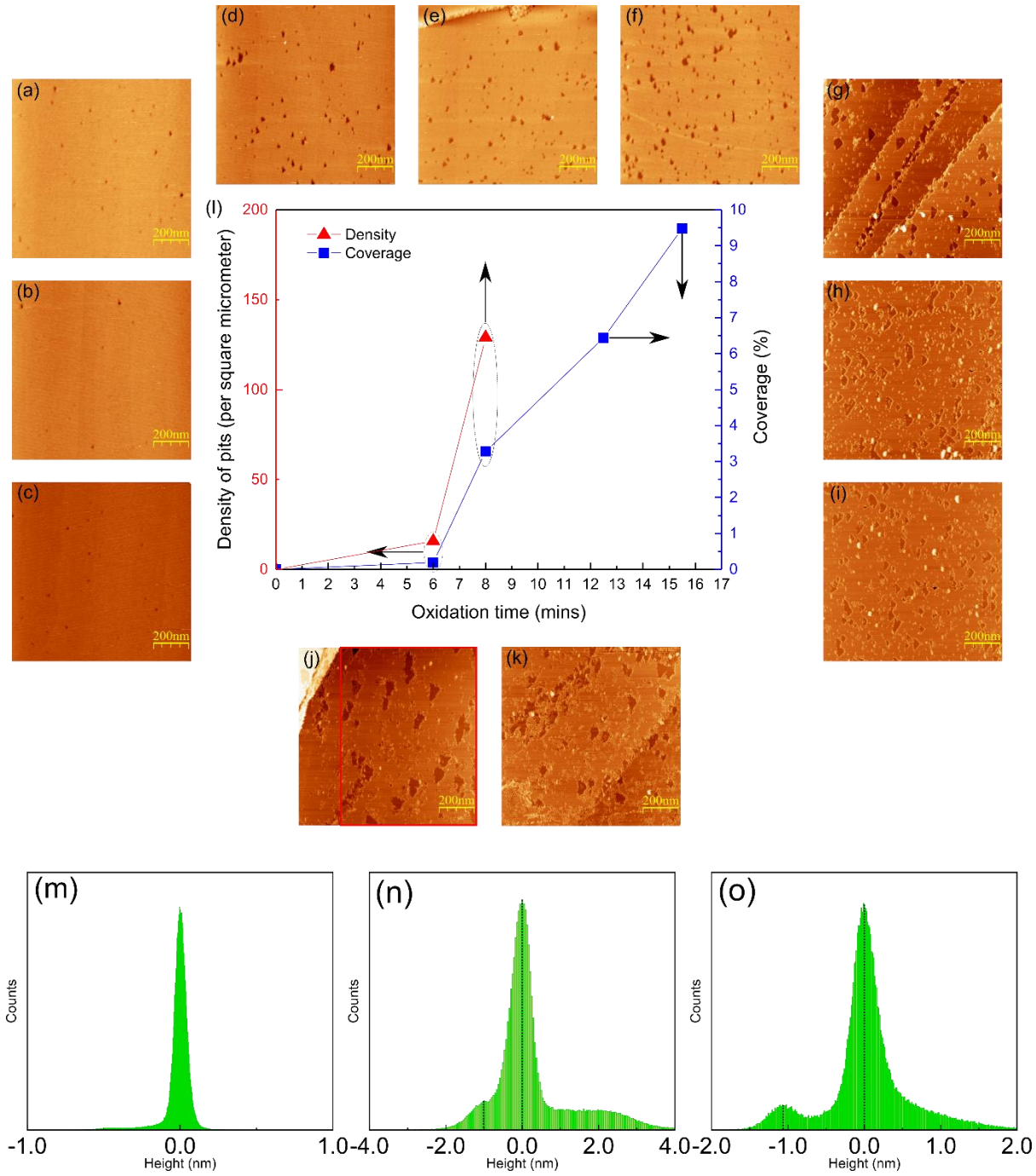

Figure 4.11. Randomly selected $Bi_2Te_{0.9}Se_{2.1}$ areas imaged at E=-0.3V. (a)-(c) Areas 1-3, E=-0.3V, after oxidative dissolution at 0.0V for 6 min. (d)-(f) Areas 4-6, after oxidative dissolution at 0.0V for 8 min. (g)-(i) Areas 7-9, after oxidative dissolution at 0.0V for 12.5 min. (j)-(k), Areas 10-11, after oxidative dissolution at 0.0V for 15.5 min. (l) Pit density and coverage as a function of oxidation time. The absence of the pit density data for the last two groups is due to redeposition. (m) Surface height analysis of (d)-(f). (n) Surface height analysis of (g)-(i). (o) Surface height analysis of the red rectangle marked area in (j) and (k).

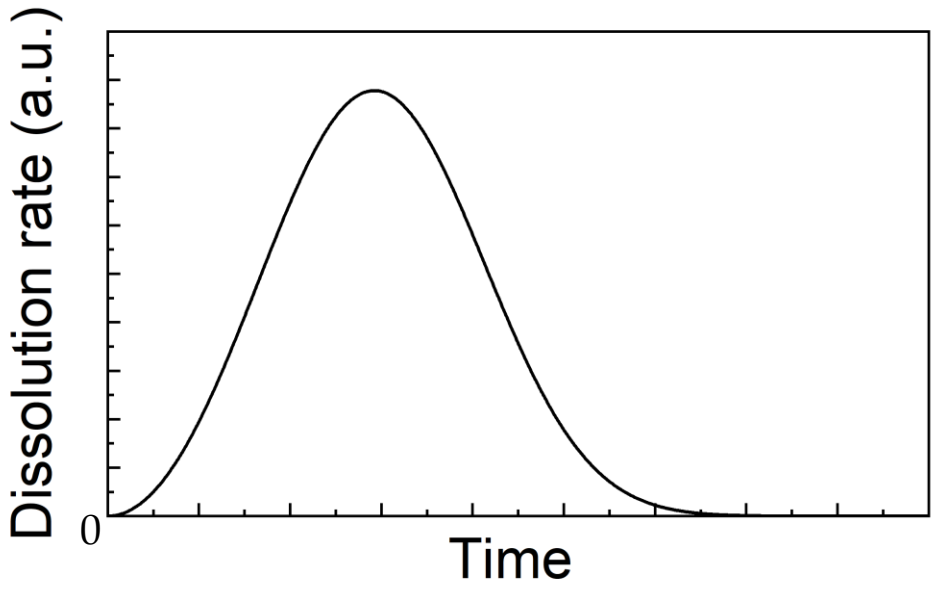

Figure 4.12. The plot of equation 4.9 showing the evolution of the dissolution rate.

4.3 Chapter Discussion

EC-STM experiments were carried out to image single-crystal surfaces of bismuth chalcogenides in situ under electrochemical control.

Parts of the results are expected. (1) At the rest potential, the surface can remain stable for several hours, whether or not it is being simultaneously scanned. The results confirmed the feasibility of electrochemical protection. (2) The first quintuple layer slowly dissolved when the surface was scanned at the oxidation potential, which demonstrates the feasibility of electrochemical oxidation. (3) Pit formation was observed after a series of mild oxidation stages. As expected, the pit density and coverage increased progressively with increasing oxidation time. (4) Redeposition of dissolved components was observed when a more negative potential was applied after oxidative dissolution, showing the partial reversibility of electrochemical modification.

However, some phenomena are unexpected. (1) Tip effects enhanced oxidative dissolution. Although the exact mechanism is still not clear, one explanation is that the tip effects are combined effects of tip-sample force and the applied potential. (2) The inner quintuple layers showed greater stability under electrochemical oxidation conditions (partial passivation), which may be attributed to the lower density of defects of the newly exposed surface. However, it was not completely passivated because a few pits

still formed on inner quintuple layers. (3) Oxidised $Sn_{0.01}Bi_{1.99}Te_2Se$ and $Bi_2Te_{0.9}Se_{2.1}$ show different surface morphologies. The heterogeneous morphology of $Bi_2Te_{0.9}Se_{2.1}$ may be attributed to the different dissolution rates of Te and Se in the outermost layers, whereas the homogeneous morphology of $Sn_{0.01}Bi_{1.99}Te_2Se$ may be attributed to the consistent dissolution rate of the Te outermost layers.

Compared to chapter 3, the results in chapter 4 provide more direct evidence of electrochemical protection and modification because the EC-STM images record the evolution of the surface morphology of bismuth chalcogenides. However, the dissolution rate observed in chapter 4 is much lower than the reaction rate calculated in chapter 3. This discrepancy can be explained by the following reasons. Firstly, the cleaving process may randomly influence the activity of the surface, thus affect the dissolution rate. Secondly, the dissolution reaction may involve more than six electrons. Therefore, the calculated reaction rate is larger than the actual rate. But the most possible reason is that the oxidation potential in chapter 4 (+0.05V vs ppy, which is ~-0.05V vs MSE) is more negative than the applied potential in chapter 3 (+0.1V vs MSE). Since the reaction rate strongly depend on the applied potential, the dissolution rate in chapter 4 decreased significantly. Consider the timescale of collecting an EC-STM image (~5min), the mild oxidation conditions in chapter 4 are more suitable for EC-STM study. Furthermore, the concepts of passivation in chapter 3 and 4 are different. In chapter 3, the surface passivated after the dissolution of more than ten quintuple layers. The residue of locally incomplete oxidation products (as the clusters in Figure 4.6b) may block the surface, therefore, impede further dissolution. In chapter 4, the surface partially passivated after the dissolution of the first quintuple layer. As discussed before, the term "passivation" only means the decreasing of electrochemical activity of the newly exposed quintuple layer. Therefore, one may expect that a more positive oxidation potential could overcome the partial passivation, as +0.1V vs MSE did in chapter 3.

4.4 Chapter Summary

In conclusion, the EC-STM was used to study the surface morphologies of bismuth chalcogenide single crystals under electrochemical control. In-situ imaging of these single crystals before and after the electrochemical modifications deliver significant physical insight and new knowledge by showing that (i) oxidative dissolution takes place via the progressive nucleation of pits rather than at step edges; (ii) there are differences between the first and subsequent quintuple layers; (iii) there are differences between different chalcogenides; (iv) the tip can enhance the dissolution process; (v) the pit coverage

increases with increasing oxidation time & the dissolution rate increases with increasing oxidation potential; (vi) redeposition of the oxidation products takes place at step edges. Finally, different models for dissolution are discussed based on the pit coverage versus oxidation time curves.

CHAPTER 5

ELECTROCHEMICAL STUDY OF BISMUTH SELENIDE SINGLE CRYSTALS

In Chapter 4, EC-STM was used to study the surface morphology of bismuth chalcogenides under electrochemical control, focussing on oxidative dissolution rather than the subsequent reductive redeposition. To provide a comprehensive picture of the latter, this chapter combines EC-STM and electrochemical impedance spectroscopy to study a typical bismuth chalcogenide Bi_2Se_3. First, EC-STM experiments, which were intended to produce deposits, were carried out. Next, electrochemical impedance spectra, collected under similar electrochemical conditions, were compared to EC-STM images to establish the link between electrochemical response and surface morphology. In particular, the electrolyte used here is different from that described in the previous chapters to be consistent with the electrochemical impedance measurements.

Bi_2Se_3 is a typical bismuth chalcogenide which has been studied by many researchers. It is a model topological insulator, a layered material and a promising platform for surface catalysis studies, as described in chapter 3. Experiments confirmed its exotic topological properties by angle-resolved

photoemission spectroscopy (ARPES) measurements [123, 124], spin pumping [19, 125] and spin torque studies [126, 127]. However, there are very few studies of its surface chemistry at ambient pressure. Since the topological properties of Bi_2Se_3 are derived from its topological surface states, surface chemistry that could influence its surface states may be strongly related to its topological properties. Therefore, the attempts to understand how electrochemical methods can be used to modify surface chemistry of Bi_2Se_3 are of great importance for adjusting and utilizing its topological properties.

5.1 EC-STM study of Bi_2Se_3 in 0.1M $NaClO_4$

Compare to the EC-STM experiments discussed in Chapter 4, these experiments have three main differences. Firstly, the electrolyte is 0.1M $NaClO_4$ rather than 0.05M Na_2SO_4 aqueous solution at pH 3 because 0.1M $NaClO_4$ is the supporting electrolyte used for electrochemical impedance measurements. Secondly, the experiments discussed in Chapter 4 were focused on dissolution caused by electrochemical oxidation, whereas the experiments discussed here focus on redeposition of dissolved components. Thirdly, the experiments discussed in Chapter 4 studied three bismuth chalcogenides and compared images of different samples to analyse the relationship between surface oxidation and elemental composition, but the experiments discussed here only studied Bi_2Se_3 as a typical bismuth chalcogenide. Instead of comparing different bismuth chalcogenides, these experiments linked two powerful techniques (EC-STM and EIS) to provide a new approach to study their surface chemistry.

5.1.1 Electrochemical oxidation and redeposition

Bi_2Se_3 single crystals used in this chapter were prepared by collaborators from Nanjing University. In this chapter, a Hg/Hg_2SO_4 electrode (MSE) was used as a reference electrode while a Pt ring was used as a counter electrode for all the experiments. The experiments were carried out with the procedures described in Chapter 2. Image processing used open source software Gwyddion.

Again, cyclic voltammetry measurements were carried out to determine potentials for electrochemical oxidation and reduction (Figure 5.1). In the first cycle, the CV shows two clear anodic peaks and subsequent cathodic peaks. Notably, the area of the anodic peaks is much larger than the area of the cathodic peaks, which indicates that only a part of oxidation products are reduced around -0.5V. Further explanation of this discrepancy will be shown in a later section. Since the open circuit potential is close to -0.2V, it was chosen as the imaging potential.

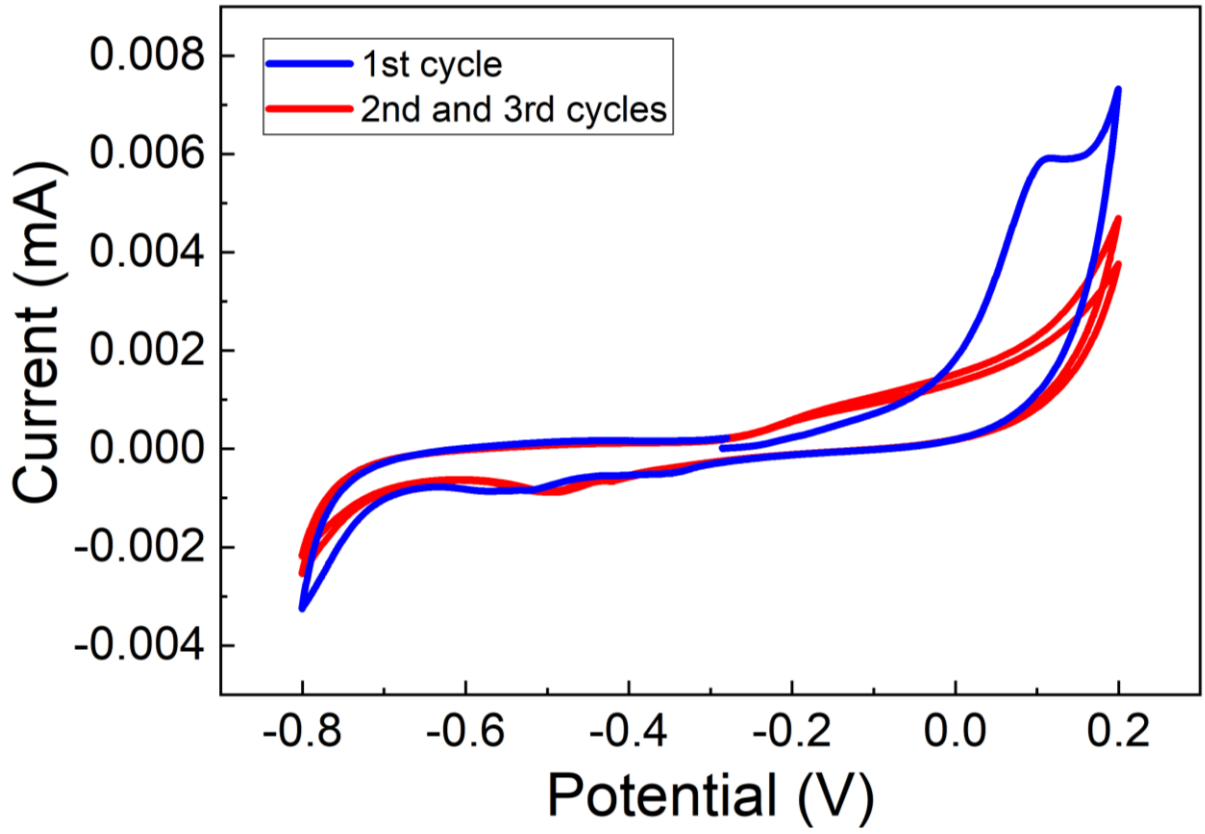

Figure 5.1. Cyclic voltammetry of a freshly cleaved Bi_2Se_3 sample measured in 0.1M $NaClO_4$. The scan rate was 10mV/s and the scan range was from -0.8V to 0.2V.

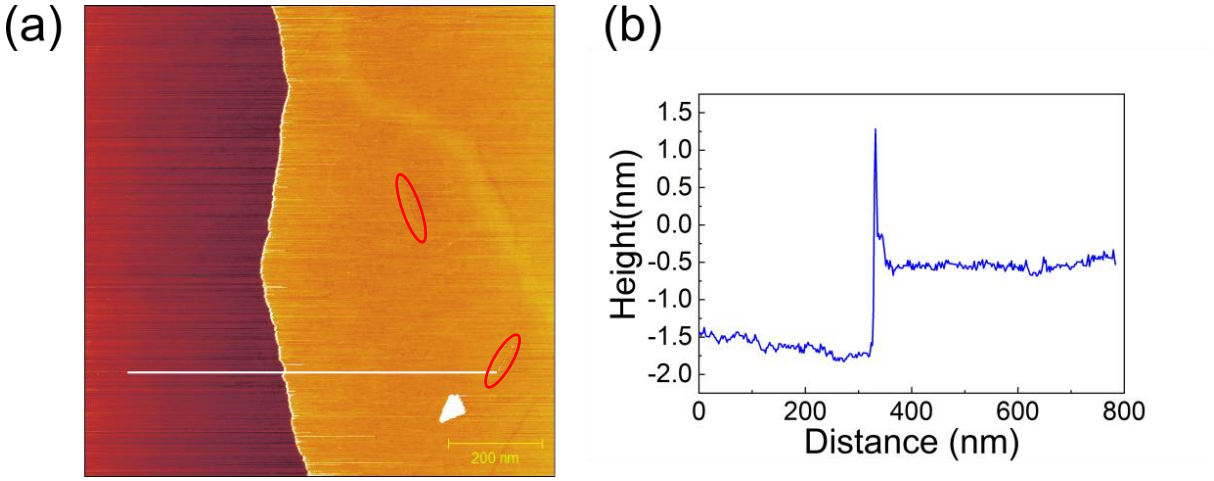

Figure 5.2. (a) Freshly cleaved Bi_2Se_3 surface imaged by EC-STM at E=-0.2V. (b) Surface profile along the line in (a). The image area is 1µm x 1µm.

A freshly cleaved Bi_2Se_3 surface imaged in 0.1M $NaClO_4$ at -0.2V with respect to MSE is shown in Figure 5.2. The surface profile shows that the step has a height equal to the quintuple layer thickness. The cracks are indicated by red dotted lines.

Figures 5.3a-5.3b show nearby regions following oxidation at 0.1 V for successive intervals of 60s. The scan area was not adjusted during the experiment, but drift is likely to have changed the imaging area slightly, as the tip was withdrawn by ~ 10 μm for each oxidation period. Similar to the images shown in Chapter 4, oxidative dissolution again generates pits of depth equal to the quintuple layer thickness, but the dissolution of the step edge is clearer. Pit formation is even more obvious when the surface is electrochemically oxidised at a more positive potential (0.2V), see Figure 5.3c-5.3d. The surface profile shown in Figure 5.3c reveals another difference between Figure 4.5 and Figure 5.3. Small clusters of ~ 1nm height tend to distribute in small pits or along the pit edges. These clusters are higher than the initial terrace height, suggesting that they are formed by deposition rather than being composed of residue that did not dissolve. Since the surface starts to dissolve along the crack, it becomes the most notable feature in the images, which is consistent with the expectation that the dissolution starts from surface defects.

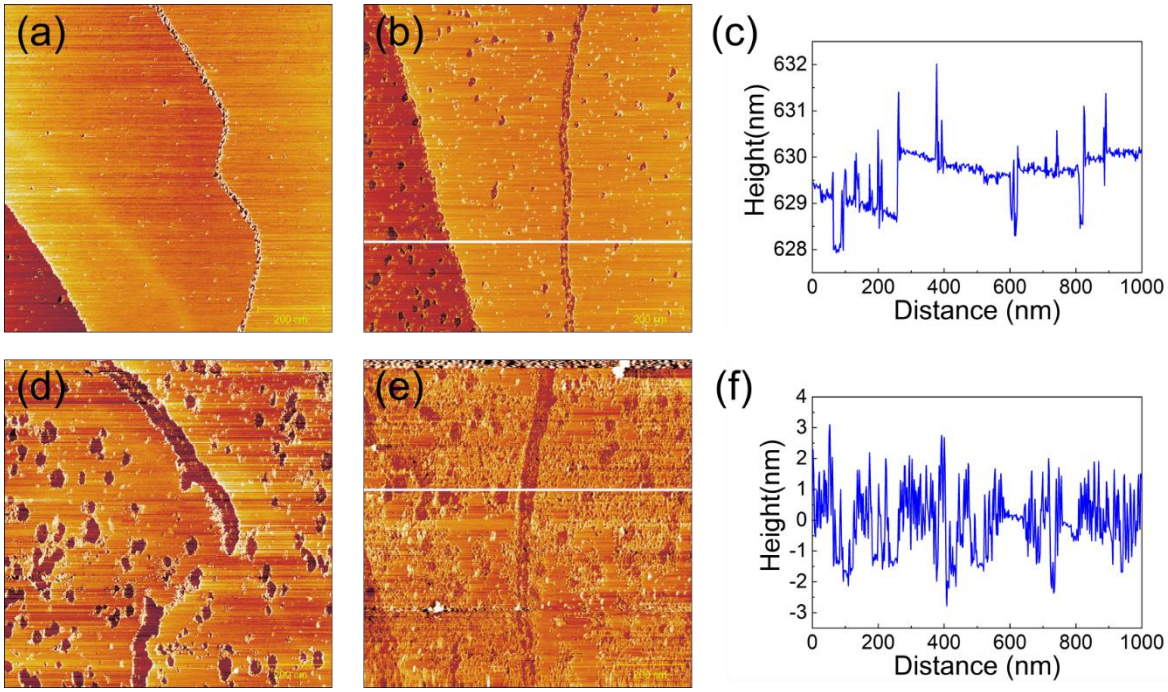

Figure 5.3. Bi_2Se_3 surface imaged at E= -0.2V, after oxidative dissolution at E = 0.1V for (a) 60s, (b) 120s. (c) Surface profile along the line in (b). Bi_2Se_3 surface after subsequent oxidative dissolution at E = 0.2V for (d) 60s, (e) 120s. (f) Surface profile along the line in (e). The image area is 1μm x 1μm.

Again, the Pourbaix diagrams are used to analyse the surface reactions, see Figures 5.4-5.5. Compared to the experiments discussed in Chapter 3 and Chapter 4, since the pH of the electrolyte has changed from 3 to 7, the solubility of Bi_2O_3 decreases significantly. Therefore, a higher proportion of Bi ions in oxidation state +3 released by Bi_2Se_3 dissolution could precipitate Bi_2O_3 at the oxidation potential. The

change of the pH also affects the oxidation of Se, but the most probable oxidation products in pH7 solution at the imaging potential are still Se ions in oxidation state +4.

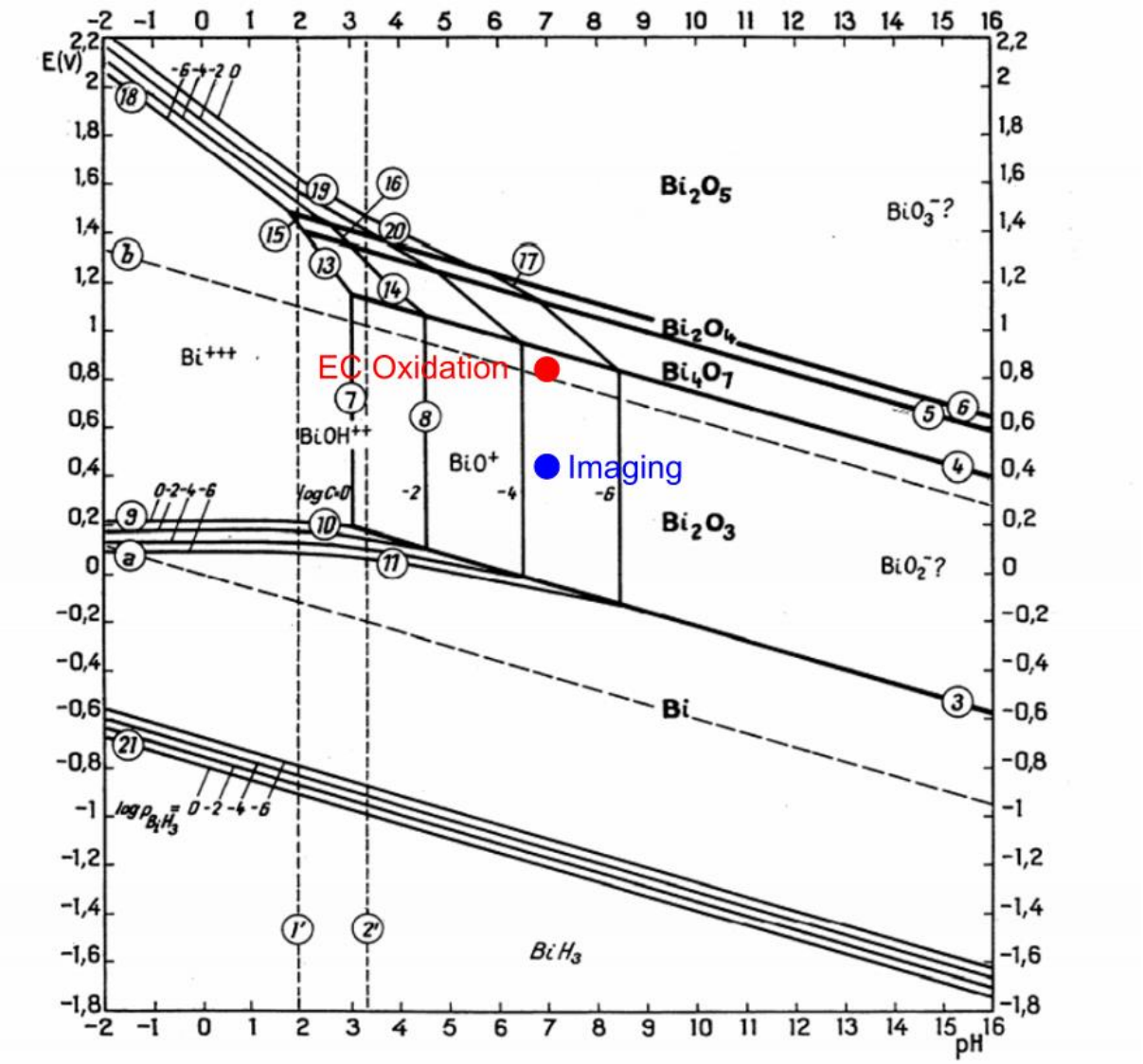

Figure 5.4. Pourbaix diagram of Bi. The electrochemical oxidation conditions are represented by the red dot (pH7, 0.2V vs MSE, which is about 0.85V vs SHE). The imaging conditions are represented by the blue dot (pH7, -0.2V vs MSE, which is about 0.45V vs SHE). Adapted from Ref.[110].

The Bi_2Se_3 redeposition potential may be more negative at higher pH for the following reasons. Firstly, any precipitation of Bi_2O_3 would reduce the availability of Bi ions in the pH7 solution. Secondly, it is more difficult to reduce Se ions at pH7, according to the Pourbaix diagram. Considering that redeposition starts at -0.4V with respect to the polypyrrole quasi-reference (about -0.5V vs MSE) in pH3

solution (Figure 4.7), the redeposition potential in pH7 could be more negative. Therefore, the small clusters observed at -0.2V with respect to MSE may be Bi_2O_3 rather than Bi_2Se_3.

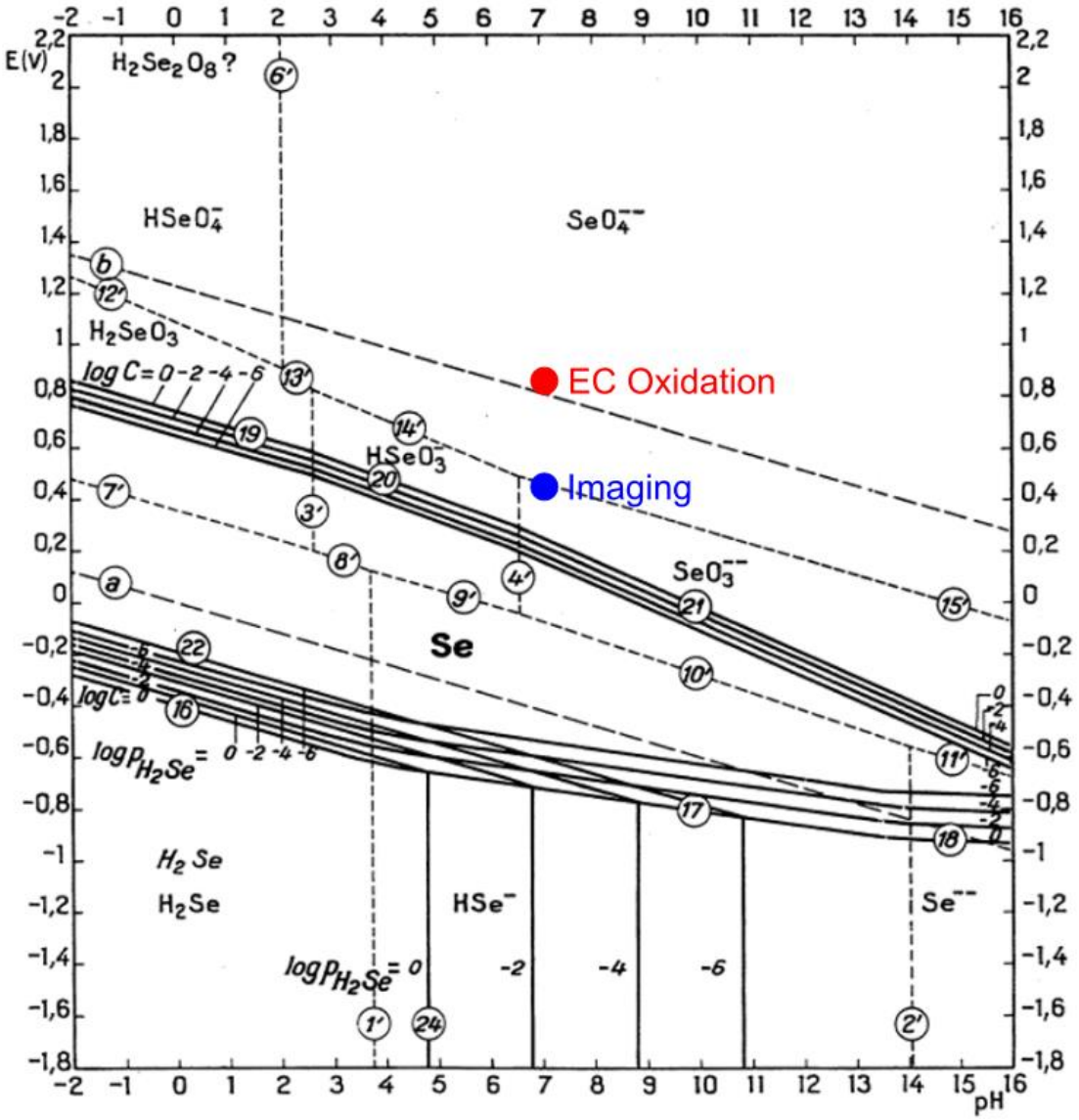

Figure 5.5. Pourbaix diagram of Se. The electrochemical oxidation conditions are represented by the red dot (pH7, 0.2V vs MSE, which is about 0.85V vs SHE). The imaging conditions are represented by the blue dot (pH7, -0.2V vs MSE, which is about 0.45V vs SHE). Adapted from Ref.[110].

5.2 EIS measurements of Bi_2Se_3 single crystals

EC-STM study provides direct spatially-resolved evidence of surface oxidation. Oxidative dissolution and adsorbed oxides change the surface morphology at the nano-scale. A natural question is whether the changes in surface morphology affect the electrochemical response. If so, how to find a link between

the microscopic morphology changes and the macroscopic electrochemical response. Here, the electrochemical impedance spectroscopy technique was used to study how electrochemical oxidation affects charge transfer resistance. The combination of EC-STM and EIS provides a new approach to study bismuth chalcogenides and can be applied to other materials.

5.2.1 Ferrocyanide/ferricyanide redox couple

Since charge transfer resistance is the resistance to the process of electron transfer from one phase to another, it depends on the electrode and electrochemical reactions being studied. A well-defined redox couple provides a reliable electrochemical reaction to simplify the analysis of impedance data. The selection of the redox couple mainly depends on its equilibrium potential, but possible reactions between the sample and the redox couple also need to be considered. The ferrocyanide/ferricyanide redox couple was used in this experiment because its equilibrium potential is in the electrochemical working window of Bi_2Se_3. In addition, no reaction is expected to happen between the sample and the redox couple.

Ferricyanide is the anion $[Fe(CN)_6]^{3-}$ (its most common salt is potassium ferricyanide $K_3[Fe(CN)_6]$). The structure of $[Fe(CN)_6]^{3-}$ is shown in Figure 5.6 (adapted from websites). A Fe^{3+} is bounded to six cyanide ligands in an octahedral geometry. The anion is easily reduced to the related ferrocyanide $[Fe(CN)_6]^{4-}$

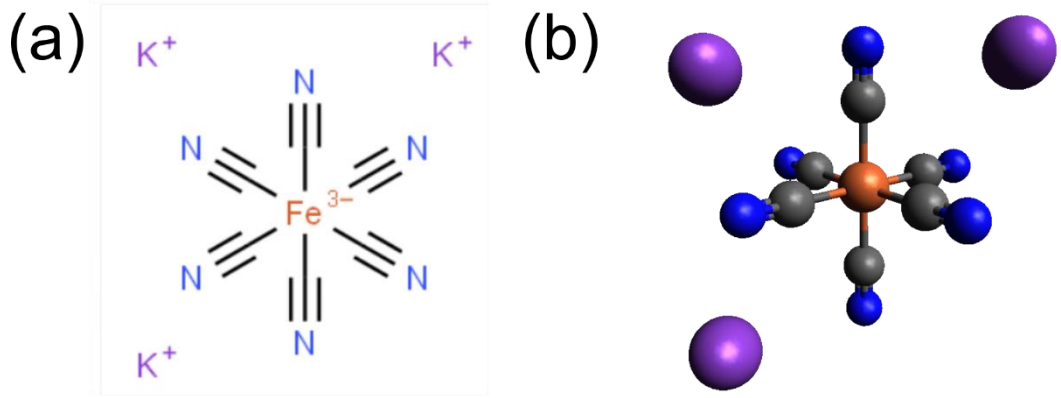

Figure 5.6. Structure of potassium ferricyanide $K_3[Fe(CN)_6]$. (a) Two-dimensional diagram, adapted from ChemSpider. (b) Three-dimensional diagram, adapted from PubChem.

without breaking any Fe-C bonds, hence the reversible redox couple $[Fe(CN)_6]^{3-}/[Fe(CN)_6]^{4-}$ is regarded as a standard redox couple in electrochemistry. Since the redox couple contains CN^-, it can react with mineral acids to release highly toxic HCN gas, although its toxicity is much less than normal cyanides due to strong Fe-C bonds. Therefore, the pH of the 3mM $K_3[Fe(CN)_6]$, 0.1M $NaClO_4$ solution used in this chapter was not adjusted.

5.2.2 CVs in $K_3[Fe(CN)_6]$ solution

The equilibrium potential for the ferrocyanide/ferricyanide redox couple was checked by CV measurements. A gold substrate and a Bi_2Se_3 sample were used as working electrodes, while the 3mM $K_3[Fe(CN)_6]$, 0.1M $NaClO_4$ solution was used as electrolyte. From the figure, the selection of the working electrode does not affect the CVs much. Specifically, Figure 5.7a shows a cathodic peak around -0.3V and a corresponding anodic peak around -0.1V, while Figure 5.7b shows a cathodic peak around -0.25V and a corresponding anodic peak around -0.15V. Since the intercepts of the CVs with the X-axis are around -0.25V and -0.15V, -0.2V was chosen for further impedance measurements.

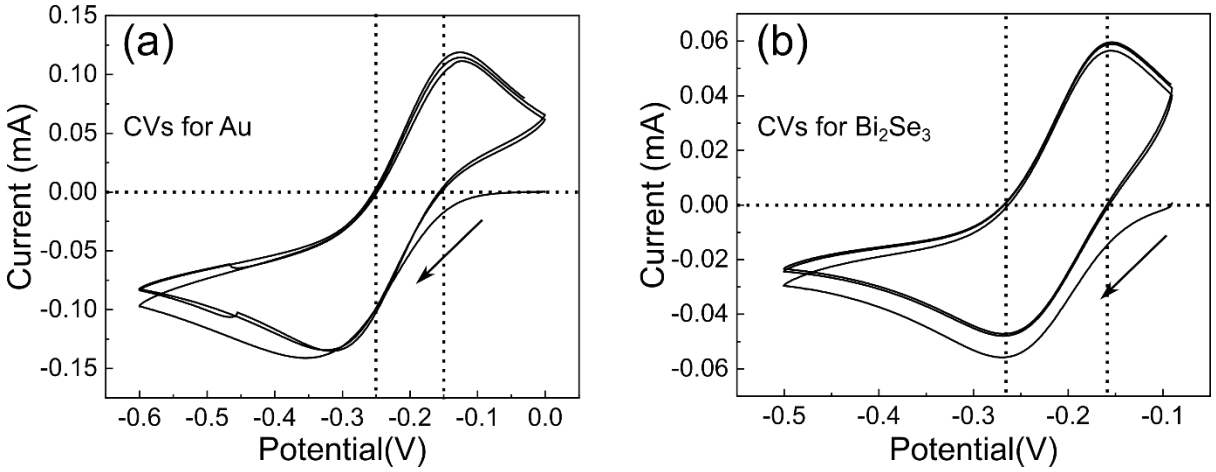

Figure 5.7. Cyclic voltammetry of (a) Au and (b) Bi_2Se_3 in 3mM $K_3[Fe(CN)_6]$, 0.1M $NaClO_4$. The scan rate was 10mV/s. The arrows indicate the sweep direction.

5.2.3 EIS measurements for samples experiencing electrochemical oxidation and reduction in $K_3[Fe(CN)_6]$ solution

Electrochemical impedance measurements were carried out. The frequency range for the AC signal was 200000 to 0.1 Hz, and its RMS amplitude 10 mV. A simple Randles circuit as described in chapter 2 was used to analyse the results, according to which the diameter of the semi-circular feature in the impedance spectrum is equal to the charge transfer resistance R_{ct}. First, a freshly cleaved Bi_2Se_3 sample was measured in 3mM $K_3[Fe(CN)_6]$, 0.1M $NaClO_4$ electrolyte at -0.2V. Next, the sample was oxidised for successive intervals of 1 minute at applied potentials of -0.1V,0.0V,0.1V and 0.2V, respectively. After

each oxidation stage, the sample was measured at -0.2V. The collected impedance spectra and current vs time curves are shown in Figure 5.8.

From the figure, electrochemical oxidation at -0.1V and 0.0V did not affect the impedance much, while electrochemical oxidation at 0.1V changed the transfer resistance considerably. Further electrochemical oxidation at 0.2V was even more effective because the semi-circular part in the corresponding spectrum has a much larger diameter. The results indicate that the critical potential for surface oxidation is

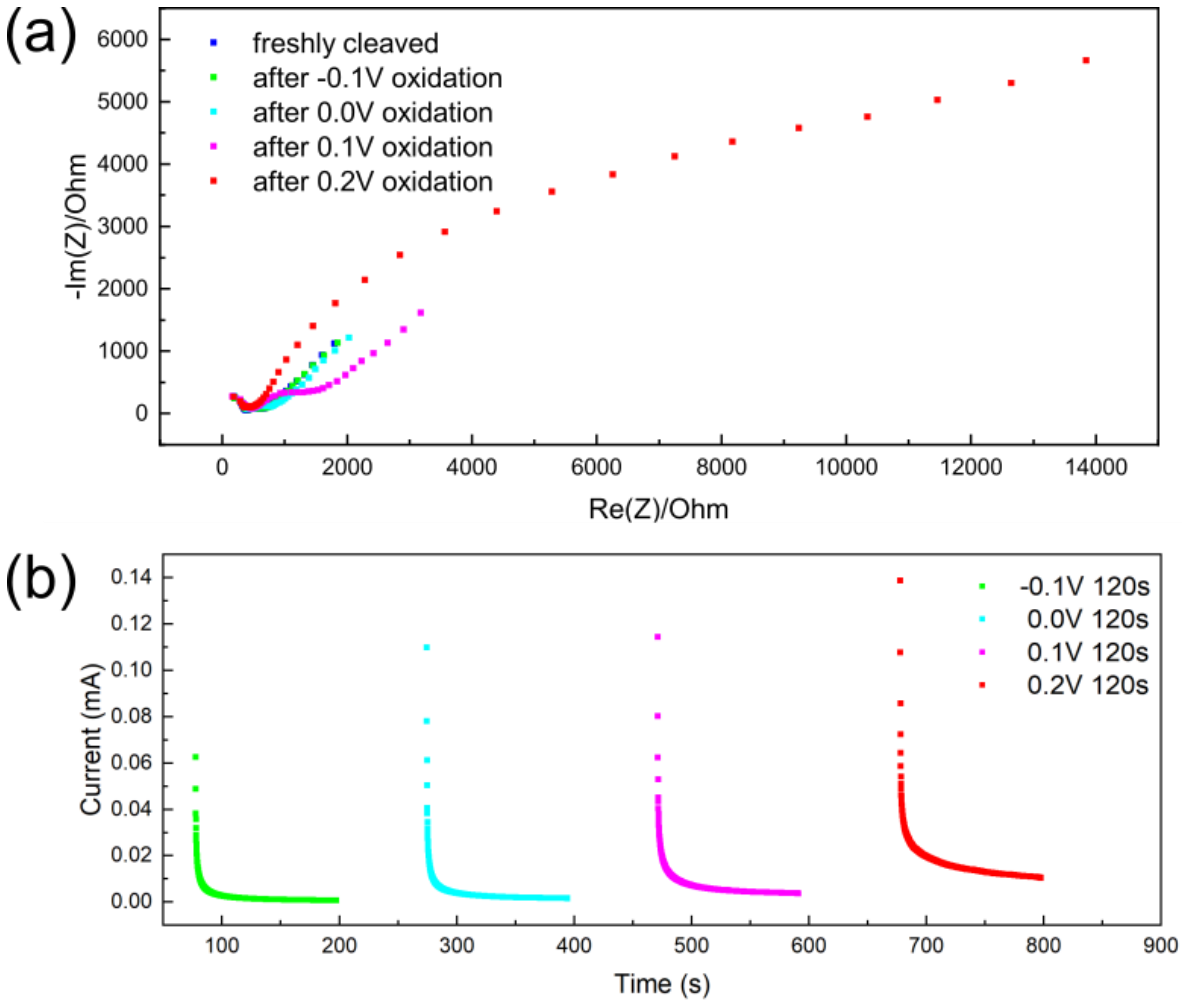

Figure 5.8. (a) Nyquist plots showing electrochemical impedance data for a sample experiencing successive electrochemical (EC) oxidation at different potentials. (b) Corresponding current vs time curves. The potential interval is 0.1V.

around 0.1V, which is similar to the oxidation potentials for the EC-STM experiments. For the current vs time curves, the initial currents increased with increasing potential, showing that the surface reaction rate was sensitive to the applied potential, see Figure 5.8b. In particular, the current decreased rapidly with increasing time, suggesting some sort of passivation. This passivation is consistent with the phenomena observed in Chapter 3 and Chapter 4. Since the impedance spectrum after electrochemical

oxidation at 0.2V showed a very large change in charge transfer resistance, successive impedance spectra were collected continuously at -0.2V for a sample oxidised at 0.2V for 120s to study the evolution of the charge transfer resistance with time after the oxidising potential was removed, see Figure 5.9. The clear difference between the first Nyquist plot and subsequent plots suggests that the surface changes on the timescale of the experiment. Furthermore, subsequent plots indicate that the surface is relatively stable after the initial relaxation process and only changes slightly over a period of several minutes.

The effect of electrochemical reduction was studied by the same method. Nyquist plots after electrochemical oxidation at 0.2V and subsequent electrochemical reduction at -0.6 V are shown in the same figure. Again, the following plots are slightly different from the initial one due to the relaxation process. Notably, the charge transfer resistance after electrochemical reduction at -0.6V is lower than the value before reduction, indicating that the electrochemical reduction at -0.6V did have a significant effect. However, it cannot restore the impedance completely.

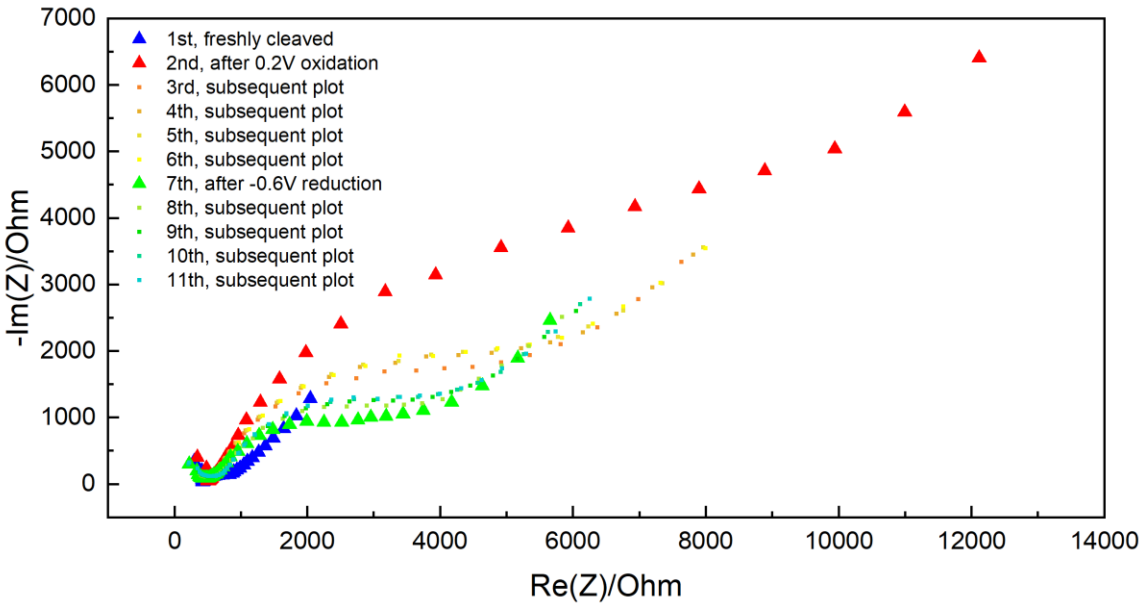

Figure 5.9. Successive Nyquist plots after electrochemical oxidation at 0.2V for 120s and electrochemical reduction at -0.6V for 600s.

An experiment using a more negative reduction potential was carried out to study the relationship between reduction potential and charge transfer resistance, see Figure 5.10. First, the freshly cleaved sample was measured at -0.2V. Afterwards, the sample was kept at -1.1V for 120s and measured at -0.2V again. Next, the sample was subjected to oxidation at +0.2V and reduction at -1.1V, with

impedance measurements taken at -0.2V after each process. Comparing the four plots, it is apparent that the electrochemical reduction at -1.1V lowers the transfer resistance to its original value.

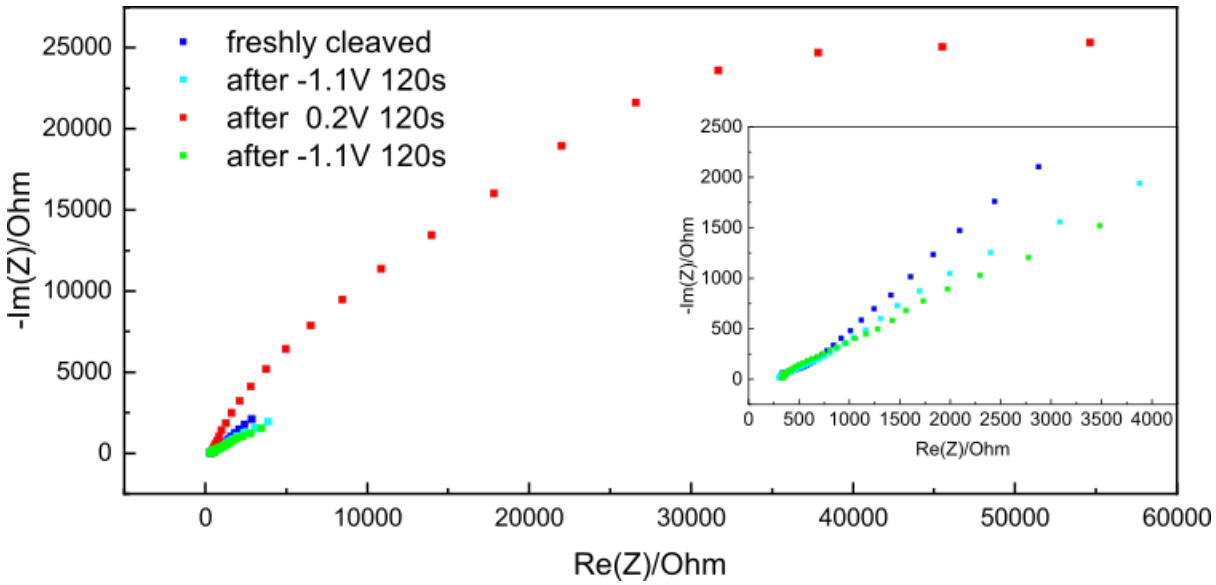

Figure 5.10. Nyquist plots for a freshly cleaved sample, the sample after electrochemical treatment at -1.1V, the sample after electrochemical oxidation at 0.2V and the sample after electrochemical reduction at -1.1V.

According to the Pourbaix diagram (Figure 5.12), -0.6V is enough for electrochemical reduction of Bi oxides in pH3 solution, but not enough for electrochemical reduction of Bi oxides in pH7 solution. The retained Bi oxides may passivate the surface and cannot easily be reduced, which may explain the CVs in Figure 5.1. However, there are other possibilities for the CVs. Firstly, the sites at which crystalline chalcogenides could re-form on reduction may be blocked. Secondly, some oxidation products may diffuse away from the surface.

The CVs and the impedance spectra after electrochemical reduction at -0.6V do suggest that part of oxidation products could be reduced at this potential. Considering the mutually induced codeposition, the potential for Bi_2Se_3 deposition should be positive than the potential for Bi deposition, therefore the reduction products at -0.6V could be Bi_2Se_3. The impedance spectra also suggest that part of Bi oxidation products could remain on the surface in pH7 at -0.6V because the transfer resistance is still higher than the original value. However, the situation is totally different at -1.1V. According to the Pourbaix diagram, -1.1V is enough to reduce Bi^{3+} to Bi^0, therefore the reduction products should be Bi_2Se_3 when Se ions exist (mutually induced codeposition). The recovery of the transfer resistance after

electrochemical reduction at -1.1V indicating that almost of oxidation products are reduced at -1.1V, which is consistent with the Pourbaix diagram and the assumption.

As a comparison with Figure 5.1, cyclic voltammograms for a freshly cleaved Bi_2Se_3 sample were recorded in the potential range from -1.2V to 0.2V, see Figure 5.11. The clear reduction peak at around -1.1V is consistent with the impedance spectra in Figure 5.10 and could be attributed to the complete reduction of the oxidation products.

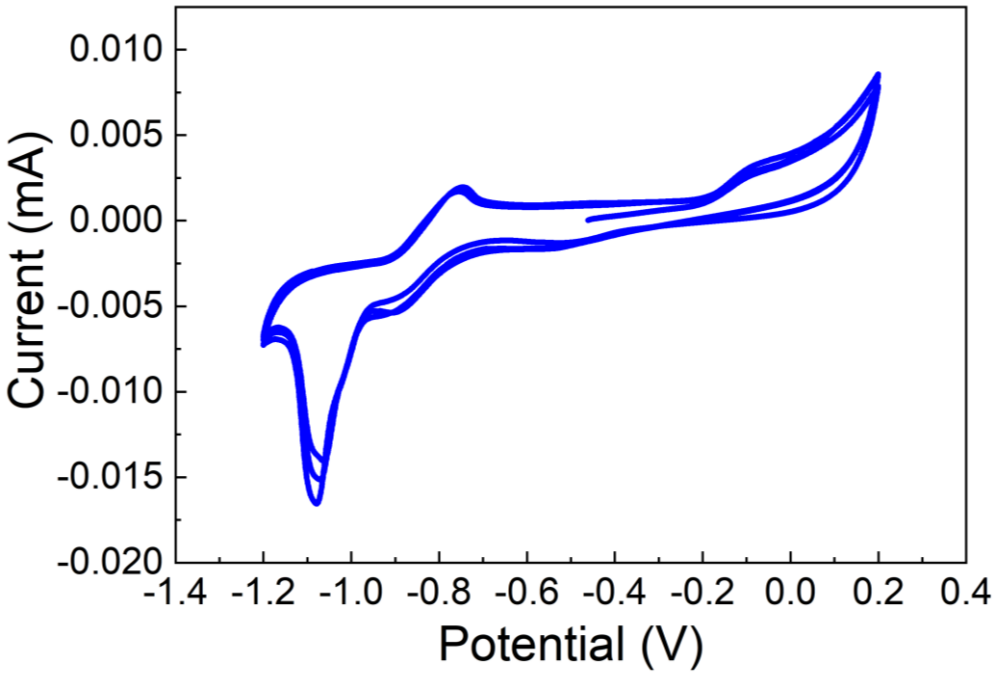

Figure 5.11. Cyclic voltammetry of a freshly cleaved Bi_2Se_3 sample measured in 0.1M $NaClO_4$. The scan rate was 10mV/s. The scan range was from -1.2V to 0.2V.

The increase of the transfer resistance of the oxidised surface could be due to adsorbed oxides. This explanation is supported by EC-STM images and impedance spectra for the surfaces that experienced EC oxidation and subsequent reduction. EC-STM images show pit formation and cluster generation. We expect the clusters to be Bi_2O_3, according to the Pourbaix diagram. The impedance spectra show that electrochemical oxidation at 0.2V increases the transfer resistance significantly. Electrochemical reduction at -0.6V restores the transfer resistance partially, and a more negative potential (-1.1V) is required to recover the initial transfer resistance. The reversibility of the transfer resistance is consistent with the reversibility of X-ray photoelectron spectra shown in Chapter 3.

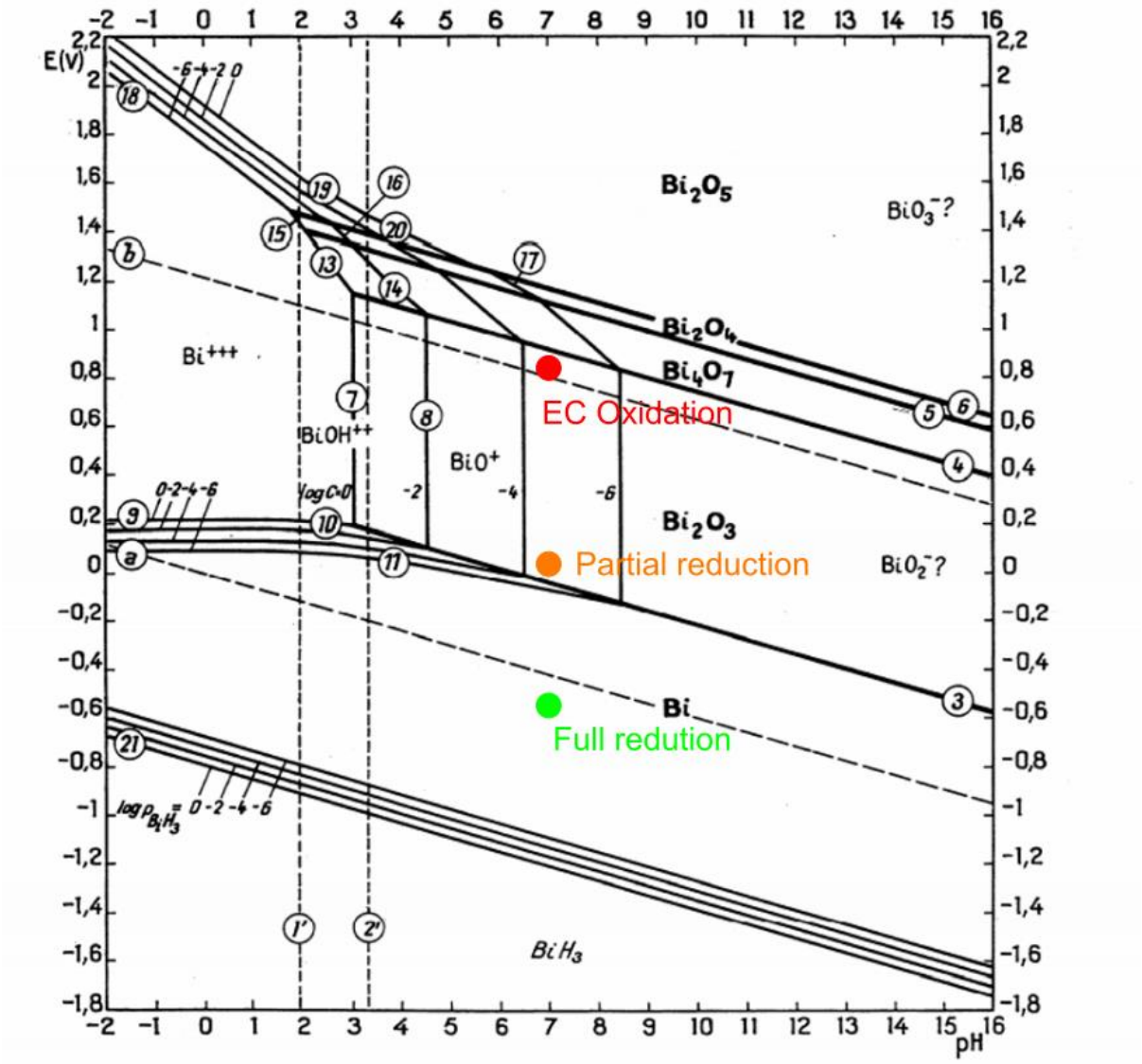

Figure 5.12. Pourbaix diagram of Bi. The electrochemical oxidation conditions are represented by the red dot (pH7, 0.2V vs MSE, which is about 0.85V vs SHE). The partial reduction conditions are represented by the orange dot (pH7, -0.6V vs MSE, which is about 0.05V vs SHE). The full reduction conditions are represented by the green dot (pH7, -1.1V vs MSE, which is about -0.55V vs SHE). Adapted from Ref.[110].

5.3 EC-STM study of Bi_2Se_3 in $K_3[Fe(CN)_6]$ solution

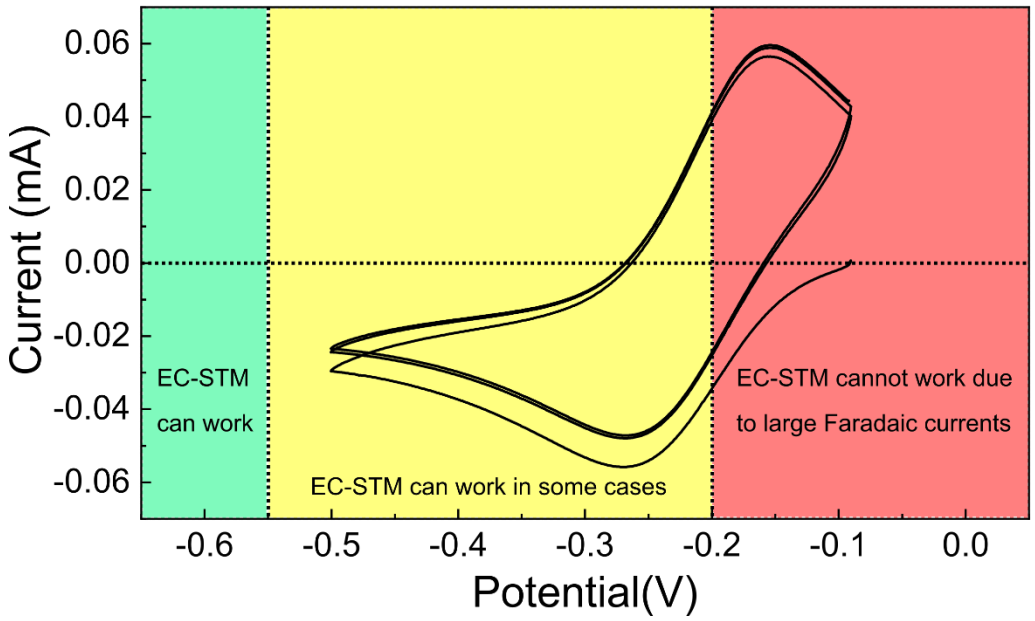

Figure 5.13 Cyclic voltammetry of Bi_2Se_3 in 3mM $K_3[Fe(CN)_6]$, 0.1M $NaClO_4$ (reused from Figure 5.7). Regions marked with different colours indicate the possibility of EC-STM imaging. The scan rate was 50mV/s.

Using the ferricyanide solution for EC-STM experiments may reveal the origin of large charge transfer resistance for the electrochemically oxidized surface. Since the exchange current contributes to EC-STM imaging, for a pre-oxidized surface, one would expect that the images collected when the redox reactions of ferrocyanide/ferricyanide are happening are different from the images collected when the reactions are finished. The spatial distribution of the exchange current could be detected by comparing two groups of images. If the exchange current and the tunnelling current have the same direction, local regions which become darker when the reactions are happening indicate the localized suppression of exchange current, vice versa. Considering the negative correlation between exchange current and charge transfer resistance, these regions may be attributed to the increase of charge transfer resistance. However, the surface cannot be imaged when the redox reactions occur due to the large faradaic current originating from the reactions. Figure 5.13 shows the CVs for Bi_2Se_3 in 3mM $K_3[Fe(CN)_6]$, 0.1M $NaClO_4$ (the same sample as Figure 5.7) and the difficulty level of collecting data in each potential region. In the potential region more positive than -0.2V (marked with red), the tip picks up a Faradaic current which is comparable to or larger than the setpoint current (up to several nA). Therefore, the sample cannot be imaged in this potential region. In the potential region from -0.55V to -0.2V (marked with yellow), the

sample can be imaged if the potential changes from a more negative value. Ferricyanide may be reduced to ferrocyanide at more negative potentials, hence no further redox reaction obstructs imaging. However, if the potential changes from a more positive value, ferricyanide starts to reduce, and the large faradaic current impedes imaging. In the potential region more negative than -0.55V (marked with green), the sample can be imaged after a relaxation time of several minutes, presumably because ferricyanide is exhausted within a relatively short time at more negative potentials.

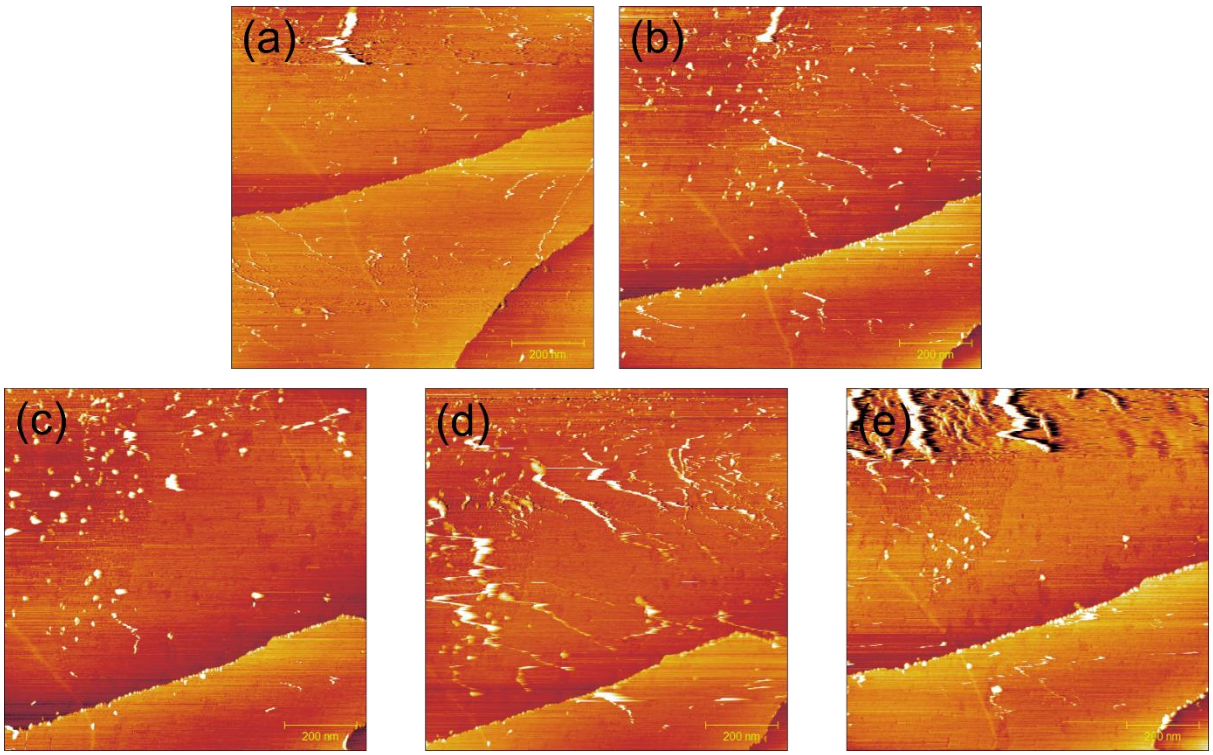

Figure 5.14. (a)-(e) Bi_2Se_3 surface imaged in 3mM $K_3[Fe(CN)_6]$, 0.1M $NaClO_4$ at E=-0.6V,-0.5V,-0.4V,-0.3V and -0.2V successively. The image area is 1μm x 1μm and the tip was held at 0.1 V relative to the sample.

Figure 5.14 shows a series of images collected in ferricyanide solution. Using ferricyanide solution results in poor imaging quality. The white patches in the images have some sort of continuity in the vertical direction, which indicates that these spikes are mobile species or related to the surface structure rather than random electrical noises. Since the tip scans the surface horizontally, random electrical noises should be horizontal spikes. The large faradaic current not only limits sample characterization but also limits tip adjustment because the tip potential is also constrained in a small region.

The attempt to image the sample at 0.0V failed. If the ferrocyanide could transform to ferricyanide at 0.0V rapidly, the faradaic current should decrease soon. However, the faradaic current was still higher than the setpoint current after a 10 minute wait. The reaction rate at 0.0V may not be enough to deplete ferrocyanide in a short time, hence the faradaic current did not reduce significantly. A more positive potential may accelerate this process, but it may also affect the sample condition.

Direct visualization of local catalytic activity has been reported, using EC-STM to measure the local noise in the tunnelling current (n-ECSTM) as an indicator of local reactivity [55, 128, 129]. However, in the experiment discussed above, the faradaic current was too large, therefore impeded imaging.

5.3 Chapter Discussion

EC-STM experiments and EIS measurements were carried out in pH7 solution (0.1M $NaClO_4$) to study the link between surface morphology of single-crystal Bi_2Se_3 and its electrochemical response.

Parts of the results are expected. (1) Smooth Bi_2Se_3 surface can be imaged at the rest potential, which indicates that the change of solution pH didn't influence the feasibility of electrochemical protection. (2) Oxidative dissolution was observed after a series of oxidation stages, although it required a more positive potential due to the change of solution pH. EC-STM images (Figure 5.3) demonstrate that pit formation originated from point defects and crack (line defects). (3) EIS measurements showing that electrochemical modification changed the charge transfer resistance considerably. Specifically, the charge transfer resistance significantly increased after electrochemical oxidation, then decreased after subsequent electrochemical reduction. Change of the charge transfer resistance may be due to precipitation and subsequent dissolution of oxides (mainly Bi oxides).

However, some phenomena are unexpected. (1) Small clusters of ~1nm height were observed in pits or along the pit edges at the rest potential after a series of oxidation stages. Consider the Pourbaix diagrams, these clusters are supposed to be Bi oxides. (2) Electrochemical reduction at -0.6V vs MSE cannot restore the charge transfer resistance completely, which is also attributed to the change of solution pH. (3) The sample can only be imaged in ferricyanide solution within a very narrow potential window due to the large faradaic current.

Compared to chapter 3, EC-STM images and EIS data collected after electrochemical oxidation still demonstrate the feasibility and efficiency of electrochemical control. However, the reversibility of electrochemical modification is confirmed by electrochemical reduction at -1.1V vs MSE rather than at

-0.6V vs MSE as chapter 3 did. The change of solution pH shifts the dissolution potential of Bi oxides (Figure 5.12), therefore a more negative potential is required to restore the charge transfer resistance (Figure 5.10). Compared to chapter 4, oxidative dissolution and precipitation of clusters were happened at more positive potentials because of higher solution pH, as discussed before.

5.4 Chapter Summary

EC-STM and electrochemical impedance techniques were used to study the electrochemical modification of single-crystal Bi_2Se_3 in 3mM $K_3[Fe(CN)_6]$, 0.1M $NaClO_4$ and 0.5M HNO_3. Compared to experiments discussed in chapter 4, this work shows that a different choice of chalcogenide (Se in place of Te) and electrolyte yields clear differences in the oxidative dissolution and subsequent reductive redeposition processes. Electrochemical oxidation leads to pit formation at locations linked to pre-existing surface features, while subsequent electrochemical reduction results in clusters generated from oxidation products. The morphology of the clusters mainly depends on the oxidation potential.

Changes in charge transfer resistance were observed through electrochemical impedance measurements and linked to surface morphology changes. In addition, an EC-STM study of Bi_2Se_3 in ferricyanide solution was discussed. The large faradaic current originating from the redox reactions of the ferrocyanide/ferricyanide redox couple obstructs image collection.

This chapter demonstrates the feasibility of establishing a link between the surface morphology and the charge transfer resistance. Clear changes in the oxidation and redeposition processes are attributed to differences in the outermost layers and the electrolyte. Metal electrodeposition using the same sample and electrolyte will be discussed in chapter 6.

CHAPTER 6

ELECTRODEPOSITION ON BISMUTH SELENIDE SINGLE CRYSTALS

The preceding chapters demonstrate that bismuth chalcogenides are promising platforms for electrochemical study. CVs and EC-STM images indicate a potential range that can protect the surface from both oxidation and reduction. This range is a reference and a starting point for EC-STM experiments. Oxidative dissolution and pit formation are observed at potentials more positive than this range. Subsequently, reductive deposition happens at potentials more negative than this range.

In this chapter, instead of changing the surface morphologies by electrochemical oxidation and reduction, extra metal ions are introduced to obtain Bi_2Se_3/metal heterostructures by electrodeposition for the following reasons. Firstly, a Bi (111) bilayer on $Bi_2Te_xSe_{3-x}$ has already been obtained using molecular beam epitaxy [130, 131]. As a two-dimensional topological insulator, the edges of a Bi bilayer possess topologically protected metallic edge states. These edge states could have effects on electrocatalysis, as discussed in Chapter 1. If the electrochemical method can generate a Bi bilayer with a high density of edges, it could provide a promising platform for surface catalysis. Secondly, it is a possible termination of a $Bi_2Te_xSe_{3-x}$ surface exposed in air, therefore the study of bismuth chalcogenides/bismuth bilayer heterostructures may reveal the reaction mechanism between bismuth chalcogenides and air. Thirdly, Bi_2Se_3/Pb (TI/superconductor) heterostructure has the potential to be an artificial topological superconductor [132, 133]. It may pave the way for experimentally realising Majorana fermions.

The main goal of this chapter is to deposit Bi and Pb on a smooth Bi_2Se_3 surface to gain knowledge of metal electrodeposition on bismuth chalcogenides. Furthermore, the possibility that the edges of the

pits could be active sites for adsorption due to dangling bonds and the evidence that the newly exposed surface exhibits significantly higher stability than the original surface suggest that the surface chemistry of the oxidised surface is of interest. Therefore, the second goal is to study metal electrodeposition on the oxidised surface to evaluate surface chemistry change.

Electrodeposition of Bi and Pb on e.g. Au substrates are well-studied. Bi electrodeposition on Au(111) and Au(100) electrodes were studied by video-rate EC-STM [134]. The structures of deposited Bi strongly depend on the facet of Au substrate. Needle-like Bi(110) deposits was obtained on Au(111) electrode, whereas Bi(111) epitaxial film formed on Au(100) substrate. The introduction of magnetic field into Bi electrodeposition was studied by X-ray diffraction and scanning electron microscope [135]. A 0.5T field significantly suppressed the dendritic growth of Bi at high current density, but no clear evidence of crystal microstructure change. Underpotential deposition of Bi monolayer on Au(111) electrode was studied by X-ray scattering and electrochemical methods [136]. The transient current and X-ray intensity revealed the transition of zero-coverage to commensurate (2x2)-Bi phase on the millisecond time scale and suggested a classic Langmuir type adsorption where the adsorption is uniform across the entire surface. Electrodeposition of Pb on Au(111) was studied by EC-STM [137]. Three different processes including terrace expansion, island growth and monolayer formation were characterized at different potentials in the underpotential range. Three-dimensional growth in the overpotential range was also imaged. Pb underpotential deposition on Au(100) was studied by EC-STM [138]. At low coverage, Pb deposition led to a step decoration, which is consistent with Ref.[137]. At higher coverage, a two-dimensional hexagonal close packed Pb overlayer was obtained. The parameters and results discussed above could be a starting point for further study. However, the deposition potential and the deposited structure may be varied due to the difference of the substrate.

6.1 Three growth modes in heteroepitaxial growth

There are three basic modes for heteroepitaxial growth[122].

(a) If the interaction of the deposited atoms with each other is stronger than with the substrate (the sum of the interface tension and the surface tension of the deposit is larger than the surface tension of the substrate), three-dimensional island growth occurs at overpotential. This growth mode is known as Volmer-Weber growth.

If the interaction of the deposited atoms with the substrate is stronger than with each other (the sum of the interface tension and the surface tension of the deposit is smaller than the surface tension of the substrate), a monolayer can be deposited at underpotential. There are two subcases (b) and (c):

(b) If the mismatch of the lattice structures of substrate and deposited metal is large, after one or more layers, three-dimensional islands are formed. This growth mode is known as Stranski-Krastanov growth.

(c) If the mismatch of the lattice structures of substrate and deposited metal is small, epitaxial growth of subsequent layers would weaken the influence of the substrate. Consequently, the deposition proceeds in the same way as bulk deposition after several layers have been deposited. This growth mode is known as Frank-van-der-Merwe growth or layer-by-layer growth.

Consider a two-dimensional nucleation for layer-by-layer growth [139], the first one or several layers grow with a lattice constant matched to the substrate (pseudomorphic), therefore a strain is caused by lattice mismatch. The extent of the mismatch is given by:

(6.1) $$\varepsilon = \frac{a_f - a_s}{a_s}$$

where a_f is the natural lattice constant of the deposited film, a_s is the lattice constant of the substrate. Consider two-dimensional nucleation with round nuclei of radius r, the elastic energy is given by:

(6.2) $$E_e = \pi r^2 C \varepsilon^2$$

where C is a constant characterizes the elastic properties of the monolayer.

The energy associated with the surface tension is:

(6.3) $$E_t = \pi r^2 (\gamma_{dep} + \gamma_i - \gamma_s)$$

where γ_{dep}, γ_i and γ_s are surface tension of the deposit, the interface and the substrate, respectively.

The boundary energy is given by:

(6.4) $$E_b = 2\pi r \beta$$

where β is the step line tension.

For a negative overpotential η, the Gibbs free energy of a nucleus contains N atoms is:

(6.5) $$\Delta G = E_e + E_t + E_b + Nze\eta = \pi r^2 C\varepsilon^2 + \pi r^2(\gamma_{dep} + \gamma_i - \gamma_s) + 2\pi r\beta + Nze\eta$$

Introduce the area of per atom Ω:

(6.6) $$\Delta G = N\Omega(C\varepsilon^2 + \gamma_{dep} + \gamma_i - \gamma_s) + 2\beta(\pi N\Omega)^{\frac{1}{2}} + Nze\eta$$

The maximum value of ΔG is given by:

(6.7)
$$\frac{d(\Delta G)}{dN} = 0$$
$$N_c = \frac{\beta^2(\pi\Omega)}{[\Omega(C\varepsilon^2 + \gamma_{dep} + \gamma_i - \gamma_s) + ze\eta]^2}$$
$$\Delta G_{\max} = -\frac{\beta^2(\pi\Omega)}{\Omega(C\varepsilon^2 + \gamma_{dep} + \gamma_i - \gamma_s) + ze\eta}$$

If $C\varepsilon^2 + \gamma_{dep} + \gamma_i - \gamma_s$ is positive. To have nucleation, the minimum value of $|\eta|$ is given by:

(6.8) $$|\eta| > \frac{\Omega(C\varepsilon^2 + \gamma_{dep} + \gamma_i - \gamma_s)}{ze}$$

The three-dimensional nucleation for Volmer-Weber and Stranski-Krastanov growth is much more complicated because the surface tension of the nucleus strongly depends on its shape. Furthermore, the elastic energy of a three-dimensional nucleus is more complicated than two-dimensional situation.

6.2 Preliminary study of silver deposition

Bi_2Se_3 single crystals used in this chapter were prepared by collaborators from Nanjing University. For all the experiments discussed in this chapter, a Hg/Hg_2SO_4 electrode (MSE) was used as a reference electrode, while a Pt ring was used as a counter electrode. EC-STM experiments were carried out to study the electrochemical behaviour of Bi_2Se_3 in a very acidic electrolyte (0.5M HNO_3) because 0.5-1.0 M HNO_3 is typically used for Bi_2Se_3 electrodeposition. -0.2V was chosen as the imaging potential because it is close to the open circuit potential.

The possible silver deposition was recorded by accident, see Figures 6.1-6.2. The nail polish insulating layer was partially removed when cleaving, therefore some silver epoxy was exposed to the electrolyte

in the subsequent experiments. A terrace with islands of height 0.2 nm is shown in Figure 6.1a. Considering the coexistence of both Bi and Se terminations of Bi_2Se_3 cleaved in air, these islands may be attributed to imperfect cleaving. EC-STM images record the evolution of the islands, see Figures 6.1b-6.1e. The scan area was not adjusted during the experiment, but the drift is likely to have changed the imaging area slightly, as the tip was withdrawn by ~ 10 μm for each oxidation period. Similar to the images shown in Chapter 5, oxidative dissolution again generates pits of depth equal to the quintuple layer thickness. These pits appear to nucleate at the edges of the low islands, which is consistent with the expectation that the dissolution starts from surface defects. Figures 6.1b-6.1e also show clusters decorating the edges of the pits that form on the Bi_2Se_3 surface. Pits and clusters are even more obvious when a cleaved Bi_2Se_3 sample is electrochemically oxidized at more positive potentials, see Figure 6.2. Well-defined pits form even after oxidation for only 1s at 0.2V. These clusters are totally different from the redeposited Bi_2Se_3 clusters in Figure 4.7 for the following reasons. Firstly, the deposition potential (-0.2V vs MSE) is more positive than the potential for Bi_2Se_3 deposition (about -0.4V vs MSE). Secondly, the size of these clusters is much larger than the size of redeposited Bi_2Se_3 clusters (compared to Figure 4.7). Thirdly, the coverage (total volume) of these clusters is much larger

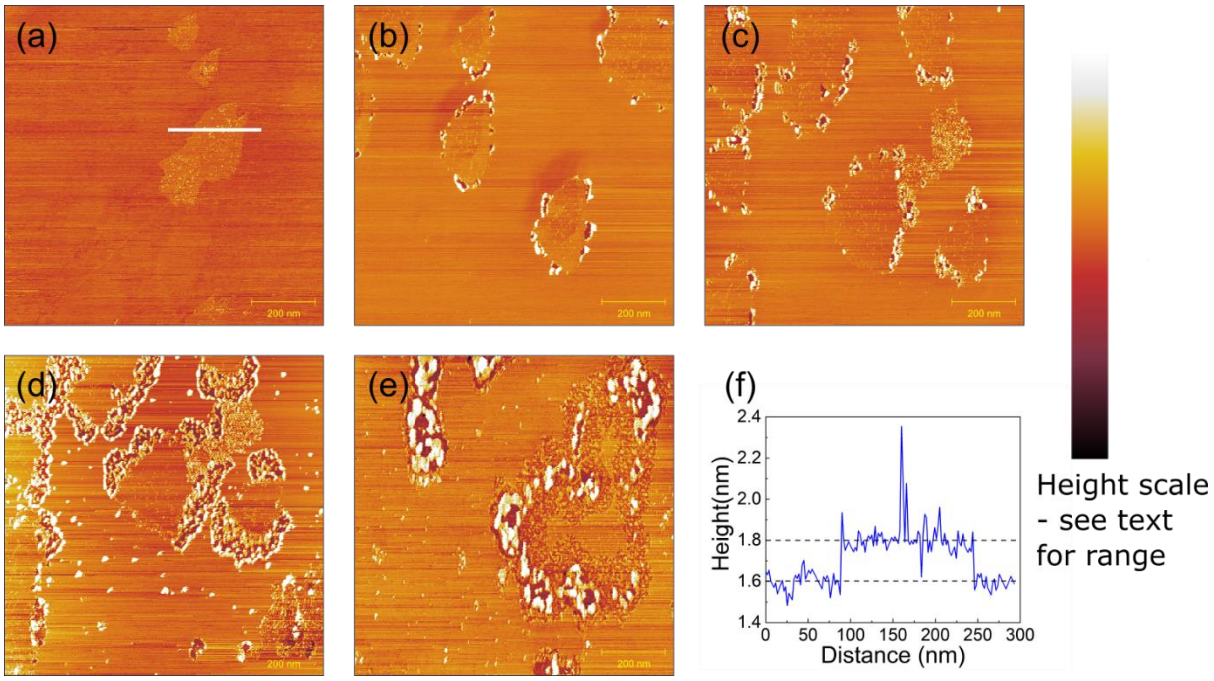

Figure 6.1. Bi_2Se_3 surface (with silver epoxy exposed) imaged by EC-STM at E= -0.2V (tip potential: 0.1V) before (a) and after oxidative dissolution at E = 0.06V for (b) 60s, (c) 120s, (d) 240s, (e) 360s. The image area is 1μm x 1μm and experiments were carried out in a 0.5M HNO_3 electrolyte. (f) Surface profile along the line in (a). The range of the height colour scale is 3.2nm for (a), 6nm for (b)-(e).

than the coverage (total volume) of pits, see Figures 6.2e-6.2f. Therefore, the origin of these clusters may relate to the exposed silver epoxy rather than Bi_2Se_3.

CVs for the EC-STM measured sample, a well-insulated new sample and silver epoxy (fixed on a gold substrate) support the assumption of silver deposition, see Figure 6.3. The reduction peak around -0.2V vs MSE is attributed to silver epoxy, because the peak is absent in the CV for the well-insulated sample and clear in the CV for silver epoxy. Furthermore, CVs shown in Figure 6.4 indicate that the redox reactions for silver epoxy are sensitive to the pH and the oxidation potential.

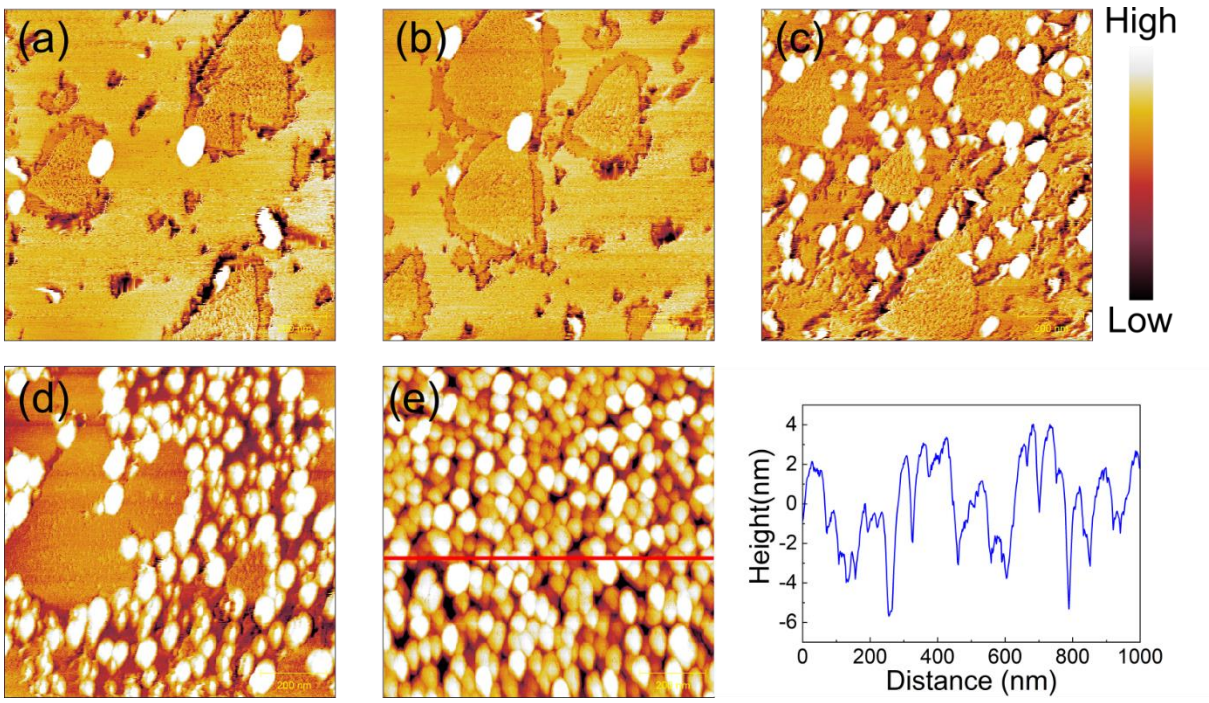

Figure 6.2. Bi_2Se_3 surface (with silver epoxy exposed) imaged by EC-STM at E = -0.2V (tip potential: 0.1V), after oxidative dissolution at E = 0.2V for (a) 1s, (b) 2s, (c) 22s, (d) 60s, (e) 120s. (f) Surface profile along the line in (e). The image area is 1μm x 1μm and experiments were carried out in a 0.5M HNO_3 electrolyte. The range of the height colour scale is 8.5nm.

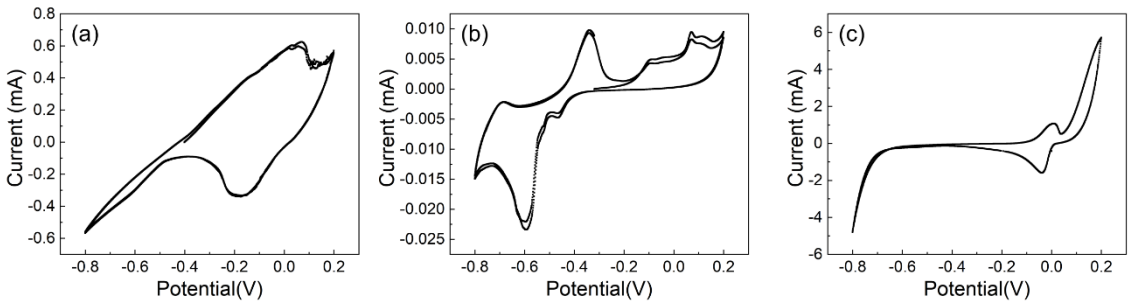

Figure 6.3. Cyclic voltammograms for (a) the EC-STM measured sample, (b) a well-insulated sample and (c) silver epoxy. The scan rate was 50mV/s.

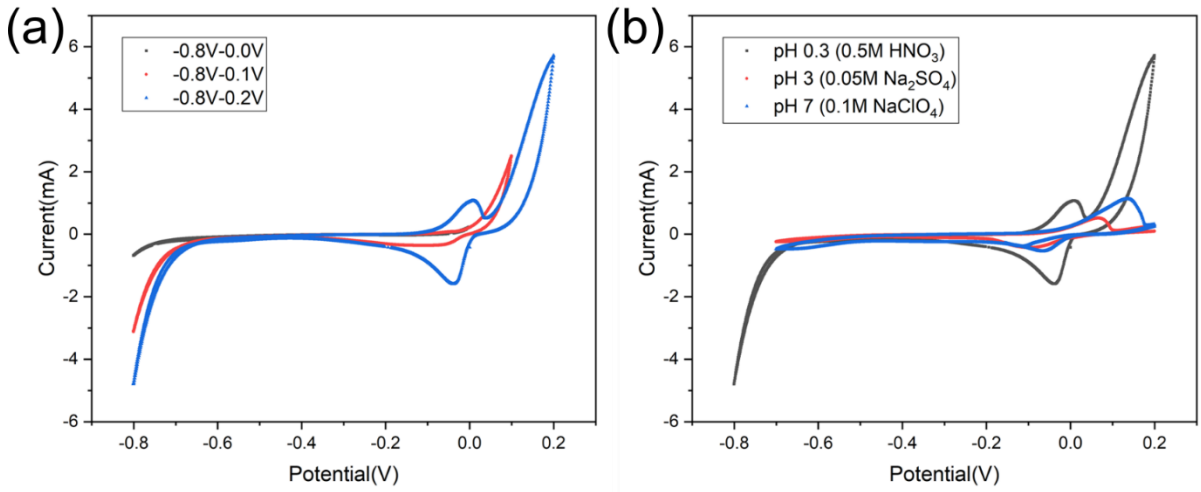

Figure 6.4. Cyclic voltammograms for silver epoxy (a) in pH0.3 electrolyte with different oxidation potentials, (b) in pH0.3, pH3, pH7 electrolytes, respectively. The scan rate was 50mV/s.

6.3 Bismuth electrodeposition

Firstly, 1mM $Bi(NO_3)_3$ / 0.5M HNO_3 and 5mM $Bi(NO_3)_3$ / 0.5M HNO_3 electrolytes were used. For the experiment using a 1mM $Bi(NO_3)_3$ / 0.5M HNO_3 electrolyte, starting at around E= -0.5V vs MSE, cathodic electrodeposition is observed, giving rise to characteristic triangular structures as shown in Figure 6.5. The triangle edges form parallel steps with a very low density of kinks, and the minimum measured step height is approximately 0.4nm. The step height and the morphology are consistent with the film orientation being Bi(111) [140, 141]. For another Bi deposition experiment using a 5mM $Bi(NO_3)_3$ / 0.5M HNO_3 electrolyte, the sample potential was kept at -0.58V for 10s. After that, the surface was imaged at E=-0.5V, where slow deposition of Bi continues, as shown by the sequence of images in Figure 6.6 and Figure 6.7. These images show clearly how a single Bi bilayer grows across a smooth terrace (note the slow growth of a Bi bilayer indicated by arrows in Figure 6.6).

Bi electrodeposition on Bi_2Se_3 is fully reversible, as shown in Figure 6.8. Firstly, the sample was imaged at -0.6V (Figure 6.8a). Then, the sample was imaged at E=-0.45V after complete Bi dissolution at this potential (Figure 6.8b). Next, the sample was imaged when changing the potential from E= -0.45V to -0.6V (Figure 6.8c). The arrow indicates where the applied potential was changed. Finally, the sample was imaged after returning to E= -0.45V (Figure 6.8d). The appearance and the disappearance of the triangular structure strongly depended on the applied potential, which indicates the reversibility of Bi deposition.

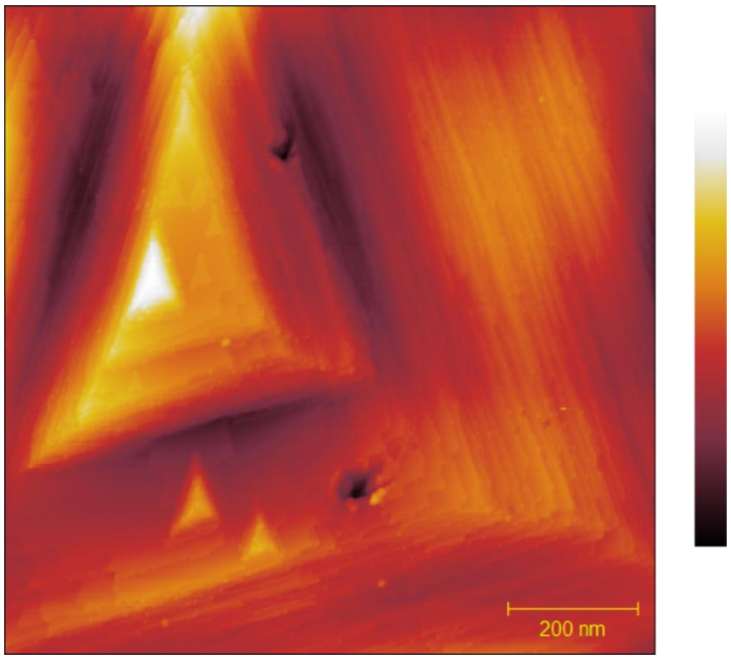

Figure 6.5. Characteristic triangular structures resulting from Bi electrodeposition on single-crystal Bi_2Se_3 at E= -0.6V for 600s from a 1mM $Bi(NO_3)_3$ / 0.5M HNO_3 electrolyte imaged by EC-STM at E= -0.5V. The image area is 1µm x 1µm and the tip was held at 0.1 V relative to the sample. The range of the height colour scale is 16.0nm.

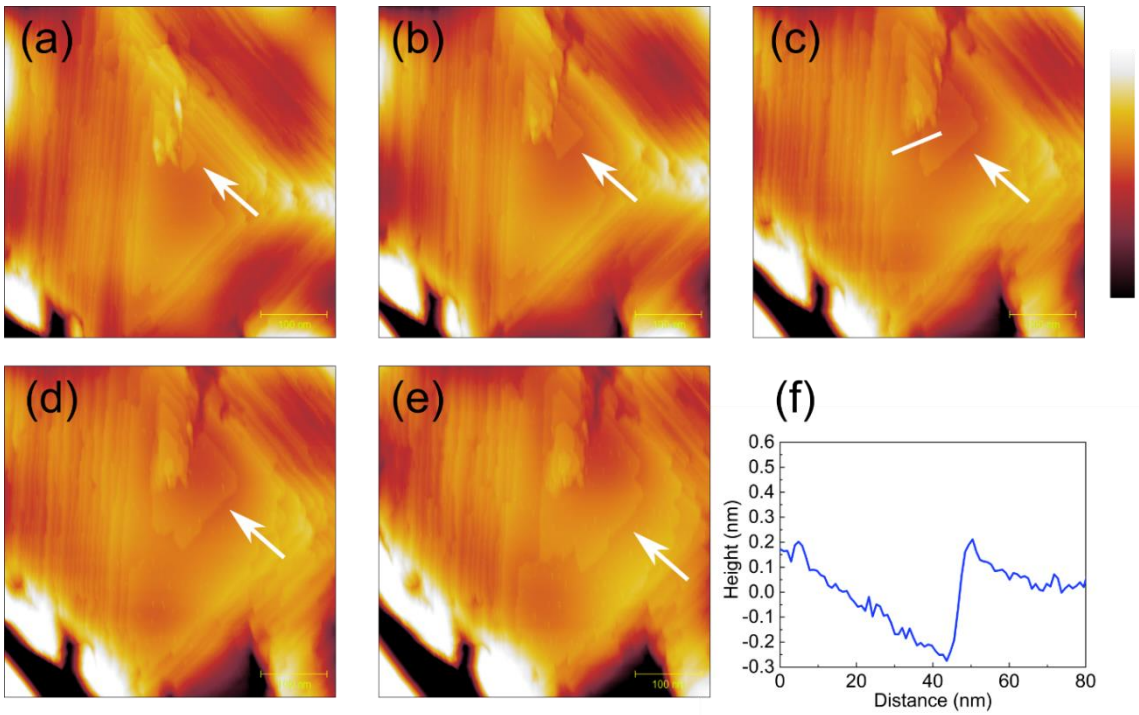

Figure 6.6. (a)-(e) A succession of 500nm x 500nm EC-STM images acquired at E= -0.5V in a 5mM $Bi(NO_3)_3$ / 0.5M HNO_3 electrolyte following initial deposition at E= -0.58V for 10s. Note the slow growth of a Bi bilayer (indicated by arrows). (f) Surface profile along the white line in (c). The tip was held at 0.1 V relative to the sample. The range of the height colour scale is 12.0nm.

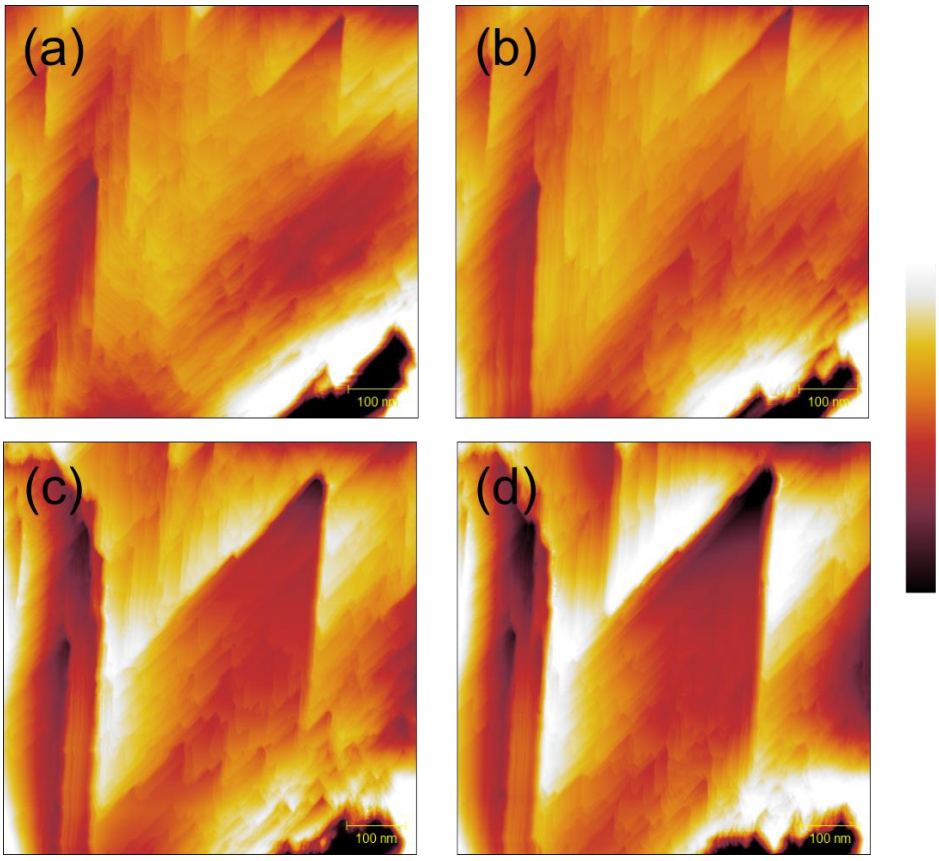

Figure 6.7. (a)-(e) A succession of 500nm x 500nm EC-STM images for Bi electrodeposition on Bi_2Se_3 (the deposition and imaging parameters are the same as Figure 6.6).

In the experiments, a sufficiently negative potential was applied so that a number of nuclei were formed on the surface. After a short period, the overpotential was reduced to a lower value so that existing nuclei could grow, but new ones were hard to form. Therefore, the overall process could be seem as instantaneous nucleation. Since the lattice mismatch of bismuth chalcogenides and metal bismuth is small, the observation of pseudomorphic growth is reasonable. For comparison, bismuth was deposited from another widely-used electrolyte 0.1M $HClO_4$/1mM Bi_2O_3 [134], see Figure 6.9. Again, triangular features were observed, although the tip condition was not perfect during the experiment. As expected, no clear difference between nitrate and perchlorate.

CVs measurements were carried out (Figure 6.10). A crossing (so-called nucleation loop) was only observed in the first cycle, which may be attributed to the nucleation process requiring activation energy provided by overpotential. The pronounced reduction peaks start at -0.5V vs MSE, which is consistent with the bismuth deposition potential. Notably, the shoulder on the reduction peak in the first and second cycles may be attributed to the reduction of pre-existed Bi_2Se_3 oxidation products.

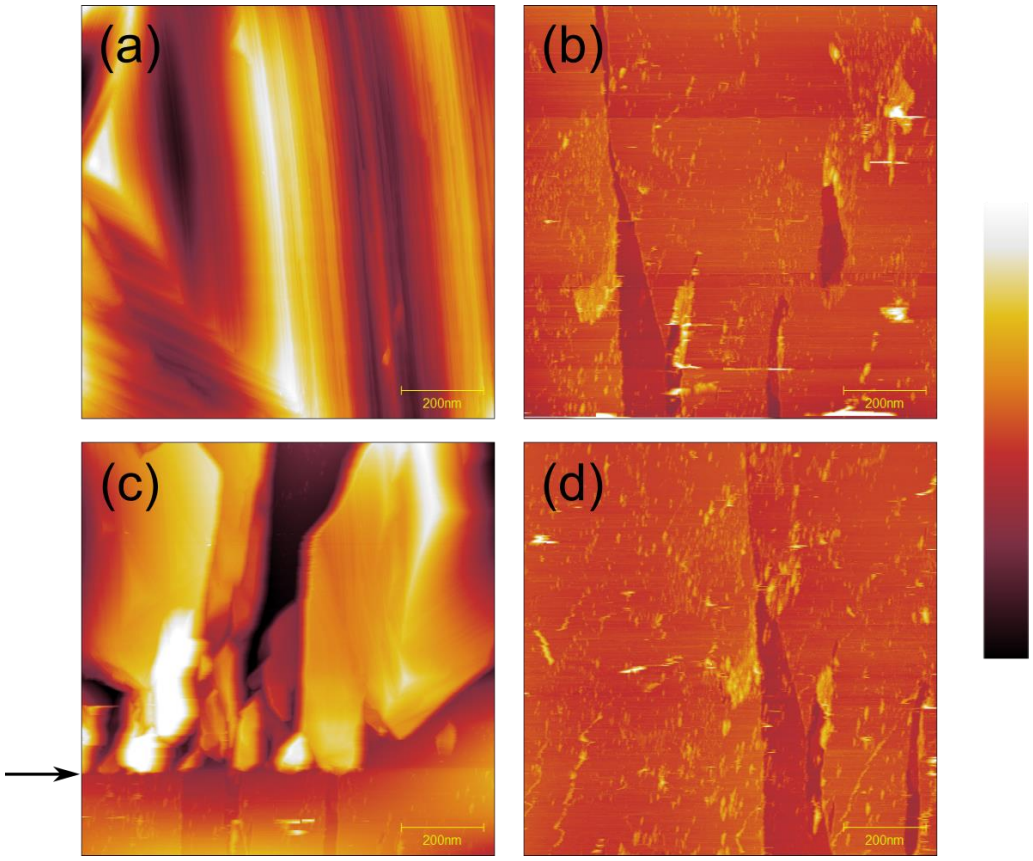

Figure 6.8. EC-STM images showing the reversibility of Bi electrodeposition on single-crystal Bi_2Se_3 from a 5mM $Bi(NO_3)_3$ / 0.5M HNO_3 electrolyte. (a) Electrodeposited Bi imaged at E= -0.6V; (b) sample surface imaged at E= -0.45V after complete Bi dissolution at this potential; (c) sample surface imaged (scanning from the bottom to the top) when changing the potential from E= -0.45V to -0.6V. The arrow indicates where the applied potential was changed; (d) sample surface imaged after returning to E= -0.45V. The image area is 1µm x 1µm, the tip was held at 0.1 V relative to the sample. The range of the height colour scale is 18 nm for (a),(b),(d) and 50nm for (c).

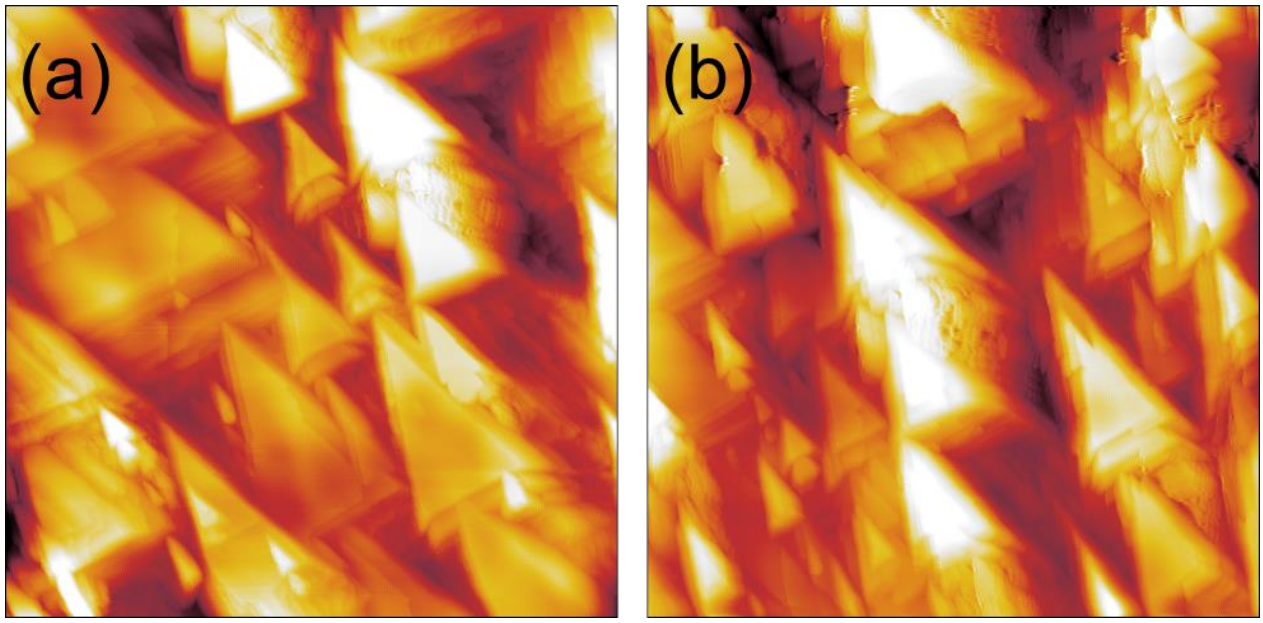

Figure 6.9. 1μm x 1μm EC-STM images acquired at E= -0.5V in a 0.1M $HClO_4$/1mM Bi_2O_3 electrolyte following initial deposition at E= -0.6V for 10s. The range of the height colour scale is 13.0nm.

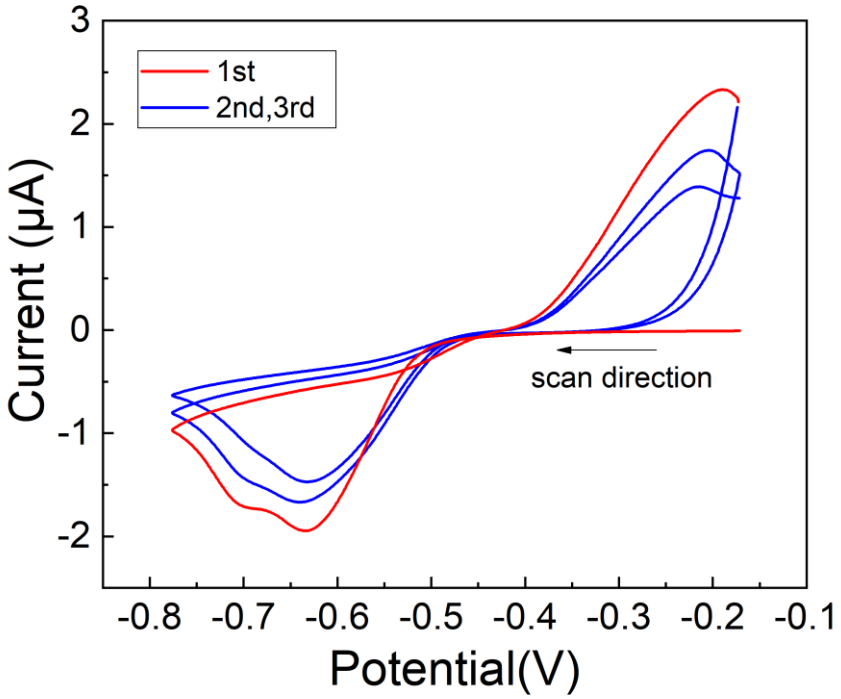

Figure 6.10. Cyclic voltammograms for Bi_2Se_3 in a 0.1M $HClO_4$/1mM Bi_2O_3 electrolyte. The scan rate was 50mV/s.

6.4 Lead electrodeposition

The stock solution was 10mM lead sulphamate ($Pb(NH_2SO_3)_2$) prepared by reacting lead carbonate ($PbCO_3$) with approximately 1M sulphamic acid (H_3NSO_3) solution (10g H_3NSO_3 in 100mL Milli-Q water). Then the stock solution was diluted to 1mM lead sulphamate with Milli-Q water.

Cyclic voltammetry measurements were carried out to determine potentials for lead deposition. A clear cathodic peak is observed at around -1.1V vs MSE, which is much more negative than the potential for Bi deposition (Figure 6.11). The loop in the CV is not a nucleation loop. The larger current for the reverse scan may instead indicate that the electrochemically active area increases due to lead deposition. Furthermore, the constant gradient in the CV shows that the ohmic potential drop is significant.

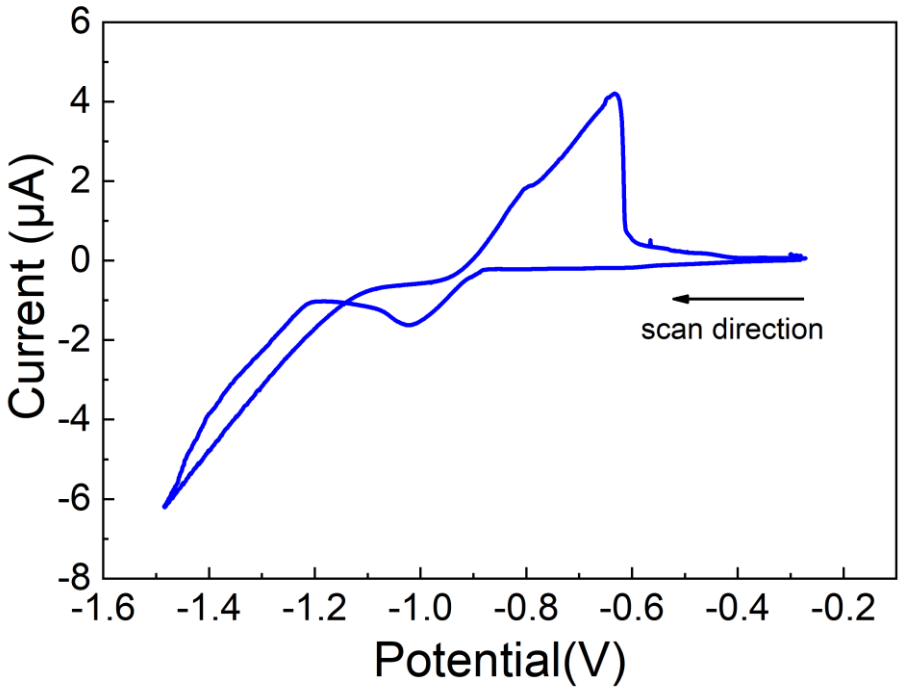

Figure 6.11. Cyclic voltammograms for Bi_2Se_3 in a 1mM lead sulphamate electrolyte. The scan rate was 10mV/s.

EC-STM was used to study the surface morphology during or after lead deposition. The bias between tip and sample was fixed at 0.2V or 0.3V to avoid lead deposition on the STM tip. By stepping the sample potential to -1.2V for several seconds then imaging the sample at -0.9V to protect the deposited features and to avoid further deposition, the initial stages of lead deposition could be characterized, see

Figure 6.12. The nucleation of lead occurred first at step edges and cracks (linear defects), which may be attributed to dangling bonds at these sites. Although the images were collected from the bottom, there was no difference in nucleation density between the lower area (scanned earlier) and the upper area (scanned later), which means the nucleation stopped at -0.9V.

-1.0V was applied to the sample to study further deposition. EC-STM images that were collected during electrodeposition show the evolution of the surface, see Figure 6.13. Again, the scan direction was from bottom to top. Since the clusters kept growing during imaging, the clusters on the upper area are larger than the clusters on the lower area. Figure 6.13a shows initial preferential deposition at step edges, but the influence of the step edges appears reduced in subsequent images due to the relatively high growth rate.

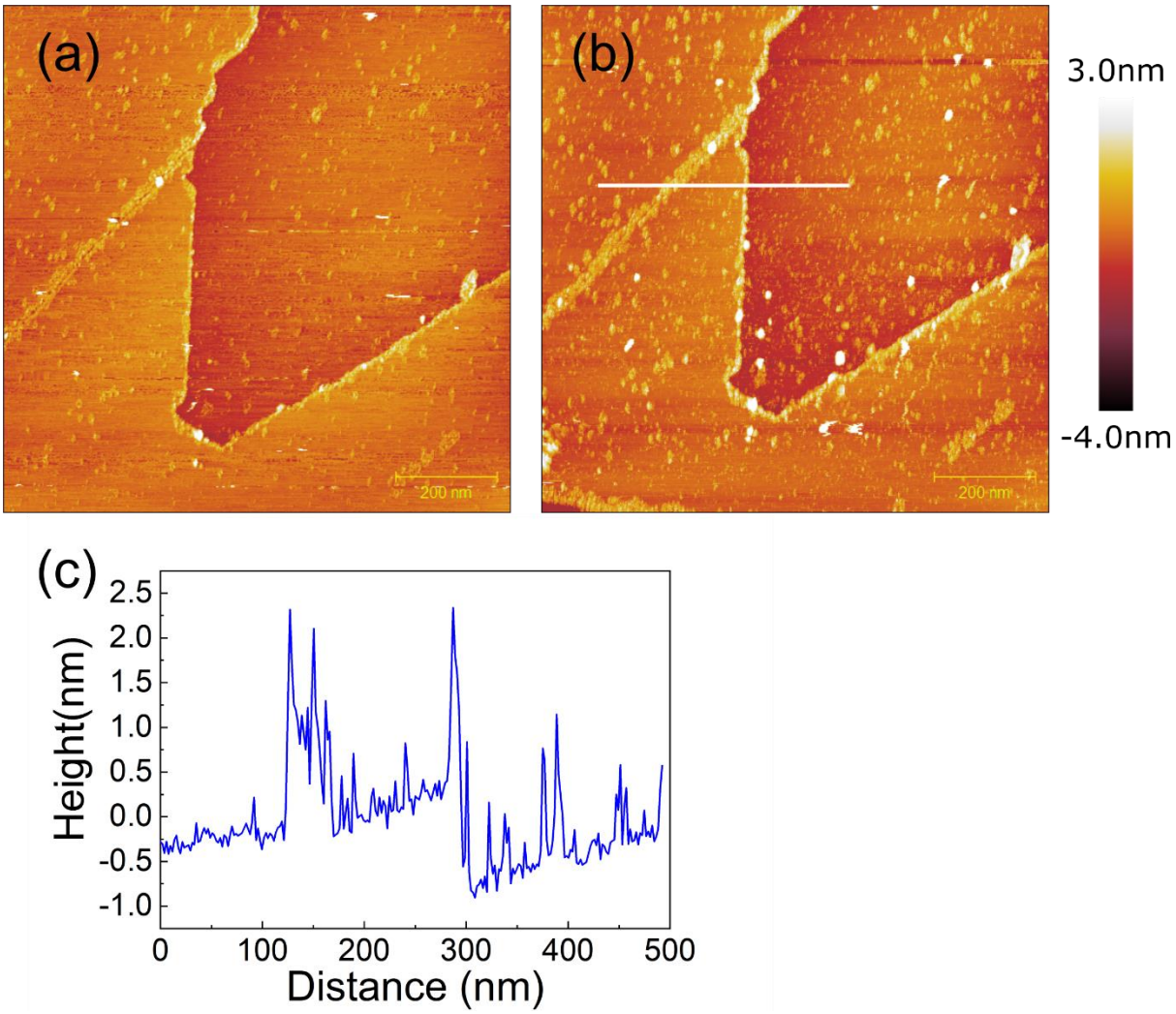

Figure 6.12. (a)-(b) 1µm x 1µm EC-STM images acquired at E= -0.9V in a 1mM lead sulphamate electrolyte following initial deposition at E= -1.2V for 1s and 3s. (c) Surface profile along the white line in (b). The tip was held at 0.2 V relative to the sample. The range of the height colour scale is 7.0nm.

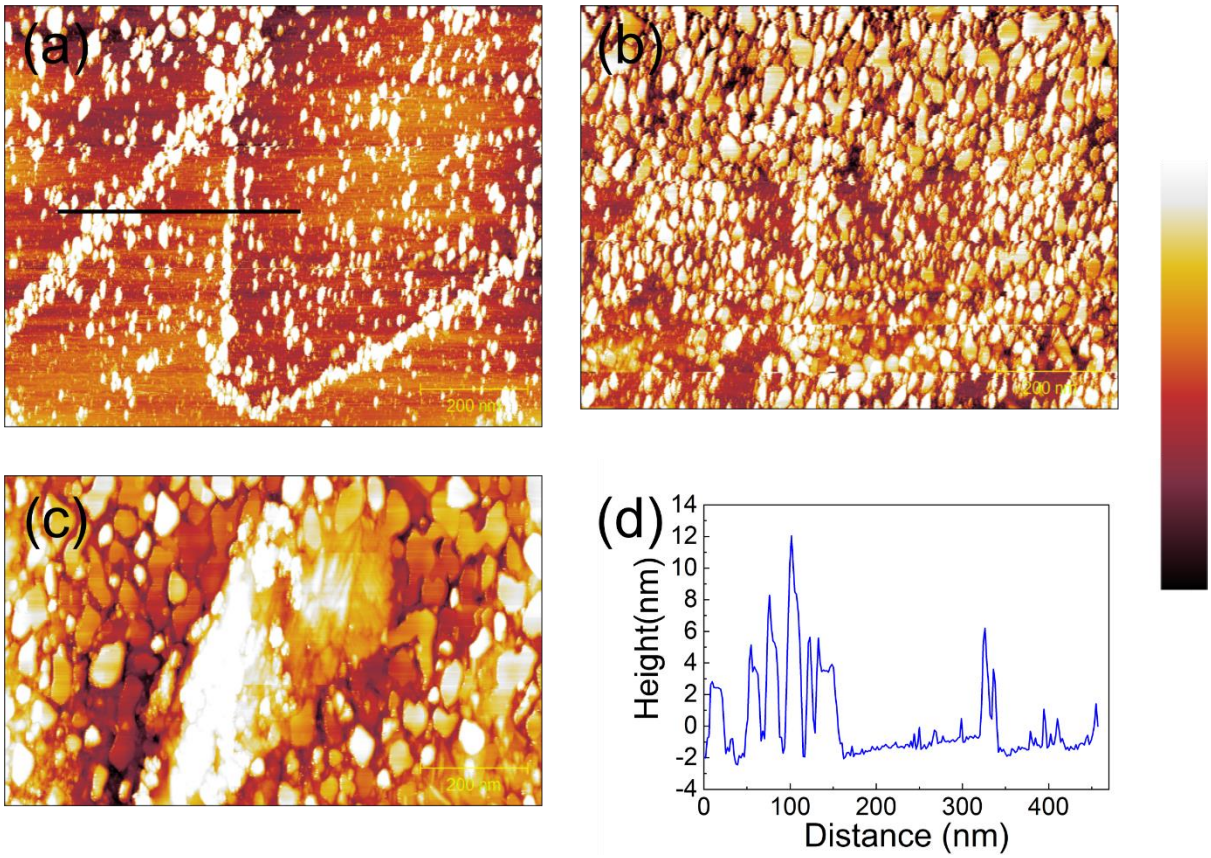

Figure 6.13. (a)-(c) A succession of EC-STM images acquired at E= -1.0V in a 1mM lead sulphamate electrolyte following initial deposition at E= -1.2V for 3s. (d) Surface profile along the black line in (a). The tip was held at 0.2 V relative to the sample. The range of the height colour scale is 9.0nm.

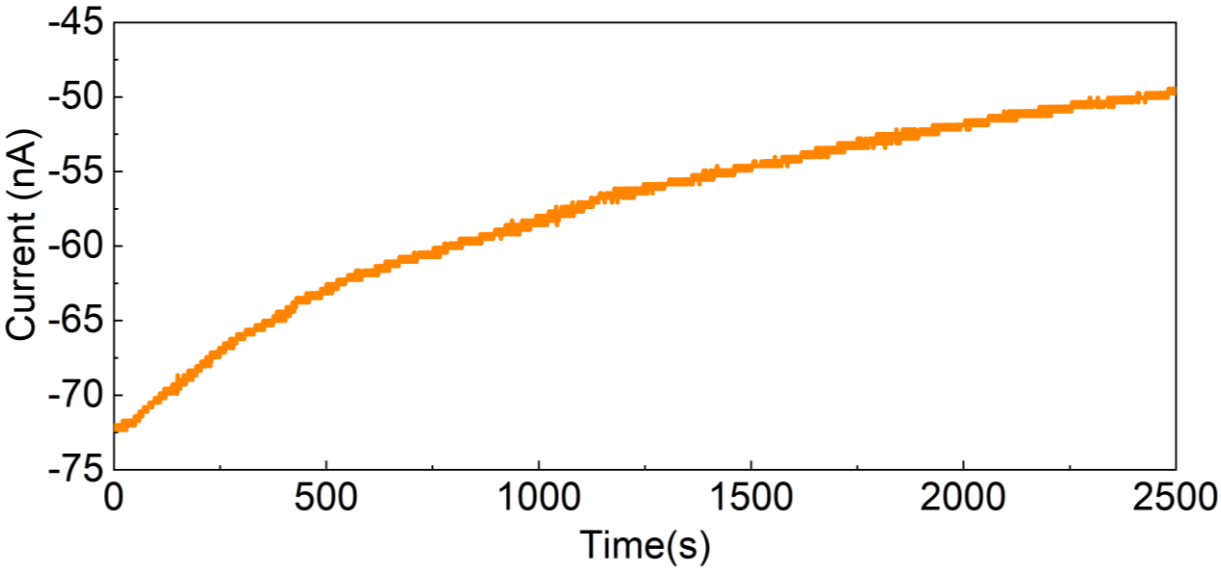

Figure 6.14. Current versus time for lead electrodeposition at -1.0V.

An I-t curve during electrodeposition is shown in Figure 6.14. For this fixed deposition potential, the

electrochemical current decreases with increasing time, which suggests that the deposition process is diffusion limited.

Figure 6.15. shows lead deposition at -1.1V, after initial nucleation at -1.2V for 10s. The growth rate is significantly higher than the rate for Figure 6.13, which can be attributed to the longer nucleation step at -1.2V and the larger overpotential. The same areas on each scan are highlighted, from which the merging of lead islands is observed. Rounded step edges and the high density of screw dislocations are the most distinctive features on the surface, which is quite different from Bi triangular structures.

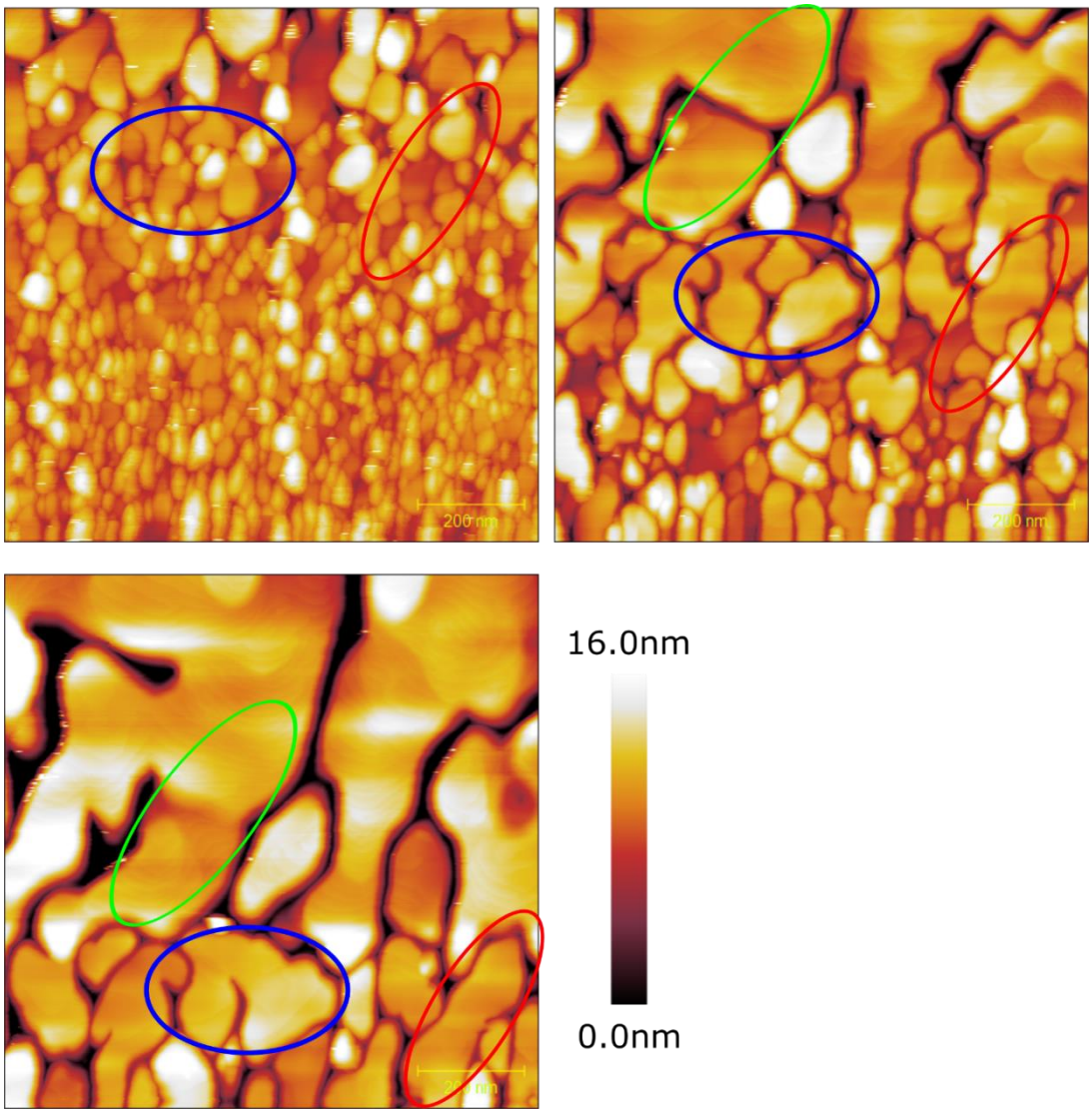

Figure 6.15. A succession of 1µm x 1µm EC-STM images acquired at E= -1.1V in a 1mM lead sulphamate electrolyte following initial deposition at E= -1.2V for 10s. The tip was held at 0.2 V relative to the sample. The range of the height colour scale is 16.0nm. The same areas on each scan are highlighted by ellipses, showing the merge of lead islands.

The difference between the chemical potential μ of the fluid phase and the equilibrium phase for liquid of vapour phase growth is called supersaturation. It is used to determine the most favourable growth mode. At very low supersaturation, Screw-Dislocation-Driven (SDD) growth is the only permitted mode because the screw dislocations step edges allow the crystal to growth at supersaturation below the threshold to create two-dimensional nuclei for layer-by-layer growth [142-144]. For electrodeposition, the driving force is the electrochemical potential which combines electrical potential with chemical potential. Therefore, the supersaturation is the difference of the electrochemical potential, which is directly related to the overpotential η ($\Delta\mu = ze|\eta|$). The high density of screw dislocations may be attributed to insufficient overpotential, because the screw dislocation step edges allow the crystal to grow even when the overpotential is not enough to create new nuclei.

Figure 6.16 and 6.17 are images of SDD growth. Comparing every two successive images, it appears that the rotation rate of the indicated screw dislocation decreases with increasing time. The decrease in the growth rate is consistent with the I-t curve shown in Figure 6.14. However, the rotation of screw dislocations in these images is not very smooth. Besides, the dislocations "merged" with each other during the measurements, which may indicate multi-tip. During lead deposition, the tip condition can change by crashing into the growing clusters. Once the tip condition changes, it is difficult to recover the situation because methods that can be applied in vacuum such as applying a high pulse to the tip cannot be used in the electrochemical environment. There are two different pathways for metal deposition: direct deposition from the solution at a growth site, or indirect deposition involving formation and subsequent surface diffusion of adatoms. In the first case, the electrode kinetics obey a modified Butler-Volmer equation, although the activation energy for ion transfer (solvent displacement) is different from the activation energy for electron transfer (solvent reorganization). However, extra variables such as the coverage of the adsorbates may be introduced to the equation, which makes the quantitative discussion complicated. In the second case, the deposition and dissolution of the adatoms may obey the Butler-Volmer equation, but subsequent surface diffusion makes things more complicated than the first case.

Even for a very simplified model that uses an unmodified Butler-Volmer equation to describe direct deposition, the unknown transfer coefficient α limits quantitative discussion. For electron transfer, α is usually close to 0.5. However, for ion transfer, the value of α could range from 0 to 1 because there is no need for Gibbs free energy curves of reactants and products to be symmetric.

Here is an example where different transfer coefficients lead to different conclusions. For an electrode reaction involving a change of n electrons, it must involve n distinct electron transfer steps. If the reaction is electron transfer controlled, the rate-determining step (RDS) is always a one-electron process. Therefore, the Butler-Volmer formulation (equation 1.9) can be written as:

(6.9) $$i = FAk_{RDS}^{0}[C_{Pb^{2+}}(0,t)e^{-\alpha f(E-E^{0'})} - C_X(0,t)e^{(1-\alpha)f(E-E^{0'})}]$$

where k_{RDS}^{0} is the standard rate constant of the rate-determining step, C_X is the concentration of the intermediate reactants.

If the overpotential is large enough (in the Tafel region), the backward term becomes negligible. Furthermore, if change of the Pb^{2+} concentration with the reaction time is ignored, equation 6.9 could be simplified as:

(6.10) $$i = FAk_{RDS}^{0}C_{Pb^{2+}}(0,t)e^{-\alpha f(E-E^{0'})} \approx FAk_{RDS}^{0}C_{Pb^{2+}}e^{-40\alpha(E-E^{0'})}$$

Considering two groups of deposition parameters -1.2V/1mM (A) and -1.3V/0.2mM (B). For $\alpha = 0.1$, the current for B is $\frac{e^{0.4}}{5}$ (~0.3) times of the current for A, which means that the deposition rate should decrease. For $\alpha = 0.9$, the current for B is $\frac{e^{3.6}}{5}$ (~7.3) times of the current for A, indicating that the deposition rate should increase. The contradiction showing that the quantitative discussion is difficult unless the transfer coefficient is known.

A more dilute electrolyte (0.2mM lead sulphamate) was used to slow down the growth rate (Figure 6.18). The deposition was very slow even at a more negative potential (-1.3V vs MSE). The amount of dissolved lead in the electrolyte in the STM cell (about 5mL) was calculated to be ~ 1e-6 mol. The atomic weight of lead is ~ 207 and the density of lead is about 11.3g/cm^3, therefore the volume was calculated to be 1.8e-5 cm^3. The sample surface area was estimated to be 0.5cm^2. If all lead ions were reduced to lead atoms then deposited on the sample, the thickness of the lead film would be about 3.6e-7m (360nm). Since the amount of deposited lead is only a small fraction of the lead in the cell, the concentration of the bulk solution does not change much. The small growth rate may be attributed to slow mass transport in ~0.2mM lead sulphamate.

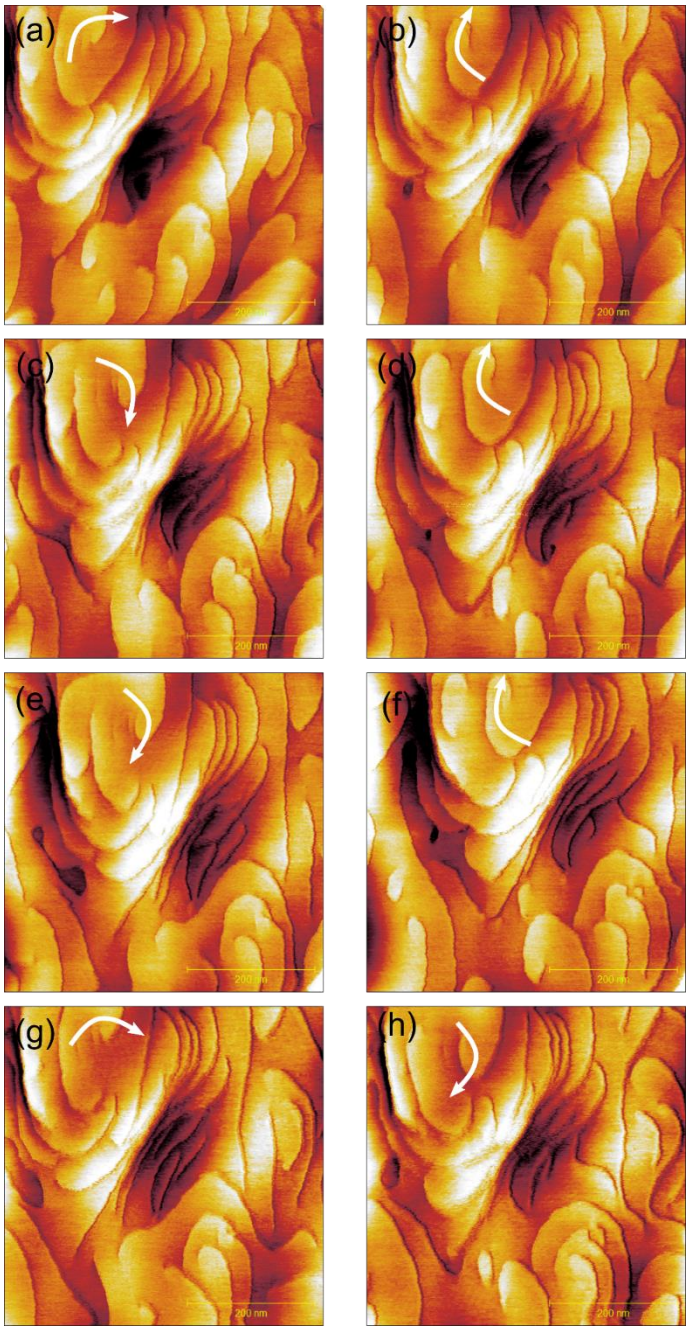

Figure 6.16. A succession of 500nm x 500nm EC-STM images acquired at E= -1.1V in a 1mM lead sulphamate electrolyte following initial deposition at E= -1.2V for 10s. The tip was held at 0.2 V relative to the sample. Screw dislocation growth is indicated by arrows. The range of the height colour scale is 1.7nm. The time interval is about 5min.

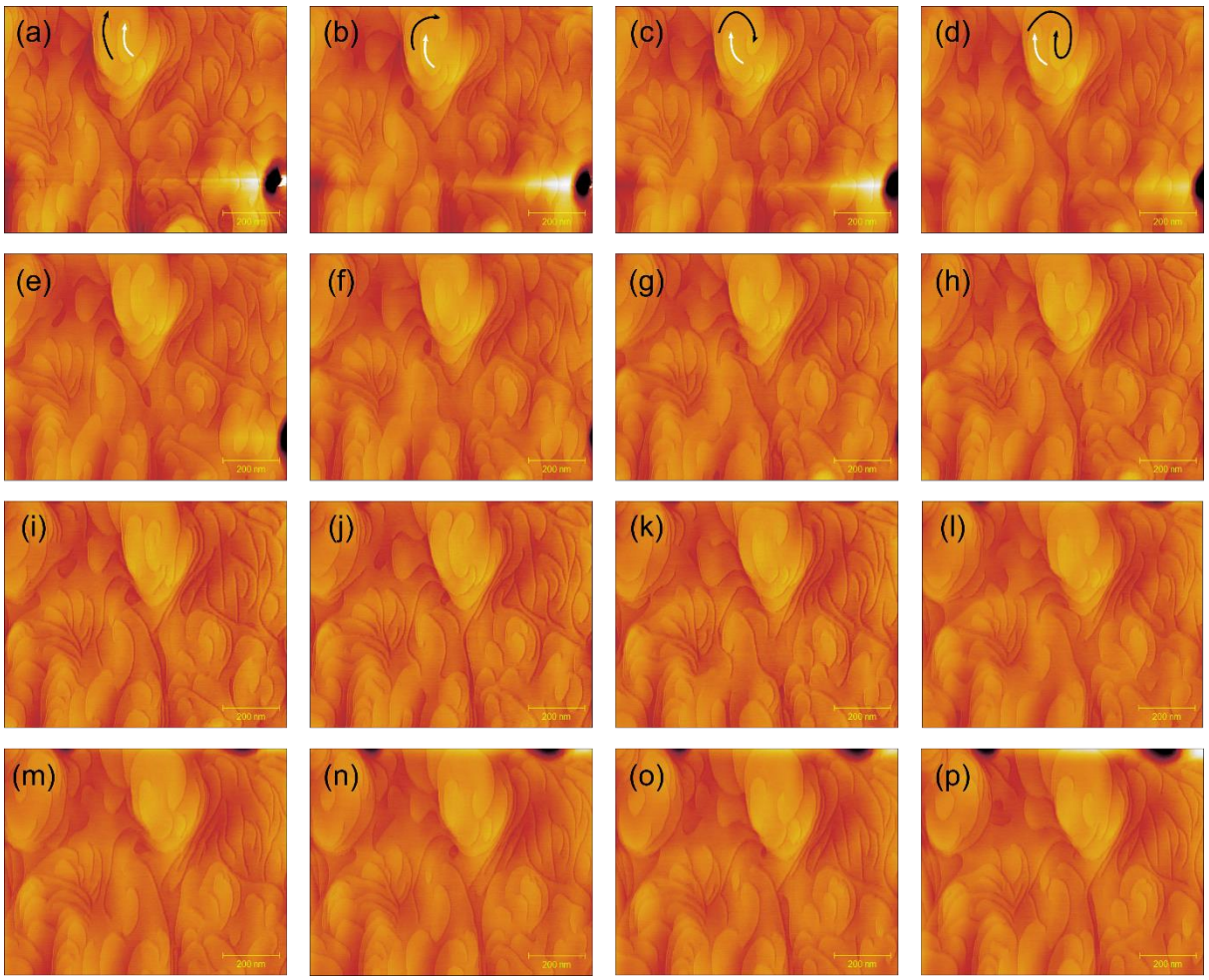

Figure 6.17. A succession of 1µm x 1µm EC-STM images acquired at E= -1.1V in a 1mM lead sulphamate electrolyte following initial deposition at E= -1.2V for 10s. The tip was held at 0.2 V relative to the sample. Screw dislocation growth is indicated by arrows. The range of the height colour scale is 8nm. The time interval is about 5min.

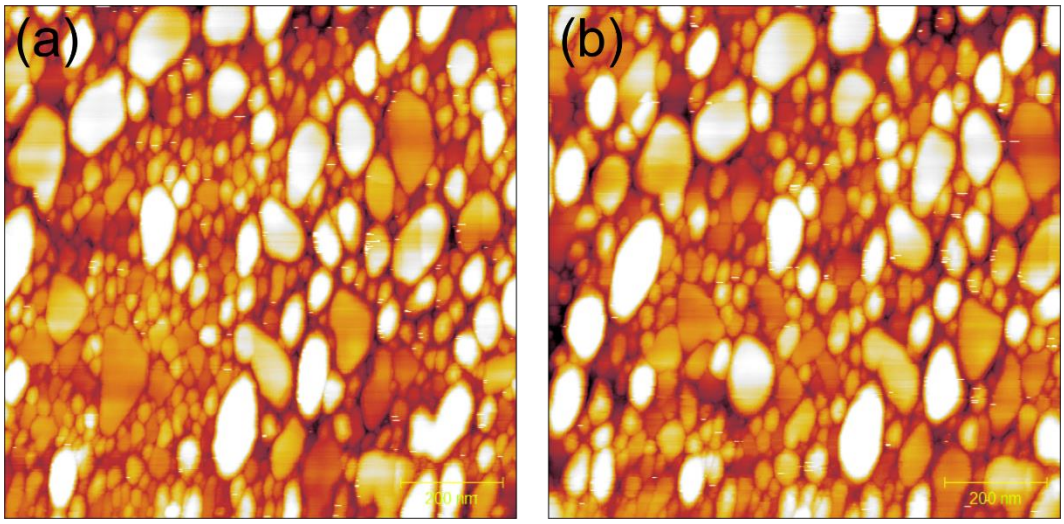

Figure 6.18. EC-STM images acquired at (a) E= -1.2V and (b) E= -1.3V in a 0.2mM lead sulphamate electrolyte. The tip was held at 0.3 V relative to the sample. The time interval is about 30min. The range of the height colour scale is 14nm.

6.5 Chapter Discussion

Metal electrodeposition on Bi_2Se_3 single crystals were carried out to obtain bismuth chalcogenides/metal heterostructures.

Parts of the results are expected. (1) Pseudomorphic growth of Bi thin films on Bi_2Se_3 was confirmed by continuously collected EC-STM images. Two different electrolytes led to similar surface morphologies. (2) Pb precipitation was observed during the experiments. Again, parts of the results are unexpected. (3) Possible Ag deposition was recorded when the silver epoxy was exposed to the electrolyte. Subsequent CVs measurements suggest that the redox reactions of silver epoxy are sensitive to the applied potential and solution pH. (4) For Pb electrodeposition, a high density of screw dislocations was observed. These distinctive features could be attributed to insufficient overpotential. However, the attempt to record the deposition process at a relatively larger overpotential was failed because the deposition rate was too fast for a conventional EC-STM to collect images.

Compared to previous chapters, electrochemical protection at the rest potential still effective, although the conditions of experiments were slightly changed. To facilitate metal electrodeposition, the solution pH was much lower than the pH of the electrolytes used in previous chapters, therefore oxidative dissolution is expected to occur at a more negative potential. However, the electrodeposition experiments need flat substrates, therefore the oxidative dissolution should be avoided.

6.6 Chapter Summary

EC-STM and cyclic voltammetric method were used to study metal (Ag, Bi and Pb) electrodeposition on Bi_2Se_3 single crystals. The deposited structures strongly depend on elements and their concentrations.

For silver deposition from exposed silver epoxy, large clusters were observed at -0.2V vs MSE. For bismuth deposition from both Bi/HNO_3 and $Bi/HClO_4$ electrolytes, characteristic triangular structures were observed at around -0.5V vs MSE. EC-STM images acquired at -0.5V following initial deposition at a more negative potential show epitaxial growth of bismuth bilayer with a very slow growth rate. Furthermore, the reversibility of Bi deposition was confirmed by repeatedly switching the sample potential between -0.6V and -0.45V. For lead deposition, three electrolytes with different lead concentrations were used. Initial nucleation of lead clusters and the merge of lead islands as well as subsequent screw-dislocation-driven growth were observed when 1mM lead sulphamate electrolyte was used. The I-t curve recorded during deposition and the successively collected EC-STM images demonstrate that the growth rate decreases with increasing time. Increasing lead concentration to 10mM resulted in straight steps and the absence of screw dislocation, whereas decreasing lead concentration to 0.2mM led to nucleation of lead clusters but limited further growth.

CHAPTER 7

CONCLUSIONS AND THE FUTURE PLAN

These studies aimed to investigate the electrochemistry of bismuth chalcogenides by determining their electrochemical response and characterizing their surface morphologies under electrochemical control. These were achieved via conventional electrochemistry methods, XPS and EC-STM.

The general background was introduced in Chapter 1, including the properties and application prospects of bismuth chalcogenides and an introduction to scanning tunnelling microscopy and electrochemical methods. The proposed experiments and the structure of this thesis were also described at the end of this chapter.

Detailed methods were discussed in Chapter 2, including preparation of samples and STM tips, selection of the reference electrode, the procedure of an EC-STM measurement, cyclic voltammetry, electrochemical impedance spectroscopy (EIS) and X-ray photoelectron spectroscopy. Subsequent experiments were carried out using the techniques and the procedures described in this chapter.

Air exposure and electrochemical redox reactions of single crystals of a bismuth chalcogenide $Bi_2Te_{0.9}Se_{2.1}$ were explored and discussed in Chapter 3, after explaining their importance as well as the motivations for studying their surface chemistry. The XPS data demonstrate the ability to control and

characterize the surface oxidation of bismuth chalcogenides in an electrochemical environment. By applying an appropriate potential (the rest potential), an oxide-free surface can be maintained. By applying an oxidation potential that is more positive than the rest potential, the surface can be oxidised on the timescale of several minutes. By applying a reduction potential that is more negative than the rest potential, the change in the surface chemistry produced by electrochemical oxidation can also be reversed. Pourbaix diagrams were used to identify possible oxidation and reduction products. For electrochemical oxidation, the most probable products are oxides of Bi,Te and Se. For electrochemical reduction, considering the mutually induced codeposition, $Bi_xTe_ySe_z$ rather than elemental Bi, Te or Se could be the most probable product. These results not only confirm that the surface chemistry of bismuth chalcogenides can be modified by electrochemical oxidation and subsequent electrochemical reduction but also suggest that bismuth chalcogenides would be a feasible platform for EC-STM study. This is followed up in Chapter 4.

As an alternative way to protect a bismuth chalcogenide surface, thiol functionalisation was also discussed in Chapter 3. The XPS for a 1,5′-pentanedithiol functionalised sample and a 1-pentanethiol functionalised sample are different. No clear evidence of oxidation can be detected from the 1,5′-pentanedithiol functionalised sample, which means that 1,5′-pentanedithiol can protect the surface from oxidation. However, clear oxidation peaks with lower intensities than the corresponding peaks for the unprotected sample are detected from the 1-pentanethiol functionalised sample, indicating that 1-pentanethiol just partially reduces the surface oxidation. The better protection ability of 1,5′-pentanedithiol may be attributed to spontaneous polymerisation.

EC-STM experiments of different bismuth chalcogenides were discussed in Chapter 4. Images were collected at the rest potential, showing atomically smooth terraces and steps with height equal to the expected quintuple layer (QL) thickness (1nm). Continuous scanning does not show significant changes in the morphology, which indicates that the freshly cleaved surfaces can remain stable for several hours at this potential.

Electrochemically oxidised surfaces were imaged by three strategies. For the first strategy, the sample was imaged at a mild oxidation potential, which means the surface was continuously dissolved during the imaging process. Clear surface dissolution accompanied by pit formation was observed when the surface was imaged at a mild oxidation potential. With increasing oxidation time, these pits only expanded in the lateral direction, keeping a pit depth of about 1nm. Until the whole quintuple layer dissolved, the newly exposed surface exhibits significantly higher stability than the original surface,

which suggests a sort of passivation. However, dissolution appeared to be more rapid where scanning took place than elsewhere, which indicates significant tip effects. For the second strategy, the sample was oxidised for successive intervals at a predetermined potential. After each oxidation stage, the sample was imaged at the rest potential to minimise tip effects. Notably, the pit density and coverage still increased progressively with increasing oxidation time, but the tip effects were significantly reduced. For the third strategy, the STM tip was removed from the electrolyte before each oxidation stage to avoid any tip influence. After each oxidation stage, several different areas were randomly selected then imaged to calculate the average pit density and coverage. There was a positive correlation between pit coverage and oxidation time. Three probable dissolution modes were discussed to explain the exact relationship between these two parameters. Furthermore, this chapter also showed the redeposition of dissolved components at a more negative potential after oxidative dissolution. The results of Chapter 4 provide real-space information for bismuth chalcogenide surface electrochemical redox reactions.

Next, the electrochemical oxidation of Bi_2Se_3 single crystals was studied in pH7 electrolyte in Chapter 5. Small clusters of about 1nm height were observed after oxidative dissolution. These clusters could be Bi_2O_3.

The effects of electrochemical redox reactions were also studied by EIS using the ferrocyanide/ferricyanide redox couple. Electrochemical oxidation significantly increased the Bi_2Se_3 charge transfer resistance, which may be attributed to adsorbed Bi oxides. Electrochemical reduction at different potentials showed different results. Reduction at -0.6V partially restored the impedance, whereas reduction at -1.1V lowered the transfer resistance to its original value. Pourbaix diagrams indicate that -0.6V is not enough for electrochemical reduction of Bi_2O_3 in pH7 electrolyte, which may explain the behaviour of the charge transfer resistance. Chapter 5 linked EC-STM and EIS to provide a new approach to study bismuth chalcogenide surface chemistry.

Finally, metal deposition on bismuth chalcogenides was studied in Chapter 6. Large clusters were observed after electrochemical oxidation of a sample that had Ag epoxy (for fixing the crystal) exposed to the electrolyte. CVs for a well-insulated sample and Ag epoxy alone made it possible to identify these clusters as Ag. This chapter also investigated the reversible growth of electrodeposited Bi films on freshly cleaved Bi_2Se_3 single crystal surfaces. Layer-by-layer growth at a very slow rate was confirmed by EC-STM images. The characteristic triangular structures of deposited Bi are consistent with the literature.

Important future work can be divided into experiments feasible with the existing instrumentation and experiments that require improved apparatus. A quantitative study of the etching rate of bismuth chalcogenides in air, in water (without electrochemical control) and in an electrochemical environment is of great help for understanding which factors are involved and to which extent these factors affect the surface dissolution. In these experiments, STM images would be collected over the same time interval in different environments. The pit coverage would be determined as a function of time.

Although SAMs were used to protect the surface from oxidation in Chapter 3, no EC-STM experiments were carried out to study the morphology of the SAMs or the adsorption of an individual organic molecule on bismuth chalcogenides. Considering the probable polymerisation for alkanedithiol, 1,5'-pentanedithiol may not be a good choice for EC-STM study. Oleic acid may be an alternative because it was used to treat nanocrystals PbS and monolayers of the dichalcogenide WS_2 [145, 146]. The enhancement of photoluminescence and mobilities in the WS_2 monolayer was attributed to the passivation of defects sites by oleic acid ligands. If oleic acid could similarly treat bismuth chalcogenides, one would expect that the treated surface would be more resistant to air oxidation and electrochemical oxidation because the oleic acid would block the oxidative dissolution which starts from defects sites. EC-STM study of oleic acid treated samples at different oxidation potentials could confirm this assumption.

Tip effects in different environments could also be studied by carrying out two groups of experiments in air, in water and in an electrochemical environment, with or without continuous scans. Furthermore, using different bias voltages to scan the sample surface could reveal the relationship between the bias voltage and the tip effects, as discussed in Chapter 4.

According to the Pourbaix diagrams, instead of being oxidised at a relatively positive potential, bismuth chalcogenides could also be reduced at a much more negative potential. At about -1.5V vs MSE, Bi in oxidation state +3 in bismuth chalcogenides could be reduced to Bi^0, leading to Bi stripping and reductive dissolution. An EC-STM experiment could be used to characterize the reduced surface, but the imaging potential would have to be more positive than the reduction potential to avoid hydrogen evolution and continuing dissolution. At the reduction potential, one would expect that the bismuth chalcogenides convert to metallic Bi and soluble chalcogenide ions in oxidation state -2. If the imaging potential is negative enough, pits and Bi clusters would be observed. If the imaging potential is sufficiently positive to oxidise metallic Bi^0 to Bi^{3+}, bismuth chalcogenides may redeposit on the surface.

EIS measurements could also be carried out to check whether the charge transfer resistance changes after reductive dissolution.

Although the initial attempt described in Chapter 5 to measure the local noise in the tunnelling current as an indicator of local reactivity and catalytic activity was unsuccessful, it could be worthwhile to try a different combination of sample/reaction. The sample surface should consist of at least two features that have different catalytic activities toward the selected reaction. In the case of bismuth chalcogenides, terraces and step edges are such features on a freshly cleaved surface. A pre-oxidised surface has at least two more: pits and pit edges. Therefore, the challenge is more how to find a suitable reaction rather than how to obtain different surface features. In the literature, the oxygen reduction reaction and hydrogen evolution reaction were studied on noble metal electrodes. Considering the electrochemical working window of bismuth chalcogenides, the oxygen reduction reaction may start at a potential that could oxidise the surface, therefore the hydrogen evolution reaction is more promising.

Improved apparatus would enable further studies. During the EC-STM experiments, the STM tip sometimes has to be removed from the electrolyte to refill the EC-STM cell because the electrolyte continually evaporates. On re-approaching, it is difficult to find the previously imaged area due to the limitations of the instrument. A high precision micropump to compensate evaporation would solve this problem and keep the experimental conditions constant. Furthermore, a combination of two micropumps would allow the electrolyte exchange without cutting off the electrochemical control. The first micropump that is connected to the container for waste electrolyte could extract the electrolyte A from the EC-STM cell, whereas the second pump that is connected to a container of electrolyte B could transfer this electrolyte into the EC-STM cell in the meantime. To avoid overflow or emptying, the flow rates for the two pumps should be the same (and small enough). This set-up would be suitable for metal deposition on oxidised bismuth chalcogenides. It would avoid redeposition of bismuth chalcogenides by changing the electrolyte containing dissolved components to the electrolyte for metal deposition. Furthermore, this set-up would also be suitable for the electrodeposition of layered structures consisting of various metal layers, because electrolytes that contain different metal ions could be transferred into the EC-STM cell in the required order. More complicated electrochemical flow cells have been designed for various purposes and can be used as references to improve the scheme [147-149].

The combination of EC-STM and EIS is promising. In-situ EC-STM images combined with EIS in the same cell would provide a better way to link the surface morphology to the electrochemical response.

This could be achieved by replacing the STM bipotentiostat with an electrochemical workstation, but significant work would be required to link the latter to the EC-STM system. In the combined system, there would be a command to switch between two working modes. In EC-STM mode, the electrochemical workstation would work as a bipotentiostat to maintain electrochemical control. In EIS mode, the tip would be removed from the electrolyte or the tip potential would be fixed to protect the tip.

A further improvement would be to build an environmental chamber. Electrochemical experiments could be carried out in an inert gas atmosphere with degassed electrolyte to study the influence of dissolved oxygen on electrochemical oxidation by utilizing the environmental chamber. Bismuth chalcogenides could also be imaged in inert gas or in degassed water (without electrochemical control) to ascertain the function of oxygen and water on normal oxidation.

Another feasible change would be to use a scanner with a higher resolution but smaller scanning area. The present scanner has a large scanning area but a relatively low resolution. In the case of our electrochemical experiments, images collected by this scanner enabled us to determine the average pit density and coverage and observe the characteristic triangular structures of electrodeposited Bi, for example. However, the relatively lower resolution also limits the ability to characterize the step/pit edges and redeposited clusters in greater detail. Higher resolution images could provide more information on the surface morphology. Firstly, fine structures of step and pit edges could reveal more details about oxidative dissolution. Secondly, atomic-resolution images of the terraces could be used to determine the crystallographic orientation of electrodeposited Bi. Thirdly, high-resolution images of the clusters may provide information to distinguish Bi oxides and redeposited bismuth chalcogenides.

The combination of Raman spectroscopy and EC-STM could provide more chemical information to determine the elemental composition of the sample surface. Tip-enhanced Raman spectroscopy (TERS) is based on the surface-enhanced Raman scattering effect (SERS), where the electric field is greatly enhanced near the surface of metal nanoparticle[150]. The initial attempt was to use a modified AFM tip as the cluster of nano metal particles [151]. The AFM and Raman spectroscopy combined system could break through the light diffraction limit, and therefore provide chemical information on the sample surface with nanometer resolution. Recent developments of TERS extend its application by using the EC-STM tip as the cluster of nano metal particles [152]. TERS collected in an electrochemical environment could provide information about local electrochemical reactions, therefore the EC-STM-TERS system is an ideal platform for in-situ electrochemical studies on the nanoscale. In the future, it

would be possible to update our EC-STM system to a more powerful EC-STM-TERS system. For electrochemical redox reactions of bismuth chalcogenides, the new system could determine the elemental composition of the redeposited clusters in-situ. Moreover, the Raman spectrum of the newly exposed quintuple layer may be slightly different from the original surface spectrum. These possible differences may reveal more details about the surface oxidation of bismuth chalcogenides.

Bibliography

[1] D. Biswas, K. Maiti, Surface-interface anomalies and topological order in Bi_2Se_3, EPL (Europhysics Letters), 110 (2015) 17001.

[2] S.K. Mishra, S. Satpathy, O. Jepsen, Electronic structure and thermoelectric properties of bismuth telluride and bismuth selenide, Journal of Physics: Condensed Matter, 9 (1997) 461-470.

[3] T.M. Tritt, M.A. Subramanian, Thermoelectric Materials, Phenomena, and Applications: A Bird's Eye View, MRS Bulletin, 31 (2011) 188-198.

[4] L. Müchler, F. Casper, B. Yan, S. Chadov, C. Felser, Topological insulators and thermoelectric materials, physica status solidi (RRL) - Rapid Research Letters, 7 (2013) 91-100.

[5] R. Venkatasubramanian, E. Siivola, T. Colpitts, B. O'Quinn, Thin-film thermoelectric devices with high room-temperature figures of merit, Nature, 413 (2001) 597-602.

[6] C. Duck Young, T. Hogan, J. Schindler, L. Iordarridis, P. Brazis, C.R. Kannewurf, C. Baoxing, C. Uher, M.G. Kanatzidis, Complex bismuth chalcogenides as thermoelectrics, XVI ICT '97. Proceedings ICT'97. 16th International Conference on Thermoelectrics (Cat. No.97TH8291), 1997, pp. 459-462.

[7] B. Poudel, Q. Hao, Y. Ma, Y. Lan, A. Minnich, B. Yu, X. Yan, D. Wang, A. Muto, D. Vashaee, X. Chen, J. Liu, M.S. Dresselhaus, G. Chen, Z. Ren, High-Thermoelectric Performance of Nanostructured Bismuth Antimony Telluride Bulk Alloys, Science, 320 (2008) 634.

[8] M.S. Dresselhaus, Intercalation In Layered Materials, MRS Bulletin, 12 (1987) 24-28.

[9] H. Wang, H. Yuan, S. Sae Hong, Y. Li, Y. Cui, Physical and chemical tuning of two-dimensional transition metal dichalcogenides, Chemical Society Reviews, 44 (2015) 2664-2680.

[10] K.J. Koski, C.D. Wessells, B.W. Reed, J.J. Cha, D. Kong, Y. Cui, Chemical Intercalation of Zerovalent Metals into 2D Layered Bi_2Se_3 Nanoribbons, Journal of the American Chemical Society, 134 (2012) 13773-13779.

[11] Y.L. Chen, J.G. Analytis, J.H. Chu, Z.K. Liu, S.K. Mo, X.L. Qi, H.J. Zhang, D.H. Lu, X. Dai, Z. Fang, S.C. Zhang, I.R. Fisher, Z. Hussain, Z.X. Shen, Experimental Realization of a Three-Dimensional Topological Insulator, Bi_2Te_3, Science, 325 (2009) 178.

[12] D. Hsieh, Y. Xia, D. Qian, L. Wray, J.H. Dil, F. Meier, J. Osterwalder, L. Patthey, J.G. Checkelsky, N.P. Ong, A.V. Fedorov, H. Lin, A. Bansil, D. Grauer, Y.S. Hor, R.J. Cava, M.Z. Hasan, A tunable topological insulator in the spin helical Dirac transport regime, Nature, 460 (2009) 1101-1105.

[13] Y. Xia, D. Qian, D. Hsieh, L. Wray, A. Pal, H. Lin, A. Bansil, D. Grauer, Y.S. Hor, R.J. Cava, M.Z. Hasan, Observation of a large-gap topological-insulator class with a single Dirac cone on the surface, Nature Physics, 5 (2009) 398-402.

[14] H. Zhang, C.-X. Liu, X.-L. Qi, X. Dai, Z. Fang, S.-C. Zhang, Topological insulators in Bi_2Se_3, Bi_2Te_3 and Sb_2Te_3 with a single Dirac cone on the surface, Nature Physics, 5 (2009) 438-442.

[15] W.-Y. Shan, H.-Z. Lu, S.-Q. Shen, Effective continuous model for surface states and thin films of three-dimensional topological insulators, New Journal of Physics, 12 (2010) 043048.

[16] M.Z. Hasan, J.E. Moore, Three-Dimensional Topological Insulators, Annual Review of Condensed Matter Physics, 2 (2011) 55-78.

[17] D. Pesin, A.H. MacDonald, Spintronics and pseudospintronics in graphene and topological insulators, Nature Materials, 11 (2012) 409-416.

[18] Y. Ando, T. Hamasaki, T. Kurokawa, K. Ichiba, F. Yang, M. Novak, S. Sasaki, K. Segawa, Y. Ando, M. Shiraishi, Electrical Detection of the Spin Polarization Due to Charge Flow in the Surface State of the Topological Insulator $Bi_{1.5}Sb_{0.5}Te_{1.7}Se_{1.3}$, Nano Letters, 14 (2014) 6226-6230.

[19] C.H. Li, O.M.J. van 't Erve, J.T. Robinson, Y. Liu, L. Li, B.T. Jonker, Electrical detection of charge-current-induced spin polarization due to spin-momentum locking in Bi_2Se_3, Nature Nanotechnology, 9 (2014) 218-224.

[20] J.C. Rojas-Sánchez, S. Oyarzún, Y. Fu, A. Marty, C. Vergnaud, S. Gambarelli, L. Vila, M. Jamet, Y. Ohtsubo, A. Taleb-Ibrahimi, P. Le Fèvre, F. Bertran, N. Reyren, J.M. George, A. Fert, Spin to Charge Conversion at Room Temperature by Spin Pumping into a New Type of Topological Insulator: α-Sn Films, Physical Review Letters, 116 (2016) 096602.

[21] E.K. de Vries, A.M. Kamerbeek, N. Koirala, M. Brahlek, M. Salehi, S. Oh, B.J. van Wees, T. Banerjee, Towards the understanding of the origin of charge-current-induced spin voltage signals in the topological insulator Bi_2Se_3, Physical Review B, 92 (2015) 201102.

[22] D. Hsieh, F. Mahmood, J.W. McIver, D.R. Gardner, Y.S. Lee, N. Gedik, Selective Probing of Photoinduced Charge and Spin Dynamics in the Bulk and Surface of a Topological Insulator, Physical Review Letters, 107 (2011) 077401.

[23] J.W. McIver, D. Hsieh, H. Steinberg, P. Jarillo-Herrero, N. Gedik, Control over topological insulator photocurrents with light polarization, Nature Nanotechnology, 7 (2012) 96-100.

[24] C. Kastl, C. Karnetzky, H. Karl, A.W. Holleitner, Ultrafast helicity control of surface currents in topological insulators with near-unity fidelity, Nature Communications, 6 (2015) 6617.

[25] Y.S. Hor, J.G. Checkelsky, D. Qu, N.P. Ong, R.J. Cava, Superconductivity and non-metallicity induced by doping the topological insulators Bi_2Se_3 and Bi_2Te_3, Journal of Physics and Chemistry of Solids, 72 (2011) 572-576.

[26] J. Xiao, L. Kou, C.-Y. Yam, T. Frauenheim, B. Yan, Toward Rational Design of Catalysts Supported on a Topological Insulator Substrate, ACS Catalysis, 5 (2015) 7063-7067.

[27] S. Chen, Y.-M. Fang, J. Li, J.-J. Sun, G.-N. Chen, H.-H. Yang, Study on the electrochemical catalytic properties of the topological insulator Bi_2Se_3, Biosensors and Bioelectronics, 46 (2013) 171-174.

[28] C.R. Rajamathi, U. Gupta, K. Pal, N. Kumar, H. Yang, Y. Sun, C. Shekhar, B. Yan, S. Parkin, U.V. Waghmare, C. Felser, C.N.R. Rao, Photochemical Water Splitting by Bismuth Chalcogenide Topological Insulators, ChemPhysChem, 18 (2017) 2322-2327.

[29] Q. Qu, B. Liu, J. Liang, H. Li, J. Wang, D. Pan, I.K. Sou, Expediting Hydrogen Evolution through Topological Surface States on Bi_2Te_3, ACS Catalysis, 10 (2020) 2656-2666.

[30] D. Li, J. Lao, C. Jiang, Y. Shen, C. Luo, R. Qi, H. Lin, R. Huang, G.I.N. Waterhouse, H. Peng, Heterostructured MoS_2@Bi_2Se_3 nanoflowers: A highly efficient electrocatalyst for hydrogen evolution, Journal of Catalysis, 381 (2020) 590-598.

[31] A.J. Bard, L.R. Faulkner, Fundamentals and applications, (2001).

[32] R.J. Wilson, S. Chiang, Structure of the Ag/Si(111) surface by scanning tunneling microscopy, Physical Review Letters, 58 (1987) 369-372.

[33] R.J. Wilson, S. Chiang, Registration and nucleation of the Ag/Si(111) $(\sqrt{3}\times\sqrt{3})R30^{\circ}$ structure by scanning tunneling microscopy, Physical Review Letters, 59 (1987) 2329-2332.

[34] S.-i. Kitamura, T. Sato, M. Iwatsuki, Observation of surface reconstruction on silicon above 800 °C using the STM, Nature, 351 (1991) 215-217.

[35] T. Matsumoto, H. Tanaka, T. Kawai, S. Kawai, STM-imaging of a $SrTiO_3$(100) surface with atomic-scale resolution, Surface Science, 278 (1992) L153-L158.

[36] B. Voigtländer, A. Zinner, Simultaneous molecular beam epitaxy growth and scanning tunneling microscopy imaging during Ge/Si epitaxy, Applied Physics Letters, 63 (1993) 3055-3057.

[37] H. Onishi, Y. Iwasawa, STM-imaging of formate intermediates adsorbed on a TiO_2(110) surface, Chemical Physics Letters, 226 (1994) 111-114.

[38] R.M. Feenstra, Scanning tunneling spectroscopy, Surface Science, 299-300 (1994) 965-979.

[39] H.J.W. Zandvliet, A. van Houselt, Scanning Tunneling Spectroscopy, Annual Review of Analytical Chemistry, 2 (2009) 37-55.

[40] H.L. Edwards, D.J. Derro, A.L. Barr, J.T. Markert, A.L. de Lozanne, Spatially Varying Energy Gap in the CuO Chains of $YBa_2Cu_3O_{7-x}$ Detected by Scanning Tunneling Spectroscopy, Physical Review Letters, 75 (1995) 1387-1390.

[41] B. Marsen, M. Lonfat, P. Scheier, K. Sattler, Energy gap of silicon clusters studied by scanning tunneling spectroscopy, Physical Review B, 62 (2000) 6892-6895.

[42] M. Kugler, Ø. Fischer, C. Renner, S. Ono, Y. Ando, Scanning Tunneling Spectroscopy of $Bi_2Sr_2CuO_{6+\delta}$: New Evidence for the Common Origin of the Pseudogap and Superconductivity, Physical Review Letters, 86 (2001) 4911-4914.

[43] J. Li, W.-D. Schneider, R. Berndt, O.R. Bryant, S. Crampin, Surface-State Lifetime Measured by Scanning Tunneling Spectroscopy, Physical Review Letters, 81 (1998) 4464-4467.

[44] Ø. Fischer, M. Kugler, I. Maggio-Aprile, C. Berthod, C. Renner, Scanning tunneling spectroscopy of high-temperature superconductors, Reviews of Modern Physics, 79 (2007) 353-419.

[45] C.J. Arguello, S.P. Chockalingam, E.P. Rosenthal, L. Zhao, C. Gutiérrez, J.H. Kang, W.C. Chung, R.M. Fernandes, S. Jia, A.J. Millis, R.J. Cava, A.N. Pasupathy, Visualizing the charge density wave transition in 2H-$NbSe_2$ in real space, Physical Review B, 89 (2014) 235115.

[46] J.S. Foster, J.E. Frommer, P.C. Arnett, Molecular manipulation using a tunnelling microscope, Nature, 331 (1988) 324-326.

[47] S. Gauthier, Atomic and molecular manipulations of individual adsorbates by STM, Applied Surface Science, 164 (2000) 84-90.

[48] G. Meyer, L. Bartels, K.-H. Rieder, Atom manipulation with the STM: nanostructuring, tip functionalization, and femtochemistry, Computational Materials Science, 20 (2001) 443-450.

[49] F. Moresco, G. Meyer, K.-H. Rieder, H. Tang, A. Gourdon, C. Joachim, Conformational Changes of Single Molecules Induced by Scanning Tunneling Microscopy Manipulation: A Route to Molecular Switching, Physical Review Letters, 86 (2001) 672-675.

[50] H. Qu, W. Yao, T. Garcia, J. Zhang, A.V. Sorokin, S. Ducharme, P.A. Dowben, V.M. Fridkin, Nanoscale polarization manipulation and conductance switching in ultrathin films of a ferroelectric copolymer, Applied Physics Letters, 82 (2003) 4322-4324.

[51] L. Grill, Functionalized molecules studied by STM: motion, switching and reactivity, Journal of Physics: Condensed Matter, 20 (2008) 053001.

[52] M. Jiang, E. Sak, K. Gentz, A. Krupski, K. Wandelt, Redox Activity and Structural Transition of Heptyl Viologen Adlayers on Cu(100), ChemPhysChem, 11 (2010) 1542-1549.

[53] M. Matsumoto, T. Manako, H. Imai, Electrochemical STM Investigation of Oxidative Corrosion of the Surface of Highly Oriented Pyrolytic Graphite, Journal of The Electrochemical Society, 156 (2009) B1208.

[54] O. Mann, W. Freyland, O. Raz, Y. Ein-Eli, Electrochemical deposition of ultrathin ruthenium films on Au(111) from an ionic liquid, Chemical Physics Letters, 460 (2008) 178-181.

[55] J.H.K. Pfisterer, Y. Liang, O. Schneider, A.S. Bandarenka, Direct instrumental identification of catalytically active surface sites, Nature, 549 (2017) 74-77.

[56] Y.-G. Kim, J.H. Baricuatro, M.P. Soriaga, Molecular Adsorption at Well-Defined Electrode Surfaces: Hydroquinone on Pd(111) Studied by EC-STM, Langmuir, 22 (2006) 10762-10765.

[57] S. Sek, EC-STM Study of Potential-Controlled Adsorption of Substituted Pyrimidinethiol on Au(111), Langmuir, 25 (2009) 13488-13492.

[58] R. Cabrera-Sierra, N. Batina, I. González, Oxidation of 1018 carbon steel in borate medium by in situ EC-STM: Surface morphology of the oxidized ferrite and pearlite phases, Materials Chemistry and Physics, 96 (2006) 343-348.

[59] K. Yoshida, A. Kuzume, P. Broekmann, I.V. Pobelov, T. Wandlowski, Reconstruction and electrochemical oxidation of Au(110) surface in 0.1 M H_2SO_4, Electrochimica Acta, 139 (2014) 281-288.

[60] Y.-G. Kim, J.H. Baricuatro, A. Javier, J.M. Gregoire, M.P. Soriaga, The Evolution of the Polycrystalline Copper Surface, First to Cu(111) and Then to Cu(100), at a Fixed CO_2RR Potential: A Study by Operando EC-STM, Langmuir, 30 (2014) 15053-15056.

[61] A.S. Hewitt, J. Wang, J. Boltersdorf, P.A. Maggard, D.B. Dougherty, Coexisting Bi and Se surface terminations of cleaved Bi_2Se_3 single crystals, Journal of Vacuum Science & Technology B, 32 (2014) 04E103.

[62] Y.N. Zhang, Communication: Surface stability and topological surface states of cleaved Bi_2Se_3: First-principles studies, The Journal of Chemical Physics, 143 (2015) 151101.

[63] M.C. Pérez, A. Rincón, C. Gutiérrez, Effect of chloride ions on the electrooxidation at low potentials of dissolved carbon monoxide on platinum, Journal of Electroanalytical Chemistry, 511 (2001) 39-45.

[64] A. López-Cudero, A. Cuesta, C. Gutiérrez, The effect of chloride on the electrooxidation of adsorbed CO on polycrystalline platinum electrodes, Journal of Electroanalytical Chemistry, 548 (2003) 109-119.

[65] B. Medgyes, X. Zhong, G. Harsányi, The effect of chloride ion concentration on electrochemical migration of copper, Journal of Materials Science: Materials in Electronics, 26 (2015) 2010-2015.

[66] K.J. Krause, F. Brings, J. Schnitker, E. Kätelhön, P. Rinklin, D. Mayer, R.G. Compton, S.G. Lemay, A. Offenhäusser, B. Wolfrum, The Influence of Supporting Ions on the Electrochemical Detection of Individual Silver Nanoparticles: Understanding the Shape and Frequency of Current Transients in Nano-impacts, Chemistry – A European Journal, 23 (2017) 4638-4643.

[67] K. Lutton, W.H. Blades, J.R. Scully, P. Reinke, Influence of Chloride on Nanoscale Electrochemical Passivation Processes, The Journal of Physical Chemistry C, 124 (2020) 9289-9304.

[68] J. Ghilane, P. Hapiot, A.J. Bard, Metal/Polypyrrole Quasi-Reference Electrode for Voltammetry in Nonaqueous and Aqueous Solutions, Analytical Chemistry, 78 (2006) 6868-6872.

[69] M. Lopes, T. Toury, M.L. de La Chapelle, F. Bonaccorso, P. Giuseppe Gucciardi, Fast and reliable fabrication of gold tips with sub-50 nm radius of curvature for tip-enhanced Raman spectroscopy, Review of Scientific Instruments, 84 (2013) 073702.

[70] N. Yokoi, S. Namba, M. Takai, Damage of STM tips during nanofabrication, Advanced Materials for Optics and Electronics, 2 (1993) 71-77.

[71] N. Yokoi, S. Ueda, S. Namba, M. Takai, Change in Scanning Tunneling Microscope (STM) Tip Shape during Nanofabrication, Japanese Journal of Applied Physics, 32 (1993) L129-L131.

[72] P.T. Kissinger, W.R. Heineman, Cyclic voltammetry, Journal of Chemical Education, 60 (1983) 702.

[73] G.A. Mabbott, An introduction to cyclic voltammetry, Journal of Chemical Education, 60 (1983) 697.

[74] D.H. Evans, K.M. O'Connell, R.A. Petersen, M.J. Kelly, Cyclic voltammetry, Journal of Chemical Education, 60 (1983) 290.

[75] R.J. Klingler, J.K. Kochi, Electron-transfer kinetics from cyclic voltammetry. Quantitative description of electrochemical reversibility, The Journal of Physical Chemistry, 85 (1981) 1731-1741.

[76] M.A. Masood, P.S. Zacharias, Electrochemical reversibility of the Cu–Cu couple in bis[2,9-di(o-substituted phenyl)-1,10-phenanthroline]-copper(I) complexes. Stability of the corresponding copper(0) species, Journal of the Chemical Society, Dalton Transactions, (1991) 111-114.

[77] T.K. Chen, Y.Y. Lau, D.K.Y. Wong, A.G. Ewing, Pulse voltammetry in single cells using platinum microelectrodes, Analytical Chemistry, 64 (1992) 1264-1268.

[78] J. Osteryoung, Voltammetry for the future, Accounts of Chemical Research, 26 (1993) 77-83.

[79] J.G. Osteryoung, M.M. Schreiner, Recent Advances in Pulse Voltammetry, C R C Critical Reviews in Analytical Chemistry, 19 (1988) S1-S27.

[80] D. Kong, J.J. Cha, K. Lai, H. Peng, J.G. Analytis, S. Meister, Y. Chen, H.-J. Zhang, I.R. Fisher, Z.-X. Shen, Y. Cui, Rapid Surface Oxidation as a Source of Surface Degradation Factor for Bi_2Se_3, ACS Nano, 5 (2011) 4698-4703.

[81] M.T. Edmonds, J.T. Hellerstedt, A. Tadich, A. Schenk, K.M. O'Donnell, J. Tosado, N.P. Butch, P. Syers, J. Paglione, M.S. Fuhrer, Stability and Surface Reconstruction of Topological Insulator Bi_2Se_3 on Exposure to Atmosphere, The Journal of Physical Chemistry C, 118 (2014) 20413-20419.

[82] C. Chen, S. He, H. Weng, W. Zhang, L. Zhao, H. Liu, X. Jia, D. Mou, S. Liu, J. He, Y. Peng, Y. Feng, Z. Xie, G. Liu, X. Dong, J. Zhang, X. Wang, Q. Peng, Z. Wang, S. Zhang, F. Yang, C. Chen, Z. Xu, X. Dai, Z. Fang, X.J. Zhou, Robustness of topological order and formation of quantum well states in topological insulators exposed to ambient environment, Proceedings of the National Academy of Sciences, 109 (2012) 3694.

[83] V.A. Golyashov, K.A. Kokh, S.V. Makarenko, K.N. Romanyuk, I.P. Prosvirin, A.V. Kalinkin, O.E. Tereshchenko, A.S. Kozhukhov, D.V. Sheglov, S.V. Eremeev, S.D. Borisova, E.V. Chulkov, Inertness and degradation of (0001) surface of Bi_2Se_3 topological insulator, Journal of Applied Physics, 112 (2012) 113702.

[84] V.V. Atuchin, V.A. Golyashov, K.A. Kokh, I.V. Korolkov, A.S. Kozhukhov, V.N. Kruchinin, S.V. Makarenko, L.D. Pokrovsky, I.P. Prosvirin, K.N. Romanyuk, O.E. Tereshchenko, Formation of Inert Bi_2Se_3(0001) Cleaved Surface, Crystal Growth & Design, 11 (2011) 5507-5514.

[85] L.V. Yashina, J. Sánchez-Barriga, M.R. Scholz, A.A. Volykhov, A.P. Sirotina, V.S. Neudachina, M.E. Tamm, A. Varykhalov, D. Marchenko, G. Springholz, G. Bauer, A. Knop-Gericke, O. Rader, Negligible Surface Reactivity of Topological Insulators Bi_2Se_3 and Bi_2Te_3 towards Oxygen and Water, ACS Nano, 7 (2013) 5181-5191.

[86] C. Yang, M. Cattelan, N. Fox, Y. Huang, M.S. Golden, W. Schwarzacher, Electrochemical Modification and Characterization of Topological Insulator Single Crystals, Langmuir, 35 (2019) 2983-2988.

[87] L.-L. Wang, D.D. Johnson, Ternary tetradymite compounds as topological insulators, Physical Review B, 83 (2011) 241309.

[88] A. Politano, M. Caputo, S. Nappini, F. Bondino, E. Magnano, Z.S. Aliev, M.B. Babanly, A. Goldoni, G. Chiarello, E.V. Chulkov, Exploring the Surface Chemical Reactivity of Single Crystals of Binary and Ternary Bismuth Chalcogenides, The Journal of Physical Chemistry C, 118 (2014) 21517-21522.

[89] B. Xu, Modulating the Conductance of a Au–octanedithiol–Au Molecular Junction, Small, 3 (2007) 2061-2065.

[90] Y. Teramae, K. Horiguchi, S. Hashimoto, M. Tsutsui, S. Kurokawa, A. Sakai, High-bias breakdown of Au/1,4-benzenedithiol/Au junctions, Applied Physics Letters, 93 (2008) 083121.

[91] R.J. Nichols, W. Haiss, S.J. Higgins, E. Leary, S. Martin, D. Bethell, The experimental determination of the conductance of single molecules, Physical Chemistry Chemical Physics, 12 (2010) 2801-2815.

[92] E.V. Basiuk, M. Monroy-Peláez, I. Puente-Lee, V.A. Basiuk, Direct Solvent-Free Amination of Closed-Cap Carbon Nanotubes: A Link to Fullerene Chemistry, Nano Letters, 4 (2004) 863-866.

[93] E.V. Basiuk, T.Y. Gromovoy, A.M. Datsyuk, B.B. Palyanytsya, V.A. Pokrovskiy, V.A. Basiuk, Solvent-Free Derivatization of Pristine Multi-Walled Carbon Nanotubes with Amines, Journal of Nanoscience and Nanotechnology, 5 (2005) 984-990.

[94] R. Zanella, E.V. Basiuk, P. Santiago, V.A. Basiuk, E. Mireles, I. Puente-Lee, J.M. Saniger, Deposition of Gold Nanoparticles onto Thiol-Functionalized Multiwalled Carbon Nanotubes, The Journal of Physical Chemistry B, 109 (2005) 16290-16295.

[95] S. Ham, S. Jeon, M. Park, S. Choi, K.-J. Paeng, N. Myung, K. Rajeshwar, Electrodeposition and stripping analysis of bismuth selenide thin films using combined electrochemical quartz crystal microgravimetry and stripping voltammetry, Journal of Electroanalytical Chemistry, 638 (2010) 195-203.

[96] L. Wang, S.-Y. Li, J.-H. Yuan, J.-Y. Gu, D. Wang, L.-J. Wan, Electron Transport Characteristics of the Dimeric 1,4-Benzenedithiol Junction, Chemistry – An Asian Journal, 9 (2014) 2077-2082.

[97] J. Zheng, J. Liu, Y. Zhuo, R. Li, X. Jin, Y. Yang, Z.-B. Chen, J. Shi, Z. Xiao, W. Hong, Z.-q. Tian, Electrical and SERS detection of disulfide-mediated dimerization in single-molecule benzene-1,4-dithiol junctions, Chemical Science, 9 (2018) 5033-5038.

[98] L.J. Perry, R. Wetzel, Disulfide bond engineered into T4 lysozyme: stabilization of the protein toward thermal inactivation, Science, 226 (1984) 555.

[99] T.E. Creighton, Disulphide bonds and protein stability, BioEssays, 8 (1988) 57-63.

[100] C. Backes, N.C. Berner, X. Chen, P. Lafargue, P. LaPlace, M. Freeley, G.S. Duesberg, J.N. Coleman, A.R. McDonald, Functionalization of Liquid-Exfoliated Two-Dimensional 2H-MoS_2, Angewandte Chemie International Edition, 54 (2015) 2638-2642.

[101] M.K. Bahl, R.L. Watson, K.J. Irgolic, X-ray photoemission studies of tellurium and some of its compounds, The Journal of Chemical Physics, 66 (1977) 5526-5535.

[102] K.-W. Zhang, D. Ding, C.-L. Yang, Y. Gan, S. Li, W.-K. Huang, Y.-H. Song, Z.-Y. Jia, X.-B. Li, Z. Zhu, J. Wen, M. Chen, S.-C. Li, Real-space characterization of reactivity towards water at the Bi_2Te_3(111) surface, Physical Review B, 93 (2016) 235445.

[103] K. Hoefer, C. Becker, D. Rata, J. Swanson, P. Thalmeier, L.H. Tjeng, Intrinsic conduction through topological surface states of insulating Bi_2Te_3 epitaxial thin films, Proceedings of the National Academy of Sciences, 111 (2014) 14979.

[104] P. Ngabonziza, R. Heimbuch, N. de Jong, R.A. Klaassen, M.P. Stehno, M. Snelder, A. Solmaz, S.V. Ramankutty, E. Frantzeskakis, E. van Heumen, G. Koster, M.S. Golden, H.J.W. Zandvliet, A. Brinkman,

In situ spectroscopy of intrinsic Bi_2Te_3 topological insulator thin films and impact of extrinsic defects, Physical Review B, 92 (2015) 035405.

[105] T.P. Debies, J.W. Rabalais, X-ray photoelectron spectra and electronic structure of Bi_2X_3 (X = O, S, Se, Te), Chemical Physics, 20 (1977) 277-283.

[106] G. Zhang, H. Qin, J. Teng, J. Guo, Q. Guo, X. Dai, Z. Fang, K. Wu, Quintuple-layer epitaxy of thin films of topological insulator Bi_2Se_3, Applied Physics Letters, 95 (2009) 053114.

[107] P. Magri, C. Boulanger, J.-M. Lecuire, Synthesis, properties and performances of electrodeposited bismuth telluride films, Journal of Materials Chemistry, 6 (1996) 773-779.

[108] M.S. Martin-Gonzalez, A.L. Prieto, R. Gronsky, T. Sands, A.M. Stacy, Insights into the electrodeposition of Bi_2Te_3, Journal of the Electrochemical Society, 149 (2002) C546-C554.

[109] M.S. Sander, A.L. Prieto, R. Gronsky, T. Sands, A.M. Stacy, Fabrication of High-Density, High Aspect Ratio, Large-Area Bismuth Telluride Nanowire Arrays by Electrodeposition into Porous Anodic Alumina Templates, Advanced Materials, 14 (2002) 665-667.

[110] M. Pourbaix, Atlas of Electrochemical Equilibria in Aqueous Solution, NACE, 307 (1974).

[111] A.-M. Netsou, U. Thupakula, J. Debehets, T. Chen, B. Hirsch, A. Volodin, Z. Li, F. Song, J. Won Seo, S. De Feyter, K. Schouteden, C. Van Haesendonck, Scanning probe microscopy induced surface modifications of the topological insulator Bi_2Te_3 in different environments, Nanotechnology, 28 (2017) 335706.

[112] C. Yang, Y. Huang, M.S. Golden, W. Schwarzacher, Electrochemical Scanning Tunneling Microscopy Study of Bismuth Chalcogenide Single Crystals, Langmuir, 35 (2019) 15100-15105.

[113] M.M.D. Ramos, A.P. Sutton, A.M. Stoneham, Effects of the STM tip on adsorbate image, Journal of Physics: Condensed Matter, 3 (1991) S127-S131.

[114] M.M.D. Ramos, A.M. Stoneham, A.P. Sutton, J.B. Pethica, Effects of the STM tip on atomic positions: an explanation for the nonobservation of adsorbed molecules?, Journal of Physics: Condensed Matter, 2 (1990) 5913-5917.

[115] Y. Nakamura, Y. Mera, K. Maeda, Diffusion of chlorine atoms on Si(111)-(7×7) surface enhanced by electron injection from scanning tunneling microscope tips, Surface Science, 487 (2001) 127-134.

[116] Y. Nakamura, Y. Mera, K. Maeda, Chlorine atom diffusion on Si(111)-(7×7) surface enhanced by hole injection from scanning tunneling microscope tips, Surface Science, 497 (2002) 166-170.

[117] K. Maeda, Y. Nakamura, Spreading effects in surface reactions induced by tunneling current injection from an STM tip, Surface Science, 528 (2003) 110-114.

[118] B.N.J. Persson, P. Avouris, The effects of the electric field in the STM on excitation localization. Implications for local bond breaking, Chemical Physics Letters, 242 (1995) 483-489.
[119] R.J. Nichols, D.M. Kolb, R.J. Behm, STM observations of the initial stages of copper deposition on gold single-crystal electrodes, Journal of Electroanalytical Chemistry and Interfacial Electrochemistry, 313 (1991) 109-119.
[120] N. Batina, D.M. Kolb, R.J. Nichols, An in situ scanning tunneling microscopy study of the initial stages of bulk copper deposition on gold(100): the rim effect, Langmuir, 8 (1992) 2572-2576.
[121] J.R. Lagraff, A.A. Gewirth, Nanometer-Scale Mechanism for the Constructive Modification of Cu Single-Crystals and Alkanethiol Passivated Au(111) with an Atomic-Force Microscope, J. Phys. Chem., 99 (1995) 10009-10018.
[122] W. Schmickler, E. Santos, Interfacial electrochemistry, Springer Science & Business Media2010.
[123] Z.H. Zhu, C.N. Veenstra, G. Levy, A. Ubaldini, P. Syers, N.P. Butch, J. Paglione, M.W. Haverkort, I.S. Elfimov, A. Damascelli, Layer-By-Layer Entangled Spin-Orbital Texture of the Topological Surface State in Bi_2Se_3, Physical Review Letters, 110 (2013) 216401.
[124] J.G. Analytis, J.-H. Chu, Y. Chen, F. Corredor, R.D. McDonald, Z.X. Shen, I.R. Fisher, Bulk Fermi surface coexistence with Dirac surface state in Bi_2Se_3: A comparison of photoemission and Shubnikov--de Haas measurements, Physical Review B, 81 (2010) 205407.
[125] M. Jamali, J.S. Lee, J.S. Jeong, F. Mahfouzi, Y. Lv, Z. Zhao, B.K. Nikolić, K.A. Mkhoyan, N. Samarth, J.-P. Wang, Giant Spin Pumping and Inverse Spin Hall Effect in the Presence of Surface and Bulk Spin−Orbit Coupling of Topological Insulator Bi_2Se_3, Nano Letters, 15 (2015) 7126-7132.
[126] A.R. Mellnik, J.S. Lee, A. Richardella, J.L. Grab, P.J. Mintun, M.H. Fischer, A. Vaezi, A. Manchon, E.A. Kim, N. Samarth, D.C. Ralph, Spin-transfer torque generated by a topological insulator, Nature, 511 (2014) 449-451.
[127] Y. Wang, P. Deorani, K. Banerjee, N. Koirala, M. Brahlek, S. Oh, H. Yang, Topological Surface States Originated Spin-Orbit Torques in Bi_2Se_3, Physical Review Letters, 114 (2015) 257202.
[128] Y. Liang, D. McLaughlin, C. Csoklich, O. Schneider, A.S. Bandarenka, The nature of active centers catalyzing oxygen electro-reduction at platinum surfaces in alkaline media, Energy & Environmental Science, 12 (2019) 351-357.
[129] Y. Liang, C. Csoklich, D. McLaughlin, O. Schneider, A.S. Bandarenka, Revealing Active Sites for Hydrogen Evolution at Pt and Pd Atomic Layers on Au Surfaces, ACS Applied Materials & Interfaces, 11 (2019) 12476-12480.

[130] T. Hirahara, G. Bihlmayer, Y. Sakamoto, M. Yamada, H. Miyazaki, S.-i. Kimura, S. Blügel, S. Hasegawa, Interfacing 2D and 3D Topological Insulators: Bi(111) Bilayer on Bi_2Te_3, Physical Review Letters, 107 (2011) 166801.

[131] S.H. Kim, K.-H. Jin, J. Park, J.S. Kim, S.-H. Jhi, T.-H. Kim, H.W. Yeom, Edge and interfacial states in a two-dimensional topological insulator: Bi(111) bilayer on Bi_2Te_2Se, Physical Review B, 89 (2014) 155436.

[132] M.-X. Wang, C. Liu, J.-P. Xu, F. Yang, L. Miao, M.-Y. Yao, C.L. Gao, C. Shen, X. Ma, X. Chen, Z.-A. Xu, Y. Liu, S.-C. Zhang, D. Qian, J.-F. Jia, Q.-K. Xue, The Coexistence of Superconductivity and Topological Order in the Bi_2Se_3; Thin Films, Science, 336 (2012) 52.

[133] M.-X. Wang, P. Li, J.-P. Xu, Z.-L. Liu, J.-F. Ge, G.-Y. Wang, X. Yang, Z.-A. Xu, S.-H. Ji, C.L. Gao, D. Qian, W. Luo, C. Liu, J.-F. Jia, Interface structure of a topological insulator/superconductor heterostructure, New Journal of Physics, 16 (2014) 123043.

[134] H. Matsushima, S.W. Lin, S. Morin, O.M. Magnussen, In situ video-STM studies of the mechanisms and dynamics of electrochemical bismuth nanostructure formation on Au, Faraday Discussions, 193 (2016) 171-185.

[135] M. Motoyama, Y. Fukunaka, S. Kikuchi, Bi electrodeposition under magnetic field, Electrochimica Acta, 51 (2005) 897-905.

[136] K. Tamura, J.X. Wang, R.R. Adžic, B.M. Ocko, Kinetics of Monolayer Bi Electrodeposition on Au(111): Surface X-ray Scattering and Current Transients, The Journal of Physical Chemistry B, 108 (2004) 1992-1998.

[137] F.-X. Wang, G.-B. Pan, Y.-D. Liu, Y. Xiao, Pb deposition onto Au(111) from acidic chloroaluminate ionic liquid, Chemical Physics Letters, 488 (2010) 112-115.

[138] U. Schmidt, S. Vinzelberg, G. Staikov, Pb UPD on Ag(100) and Au(100) — 2D phase formation studied by in situ STM, Surface Science, 348 (1996) 261-279.

[139] H. Ibach, Physics of surfaces and interfaces, Springer2006.

[140] Z.L. Bao, K.L. Kavanagh, Epitaxial Bi / GaAs(111) diodes via electrodeposition, Applied Physics Letters, 88 (2006) 022102.

[141] H. Hattab, E. Zubkov, A. Bernhart, G. Jnawali, C. Bobisch, B. Krenzer, M. Acet, R. Möller, M. Horn-von Hoegen, Epitaxial Bi(111) films on Si(001): Strain state, surface morphology, and defect structure, Thin Solid Films, 516 (2008) 8227-8231.

[142] S.A. Morin, A. Forticaux, M.J. Bierman, S. Jin, Screw Dislocation-Driven Growth of Two-Dimensional Nanoplates, Nano Letters, 11 (2011) 4449-4455.

[143] L. Chen, B. Liu, A.N. Abbas, Y. Ma, X. Fang, Y. Liu, C. Zhou, Screw-Dislocation-Driven Growth of Two-Dimensional Few-Layer and Pyramid-like WSe_2 by Sulfur-Assisted Chemical Vapor Deposition, ACS Nano, 8 (2014) 11543-11551.

[144] A. Zhuang, J.-J. Li, Y.-C. Wang, X. Wen, Y. Lin, B. Xiang, X. Wang, J. Zeng, Screw-Dislocation-Driven Bidirectional Spiral Growth of Bi2Se3 Nanoplates, Angewandte Chemie International Edition, 53 (2014) 6425-6429.

[145] D. Zherebetskyy, M. Scheele, Y. Zhang, N. Bronstein, C. Thompson, D. Britt, M. Salmeron, P. Alivisatos, L.-W. Wang, Hydroxylation of the surface of PbS nanocrystals passivated with oleic acid, Science, 344 (2014) 1380.

[146] A.O.A. Tanoh, J. Alexander-Webber, J. Xiao, G. Delport, C.A. Williams, H. Bretscher, N. Gauriot, J. Allardice, R. Pandya, Y. Fan, Z. Li, S. Vignolini, S.D. Stranks, S. Hofmann, A. Rao, Enhancing Photoluminescence and Mobilities in WS_2 Monolayers with Oleic Acid Ligands, Nano Letters, 19 (2019) 6299-6307.

[147] G.D. O'Neil, S. Ahmed, K. Halloran, J.N. Janusz, A. Rodríguez, I.M. Terrero Rodríguez, Single-step fabrication of electrochemical flow cells utilizing multi-material 3D printing, Electrochemistry Communications, 99 (2019) 56-60.

[148] E. Sahlin, A. ter Halle, K. Schaefer, J. Horn, M. Then, S.G. Weber, Miniaturized Electrochemical Flow Cells, Analytical Chemistry, 75 (2003) 1031-1036.

[149] M. Kitayama, R. Koga, T. Kasai, A. Kouzuma, K. Watanabe, Structures, Compositions, and Activities of Live Shewanella Biofilms Formed on Graphite Electrodes in Electrochemical Flow Cells, Applied and Environmental Microbiology, 83 (2017) e00903-00917.

[150] A. Otto, I. Mrozek, H. Grabhorn, W. Akemann, Surface-enhanced Raman scattering, Journal of Physics: Condensed Matter, 4 (1992) 1143-1212.

[151] R.M. Stöckle, Y.D. Suh, V. Deckert, R. Zenobi, Nanoscale chemical analysis by tip-enhanced Raman spectroscopy, Chemical Physics Letters, 318 (2000) 131-136.

[152] G. Goubert, X. Chen, S. Jiang, R.P. Van Duyne, In Situ Electrochemical Tip-Enhanced Raman Spectroscopy with a Chemically Modified Tip, The Journal of Physical Chemistry Letters, 9 (2018) 3825-3828.